Unravelling Turbulent Emulsions with lattice-Boltzmann simulations

Mukherjee, Siddhartha

DOI
10.4233/uuid:e98f7bbf-4639-49fc-96a4-b3543da637fc

Publication date
2019

Document Version
Final published version

Citation (APA)
Mukherjee, S. (2019). *Unravelling Turbulent Emulsions with lattice-Boltzmann simulations*. [Dissertation (TU Delft), Delft University of Technology]. https://doi.org/10.4233/uuid:e98f7bbf-4639-49fc-96a4-b3543da637fc

Unravelling Turbulent Emulsions

with lattice-Boltzmann simulations

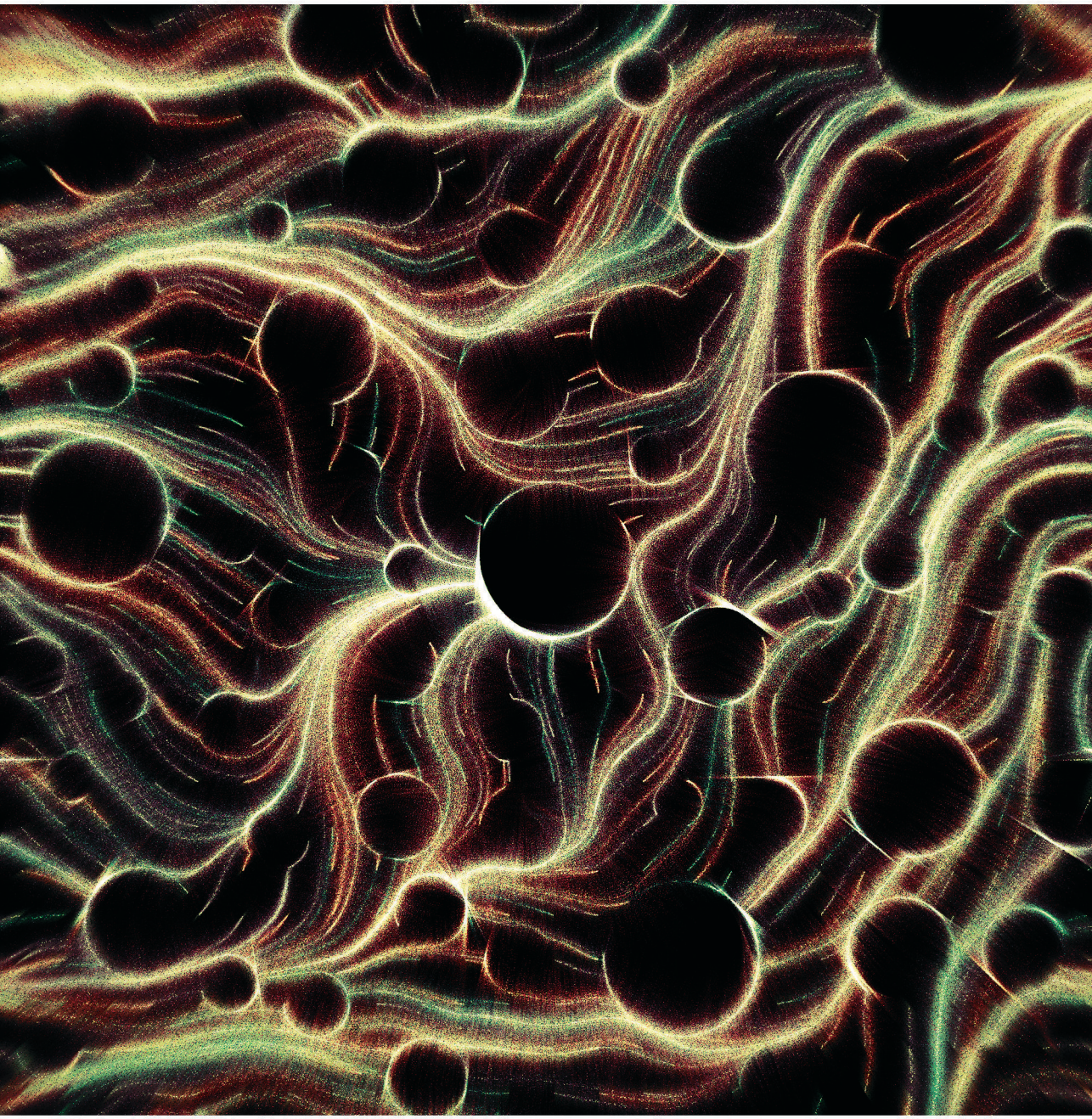

Siddhartha Mukherjee

UNRAVELLING TURBULENT EMULSIONS

WITH LATTICE-BOLTZMANN SIMULATIONS

UNRAVELLING TURBULENT EMULSIONS

WITH LATTICE-BOLTZMANN SIMULATIONS

Dissertation

for the purpose of obtaining the degree of doctor
at Delft University of Technology,
by the authority of the Rector Magnificus prof. dr. ir. T.H.J.J. van der Haagen,
chair of the Board of Doctorates,
to be defended publicly on 10 December, 2019 at 1500 hrs

———

by

Siddhartha MUKHERJEE

Master of Science in Mechanical Engineering, Delft University of Technology, the Netherlands
born in Kanpur, India

This dissertation has been approved by the promotors.

promotor: Prof. dr. ir. H.E.A. Van den Akker
promotor: Dr. S. Kenjereš, Dipl-Ing.

Composition of the doctoral committee:

Rector Magnificus,	chairperson
Prof. dr. ir. H.E.A. Van den Akker,	Delft University of Technology, promoter
Dr. S. Kenjereš, Dipl-Ing.,	Delft University of Technology, promoter
Independent members:	
Prof. dr.-Ing. Habil M. Krafczyk,	TU Braunschweig, Germany
Prof. dr. R.V. Calabrese,	University of Maryland, USA
Prof. dr. A. Soldati,	TU Wien, Austria
Prof. dr. ir. B.J. Boersma,	Delft University of Technology
Dr. L.M. Portela,	Delft University of Technology
Reserve member:	
Prof. dr. H.J.J. Jonker,	Delft University of Technology

Keywords: Turbulence, emulsions, droplet dynamics, simulations

Printed by: Ipskamp Printing

Front & Back: An algorithmic design, combining a Perlin flow field with a simple obstacle avoiding routine.

ISBN 978-94-6384-093-4

An electronic version of this dissertation is available at
http://repository.tudelft.nl/.

Dedicated to Achhima and Dadu.

“dekh zindāñ se pare rañg-e-chaman josh-e-bahār,
raqs karnā hai to phir paañv kī zanjīr na dekh.”

~ Majrooh Sultanpuri

“Look beyond the bars of your confine,
At the bloom of spring with joy replete,
If you ‘want’, not merely ‘wish’, to dance,
Don’t look at the shackles on your feet.”

“shauq-e-dīdār agar hai to nazar paidā kar.”

~ Ameer Minai

(Famously quoted by noted journalist Ravish Kumar as the most important lesson of all his schooling.)

“If you have the passion to *see*, then you must birth the right vision.”

SUMMARY

The mixing of two immiscible fluids, often under turbulent conditions, can lead to the formation of an emulsion, where droplets of one fluid are embedded in another fluid. The occurrence of emulsions is commonplace across industries, ranging from the oil industry to food processing and biotechnology. Why emulsions serve diverse applications, in grossly simple terms, is due to their structural organization, as the two fluids in an emulsion form exhibit very different physical properties than they do when separated. The stability of the emulsion structure, hence, is key for its utility. The presence of impurities, or surfactants, in the constituent fluids, greatly enhances emulsion stability, by preventing the coalescence of droplets (which would lead to phase segregation). Emulsion research, over the past century, has developed into a thriving field, driven by the force of detailed experimentation that has significantly informed modeling, control and design of processes dealing with emulsification.

Despite being predictable to a degree, the true nature of droplet dynamics at the heart of emulsification remains unknown. It is experimentally exceedingly difficult to illumine the evolution of interfaces undergoing coalescence and breakup, while simultaneously reporting the three-dimensional, turbulent flow features. It is slowly becoming feasible, however, to tackle these problems by using numerical simulations. Such simulations, too, involve a level of modeling complexity and pose heavy computational demands, and have hence remained an exception. It is only now becoming feasible to simulate such complex flows, allowing us to augment experiments with numerical insights. In this thesis, we attempt to unravel emulsification (to a small extent) by using simulations resolving both flow and interfaces, while considering fluids with impurities.

We begin with a brief investigation into the choice of numerical method applicable for the problem, in Chapter 2. The main requirements were (1) simulating interface resolving multiphase flows, i.e. allowing for coalescence and breakup without models, (2) simulating impure fluids, i.e. incorporating surfactant effects and (3) simulating resolved turbulent flows, involving a range of length and time scales. The associated computational demands mandate that the numerical technique should be suited to provide reasonable results within reasonable time. We show that different numerical techniques for simulating multiphase flows are still not very robust. Seemingly minor differences, between the implementation and modeling of the interface, can lead to different results, even for simple flow problems. Between the volume-of-fluid and lattice-Boltzmann methods, we chose the latter for the remainder of our study because it allows simulating surfactants with relative ease, along with the benefit of faster computations when considering turbulent flows.

We then present a simplification of a surfactant model present in the literature in Chapter 3, to simulate surfactant-laden droplet flows. We reproduce, qualitatively, several features relevant for simulating surfactant effects on droplet dynamics. This includes preferential seeking of interfaces by the surfactant, a reduction in surface tension between the two fluids and modification of droplet dynamics. However, the proposed

model is found to have two shortcomings. The surfactant is found incapable of autonomously inhibiting coalescence, which requires additional numerical mechanisms, like the multiple-belt interparticle force method (well known in the literature). The other limitation of the model is the dependence of multiple output system parameters (like density ratio and surface tension), on the input parameters (like repulsion strength and density). The pseudopotential lattice-Boltzmann method does not allow an easy separation between cause and (multiple) effects of this kind.

Before simulating turbulent emulsions, in Chapter 4, we investigate coherent structures that arise in turbulent flows. The form of these structures is a crucial (unanswered) question regarding turbulence, which holds key to turbulence flow organization and dynamics, and their effects on Lagrangian objects like droplets that are influenced by turbulence fluctuations. Although the hierarchy of turbulence scales has never been observed, the concept is often invoked in turbulence theory, including the Kolmogorov-Hinze theory of droplet breakup, which is at the heart of emulsification. We develop tools to identify and disentangle flow structures that arise in homogeneous, isotropic, single-phase turbulence. The tools are based upon correlation concepts and Helmholtz decomposition techniques. We show, for the first time, that high kinetic energy structures form *jet-like* streamlines, while (as is known from literature) high enstrophy regions are consistently associated with *swirling-flow*. Using the Biot-Savart reconstruction, we further show that high kinetic energy *jets* are neither self-generating, nor induced by strong vorticity. Their coherence is induced dominantly by the non-local, intermediate vorticity. High enstrophy structures, on the other hand, are a superposition of the background vorticity induced velocity field and a degree of self-generated strengthening of swirling flow. Further research on the dynamics and evolution of these structures will help describe turbulence as an emergent organization of simpler dynamical blocks. These results hint at an alternative view of turbulence organization, where the flow field is emergent from the non-local and non-linear interaction of structures dominated by the background vorticity field. This view casts into doubt the usual "hierarchy of structures" concept that has been classically adopted.

In Chapter 5, we then investigate turbulent emulsions, for the time being, formed from two pure fluids. This is because first, we need to understand the dynamics of a pure system, before introducing the additional complexity of impurities. Secondly, the surfactant model of Chapter 3 requires modifications before being suitable for inhibiting coalescence, specially under turbulent conditions. This chapter presents several new physical findings regarding the dynamics of turbulent emulsions and emulsion morphology. We show that emulsions obtain a morphology determined by the volume fraction of the dispersed fluid, surface-tension and turbulence intensity, along with the forcing wavenumber of the turbulence generation in the periodic box of the simulation. Under the influence of strong turbulence, droplet sizes follow a strong power-law distribution. The multiphase kinetic energy spectra is shown to bear the marks of coalescence and breakup, at scales smaller than and larger than the Hinze scale, respectively. Droplets are shown to enhance vortex compression and axial strain turbulence topologies, possibly due to elastic interfaces counter-acting increase in surface area. The breakup-coalescence 'equilibrium' is shown to have a limit-cycle like dynamics. A series of time-delayed intermittency correlations link fluctuations in power input to fluctuations in energy dissipation, which further link to fluctuations in droplet number density.

The ‘equilibrium’ is marked by alternating coalescence and breakup dominated dynamics. These findings shed new light on emulsification, which may help in improving the model formulation for coalescence and breakup kernels. Directions for future research, which shall improve the fundamental understanding of droplet dynamics in turbulence, have also been outlined in Chapter 6.

Overall, this thesis shows how several existing numerical methods can be combined (with small modifications), to simulate complex flow problems like turbulent emulsification. These simulations, while being limited often in the extent of the parameter space that can be explored, reveal in unprecedented detail the intricacies of the system dynamics. The greater challenge, then, becomes interpreting the data and asking the right questions that will illumine the core phenomena. As simulations such as these slowly become more commonplace, research into emulsions, droplet-laden flows and turbulence organization can begin to ask experimentally obscure questions. Notwithstanding, experimental efforts need to concurrently be made to steer numerical studies closer to observations. With a strong synergy between the two, numerical simulations will be a candle in the dark.

SAMENVATTING

Het mengen van twee niet-mengbare vloeistoffen, vaak onder turbulente omstandigheden, kan leiden tot het vormen van een emulsie, waarin druppels van de ene vloeistof in de andere vloeistof zijn ingebed. Emulsies komen in vele vakgebieden voor, variërend van de olie industrie tot voedselverwerking en biotechnologie. Dat emulsies voor vele toepassingen worden ingezet, komt simpel gezegd door hun interne structuur, waardoor een emulsie van twee vloeistoffen heel andere fysieke eigenschappen ten toon spreidt dan de afzonderlijke vloeistoffen. De stabiliteit van de emulsiestructuur is daarom essentieel voor haar nut. De aanwezigheid van onzuiverheden, of van oppervlakte-actieve stoffen ("surfactants"), in de twee vloeistoffen bevordert de stabiliteit van emulsies aanzienlijk, doordat deze de samensmelting ("coalescentie") van druppels voorkomt die kan leiden tot fasescheiding. Het onderzoek aan emulsies heeft zich in de afgelopen eeuw ontwikkeld tot een bloeiend vakgebied, dankzij de gedetailleerde experimenten die aanzienlijk hebben bijgedragen aan het modelleren, beheersen en ontwerpen van processen waarbij emulsies bij zijn betrokken.

Ondanks het feit dat een zekere mate van voorspelbaarheid is bereikt, blijft de ware aard van de druppeldynamiek bij de emulsievorming onbekend. Het is nog steeds ontzettend moeilijk met experimenten licht te werpen op het ontstaan van grensvlakken bij het samensmelten en opbreken van druppels en tegelijkertijd de driedimensionale turbulente stromingseigenschappen te beschrijven. Langzaam maar zeker wordt het echter haalbaar numerieke simulaties te gebruiken om deze problemen aan te pakken. Ook zulke simulaties vereisen een zekere mate van complexe modellering en trekken een zware wissel op computerkracht, waardoor ze tot op heden een uitzondering zijn. Pas nu wordt het haalbaar zulke complexe stromingen te simuleren, waardoor we experimentele kennis kunnen uitbreiden met inzichten uit simulaties. In dit proefschrift proberen we emulsievorming (enigszins) te ontrafelen door voor vloeistoffen met onzuiverheden de stroming en de grensvlakken expliciet op te lossen.

We beginnen in hoofdstuk 2 met een kort onderzoek naar de numerieke methode die voor dit probleem toepasbaar is. De voornaamste vereisten waren (1) het expliciet oplossen van de grensvlakken in de meerfasenstroming zodat samensmelting en opbreken van druppels niet hoeft te worden gemodelleerd, (2) het simuleren van onzuivere vloeistoffen waardoor effecten van surfactants worden meegenomen en (3) het oplossen van turbulente stromingen op een reeks van lengte- en tijdschalen. De bijbehorende rekenvereisten moeten het toelaten dat de numerieke techniek binnen redelijke tijd redelijke resultaten oplevert. We tonen aan dat verschillende numerieke technieken voor het simuleren van meerfasenstroming nog steeds niet erg robuust zijn. Ogenschijnlijk kleine verschillen tussen de implementatie en de modellering van het grensvlak kunnen leiden tot verschillende resultaten, zelfs voor simpele stromingsproblemen. We verkiezen een lattice-Boltzmann methode boven een volume-of-fluid methode, omdat surfactants daarmee relatief makkelijk kunnen worden gesimuleerd en turbulente stromingen sneller kunnen worden doorgerekend.

In hoofdstuk 3 bespreken we een vereenvoudiging van een in de literatuur bestaand surfactantmodel om stromingen van druppels met surfactants te simuleren. We reproduceren kwalitatief verschillende eigenschappen relevant voor het simuleren van surfactanteffecten op druppeldynamica. Zo concentreert de surfactant zich bij voorkeur aan grensvlakken, verlaagt hij de oppervlaktespanning tussen de twee vloeistoffen en verandert hij de druppeldynamica. Echter, het model heeft op twee vlakken tekortkomingen. De surfactant blijkt de druppelsamensmelting niet zelf te kunnen beletten zodat daarvoor verdere numerieke mechanismen nodig zijn, zoals de "multiple-belt interparticle force" methode (bekend uit de literatuur). De andere beperking van het model is dat meerdere uitvoersysteemparameters (zoals de dichtheidsverhouding en de oppervlaktespanning) afhangen van de invoerparameters (zoals de afstotingskracht en de dichtheid). De pseudopotentiaal lattice-Boltzmann methode staat geen gemakkelijke scheiding toe van oorzaak en de (verschillende) effecten.

Voordat we turbulente emulsies simuleren, bestuderen we in hoofdstuk 4 coherente structuren die in turbulente stromingen ontstaan. De vorm van deze structuren is een cruciale (onbeantwoorde) vraag over turbulentie, die de sleutel is tot begrip van de organisatie van turbulente stroming, de dynamica, en de effecten van turbulentie op de Lagrangiaanse objecten zoals druppels die worden beïnvloed door turbulente fluctuaties. Hoewel de hiërarchie van turbulentieschalen nooit is waargenomen, wordt het concept vaak gehanteerd in de turbulentietheorie, zo ook in de Kolmogorov-Hinze theorie voor het opbreken van druppels, wat zeer belangrijk is voor emulsievorming. We ontwikkelen gereedschappen om stromingsstructuren te identificeren en te ontwarren die ontstaan in homogene isotrope éénfase turbulentie. De gereedschappen zijn gebaseerd op correlatieconcepten en Helmholtz decompositietechnieken. We demonstreren voor het eerst dat structuren met een hoge kinetische energie jet-achtige stroomlijnen vormen, terwijl (zoals bekend uit de literatuur) gebieden met hoge enstrofie altijd gerelateerd zijn aan een sterke vorticiteit. Met de Biot-Savart reconstructie tonen we voorts aan dat jets met een hoge kinetische energie niet zelfgenererend zijn en ook niet worden geïnduceerd door een sterke vorticiteit. De coherentie van deze jets wordt voornamelijk bepaald door de niet-lokale, meer gematigde vorticiteit. Structuren met een hoge enstrofie, daarentegen, zijn een superpositie van het snelheidsveld geïnduceerd door de achtergrondsvorticiteit, en een zekere mate van zelf-gegenereerde versterking van wervelende stroming. Verder onderzoek naar de dynamica en evolutie van deze structuren zal het mogelijk maken turbulentie te beschrijven als een zich ontwikkelende organisatie van simpelere dynamische blokken. Deze resultaten wijzen op een alternatieve kijk op de organisatie van turbulentie, waarbij het stromingsveld voortkomt uit de niet-lokale en niet-lineaire interactie van structuren die worden gedomineerd door het achtergrondsvorticiteitsveld. Deze zienswijze trekt de traditionele kijk op turbulentie als een "hiërarchie van structuren" in twijfel.

In hoofdstuk 5 onderzoeken we dan turbulente emulsies, vooralsnog gevormd uit twee zuivere vloeistoffen. We doen dit omdat we eerst begrip moeten vormen van de dynamica van een zuiver systeem, alvorens we de grotere complexiteit van onzuiverheden introduceren. Voorts behoeft het surfactantmodel uit hoofdstuk 3 aanpassingen voor het geschikt is coalescentie af te remmen, zeker onder turbulente omstandigheden. In dit hoofdstuk presenteren we verschillende natuurkundige bevindingen betreffende turbulente emulsies en emulsiemorfologie. We tonen aan dat de morfologie van emulsies

wordt bepaald door de volumefractie van de gedispergeerde fase, de oppervlaktespanning en, de intensiteit van de turbulentie alsmede het golfgetal waarmee de turbulentie wordt aangedreven in de periodieke doos van de simulatie. Onder invloed van sterke turbulentie volgt de druppelgrootte een kansverdeling volgens een sterk machtsverband. De meerfasen kinetische-energiespectra vertonen de kenmerken van coalescentie en druppelopbreking op schalen respectievelijk kleiner dan en groter dan de Hinze-schaal. We vinden dat druppels wervelcompressie en turbulentietopologieën van axiale vervorming versterken, misschien doordat elastische grensvlakken de vergroting van het oppervlak tegenwerken. Het opbreek-coalescentie "evenwicht" heeft de dynamica van een limietcyclus. Een reeks in de tijd vertraagde intermitterende correlaties koppelen fluctuaties in vermogenstoevoer aan fluctuaties in energiedissipatie, die weer relateren aan fluctuaties in druppelaantaldichtheid. Het "evenwicht" wordt gekarakteriseerd door dynamica die afwisselend wordt gedomineerd door coalescentie en opbreking. Deze bevindingen werpen een nieuw licht op emulsievorming en kunnen helpen bij het opstellen van een model voor coalescentie- en opbreekkernels. In hoofdstuk 6 worden ook richtingen voor toekomstig onderzoek geschetst, die ons fundamentele begrip van druppeldynamica onder turbulente condities zullen vergroten.

Dit proefschrift laat zien hoe meerdere bestaande numerieke technieken (met kleine wijzigingen) kunnen worden gecombineerd om complexe stromingsproblemen, zoals turbulente emulsievorming, te bestuderen. Hoewel deze simulaties veelal slechts een beperkte parameterruimte beslaan, tonen ze de complexe details van de systeemdynamiek met een tot nu toe ongeëvenaarde precisie. De grootste uitdaging wordt nu het analyseren van de data en het stellen van de juiste vragen om de kernverschijnselen te doorgronden. Nu zulke simulaties langzaam gebruikelijker worden kan op het gebied van emulsies, stromingen met druppels en turbulentie-organisatie onderzoek worden gedaan naar vragen die met experimenten onduidelijk blijven. Desalniettemin moeten naast simulaties ook experimenten blijven worden uitgevoerd, zodat numeriek onderzoek aan waarnemingen kan worden geijkt. Slechts met een sterke synergie tussen de twee onderzoeksmethoden zullen numerieke simulaties een licht in de duisternis zijn.

CONTENTS

1

INTRODUCTION

THE keywords in the phrase "*simulating surfactant-laden turbulent emulsions*" tie together the work done in this thesis. Before the details involved in realizing this work (to the small extent that we could in this thesis) are discussed and the outline for the thesis laid out, these key concepts have been explained briefly to acquaint the reader with the general idea behind these individually exhaustive topics.

1.1. EMULSIONS

Emulsions are liquid—liquid dispersions where a dense suspension of droplets of one fluid, called the dispersed phase, is embedded in another fluid called the continuous (or carrier) phase, the two fluids being essentially immiscible. Figure 1.1 shows a sketch of the microstructure of a typical emulsion. The dense packing of polydispersed droplets and the presence of large interfacial areas separating the two fluids is seen clearly.

The difference between an emulsion and its constituent fluids is primarily structural, where the dispersed phase being present in the form of densely packed droplets lends the emulsion physical properties markedly different from its constituent fluids when they are completely demixed. These properties can be both physically relevant and quantifiable, like rheology (viscosity), strength and stability; or perceptual and unquantifiable, like taste and texture. It is due to these enhanced properties that emulsions find relevance in various industries. For instance, in food processing, emulsions lend the characteristic texture and taste to products like butter and mayonnaise [1]. Emulsions can be Janus-faced to the oil and gas industry, where on the one hand they can be detrimental to crude oil production [2], or to the contrary, enable enhanced oil recovery [3]. Emulsions are also being used as miniature laboratories in microfluidic devices, where living cells can be compartmentalized into individual droplets [4]. They are also highly relevant to the production of various cosmetic products that are manufactured in emulsion form. A final example is that of analogue photography—where light sensitive emulsions [5] have long been used in photographic films to give the characteristic tones, grain and colours to photographs, another related example being the wet-plate collo-

1

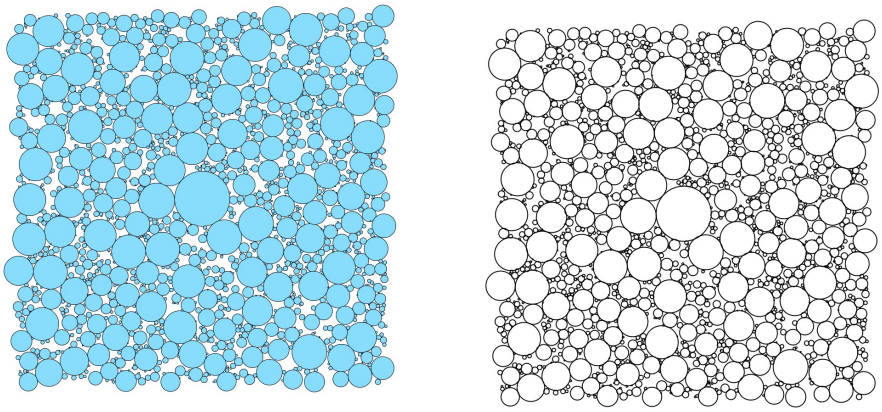

(a) The dispersed phase in an emulsion, comprising a distribution of droplets of different sizes.

(b) The same dispersion, where the interfaces have now been highlighted.

Figure 1.1: A sketch of a typical emulsion micro-structure. (Made using a custom circle packing algorithm in *Processing*.)

dion process [6]—as it turns out, emulsions have enabled the preservation of memories by immobilizing light.

The morphology of an emulsion depends upon the physical properties of its constituent fluids (like density, viscosity and surface tension), the ratio in which the fluids have been mixed, and the mixing conditions during preparation (shear rate, turbulence intensity, rate of energy dissipation etc.). So even if only the final state of the emulsion is considered of relevance, the associated parameter space is quite large which makes such a system difficult to predict. Although, with over a century of experimentation and modeling, emulsification has become well controlled in certain circumstances, even though the underlying dynamics of emulsification remains obscure.

The common physical mechanism involved in most emulsification processes is the breakup of droplets of the dispersed phase, which is mediated by shear stresses arising in flow which can be either laminar[1] or turbulent. Droplet breakup increases the interfacial area S_A in the dispersion, consequently increasing the surface energy (albeit reversibly). This excess energy makes emulsions inherently unstable, prone to structural collapse by droplet coalescence, making the lifetime of an emulsion a problem of stability. Depending on the application, a long lifetime emulsion may or may not be desired, where in the latter case special steps must be taken to de-emulsify the fluid mixture to separate the constituent fluids. An emulsion is stable as long it retains its dispersion morphology, which is destroyed when droplets begin to coalesce. Most naturally and artificially formed emulsions are usually very stable, the reason for which is the presence of addi-

[1] As is being studied by my collaborators Dr. A. Safdari and Dr. M. Pourtousi together with Dr. O. Shardt and Prof. dr. H.E.A. Van den Akker in the Bernal Institute, University of Limerick, Ireland. They consider a dense suspension in Couette flow, where a constant shear rate leads to dispersion formation at high viscosity values.

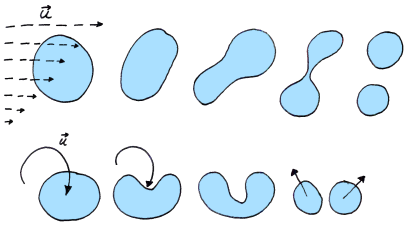

(a) Droplet breakup due to shear and interaction with an eddy.

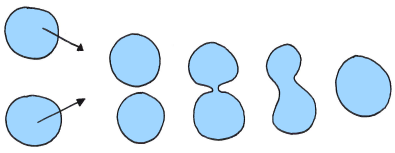

(b) Coalescence of two droplets after collision.

Figure 1.2: Sketches showing the processes of breakup and coalescence of droplets. (Hand drawn)

tional species or impurities that inhibit droplet coalescence. These impurities can be of different kinds, for instance colloidal particles leading to the formation of Pickering emulsions [7, 8], long chain polymeric hydrocolloids [9], proteins [10], starch nanocrystals [11], or the more commonly encountered molecules called *surfactants* [12].

1.2. SURFACTANTS: THE SINEWS OF STABILITY

Surfactants are large molecules with a bipolar structure that comprise a long hydrocarbon tail which is hydrophobic, and a polar head which is hydrophilic (this is why they are also referred to as *amphiphiles*). When present in a liquid-liquid mixture like oil and water, surfactants selectively seek out interfaces with their tails residing in the oil-phase and head in the water-phase (hence also attaining a specific orientation with respect to the interfacial surface). All soaps and detergents are essentially surfactants and work by exploiting this preferential interfacial residence of surfactant molecules.

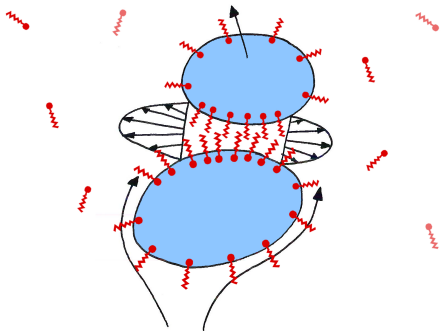

Figure 1.3: A sketch of surfactant-laden droplets in approach. The finite sized surfactant molecules are shown to create a steric repulsion between the interfaces, which prevents the thin film in between from draining, hence shielding droplet coalescence. (Hand drawn)

When surfactants cover interfaces, they also begin to inhibit droplet coalescence. There are a few reasons for this—the first being the steric-repulsion between surfactant molecules residing on interfaces in approach. This repulsion prevents film drainage be-

tween the interfaces, consequently preventing coalescence. Surfactants can also prevent film drainage by immobilizing the interface. This occurs when the interfacial boundary condition transitions from free-slip (fully mobile) for a clean droplet, to no-slip (i.e. a rigid surface) for fully surfactant-loaded interfaces. Repulsion between interfaces can also occur due to the presence of charges on the interface, since surfactants interact with the thin electric double layers that are formed around all interfaces. The other mechanism for coalescence inhibition is related to the fact that the formation of smaller droplets increases surface energy in the system, which can be quantified as $E_\gamma = S_A\gamma$, where γ is the interfacial tension, and S_A is the total interfacial area. Since coalescence of droplets tries to minimize E_γ, another route by which surfactants inhibit coalescence is by reducing the interfacial tension between the fluids, hence reducing the excess surface energy ΔE_γ formed by the breakup of droplets. If γ is reduced to zero, droplet breakup can occur spontaneously, as there is no energetic penalty on the formation of interfaces.

Apart from coalescence inhibition, surfactants also greatly influence the dynamics of droplets by modifying flow. Variations in surfactant concentration along the interface, such as may be caused by external convection around a droplet that sweeps surfactants along the interface causing fore-aft asymmetry in the surfactant distribution, gives rise to gradients in interfacial tension. This in turn drives Marangoni convection, which generally opposes the external convection driven circulation inside the droplet. The droplet devoid of internal convection begins to behave more like a rigid sphere, which experiences a higher drag force than a clean droplet. Marangoni convection can also lead to local interfacial hardening, if the surfactant concentration becomes saturated. These phenomena, together, can significantly alter the droplet dynamics, which already for clean (surfactant-free) systems is a complicated affair when the underlying flow is turbulent.

1.3. TURBULENCE: A PLAYGROUND OF INSTABILITIES

Turbulence can broadly be described as irregular fluid motion across a range of length and time scales that occurs when instabilities amplify to dominate the flow, a typical turbulence flow field has been shown in figure 1.4. It is a very ubiquitous physical phenomenon, and has been encountered at lengthscales ranging from Angstroms to light years - in which it has "*no other analogue in all of physics*"[2]. That said, turbulence also eludes *precise* definition or mathematical description, and has been famously called the "*graveyard of theories*" by Liepmann [13]. Before the relevance of turbulence to this thesis is discussed, the diversity of its associated phenomena can be glimpsed by considering how researchers have described turbulence at the *beginning* of their famous books/articles. This shows the many faces of the problem, and a few such examples have been cited below.

Batchelor [14] begins by mentioning that at low viscosities, "*the velocity* [fluctuations] *at any time and position...are not found to be the same...when measured under seemingly identical conditions*" while the "*average properties are determined uniquely*" - which highlights two important and connected aspects. First is the sensitivity to initial conditions, and the second is essentially the philosophy of Reynolds decomposition of a turbulent variable into mean and fluctuating parts (where only the former is repro-

[2] As described by Prof. K.R. Sreenivasan in the 2018 Chandrashekhar lectures delivered at ICTS, Bangalore, India.

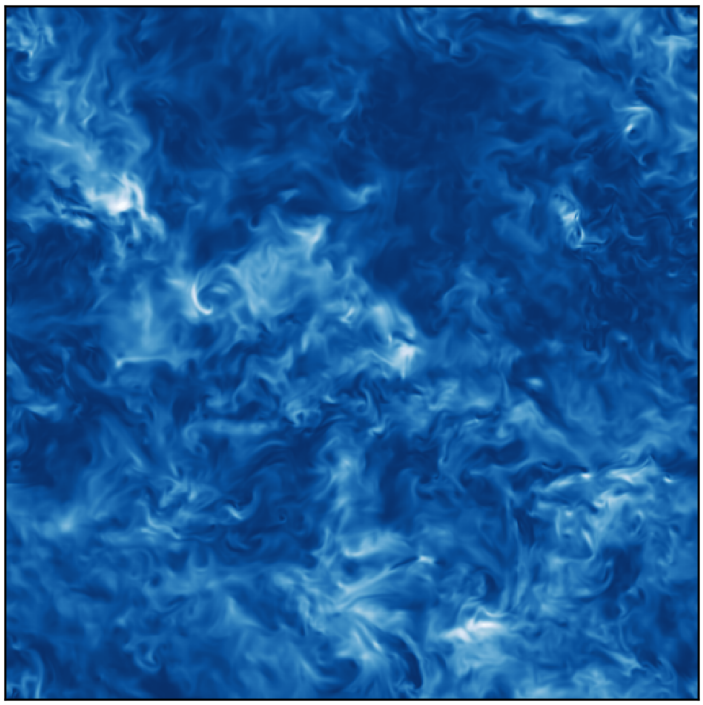

Figure 1.4: Snapshot of a typical turbulence flow field. This image shows the turbulent kinetic energy (at a single plane from a 3D simulation). Structures over various lengthscales can be seen here. (From one of the simulations done for Chapter 4.)

ducible in an experiment). Pope [15] starts off with the same idea, which has allowed modeling turbulence in countless engineering circumstances, to varying degrees of detail and accuracy. Ruelle and Takens [16] begin by tying turbulence inextricably to chaos - "*fluid motion* [that] *becomes very complicated, irregular and chaotic*" at "*sufficiently large, steady action*". Tennekes and Lumley [17] begin by describing turbulence in terms of its properties like "*irregularity, diffusivity, three-dimensional vorticity fluctuations and dissipation*". Frisch [18] highlights at the outset how the phenomenology of turbulence could not have been divined from the Navier-Stokes equations alone and it is only explained *after* looking at experimental facts (essentially pointing at its *emergent* nature), just as "*life cannot be explained from the equation of quantum mechanics*". Turbulence is then tied to the fundamental concept of "*breaking and restoration of symmetries*". Davidson [19] points to the unresolved (though seemingly simple) question - "*How fast does kinetic energy decay in a cloud of turbulence?*", which is closely tied to the concept of "*intermittency*". Lastly, Tsinober [13] begins by making the distinction between the "*nature of the phenomenon of turbulence*" and the "*nature of the problem of turbulence*", the two not being synonymous as one is the phenomenon itself while the other is the human description of it. In his characteristic wit, he urges us to develop our "*own judgement*

1

based upon the huge literature" and "*separate the 'essence' from the 'the water'*"[3].

Turbulence is perhaps the most natural state of fluid motion dominated by inertia, as long as there is a constant energy injection mechanism and a source of instabilities. For fully developed turbulent flow at high Reynolds numbers (i.e. the ratio of inertial forces to viscous forces), a balance is achieved between the energy injection rate and the rate of energy dissipation (by viscosity, into heat). These two processes, however, happen at very different scales - the former is at the largest scales of motion i.e. $\mathscr{L}$, which then via the dynamics of turbulence, leads to the generation of a range of smaller scales. The smallest scales η are those where inertial and viscous forces locally balance out, and it is at these scales that the kinetic energy is dissipated. Kolmogorov hypothesized the existence of a *universal* range of scales $\eta \ll l \ll \mathscr{L}$ (also called the inertial range) where the only activity is the transfer of energy from a relatively larger scale to a relatively smaller scale. For these range of scales, the kinetic energy $E(k)$ is found to scale as $k^{-5/3}$ where k is the wavenumber associated with a lengthscale. This range is independent of the anisotropy of the largest scales (i.e. the energy injection scale), and the extent of the inertial range of scales is a measure of the turbulence intensity.

In this thesis, we consider emulsification under the influence of turbulence, which is the physically encountered situation in many real processes that generate emulsions, for instance, those using homogenizers [20]. We further limit ourselves to droplets in the inertial range of turbulence (sub-Kolmogorov droplets are also known to break due to viscous stresses [21]). The main effect of turbulence on droplets of sizes comparable to the inertial range scales is to cause fragmentation of large droplets into smaller daughter droplets. This is mediated by shear stresses across the droplet diameter, which cause droplet deformation. If the droplets exceed a critical size, they tend to break into smaller droplets. This can be characterized by the critical Weber number (the ratio between inertial forces and surface tension forces) We_{crit}, which Hinze [22] expressed as a function of the energy dissipation rate ϵ to predict a scaling for the maximum stable droplet diameter d_{max}, for an *inviscid* drop. Note that d_{max} is also frequently referred to as the "Hinze scale" (which is how we refer to this quantity as well, for clarity, in this thesis), however, Hinze did not name this scale as such, and it is not known to the author where this nomenclature first appeared in the literature.

It has been found for the breakup of bubbles that We_{crit} predicted by the Kolmogorov-Hinze theory is a factor 10 times larger than the We_{crit} for liquid-liquid dispersions, even though the breakup mechanism for bubbles and droplets was found to be essentially the same [23]. Levich [24] proposed a modification of the Kolmogorov-Hinze theory to account for this difference, bringing We_{crit}, both for droplet and bubbles, close to unity. This was done by forming a Weber number as the ratio of the disruptive stress (arising from *internal* dynamic pressure fluctuations, as opposed to *external* in Kolmogorov-Hinze theory), and cohesive stress acting on a bubble (which takes into account surface tension and an idealized approximation of bubble deformation), see, for instance Hesketh *et al.* [23], Ko [25]. In our study, since we deal with droplets (and not bubbles), we refer to the original Kolmogorov-Hinze scaling.

Under the action of turbulence, droplets larger than the Hinze scale break up in a cas-

[3] It is almost a Delft tradition to introduce turbulence using the ancient Eastern parable of blind men trying to describe the whole of an elephant, by touching just one part of it. As far as a complete description of turbulence goes, we have still not addressed the elephant in the room.

cading (breakup) process, and it was proposed by Garrett *et al.* [26] that the droplet distribution follows a $d^{-10/3}$ power law scaling, which was also found by Deane and Stokes [27] for air bubbles in breaking ocean waves. This process generates a typical droplet morphology characterizing the emulsion. The major questions involved are

- What are the dominant droplet breakup mechanisms?
- What is the nature of droplet-turbulence interactions?
- Is there an equilibrium steady state of coalescence and breakup?
- Can a desired emulsion morphology be achieved?

As mentioned earlier, these processes in the presence of surfactants can be significantly altered.

1.4. CHALLENGES INVOLVED

Droplet dynamics in turbulence is intrinsically three dimensional, with highly localized surfactant effects that bear consequences for the global properties of the emulsion. These, coupled with the fact that emulsions are optically opaque (at least to the visible range of light), makes the physics highly intractable to experiments. Further, intrusive measurements can effect the phenomenon itself, which can be detrimental to measuring the spatial distribution of velocity required for quantifying velocity gradients, a crucial aspect that governs droplet breakup. So far, our knowledge on emulsions via experiments is limited to statistical or integral quantities (for instance droplet size distribution or the rate of kinetic energy dissipation), that are more or less well defined but do not shed light on the dynamics of emulsification. Even for pure fluid systems (i.e. without surfactants) a debilitating aspect is the range of scales involved in these processes, where droplets can have sizes in the range $10^{-6} < d < 10^{-3}$ [m], turbulent flow can have length-scales between $10^{-6} < l < 10^{0}$ [m], and industrial scale equipment can be of the size of $\sim \mathcal{O}10^{1}$ [m] - the entire range varying over $7-8$ orders of magnitude. Surfactants interact with interfaces at the molecular level, which is a further $2-3$ orders of magnitude below the smallest droplet size. This shrouds the optimization of existing emulsification processes as well as development of new ones in uncertainty, rendering decision making an art rather than a science.

Solutions have been sought by conducting idealized physical and numerical experiments of coalescence and breakup. These reveal, in detail, the dynamics for well defined conditions [28, 29], for example two particles approaching each other in simple shear flow. Coalescence and breakup in large scale systems are then modeled with the help of so-called 'kernels' derived on the basis of the simplified experiments. There are a few flaws in this approach, even though from a modeling perspective it has its merits. First is that there is no easy extrapolation from results found for small, idealized systems to the multiple droplet, large scale regimes encountered in practice. This makes it difficult to also validate the breakup and coalescence kernels available in literature against experiments, since they involve assumptions regarding dynamical processes difficult to experimentally observe. For instance, high energy dissipation causes increase in collision frequency but decreases collision efficiency, which can be difficult to measure. Or the effect of droplet viscosity partially immobilizing the interface but retarding droplet flattening.

A second shortcoming of kernel formulations is that the high degree of empiricism often neglects crucial dynamics underlying the system. Lastly, the effect of surfactants is either completely ignored, or corrected for in an ad-hoc manner in these kernels.

It is these issues that we attempt to address with this thesis - i.e. aiming to reduce the level of empiricism involved in the modeling of emulsification processes by including the dynamical aspects of emulsification. Often, the challenge undertaken in this task turned out greater than anticipated at the outset. Instead of solving the problem, the process of studying it revealed its true dimensions, along with the extent of our lack of understanding. Keeping that in mind, the outline of the thesis is presented below where we work on three connected issues namely (1) *objectively choosing a numerical method* appropriate for simulating liquid-liquid emulsions, (2) *simulating surfactant-laden emulsions* and finally (3) *simulating emulsions in a fully turbulent regime*, allowing for droplet breakup and coalescence to investigate the dynamics. These problems are interspersed with additional practical issues, all of which are worth noting and shall hence be touched upon briefly.

1.5. OUTLINE OF THE THESIS

This thesis consists of three studies as mentioned above, along with a study on the identification of structures in turbulence, each forming a chapter. These chapters being in the form of papers obscures the wider context and background into which they fit. A small motivation and history is hence provided, as to the 'how' and 'why' regarding our decisions to proceed in a particular direction. More importantly, a few issues are mentioned regarding methods that did not work, and possible causes for their failure - these might even be more interesting for a reader invested in similar studies, than the results obtained from successful simulations.

1.5.1. CHAPTER 2: CHOICE OF NUMERICAL METHOD

The first major challenge regarding the simulations was a (debated) choice of the numerical method that was to serve as a base for this study. The main requirements of the technique to be employed were an ability to simulate droplet coalescence and breakup, including the effects of surfactants and fully resolving turbulent flow, while doing all this within a 'reasonable' amount of time. This meant that Euler-Euler two-fluid approaches cannot be employed (since they do not resolve interfacial dynamics), and also rely upon turbulence modeling using the RANS approach, while we intend to perform DNS simulations. We also wanted the technique to be as simple as possible, and to develop it using open-source software. This cast into conflict the familiar world of finite-volume methods against the abstract precincts of the lattice-Boltzmann method (where the latter still holds an ability to knit editorial eyebrows into suspicion). The techniques considered for this thesis have been described below (while other techniques could also be used).

FINITE VOLUME: VOLUME-OF-FLUID METHOD

Generally in the finite-volume method, the equations for the conservation of mass and evolution of momentum of a fluid are solved. For an incompressible fluid, conservation of mass reduces to the continuity equation, which then together with the Navier-Stokes

equation (momentum evolution) can be written as follows

$$\nabla \cdot \mathbf{u} = 0$$
$$\frac{\partial \mathbf{u}}{\partial t} + \mathbf{u} \cdot \nabla \mathbf{u} = -\frac{1}{\rho}\nabla p + \nu \nabla^2 \mathbf{u} + \frac{\mathbf{F}}{\rho} \tag{1.1}$$

Here $\mathbf{u}$ is the fluid velocity, ρ density, p pressure, ν kinematic viscosity and $\mathbf{F}$ incorporates all body forces. Numerically, these equations are solved with an iterative solution procedure to couple the pressure to the velocity satisfying the continuity equation.

There are several ways to simulate interface resolving multiphase flows with the finite-volume method, which are broadly classified into 'interface tracking' and 'interface capturing' methods [30, 31]. Interface tracking methods explicitly define the interface as a surface, which moves and evolves along with the flow and hence must be tracked. The flow on both sides of the interface is resolved and coupled with appropriate interfacial boundary conditions taking into account the effect of surface tension. These include front-tracking [32, 33] and moving-mesh techniques [34, 35]. Interfaces in these methods are infinitely sharp, and special procedures are required in some cases to allow for coalescence and breakup, which involves models for film drainage and additional mesh cut-and-merge algorithms. Interface capturing methods operate on a fixed computational grid, and solve for the evolution of an interface function which gives the position of the interface. This includes the level-set method [36, 37], volume-of-fluid (VoF) method [38], free-energy based phase-field methods [39, 40].

In this study we focused on VoF, readily available in OpenFOAM, which offered a few advantages. First was a straightforward method for capturing evolving interfaces using a phase indicator (α) transport equation which has the basic form of

$$\frac{\partial \alpha}{\partial t} + \nabla \cdot (\mathbf{u}\alpha) = 0 \tag{1.2}$$

where the value of α (equal to 0 or 1) represents one fluid or the other, and $0 < \alpha < 1$ marks the interfaces. Using the α field, surface tension effects are incorporated into the Navier-Stokes equation, for instance by using the continuum surface force formulation [41]. The two immiscible fluids are modeled with a single fluid formulation, as the Navier-Stokes equations are solved for a 'fictitious' fluid with physical properties like density and viscosity $\psi \in \{\rho, \nu\}$ taken to be a phase-indicator weighted mean of the properties of the two constituent fluids.

$$\psi = \psi_1 \alpha + \psi_2 (1 - \alpha) \tag{1.3}$$

This approach makes it easy to simulate two *completely* immiscible fluids with widely different density and viscosity ratios (although extremely high and low values do introduce caveats). The second advantage (common to finite-volume based methods) was the ease of interpretation of parameters, and hence results, in both dimensional and non-dimensional terms.

VoF also posed several limitations, first of which was the generation of spurious currents due to inaccuracies in the curvature determination required for the surface tension force. Despite numerical remedies like artificial interface smoothening [42] to reduce curvature gradients, spurious currents can be significant and can begin to dominate the

dynamics of small droplets, influencing droplet coalescence and breakup. It can even be difficult to simulate a droplet at rest since the convection generated by spurious currents moves the droplet around in a random walk. Further, VoF involves significant computational cost exacerbated by the requirement for solving an additional species transport equation along with the iterative pressure-velocity fluid solver. Simulating droplets in turbulence with the VoF method could become prohibitively expensive, particularly for the very long simulations required for collecting turbulence statistics.

The last, and perhaps most significant limitation of VoF (solely from the perspective of this work), was the requirement for rather complicated modifications to the original VoF solver to enable simulating surfactants. To hint at the acuteness of this problem, it suffices to consider how a handful of state-of-the-art studies tried to simulate soluble surfactants. The surfactant is treated as a passive scalar with its own bulk transport equation (coupled to the VoF equations). This is mostly a trivial modification, except when accounting for difference in solubility of the surfactant in the two fluids, in which case the interfacial concentration jump needs to be accounted for and results were found to be solver dependent[4].

The adsorption of surfactants onto interfaces poses the biggest challenge, since VoF does not 'track' and geometrically define interfaces explicitly, and it is only upon considering the α−field that the presence of an interface becomes evident. This is overcome by constructing surface meshes around interfaces [45], onto which the surfactant species is allowed to adsorb (and desorb from) following a pre-set adsorption (and desorption) isotherm. To further simulate surfactant redistribution and concentration gradients on the interface (where the latter gives rise to surface tension gradients crucial for simulating Marangoni effects), an additional surface transport equation needs to be solved in conjunction to the volumetric transport. Numerically, this can also introduce mass conservation errors. So far, this has mostly been done on a single rising bubble, barely allowed to deform [45–47]. The extension to droplets that can break or coalesce will rapidly digress into the tedious realm of dynamic surface meshing and mesh topology, which relies heavily on ad-hoc mesh cut and merge algorithms which can be very accurate but computationally challenging [48]. Given that none of these additional algorithms were available to begin with, using VoF for this study was eventually discounted as an option.

There was the additional possibility of inventing a new method for simulating surfactants with VoF, where instead of identifying and constructing meshes around interfaces, the α gradient at the interface could be exploited with some form of potential force functions that would urge the surfactant to seek out interfaces instead of residing in the bulk. If at all possible, what would have been a new modification to VoF, was already well known within the lattice-Boltzmann (LB) method.

[4] The continuous species transport (CST) method of Marschall *et al.* [43] gave accurate results for composite semi-infinite media with varying diffusivity, in comparison to analytical solutions from Crank *et al.* [44], when using the *harmonic* interpolation for diffusion terms in OpenFOAM. The validation by Marschall *et al.* [43] is essentially a comparison of the discretization in OpenFOAM to a high-resolution, 1D MATLAB implementation of the same discretization scheme - which is not a validation of the CST method itself.

PSEUDOPOTENTIAL LATTICE-BOLTZMANN METHOD

The lattice-Boltzmann (LB) method is a mesoscopic numerical technique based upon the Boltzmann equation that can be written compactly as

$$\frac{df}{dt} = \Omega(f) \tag{1.4}$$

where f is the particle distribution function, $f(\mathbf{x}, \xi, t)$, which can be considered a generalization of density which takes into account the particle velocity ξ [49]. The total derivative of f can be written out as

$$\frac{df}{dt} = \left(\frac{\partial f}{\partial t}\right)\frac{dt}{dt} + \left(\frac{\partial f}{\partial x_\beta}\right)\frac{dx_\beta}{dt} + \left(\frac{\partial f}{\partial \xi_\beta}\right)\frac{d\xi_\beta}{dt} \tag{1.5}$$

where the $dx_\beta/dt = \xi_\beta$ is the particle velocity and $d\xi_\beta/dt = F_\beta/\rho$ is the specific body force. Replacing these gives the Boltzmann equation with a body force F_β as

$$\frac{\partial f}{\partial t} + \xi_\beta\frac{\partial f}{\partial x_\beta} + \frac{F_\beta}{\rho}\frac{\partial f}{\partial \xi_\beta} = \Omega(f) \tag{1.6}$$

In LB, the discretized Boltzmann equation is solved on a space-momentum lattice for the transport of the discrete particle distribution f_i (i being the number of velocity directions). The collision operator $\Omega(f)$ can be simplified in various ways, the most common being a BGK approximation [50], which links collision frequency to the macroscopic fluid viscosity. The idea behind the BGK approximation is to drive the system to local (Maxwell-Boltzmann) equilibrium at a linear rate, even if the overall system is far from equilibrium (as would be the case for turbulent flow, for instance). Although often counted among the 'particle' based methods, there are no particles involved in LB apart from their concept being implicit in the distribution function (hence the method is *meso*-scopic). The Navier-Stokes equations can be derived from the Boltzmann equation using the Chapman-Enskog expansion, which is why LB can be used to simulate fluids in general, although the method is rooted in kinetic theory generally valid for gases only. The LB equation can accurately proxy the Navier-Stokes equations, generating flows that satisfy conservation of mass (continuity) and momentum. However, LB solves for weakly compressible flow and has a finite speed of sound in the system. The flow velocities being simulated should hence be in the low Mach number limit to satisfy the incompressibility condition. The LB equation turns out to be much simpler to numerically solve, where the algorithm comprises of two steps, namely 'streaming' and 'collision'. Further, all particle interactions are localized, whereby the method is highly conducive for massive parallelization [49, 51].

LB brings the remarkable advantages of computational speed and the ease of simulating multiphase flows. LB based multiphase solvers are classified under the category of diffuse interface methods, where the interfaces separating fluids are smeared over a few grid cells. Like in VoF, the interface in LB is not tracked, and it is through the variation in density of a fluid component (analogous to the variation of the phase indicator function α in VoF), that the interface can be defined. This can be seen in the middle and right panels of figure 1.5, where the red and blue fluids are separated by thin, diffuse interfaces. There are fundamentally different multiphase models within the LB

framework, where in this thesis we have used the "pseudopotential" (PP) method. In PP-LB, inter-component interactions are modeled using a potential-like, nearest-neighbour force that acts between components. This force is usually repulsive for inter-component interactions (between dissimilar fluid parcels), and attractive for intra-component interactions (within the same fluid parcel). This causes spontaneous phase segregation between two fluids that are initially mixed (also known as coarsening or spinodal decomposition, figure 1.5 shows such a process), and allows naturally for coalescence and breakup (albeit with other caveats[5]).

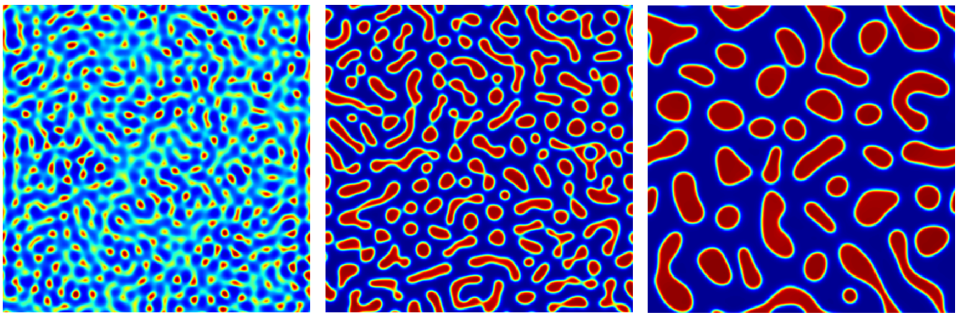

Figure 1.5: A phase segregation simulation shows how small droplets are formed due to repulsion between the two constituent fluids (shown in blue and red), which then grow via coalescence (left to right). (From one of the simulations done for Chapter 3.)

A further point to be noted is the difference between single-component multiphase LB and multi-component multiphase LB. In the former, a single fluid is modeled using an equation of state, such that if the fluid is at a sub-critical temperature, there are two stable density values it can assume (corresponding to the vapor and liquid halves of the spinodal curve), hence initiating phase segregation. In multi-component multiphase LB, there are multiple fluid components, where each fluid can be either ideal or non-ideal, and there are interaction forces (usually repulsive) acting between fluids. Such systems result in fluid mixtures with A-rich and B-rich regions, with small amounts of A dissolved in B and vice-versa.

One of the drawbacks of LB is that it has significantly higher memory requirements than finite volume techniques. The distribution function f usually has components along 19 directions when discretized on a three dimensional lattice (the number can be lower or higher depending upon the flow being simulated). This means, that for every fluid component, 19 variables need to be stored at *each* grid point - which makes the memory requirement scale as $N^3 \times 19 \times m \times 8$ [bits], where m is the number of fluid components being simulated (in finite-volume methods, the number of variables to be stored at each grid point is fewer as one needs to only store three velocity components, pressure and an additional species volume fraction - if density and viscosity are kept constant). This can soon become prohibitive for increasing grid sizes, although given the state of present-day processors, memory limitations will not become the first hur-

[5] These are issues common to diffuse interface methods, namely a preference for coalescence when interfaces overlap and the dissolution of small droplets which are inherently unstable. In Chapter 5, these issues are discussed at length.

dle. A greater challenge PP-LB poses is the interpretation of all parameters in the model which can be only made to coincide with real-world parameters upon constructing dimensionless number groups. Further, some parameters like the liquid-liquid repulsion coefficient (the so-called G values) gives rise to the interfacial tension γ between the fluids, although γ can only be calculated *a posteriori* from a simulation - making exact control of physical properties a difficult task. This can be alleviated by parameter space testing (a taste of which is presented in Chapter 3 for surfactant laden emulsions), to ascertain the functional form of the dependence between input parameters and output properties. Overcoming this limitation can be cumbersome, and although it is not a severe problem, it often works against LB by being disagreeable to researchers better versed the with finite volume framework of problem formulation which is more straightforward.

INTER-COMPARISON STUDY

To ascertain the relative strengths and weaknesses of the VoF and single-component PP-LB methods, an intercomparison study was performed which is presented in Chapter 2. This was a first of study its kind performed on liquid-liquid systems, while a similar comparison between front-tracking and lattice-Boltzmann has been performed for simulating rising bubbles [52]. One of the greatest challenges this comparison posed was the formulation of a problem that could be commonly solved by VoF and single-component PP-LB alike, where both methods were used in their primitive form with minor modifications. Upon simulating falling droplets, a deceptively simple problem, it was found that different numerical methods can predict different results, even when they closely agree over numerical benchmarks (as is shown for VoF simulations using OpenFOAM and FLUENT). This casts into doubt the usual practice of validating solvers using purely numerical benchmarks, particularly for multiphase flows where the points of departure between different simulation techniques are many. For this reason, and from the general lessons learned from the inter-comparison study, this thesis does not endorse *either* VoF of PP-LB unconditionally. Multiphase numerical solvers, despite being around for decades, are still in their infancy with regards to robustness. The only viable suggestion is to assess techniques by pitching them in direct comparison for the designated problem one intends to solve. For this thesis, the PP-LB method was chosen because of the low spurious currents at low density ratios, and upon considering the next steps that were to be taken in this work for simulating surfactant laden turbulent emulsions. PP-LB allowed a conceptually and practically simple method for simulating surfactants, and provided an advantage in computational time (by a significant factor), which would facilitate the demanding 3D simulations of turbulence to be performed within reasonable time.

1.5.2. CHAPTER 3: SIMULATING SURFACTANTS WITH PP-LB

A first difference between surfactant molecules as described earlier in this introduction and 'numerically simulated' surfactants is that the latter must be treated as a species or fluid in the continuum sense. It is neither feasible, nor necessary to simulate individual surfactant molecules, so long as surfactant effects can be adequately represented in the modeling approach. The one aspect that is essential here is the solubility of surfactants in the two fluids, since clean droplets in passing through an impure fluid will rapidly accumulate surfactants at the interface. Hence any method that restricts surfactants only

to interfaces cannot be used for our intended applications, and the surfactant species must be allowed volumetric transport, as well as transport along the interface. Volumetric transport and partial miscibility of surfactants is implicitly present in the PP-LB method when the surfactant is treated as an additional fluid component.

In Chapter 3, a model for surfactants using PP-LB is presented, which is a simplification of the Nekovee *et al.* [53], Chen *et al.* [54] model. A three component (all non-ideal, following the Carnahan-Starling EOS) system is simulated, where two of the components form an emulsion (with density and viscosity ratio ~ 1). The third component is the surfactant, which has a lower concentration[6], around $\mathcal{O}(10^{-3})$ in comparison to the two major components. This is done to mimic physical systems where surfactants are usually present in very small amounts, even a few parts per million. Also, having a high surfactant density will lead to a ternary system with three immiscible fluids where the surfactant can form sizable droplets of its own, which was not the objective. Such a ternary system is considered in Chen *et al.* [54], where the surfactant density is almost comparable to the density of the fluids. Non-ideal EOS modeling allows varying the reduced temperature of the components to achieve different density ratios as required.

The surfactant is repelled by the two other fluid components, which are also mostly immiscible. This makes the surfactant accumulate at interfaces (see figure 1.6), and varying the ratio of the repulsion acting on it from the two component fluids can change its miscibility in the fluid components. Here we ignore any dipole behaviour of the surfactant, electric fields and long range repulsions. These are the simplifications we allow ourselves in comparison to Nekovee *et al.* [53], Chen *et al.* [54], as their model is relatively complex. Although their model has found application in simulating several exotic fluid mixtures and configurations (explained in more detail in Chapter 3), it has not been used to simulate more commonly encountered surfactant laden multiphase flow problems. We wanted to describe a surfactant in as simple terms as possible - to which additional complexity can be introduced depending on the requirements of the application.

We perform a parameter space study of our proposed model, and show for the first time a reduction in surface tension between the two fluid components arising completely from inter-particle interaction forces. This surface tension reduction resembles a family of Langmuir isotherms, without any pre-set isotherms being imposed upon the system (as is usually done in alternative techniques employing LB and FV). The surfactant was shown to influence the dynamics of droplet formation at an aperture.

The main shortcoming of this work was the inability to simulate coalescence inhibition with the proposed method. Although, by varying the surface tension between the components as a function of the local surfactant density, droplet coalescence was shown to be arrested to some degree. Achieving coalescence inhibition more accurately requires additional extensions to the model, the most obvious ones being a long-range repulsion in the constituent fluids as proposed by Falcucci *et al.* [55], or a similar long range repulsion in the surfactant such that approaching interfaces are slowed down which will prevent film drainage, hence preventing coalescence. The latter may be more difficult to achieve in the current model due to the lower density of the surfactant, which would generate a weaker repulsion force unable to counteract the attractive forces of coalesc-

[6] In LB parlance, 'concentration' and 'density' are often used inter-changeably. What both terms denote is the total mass of the component, divided by the total volume of the system. Low density of a component means that, within the region of consideration, it has a lower density in comparison to other components.

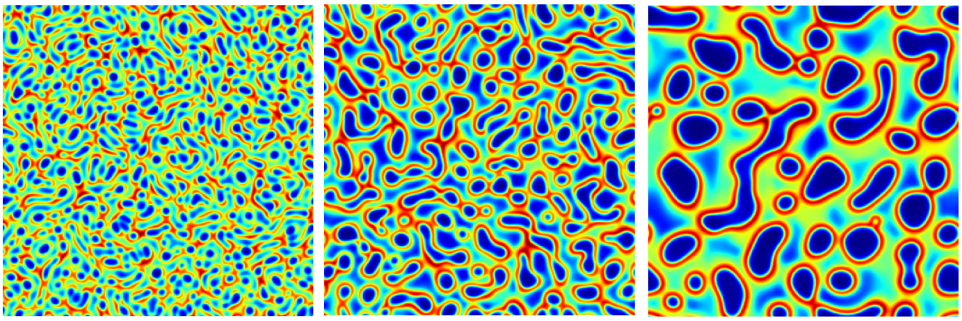

Figure 1.6: Surfactants added to a phase segregation simulation (with blue to red via green representing low to high concentrations). The surfactant is more miscible in the continuous phase, and collects strongly around interfaces. (From one of the simulations done for Chapter 3.)

ing droplets. The other limitation the current model posed was regarding independent control of all parameters in the system. There are several 'control' parameters like the various inter-component repulsion strengths, initial densities and equation of state variables - all of which together determine the final system state in terms of the liquid-liquid density ratio and surface tension. Although there is direct correspondence between the control parameters and the final system state, significantly more work is required to ascertain the form of their dependence. It may indeed not be possible to vary individual system properties with this approach, and instead, varying a single control parameter may have multiple consequences on the state of the physical system being simulated.

1.5.3. CHAPTER 4: STRUCTURES IN TURBULENCE

The first step towards simulating turbulent emulsions was implementing a turbulence forcing mechanism in the LB framework, while considering a single-phase fluid. The adopted method created a low wavenumber spectral force, which had a similar form to Alvelius [56], Ten Cate *et al.* [57], although it was constructed in real space following Biferale *et al.* [58]. Applying this force to a fluid initially at rest generated statistically stationary, homogeneous isotropic turbulence, where the energy input is balanced by the energy dissipation. These simulations were readily validated by testing the correlation functions, structure functions and the energy spectra.

The classical adage used to explain turbulence is a hierarchy of velocity-field structures, that in superposition give the flow its various characteristics. These are conceptually referred to as "vortices" or "eddies", and often "coherent structures". This idea dates back to Richardson's famous verse summarizing an "eddy breakup" mechanism believed to drive a turbulence cascade, where large scales generate successively finer scales:

> "*Big whorls have little whorls, that feed on their velocity,*
> *And little whorls have lesser whorls, and so on to viscosity.*"
> ~ L.F. Richardson [59]

So far, such a cascading process has not been shown in the real space where the phenomenon of turbulence occurs, although ample evidence for it has been found in other representational spaces [60]. There have also been significant efforts to characterize and

identify the "coherent structures" of turbulence, which has led to a wealth of literature and tools. The dynamics and the form of turbulence structures is an important aspect also with regards to our study, since the turbulence cascade has a directional energy flux from larger to smaller scales. Addition of particles or droplet to turbulence will fundamentally modify this process, and possibly introduce newer routes of energy transfer, including the possibility of inverse fluxes. Droplets, especially, can interact with turbulence across different lengthscales, and hence can potentially influence typical flow structures. Furthermore, the classical prediction of droplet sizes in a turbulent flow, following the Kolmogorov-Hinze theory, depends on an assumption of a cascade.

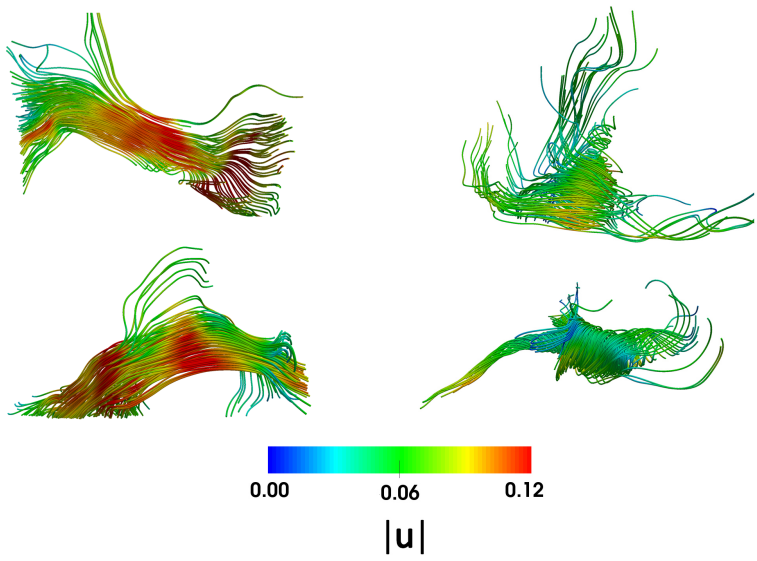

Figure 1.7: Typical structures from homogeneous isotropic turbulence simulations, shown as (total velocity) streamlines generated at the core of the associated correlation kernels. Left: Two instances of high kinetic energy regions that show the *jet-like* structure. Right: Two instances of high enstrophy regions that have a strong swirling motion. The colours represent velocity magnitude $|\mathbf{u}|$ in non-dimensional lattice units. (Selected results from Chapter 4.)

In Chapter 4, we focus on a few basic questions regarding turbulence structures, namely what are the typical forms of the spatial structures that arise in instantaneous velocity and vorticity field realizations, and their spatial organization. These are neither statistically emerging structures, nor do they emerge from averaging procedures. So far, most work done on identifying coherent structures utilize *point* concepts based upon the velocity gradient tensor [61–63]. Although these are useful for various applications, they cannot be used to identify spatially finite, velocity structures. This is because a finite structure in the velocity field $\mathbf{u}$ is generated by the integral contributions of the global divergence ($\nabla\cdot\mathbf{u}$) and curl ($\nabla\times\mathbf{u}$) fields, along with the far-field influence (if any), according to the Helmholtz decomposition. Point criterion, like Q, R (i.e. the second and third invariants of the velocity gradient tensor $A_{ij}=\partial u_i/\partial x_j$) for instance, describe the velocity field within the infinitesimal neighbourhood of each point in the flow field.

Although several of these points may be connected to form a structure with a certain value of Q everywhere, this may not reflect structure in the velocity field itself, which is formed by the global integral of the velocity gradients. The Helmholtz decomposition helps overcome this, and further, it can be used to disentangle the *local* (or *near-field*) and *non-local* (*far-field*) velocity gradient contributions to a local velocity structure.

This study first introduces new mathematical tools to identify spatially coherent flow regions, and then, utilizing the specific form of the Helmholtz decomposition valid for incompressible flows—the Biot-Savart law—identifies the vorticity contributions to these typical structures. By treating 'coherence' to mean 'correlation' in a spatial sense, correlation pseudo-vectors are generated using various definitions involving the velocity and vorticity fields, including correlations developed based upon the nature of the Biot-Savart law itself. Our study shows, for the first time, that high kinetic energy regions are consistently *jet-like*, with nearly parallel streamlines at the core of the correlation kernels. High vorticity regions, as was known, are associated with strong swirling flow in their vicinity. Examples of these flow types are shown in figure 1.7. Interestingly, the Biot-Savart reconstruction of the velocity field shows that high kinetic energy regions are generated by non-local, intermediate vorticity contributions, and lack any significant vorticity of their own. The swirling regions of high vorticity are a superposition of background vorticity induced flow and self-generating swirling motion. Strong vorticity regions remain mostly non-interacting, and their Biot-Savart contribution rapidly decays. High kinetic energy and high vorticity regions are also found to remain mutually exclusive in space, showing how these dynamically different entities populate the volume of the flow field.

This study opens a new door into studying spatial turbulence structures from a geometric perspective. The Biot-Savart rule emerges as a very useful tool for disentangling turbulence structures from their state of superposition. Further extending these ideas to studying the dynamics and time evolution of structures will reveal their life-cycles, possibly shedding light on complex phenomena like eddy interactions, breakup and the inter-scale interactions, all in real-space. These ideas also readily extend to other vector fields emerging in electromagnetism, magnetohydrodynamics or soft active matter flows.

1.5.4. CHAPTER 5: SIMULATING TURBULENT EMULSIONS

In Chapter 5, direct numerical simulations (DNS) of turbulent emulsions are performed for surfactant free fluids using the PP-LB method. The lengthscales resolved in these simulations range from the turbulence forcing scale $\mathscr{L}$ (large scale energy injection), a significant inertial range of scales (which follow the $E(k) \sim k^{-5/3}$ Kolmogorov scaling), extending down to the dissipation range ($\sim \eta$). Droplet diameters d after turbulent emulsification (in physical systems) will be typically $d \ll \mathscr{L}$, as any large initial volumes of the dispersed phase will soon fragment to sizes smaller than the large scale turbulence. Further, since the grid size $\Delta x \sim \eta$, droplets below roughly 10η will be unstable (due to diffuse interface effects, as discussed in the chapter) and droplets smaller than η cannot be resolved. The possible droplet sizes in the system hence fall in the range $\eta < d \ll \mathscr{L}$. For a fixed turbulence intensity, a lengthscale for the maximum stable droplet diameter can be estimated, which is called the "Hinze scale" after Hinze [22] (although valid for dilute, inviscid suspensions, while ignoring coalescence). This lengthscale typically

separates the unstable and stable droplet sizes, which are more prone to break up and coalesce, respectively. The Hinze scale, since it depends on dissipation, is also an intermittent quantity, and hence represents a distribution of droplet sizes in the system, specially when coalescence is not being inhibited (such that larger droplets are continuously formed as well, which are prone to break up). In this study, we intend to resolve droplets in the inertial range of turbulence. Hence d will have a distribution ranging from several times larger than the Taylor lengthscale λ up to several times the Kolmogorov scale η. The situation is shown in figure 1.8 with regards to the lengthscales of the system.

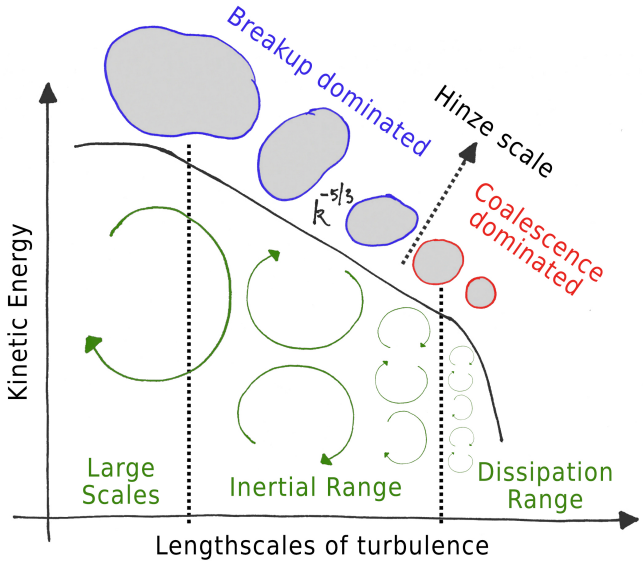

Figure 1.8: Schematic of the kind of turbulent emulsion system in consideration. Droplets are simulated in the inertial range (while Kolmogorov size droplets, or smaller, cannot be simulated). The Hinze [22] scale differentiates unstable droplet sizes (more prone to breakup) from stable droplet sizes (more prone to coalesce). (Hand drawn.)

We began with the multicomponent setup developed for Chapter 3, while ignoring the surfactant component, to start with a pure, two-fluid system. The turbulence forcing scheme, as used in Chapter 4, was adapted for this setup. To simulate turbulence, a separation of scales is required, which can be achieved by either having a very large domain (and energy injection scale), or a low viscosity which allows the generation of small scales. Both work equivalently, as far as turbulence alone is considered, due to the lack of an inherent lengthscale in the system. Although, since the first approach is computationally unfeasible, the second method is usually adopted. Doing so, it was soon found that the non-ideal fluid setup of Chapter 3 was incompatible with low viscosity values. The problem was viscosity dependent phase-segregation between the two fluids, which became weaker at low viscosity values. Due to this, sharp interfaces were not formed and the two fluid components remained dissolved in one another. This eventually was found to be a known issue [64], which could be remedied to an extent by using

a different forcing scheme for the pseudopotential interactions (unrelated to the turbulence forcing scheme which is a volumetric force field generation mechanism and not a numerical scheme). Since the turbulent emulsions work also exclusively focused on low density ratio systems, this would have implied keeping the non-ideal fluid components at above critical temperatures (to prevent intra-component phase separation, required to ensure a liquid-liquid final composition). This would render the polynomial operations associated with the CS-EOS redundant. With these considerations in mind, the setup was changed to two ideal Shan-Chen fluid components, separated by a repulsive pseudopotential force, which has been used before in literature to simulate turbulent dispersions [58, 65, 66]. In this setup, viscosity could be reduced to a sufficient degree, along with ensuring phase-segregation, to have well developed multiphase turbulence. Note that the proposed setup can also be easily used for various different configurations, like simulating sub-Kolmogorov droplets.

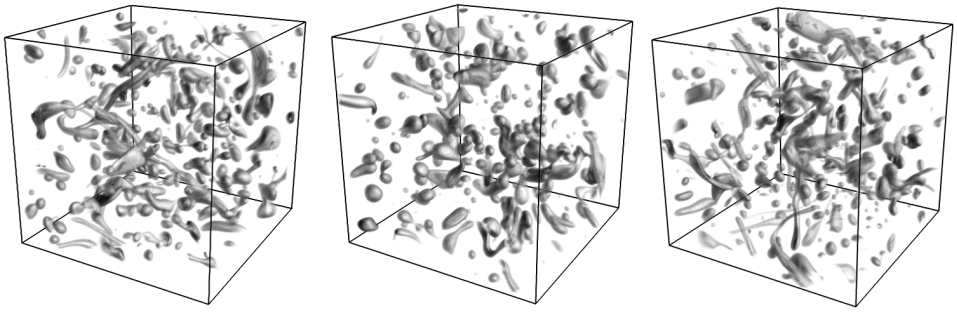

Figure 1.9: Dispersed phase in a turbulent emulsion. The three snapshots show how a characteristic morphology is achieved and there is a constant interplay of coalescence and breakup. (From simulations performed for Chapter 5.)

The dynamics of the dispersion formation process is revealed in great detail with these simulations, which are possible in certain regions of the turbulent emulsions parameter space. The most important consideration is having a turbulence intensity that causes droplet fragmentation without overpowering the pseudopotential repulsion completely, in which case the two fluids would become miscible (as also happens in the real world). Through long duration simulations (upto 300 turnover timescales), we report emulsion formation of different morphologies depending on the volume fraction, interfacial tension and turbulence intensity. Analysis of the quasi-equilibrium of coalescence and breakup is presented, where the state variables (kinetic energy, dissipation, droplet number density and surface energy) are found to evolve as time delayed limit cycles. Lastly, modification of turbulence at a spectral level and modification of the small-scale turbulence flow topology (characterized by the velocity-gradient tensor invariants) is presented.

So far, this study was limited to clean fluid systems as there is a lack of understanding of droplet dynamics even for pure fluids. Studies on interface resolving turbulent emulsion simulations (like Chapter 5) have only recently become feasible [21], and there is yet a lot that remains to be explained regarding these systems. Studying the effect of surfactants on the dynamics is still a step to be taken in the future, although with this

thesis we present the necessary tools that need to be combined for such studies. The only work that had been done on surfactant laden turbulent emulsions until 2019 was by Skartlien *et al.* [67, 68], where they show that the surfactant *does not* influence the emulsion structure significantly. This although true for their system, cannot be the general conclusion as it is known that surfactants effect emulsification significantly. Very recently, Soligo *et al.* [69] have shown how coalescence is inhibited for droplets in turbulent channel flow due to surfactants. The challenge remains in simulating stronger surfactant effects and spanning a wider range of the associated parameter space (Re_λ) numerically to directly compare clean and surfactant-laden systems.

1.5.5. CHAPTER 6: CONCLUSIONS AND OUTLOOK

Finally in Chapter 6, the conclusions of this work have been presented. Based upon the findings, the most interesting and relevant next questions worth investigating have been discussed. A section devoted to comparing nature and numerics is also presented - to highlight aspects of this work that find close correspondence in natural phenomena and those that do not. This is always an important aspect for modeling work, specially numerics and CFD of the kind presented in this thesis. More often than not, it is impossible to accurately simulate natural phenomena, however, with the right approximations, the disparity can be reduced to an agreeable minimum. The chapter closes with a brief outlook on this thesis.

REFERENCES

[1] D. J. McClements, *Food emulsions: principles, practices, and techniques* (CRC press, 2015).

[2] S. L. Kokal *et al.*, *Crude oil emulsions: A state-of-the-art review,* SPE Production & facilities **20**, 5 (2005).

[3] I. M. Banat, *Biosurfactants production and possible uses in microbial enhanced oil recovery and oil pollution remediation: a review,* Bioresource technology **51**, 1 (1995).

[4] A. D. Griffiths and D. S. Tawfik, *Miniaturising the laboratory in emulsion droplets,* Trends in biotechnology **24**, 395 (2006).

[5] F. L. White and G. H. Keyes, *Photographic emulsion,* (1939), uS Patent 2,166,736.

[6] E. Ostroff and T. H. James, *Gelatin silver halide emulsion: A history,* The Journal of Photographic Science **20**, 146 (1972).

[7] S. U. Pickering, *Cxcvi.—emulsions,* Journal of the Chemical Society, Transactions **91**, 2001 (1907).

[8] S. Melle, M. Lask, and G. G. Fuller, *Pickering emulsions with controllable stability,* Langmuir **21**, 2158 (2005).

[9] E. Dickinson, *Hydrocolloids as emulsifiers and emulsion stabilizers,* Food hydrocolloids **23**, 1473 (2009).

[10] D. J. McClements, *Protein-stabilized emulsions,* Current opinion in colloid & interface science **9**, 305 (2004).

[11] C. Li, P. Sun, and C. Yang, *Emulsion stabilized by starch nanocrystals,* Starch-Stärke **64**, 497 (2012).

[12] M. J. Rosen and J. T. Kunjappu, *Surfactants and interfacial phenomena* (John Wiley & Sons, 2012).

[13] A. Tsinober, *The essence of turbulence as a physical phenomenon,* Dordrecht: Springer. doi **10**, 978 (2014).

[14] G. K. Batchelor, *The theory of homogeneous turbulence* (Cambridge university press, 1953).

[15] S. B. Pope, *Turbulent flows* (Cambridge university press, 2000).

[16] D. Ruelle and F. Takens, *On the nature of turbulence,* Les rencontres physiciens-mathématiciens de Strasbourg-RCP25 **12**, 1 (1971).

[17] H. Tennekes and J. L. Lumley, *A first course in turbulence* (MIT press, 1972).

[18] U. Frisch, *Turbulence: the legacy of AN Kolmogorov* (Cambridge university press, 1995).

[19] P. Davidson, *Turbulence: an introduction for scientists and engineers* (Oxford University Press, 2015).

[20] J. Davies, *Drop sizes of emulsions related to turbulent energy dissipation rates,* Chemical Engineering Science **40**, 839 (1985).

[21] S. Elghobashi, *Direct numerical simulation of turbulent flows laden with droplets or bubbles,* Annual Review of Fluid Mechanics **51**, 217 (2019).

[22] J. Hinze, *Fundamentals of the hydrodynamic mechanism of splitting in dispersion processes,* AIChE Journal **1**, 289 (1955).

[23] R. Hesketh, T. Fraser Russell, and A. Etchells, *Bubble size in horizontal pipelines,* AIChE journal **33**, 663 (1987).

[24] V. G. Levich, *Physicochemical hydrodynamics* (Prentice-Hall Inc., 1962).

[25] D. Ko, *Breakage of Single Droplets in 2-D Inertial Flows*, Ph.D. thesis, University of Maryland (2018).

[26] C. Garrett, M. Li, and D. Farmer, *The connection between bubble size spectra and energy dissipation rates in the upper ocean,* Journal of physical oceanography **30**, 2163 (2000).

[27] G. B. Deane and M. D. Stokes, *Scale dependence of bubble creation mechanisms in breaking waves,* Nature **418**, 839 (2002).

[28] N. Ashgriz and J. Poo, *Coalescence and separation in binary collisions of liquid drops,* Journal of Fluid Mechanics **221**, 183 (1990).

[29] K.-L. Pan, P.-C. Chou, and Y.-J. Tseng, *Binary droplet collision at high weber number,* Physical Review E **80**, 036301 (2009).

[30] T. E. Tezduyar, *Interface-tracking and interface-capturing techniques for finite element computation of moving boundaries and interfaces,* Computer Methods in Applied Mechanics and Engineering **195**, 2983 (2006).

[31] S. Mirjalili, S. S. Jain, and M. Dodd, *Interface-capturing methods for two-phase flows: An overview and recent developments,* Center for Turbulence Research Annual Research Briefs , 117 (2017).

[32] S. O. Unverdi and G. Tryggvason, *A front-tracking method for viscous, incompressible, multi-fluid flows,* Journal of computational physics **100**, 25 (1992).

[33] S. Popinet and S. Zaleski, *A front-tracking algorithm for accurate representation of surface tension,* International Journal for Numerical Methods in Fluids **30**, 775 (1999).

[34] S. Quan and D. P. Schmidt, *A moving mesh interface tracking method for 3d incompressible two-phase flows,* Journal of Computational Physics **221**, 761 (2007).

[35] Ž. Tuković and H. Jasak, *A moving mesh finite volume interface tracking method for surface tension dominated interfacial fluid flow,* Computers & fluids **55**, 70 (2012).

[36] S. Osher and J. A. Sethian, *Fronts propagating with curvature-dependent speed: algorithms based on hamilton-jacobi formulations,* Journal of computational physics **79**, 12 (1988).

[37] J. A. Sethian and P. Smereka, *Level set methods for fluid interfaces,* Annual review of fluid mechanics **35**, 341 (2003).

[38] C. W. Hirt and B. D. Nichols, *Volume of fluid (vof) method for the dynamics of free boundaries,* Journal of computational physics **39**, 201 (1981).

[39] J. W. Cahn and J. E. Hilliard, *Free energy of a nonuniform system. i. interfacial free energy,* The Journal of chemical physics **28**, 258 (1958).

[40] L.-Q. Chen, *Phase-field method of phase transitions/domain structures in ferroelectric thin films: a review,* Journal of the American Ceramic Society **91**, 1835 (2008).

[41] J. U. Brackbill, D. B. Kothe, and C. Zemach, *A continuum method for modeling surface tension,* Journal of computational physics **100**, 335 (1992).

[42] B. Lafaurie, C. Nardone, R. Scardovelli, S. Zaleski, and G. Zanetti, *Modelling merging and fragmentation in multiphase flows with surfer,* Journal of Computational Physics **113**, 134 (1994).

[43] H. Marschall, K. Hinterberger, C. Schüler, F. Habla, and O. Hinrichsen, *Numerical simulation of species transfer across fluid interfaces in free-surface flows using openfoam,* Chemical engineering science **78**, 111 (2012).

[44] J. Crank *et al.*, *The mathematics of diffusion* (Oxford university press, 1979).

[45] Z. Tukovic and H. Jasak, *Simulation of free-rising bubble with soluble surfactant using moving mesh finite volume/area method,* in *Proceedings of 6th International Conference on CFD in Oil & Gas, Metallurgical and Process Industries, no. CFD08-072* (2008).

[46] K. Hayashi and A. Tomiyama, *Effects of surfactant on terminal velocity of a taylor bubble in a vertical pipe,* International Journal of Multiphase Flow **39**, 78 (2012).

[47] M. Muradoglu and G. Tryggvason, *Simulations of soluble surfactants in 3d multi-phase flow,* Journal of Computational Physics **274**, 737 (2014).

[48] Y. Renardy and M. Renardy, *Prost: a parabolic reconstruction of surface tension for the volume-of-fluid method,* Journal of computational physics **183**, 400 (2002).

[49] T. Krüger, H. Kusumaatmaja, A. Kuzmin, O. Shardt, G. Silva, and E. M. Viggen, *The lattice boltzmann method,* Springer International Publishing **10**, 978 (2017).

[50] P. L. Bhatnagar, E. P. Gross, and M. Krook, *A model for collision processes in gases. i. small amplitude processes in charged and neutral one-component systems,* Physical review **94**, 511 (1954).

[51] S. Succi, *The lattice Boltzmann equation: for fluid dynamics and beyond* (Oxford university press, 2001).

[52] K. Sankaranarayanan, I. Kevrekidis, S. Sundaresan, J. Lu, and G. Tryggvason, *A comparative study of lattice boltzmann and front-tracking finite-difference methods for bubble simulations,* International Journal of Multiphase Flow **29**, 109 (2003).

[53] M. Nekovee, P. V. Coveney, H. Chen, and B. M. Boghosian, *Lattice-boltzmann model for interacting amphiphilic fluids,* Physical Review E **62**, 8282 (2000).

[54] H. Chen, B. M. Boghosian, P. V. Coveney, and M. Nekovee, *A ternary lattice boltzmann model for amphiphilic fluids,* Proceedings of the Royal Society of London. Series A: Mathematical, Physical and Engineering Sciences **456**, 2043 (2000).

[55] G. Falcucci, G. Bella, G. Chiatti, S. Chibbaro, M. Sbragaglia, S. Succi, *et al.*, *Lattice boltzmann models with mid-range interactions,* Commun. Comput. Phys **2**, 1071 (2007).

[56] K. Alvelius, *Random forcing of three-dimensional homogeneous turbulence,* Physics of Fluids **11**, 1880 (1999).

[57] A. Ten Cate, E. Van Vliet, J. Derksen, and H. Van den Akker, *Application of spectral forcing in lattice-boltzmann simulations of homogeneous turbulence,* Computers & fluids **35**, 1239 (2006).

[58] L. Biferale, P. Perlekar, M. Sbragaglia, S. Srivastava, and F. Toschi, *A lattice boltzmann method for turbulent emulsions,* in *Journal of Physics: Conference Series*, Vol. 318 (IOP Publishing, 2011) p. 052017.

[59] L. Richardson, *Weather prediction by numerical process* (Cambridge university press, 2007).

[60] A. Alexakis and L. Biferale, *Cascades and transitions in turbulent flows,* Physics Reports **767**, 1 (2018).

[61] J. Jeong and F. Hussain, *On the identification of a vortex,* Journal of fluid mechanics **285**, 69 (1995).

[62] Y. Dubief and F. Delcayre, *On coherent-vortex identification in turbulence,* Journal of turbulence **1**, 011 (2000).

[63] A. Lozano-Durán and J. Jiménez, *Time-resolved evolution of coherent structures in turbulent channels: characterization of eddies and cascades,* Journal of Fluid Mechanics **759**, 432 (2014).

[64] A. Zarghami, N. Looije, and H. Van den Akker, *Assessment of interaction potential in simulating nonisothermal multiphase systems by means of lattice boltzmann modeling,* Physical Review E **92**, 023307 (2015).

[65] P. Perlekar, L. Biferale, M. Sbragaglia, S. Srivastava, and F. Toschi, *Droplet size distribution in homogeneous isotropic turbulence,* Physics of Fluids **24**, 065101 (2012).

[66] P. Perlekar, R. Benzi, H. J. Clercx, D. R. Nelson, and F. Toschi, *Spinodal decomposition in homogeneous and isotropic turbulence,* Physical review letters **112**, 014502 (2014).

[67] R. Skartlien, B. Grimes, P. Meakin, J. Sjöblom, and E. Sollum, *Coalescence kinetics in surfactant stabilized emulsions: Evolution equations from direct numerical simulations,* The Journal of chemical physics **137**, 214701 (2012).

[68] R. Skartlien, E. Sollum, and H. Schumann, *Droplet size distributions in turbulent emulsions: Breakup criteria and surfactant effects from direct numerical simulations,* The Journal of chemical physics **139**, 174901 (2013).

[69] G. Soligo, A. Roccon, and A. Soldati, *Coalescence of surfactant-laden drops by phase field method,* Journal of Computational Physics **376**, 1292 (2019).

2

INTER-COMPARISON OF PP-LB AND VOF

"What we observe is not nature in itself, but nature exposed to our method of questioning."

~ Werner Heisenberg

Heisenberg's aphorism highlighting the nature of scientific theories rings doubly true for numerical modelling. Typically, numerical methods are designed for robustness and applicability across a tapestry of problems. In practice, the limits of their universality is difficult to ascertain, specially for computational fluid dynamics of multiphase flows, where there are numerous models that all differ in principle. This causes two disparate issues. Often researchers adhere to a preferred method due to reasons simply of legacy, and are unable to move on to a different approach. On the other hand, new methods are readily developed with the promise of widespread application, although they have not been amply tested. While there are benefits both in long standing familiarity with a numerical tool and ready acceptance of newer, improved methods, the two are better reconciled when pitched in direct comparison to each other. Such comparisons are crucial in improving our understanding of numerics, specially when different techniques agree with each other sufficiently when applied to well defined numerical benchmarks but begin to disagree when applied to realistic problems. Such work can be tedious to perform, and is unfortunately under-appreciated[1]*. In this chapter, a quantitative analysis of the pseudopotential lattice-Boltzmann and volume-of-fluid methods is presented, focusing on low density ratio fluids (representative of emulsions) to simulate falling liquid droplets at low Re and Eo numbers.*

This chapter has been published in the *International Journal of Heat and Fluid Flow*, 2018 [1].

[1] With the editor of a prominent numerics journal having decreed "the comparison could have been valuable to the community, but it has been carried out for low *Re* and low density ratio fluids - *which are of little interest*".

2.1. INTRODUCTION

With multiphase flow simulations becoming commonplace in describing and designing engineering applications, numerous techniques have been developed to numerically solve these flows [2, 3]. In addition, this has provided unprecedented insight into flow physics at the scale of individual droplets and bubbles which in many cases is relevant at the larger scale of reactors or processes. This has in turn greatly benefited emulsion research dealing with liquid-liquid flows [4–6], where performing experiments to obtain high resolution spatio-temporal data is often not feasible. Many food and personal care products consist of liquid-liquid emulsions with a low density ratio. In the oil industry, separating water from oil (in particular downhole water/oil separation, leaving the water underground) is a tremendously relevant issue [7], as many oil sources not just produce oil and gas but also water in increasing amounts. Also the concept of Enhanced Oil Recovery (EOR) [8] in which steam is injected into oil containing reservoirs to increase oil production results in large amounts of fine liquid-liquid emulsions which need treatment. In the polymer industry, quite a few polymers are produced by means of emulsion polymerization processes [9]. Reliable simulations of these widely different processes require an accurate description of the flow physics at the droplet scale. The existence of myriad simulation techniques presents another caveat - which method is most applicable to a specific problem? This calls for studies that reveal particular strengths and shortcomings of these simulation techniques when directly compared, however in the case of interface resolving multiphase flows, such studies are difficult to come by.

To the best of the authors' knowledge, among the very few other studies comparing a mesoscopic technique to a continuum technique for multiphase flow are the comparison between a two fluid free energy LB approach and a volume of fluid method by Takada *et al.* [10], between a pseudopotential LB and a front-tracking finite-difference method for rising bubbles by Sankaranarayanan *et al.* [11] and between a free energy LB formulation and a phase field method by Scarbolo *et al.* [12]. We compare two widely used techniques based on very different principles, namely the finite volume based Volume of Fluid (VOF) method and the mesoscopic, single-component multiphase pseudopotential lattice-Boltzmann method (PP-LB) and focus on specific challenges faced when simulating fluids at low density ratio. Generally, multiphase flows can contain single or multiple fluid components in different phases, for instance a fluid existing simultaneously in its liquid and vapour phase, or two immiscible liquids like oil and water. The most elusive problem here is the accurate representation of the phase separating interface, that essentially emerges from the microscopic interactions at the molecular level, detached from the continuum regime of hydrodynamics, and which can undergo complex deformations during the evolution of the flow. VOF and PP-LB differ greatly in how they simulate interface dynamics. Both techniques have particular points of strength, but they also bring a set of shortcomings that are easily overlooked - we address them both in the course of our study.

VOF is one of the first techniques developed for multiphase flow simulations based on the finite volume method (FVM) [13]. Using VOF, one solves an additional advection equation for a boolean valued phase indicator function, marking the two *immiscible* fluids. In principle, at the interface, this indicator value changes rapidly from 0 to 1 (or vice-versa) marking the two phase regions. Further, all physical properties are modeled as phase averages, hence working with an effective *single-fluid* formulation of the

Navier-Stokes equation. This method has been demonstrated to perform well for a wide range of multiphase flow problems and can reproduce an appreciably sharp interface undergoing arbitrarily large deformations [14].

Also over the past two decades, PP-LB has emerged as a versatile alternative to conventional finite volume techniques for simulating multiphase flows [15]. It was first proposed by Shan and Chen [16, 17] and is based on a mesoscopic kinetic equation for particle distribution functions, and has been used for various fluid mechanics and engineering problems [18, 19]. In this method, particle interactions are modeled by an interparticle force which causes a single-component fluid to spontaneously segregate into two phases of different densities that change smoothly from one bulk value to another. The interface emerges automatically and is characterized by monitoring the variation in density, and is therefore no longer a mathematical boundary and no explicit interface tracking/capturing technique is required. Moreover, surface tension effects emerge automatically from the underlying Boltzmann dynamics. The single-component PP-LB is the most widely used LB based model due to its simplicity and versatility, remarkable computational efficiency and clear representation of the underlying microscopic physics.

Evidently, VOF and PP-LB simulate multiphase flows very differently, the first being a continuum approach and the latter mesoscopic. The main point of departure is that in VOF, the two (or more) fluids are completely immiscible and interfacial dynamics is modeled with a specified surface tension force. While in single-component PP-LB, the two fluids are modeled as the liquid and vapor phases of the same non-ideal component [20], which coexist due to phase separation [21]. Immiscibility of the two phases in PP-LB is ensured by a repulsive interaction parameter, consequently leading to surface tension effects. Owing to these differences, a direct comparison between the strengths and weaknesses of the two methods can benefit a user by providing motivation for selecting either technique, for one might be better suited to a specific problem than the other. Previously [22], the authors attempted such an intercomparison and it was observed that even after a careful formulation of identical test cases, predicted results can vary between the two methods. In this study, we investigate this discrepancy further to more conclusively remark on the predictive aspects of VOF vis-à-vis PP-LB.

We begin with a description of PP-LB (our own in-house code implementation using FORTRAN 90 as well as an implementation in the open source "parallel lattice-Boltzmann solver" Palabos-v1.5r1), and the VOF method (using the standard OpenFOAM and FLUENT VOF solvers, along with modifications to the OpenFOAM solver). We first address the so-called spurious velocities that emerge in both methods as numerical artifacts and can be a limiting constraint on the accuracy of results. We also compare the thickness of the interface as produced by these methods, and show that sharper interfaces are achieved at the cost of higher spurious velocities. Next we simulate falling droplets with a low density ratio (2D and 3D in VOF, and 2D in LB) to compare how well the methods predict the velocity evolution, terminal Reynolds number and droplet shape. This comparison is performed in a small region of the phase-space governing falling droplets, corresponding to the spherical and ellipsoidal regions of the shape regime map of Clift *et al.* [23] (henceforth called the Clift map). We then discuss the specific challenges faced for the two methods and conclude with our main findings.

2.1.1. SINGLE-COMPONENT PP-LB

The standard lattice-Boltzmann equation with a single relaxation time [24] is written as

$$\frac{f_i(\mathbf{x}+\mathbf{e}_i\Delta t, t+\Delta t) - f_i(\mathbf{x}, t)}{\Delta t} = \frac{1}{\tau}\left(f_i(\mathbf{x}, t) - f_i^{\mathrm{eq}}(\mathbf{x}, t)\right) + \mathbf{S}_i \tag{2.1}$$

where $f_i(\mathbf{x}, t)$ is the density distribution function associated with discrete velocity direction i, τ is the relaxation time and $\mathbf{S}_i$ represents a general source term added into the lattice-Boltzmann equation (which is related to all thermodynamic and hydrodynamic forces). The discrete velocities $\mathbf{e}_i$ in the i^{th} - direction, for the D2Q9 lattice are given by $\mathbf{e}_0 = 0$ and $\mathbf{e}_i = \lambda_i(\cos\theta_i, \sin\theta_i)$ with $\lambda_i = 1, \theta_i = (i-1)\pi/2$ for $i = 1-4$ and $\lambda_i = \sqrt{2}, \theta_i = (i-5)\pi/2 + \pi/4$ for $i = 5-8$. The order numbers $i = 1-4$ and $i = 5-8$ represent the rectangular and the diagonal directions of the lattice respectively. In Eq. 2.1, f_i^{eq} is the equilibrium distribution function and is calculated as

$$f_i^{\mathrm{eq}} = w_i\rho\left[1 + \frac{\left(\mathbf{e}_i\cdot\mathbf{u}^{\mathrm{eq}}\right)}{c_s^2} + \frac{\left(\mathbf{e}_i\cdot\mathbf{u}^{\mathrm{eq}}\right)^2}{2c_s^4} - \frac{\left(\mathbf{u}^{\mathrm{eq}}\cdot\mathbf{u}^{\mathrm{eq}}\right)}{2c_s^2}\right] \tag{2.2}$$

where $c_s^2 = 1/3$ is the lattice speed of sound, w_i are the weighting factors equal to $4/9$ for $i = 0$, $1/9$ for $i = 1-4$ and $1/36$ for $i = 5-8$, and $\mathbf{u}^{\mathrm{eq}}$ is the equilibrium velocity. Also, the local mass density, local velocity and the kinematic viscosity in lattice units for each component are calculated as $\rho = \sum_i f_i$, $\mathbf{u} = \left(\sum_i \mathbf{e}_i f_i\right)/\rho$ and $\nu = (\tau - 0.5)/3$ respectively (while the dynamic viscosity $\mu = \rho\nu$).

The force $\mathbf{F}$ acting on a multiphase system includes external body forces, $\mathbf{F}_{\mathrm{body}}$ (e.g. gravity) and the mean field inter-particle interaction force, $\mathbf{F}_{\mathrm{int}}$, and is written as $\mathbf{F} = \mathbf{F}_{\mathrm{body}} + \mathbf{F}_{\mathrm{int}}$. Based on the original pseudopotential model [17], the so called $\beta-$scheme [25] has been introduced for the interaction force for a single-component multiphase system as follows:

$$\mathbf{F}_{\mathrm{int}} = -\beta\left[\psi(\mathbf{x}, t)\, G\sum_i \psi(\mathbf{x}+\mathbf{e}_i\Delta t, t)\,\mathbf{e}_i\Delta t\right] + \frac{1-\beta}{2}\left[G\sum_i w_i\left[\psi(\mathbf{x}+\mathbf{e}_i\Delta t, t)\right]^2\mathbf{e}_i\Delta t\right] \tag{2.3}$$

where $\Delta t = 1$ is the time interval and G denotes the interaction parameter, with $G < 0$ representing an attractive force between the particles. Compared to the original pseudopotential interaction force, the $\beta-$scheme has more isotropy and by choosing a proper value for β, the thermodynamic inconsistency and magnitude of spurious velocities can be greatly reduced [25–27]. It has been shown that by setting $\beta = 1.25$ the density ratio in LB matches well with the analytical equation of state (EOS) [26]. Note that by choosing $\beta = 1$, the $\beta-$scheme reduces to the original pseudopotential model. In Eq. 2.3, $\psi(\mathbf{x}, t)$ is called the pseudopotential function and is calculated by [21]

$$\psi(\mathbf{x}, t) = \sqrt{\frac{2\left(p_{\mathrm{EOS}} - \rho c_s^2\right)}{G}} \tag{2.4}$$

where p_{EOS} is the pressure calculated from the desired EOS. Here, the Carnahan-Starling (C-S) EOS is used [21], which is implemented as

$$p_{\mathrm{EOS}} = \rho T\left[\frac{1+\rho+\rho^2-\rho^3}{(1-\rho)^3}\right] - \rho^2 \tag{2.5}$$

The reduced temperature and density are defined as $T_r = T/T_c$ and $\rho_r = \rho/\rho_c$ where $T_c = 0.09432$ and $\rho_c = 0.11911$ are the critical temperature and density, in lattice units, related to the C-S EOS, these values have been take from Zarghami *et al.* [26]. In order to mimic the continuous phase behavior as expressed by the Navier-Stokes equations, usually, a source term representing the mean field inter-particle interaction force is added to the lattice-Boltzmann equation (see Eq. 2.1). One of the most stable and common force implementation schemes is the exact difference method (EDM) which is directly derived from the Boltzmann equation [28], and is given as

$$\mathbf{S}_i = f_i^{\mathrm{eq}}\left(\rho, \mathbf{u} + \mathbf{F}\Delta t/\rho\right) - f_i^{\mathrm{eq}}\left(\rho, \mathbf{u}\right) \tag{2.6}$$

The equilibrium velocity $\mathbf{u}^{\mathrm{eq}}$, and the real fluid velocity $\mathbf{U}$ can be calculated as

$$\mathbf{U} = \mathbf{u}^{\mathrm{eq}} = \mathbf{u} + \frac{\Delta t}{2\rho}\mathbf{F} \tag{2.7}$$

In order to incorporate gravitational and buoyancy forces in the model, the body force can be defined in one of the following ways depending on the specific problem being simulated and the domain boundary conditions

$$\mathbf{F}_{\mathrm{body}} = \rho g \tag{2.8}$$

$$\mathbf{F}_{\mathrm{body}} = (\rho - \rho_{\mathrm{vap}})g \tag{2.9}$$

$$\mathbf{F}_{\mathrm{body}} = (\rho - \hat{\rho})g \tag{2.10}$$

where g is the downward gravitational acceleration, ρ is the local density, ρ_{vap} is the vapor density and $\hat{\rho}$ is the averaged density over the whole computational domain. Since we use a fully periodic domain for the LB simulations, Eq. 2.10 is the most appropriate implementation of the body force [29–31]. This ensures that the average value of $\mathbf{F}_{\mathrm{body}}$ in the computational domain is zero and no net momentum is added to the system, so the droplet and surrounding fluid do not keep accelerating downward indefinitely [31]. The recovered macroscopic Navier-Stokes equations from LB are as follows

$$\begin{aligned}
\frac{\partial \rho}{\partial t} + \nabla\cdot\mathbf{u} &= -\frac{\Delta t}{2}\nabla\cdot\mathbf{F} \\
\frac{\partial \rho\mathbf{u}}{\partial t} + \nabla\cdot(\rho\mathbf{u}\mathbf{u}) &= -\nabla p + \nu\nabla\cdot\left[\rho\left(\nabla\mathbf{u} + (\nabla\mathbf{u})^T\right)\right] + \mathbf{F} \\
&\quad - \frac{\Delta t}{2}\epsilon\frac{\partial \mathbf{F}}{\partial t_1} - \Delta t\nabla\cdot\left[\frac{1}{2}(\mathbf{u}\mathbf{F} + \mathbf{F}\mathbf{u}) + \Delta t\frac{\tau}{\rho}\mathbf{F}\mathbf{F}\right]
\end{aligned} \tag{2.11}$$

One can see that an additional nonlinear relaxation-time dependent term is introduced when recovering the NS equations using the EDM scheme and when applying the Chapman-Enskog expansion. The scheme will be consistent with the macroscopic equations if the temporal and spatial changes of the force vary only slightly (or the force term be constant), and if the last term within brackets of Eq. 2.11 be negligible. However, the last term may have a great influence on the solution due to the velocity gradient. It has been shown [26, 32] that the term $\rho^{-1}\mathbf{F}\mathbf{F}$ is capable of enhancing numerical stability. This term has a non-zero value only at the phase interface, as a result of the fluid particle interaction (which in itself does not appear in the NS equations). This enables one to simulate high density ratios when using the EDM scheme.

2.1.2. VOF IN OPENFOAM

OpenFOAM (version 2.3.0) [33, 34] which stands for Open Field Operation and Manipulation, is a highly flexible open source C++ library of finite volume based solvers for differential equations, operating on scalar, vector and tensor fields. It provides a VOF solver called *interFoam* - which is employed in this study and has been widely used and validated [35–39]. It solves the mass conservation and momentum equation for incompressible fluid flow along with the transport of a phase indicator function α which differentiates the two phases. This α is ideally a step function such that it goes from 1 to 0 as one moves from one phase to the other. Once a simulation is initialized with a sharp profile of α, the interface gets diffused over a few cells, which can in principle be confined to an arbitrarily narrow region with mesh refinement, and several methods have been proposed to limit this effect [40]. The interface between the two fluids is taken to be the contour of $\alpha = 0.5$. This approach assumes that each phase moves with the center of mass velocity such that $\mathbf{u} = \mathbf{u}_{\alpha_1} = \mathbf{u}_{\alpha_2}$ and is acted upon by one pressure field. The following equations are solved by interFoam

$$\nabla \cdot \mathbf{u} = 0$$

$$\frac{\partial \rho u}{\partial t} + \nabla \cdot (\rho \mathbf{u}\mathbf{u}) = -\nabla p^{\star} + \nabla \cdot (2\mu \mathbf{S}) + \mathbf{f}_b + \mathbf{f}_\sigma \tag{2.12}$$

$$\frac{\partial \alpha}{\partial t} + \nabla \cdot (\mathbf{u}\alpha) + \nabla \cdot (\mathbf{u}_c \alpha(1-\alpha)) = 0 \tag{2.13}$$

where $\mathbf{f}_b$ denotes body forces (like gravity), $\mathbf{f}_\sigma$ is surface tension force (explained below), $2\mu\mathbf{S}$ is the deviatoric stress with $\mathbf{S}$ the rate of strain tensor $\mathbf{S} = \frac{1}{2}\left(\nabla\mathbf{u} + \nabla\mathbf{u}^T\right)$ and μ is the dynamic viscosity. Here $p^{\star}$ is the modified pressure found by removing the hydrostatic component from the pressure, and is calculated as [41]

$$p^{\star} = p - \rho \mathbf{g} \cdot \mathbf{x} \tag{2.14}$$

where $\mathbf{g}$ and $\mathbf{x}$ are the gravity and position vectors respectively. Therefore the term $\nabla p^{\star}$ expands to

$$\nabla p^{\star} = \nabla p - \rho \mathbf{g} - \mathbf{g} \cdot \mathbf{x} \nabla \rho \tag{2.15}$$

The last term of Eq. 2.13 of the phase indicator transport equation $\nabla \cdot (\mathbf{u}_c \alpha(1-\alpha))$ is an *interface compression* term used to maintain a sharp interface between the phases. The calculation of $\mathbf{u}_c$ follows [42], where the compression velocity is given as

$$\mathbf{u}_c = \min\left(c_\alpha \left|\frac{\phi}{|\mathbf{S}_f|}\right|, \left|\frac{\phi}{|\mathbf{S}_f|}\right|_{\max}\right) \tag{2.16}$$

where $0 < c_\alpha < 1$ limits the compression velocity to below the maximum face flux velocity $\phi/|\mathbf{S}_f|$ [43], where $\mathbf{S}_f$ is the cell face vector. This term is active only in the interface region due to the $\alpha(1-\alpha)$ factor (conceptually similar to the extra term appearing in the LB formulation of the NS equation, see the description following Eq. 2.6). This technique helps preserve interface sharpness, though it comes at the cost of exaggerating the parasitic currents [38], which will be discussed shortly. All physical properties ψ in this formulation are given as

$$\psi = \psi_1 \alpha + \psi_2 (1-\alpha) \qquad \text{where} \quad \psi \in \{\rho, \mu, c\} \tag{2.17}$$

The surface tension force in the momentum equation, $\mathbf{f}_\sigma$, is adopted based upon the Continuous-Surface-Force (CSF) formulation [44], given as

$$\mathbf{f}_\sigma = \sigma\kappa\nabla\alpha \qquad \text{with} \quad \kappa = -\nabla\cdot\left(\frac{\nabla\alpha}{|\nabla\alpha|}\right) \tag{2.18}$$

where σ is a specified constant surface tension. It is the inaccuracies in determination of the curvature κ that lead to parasitic currents in VOF. Lafaurie *et al.* [45] proposed an improved calculation of the curvature reducing parasitic currents, where the α field is converted to a smoother field $\tilde{\alpha}$ using a Laplacian filter as follows

$$\tilde{\alpha}_P = \frac{\sum_{f=1}^{n} \alpha_f |\mathbf{S}_f|}{\sum_{f=1}^{n} |\mathbf{S}_f|} \tag{2.19}$$

where P denotes the cell index and f denotes the face index. This modified formulation can be used to reduce the parasitic currents by an order of magnitude [38].

DYNAMIC MESH REFINEMENT FOR 3D SIMULATIONS

For 3D VOF simulations, dynamic mesh refinement [46] as available in OpenFOAM was used to reduce the computational cost. This allows the use of a relatively coarse base mesh, while grid cells around the interface can be dynamically refined based on the value of the α-field (a criterion of $0.1 < \alpha < 0.9$ has been used in this study). Every octagonal cell that satisfies the refinement criterion has each dimension cut in half, resulting in 8 smaller octagonal cells, the result being a 2 : 1 refinement. This process is repeated up to two times, resulting in a factor four times finer mesh in the region around the interface.

PRESSURE-VELOCITY COUPLING

OpenFOAM provides two pressure-velocity coupling procedures for the iterative solver. First is the well known PISO algorithm [47], which corrects iteratively for the pressure and velocity for the number of times prescribed by the parameter *inner corrector*. The second is the PIMPLE algorithm, which is a combination of the SIMPLE [48] algorithm with PISO. The PIMPLE algorithm has *outer correctors* along with the *inner correctors* of PISO. It solves the entire PISO loop several times, the main difference being that the α field is also corrected by PIMPLE (unlike with PISO). If the time step size is small enough (i.e. a small enough maximum cell Courant number $Co_{\max} = u\Delta t/\Delta x$, where Δx and Δt are the grid size and time step size, respectively), then the α field should not change much within a time step and PISO and PIMPLE are expected to give very similar results. We have tested both algorithms in this study.

2.1.3. VOF IN FLUENT

The explicit VOF method in FLUENT (version 15.7) is equivalent to the implementation in OpenFOAM in terms of the momentum; the volume fraction equation differs depending upon the interface reconstruction approach. The FLUENT default is the geometrical reconstruction scheme based upon Youngs [49]. For this scheme, the volume fraction equation simply reads:

$$\frac{\partial\alpha}{\partial t} + \nabla\cdot(\mathbf{u}\alpha) = 0 \tag{2.20}$$

and a piecewise-linear interface construction (PLIC) scheme is used to determine the face fluxes of α. Alternatively, a "Compressive" scheme can be chosen from the available options (others being "HRIC" and "CICSAM" - which have not been used in this study). The Compressive scheme has been implemented in FLUENT via the volume fraction discretization equation

$$\alpha_f = \alpha_d + \beta \nabla \alpha_d \tag{2.21}$$

with α_f the face value and α_d the value in the donor cell, further details can be found in Ubbink [50]. Prescribing $\beta = 2$ amounts to the Compressive scheme, as it increases the flux of α being accepted from the donor cell. (while $\beta = 0$ yields a $1^{\text{st}}-$order upwind discretization as $\alpha_f = \alpha_d$). The momentum equation is discretized using $2^{\text{nd}}-$ order upwind and the 3^{rd} order *MUSCL* scheme, which is a blend between second order upwind and central differencing:

$$\phi_f = \theta \left[\frac{1}{2}\left(\phi_0 + \phi_1\right) + \frac{1}{1}\left(\nabla\phi_o \cdot \mathbf{r_0} + \nabla\phi_o \cdot \mathbf{r_1}\right) \right] + (1-\theta)\left[\phi_0 + \nabla\phi_0 \cdot \mathbf{r_0}\right] \tag{2.22}$$

This gives the following FLUENT approaches:

1. 3^{rd}-order MUSCL using "Compressive" Scheme

2. 3^{rd}-order MUSCL using "Geometrical-Reconstruction" Scheme

For all cases, the SIMPLE scheme for pressure-velocity coupling and a staggered grid (PRESTO, i.e Pressure Staggering Option scheme [48]) for pressure interpolation was used. A first order implicit, adaptive time-stepping was used with a Courant criterion of $Co_{\max} = 0.25$. We also tested results from the $2^{\text{nd}}-$ order upwinding scheme, which were identical to those from the MUSCL scheme. Hence all forthcoming FLUENT results shown are those obtained using the MUSCL scheme.

2.2. THEORETICAL DISCUSSION

2.2.1. DIMENSIONAL ANALYSIS

We simulate falling droplets, a relevant multiphase flow problem along with rising bubbles, where the dynamics is commonly influenced by buoyancy, drag, gravity, surface tension and other forces depending on the fluid properties. The interplay of these forces results in different droplet/bubble behaviours, depending on droplet/bubble size, density ratio and viscosity ratio of the fluids. Carrying out a dimensional analysis of the relative (slip) velocity for a falling (rising) droplet (bubble) in another fluid shows that the problem is completely described by four non-dimensional parameters [51]: the density ratio ($\rho^\star$), the dynamic viscosity ratio ($\mu^\star$), the Eötvös number (Eo, also called the Bond number) and the Galilei number (Ga) defined as

$$\begin{aligned}
\text{Density Ratio: } \rho^\star &= \frac{\rho_i}{\rho_o} \\
\text{Dynamic Viscosity Ratio: } \mu^\star &= \frac{\mu_i}{\mu_o} \\
\text{Eötvös Number: } Eo &= \frac{\Delta\rho g d^2}{\sigma} \\
\text{Galilei Number: } Ga &= \frac{\sqrt{g\rho_o\Delta\rho d^3}}{\mu_o}
\end{aligned} \tag{2.23}$$

where $\Delta\rho = |\rho_o - \rho_i|$, the subscripts i, o denoting properties inside and outside the droplet/bubble region respectively. Also, g, d and σ are the gravitational acceleration, the initial diameter of droplet and surface tension. For our discussion and subsequent formulation of cases based on the Clift map, we also define the Reynolds (Re), Morton (M) and Weber (We) numbers

$$\begin{aligned}
\text{Reynolds Number: } Re &= \frac{\rho_o u_t d}{\mu_o} \\
\text{Morton Number: } M &= \frac{\mu_o^4 \Delta\rho g}{\rho_o^2 \sigma^3} \\
\text{Weber Number: } We &= \frac{\rho_o u_t^2 d}{\sigma}
\end{aligned} \tag{2.24}$$

where u_t is the terminal velocity of the droplet. Note that Ga is similar to Re, but is defined using the characteristic gravitational velocity ($\sqrt{(\Delta\rho/\rho_o)gd}$) rather than the terminal velocity [52]. This becomes useful in some flow regimes where a falling droplet or rising bubble may never display a steady terminal velocity, and even if it does, the terminal velocity is unknown a priori and depends on several physical quantities; the gravitational velocity scale then is better defined.

2.2.2. FLOW REGIME MAP

A well-known regime map based on experimental correlations has been presented by Clift *et al.* [23], which is used as a common reference for predicting the terminal velocity and final shape of rising air bubbles in water, also applicable to low density ratio droplets. Based on this map, the main regimes depending on the final shape of the bubble are the spherical, ellipsoidal and spherical cap regimes. The surface tension and the viscous forces are dominant in the spherical regime and the bubble size is small ($d < 1.3$ [mm]), the bubble shape remaining spherical or nearly-spherical. Here, the Hadamard-Rybzynski [53, 54] solution for flow past viscous spheres applies, which is given as

$$u_t = \frac{g d^2 \Delta\rho}{6\nu_o}\left(\frac{1+k}{2+3k}\right) \tag{2.25}$$

where $k = \nu_o/\nu_i$ ($k = 1$ in this study). In the ellipsoidal regime which ranges from $0.25 < Eo < 40$, surface tension is the dominant parameter and the bubble size is typically $1.3 < d < 6$ [mm]. Here, the terminal velocity can be approximated by correlations suggested

by Mendelson [55]

$$u_t = \left(\frac{2.14\sigma}{\rho_o d} + 0.505 g d \right)^{0.5} \tag{2.26}$$

Finally, the spherical cap regime occurs when the bubble size is large ($d > 6$ [mm]) and $Eo > 40$, and is governed by inertial forces which generate higher deformation by inducing higher pressure on the front and rear of the bubble, and lower pressure at the sides [29]. The wobbling, skirted or dimpled spherical cap sub-regimes may also emerge in case of an unsteady rising bubble.

Whether this regime map is also applicable to falling droplets can be ascertained by comparing the conditions under which bubbles and droplets have the same dynamics and evolution history, i.e. they rise or fall to a similar relative position over the same time and acquire the same shape and velocity. As reported in recent literature [51, 56], this is ensured by the conditions

$$\begin{aligned} Ga_d &= Ga_b \\ \rho_d^\star &= \frac{\rho_b^\star}{2\rho_b^\star - 1} \end{aligned} \tag{2.27}$$

where the subscripts d, b refer to the droplet and bubble respectively. Further in accordance to the Boussinesq approximation, the influence of circulation inside the fluid particle on its surface should be considered [56], which gives the condition $\rho_b^\star = 2 - \rho_d^\star$ and $\mu_b^\star = \mu_d^\star$. Once $\rho_d^\star > 2$, no exact equivalent of a bubble can be found [51, 57, 58]. Essentially, the dynamics of droplet motion becomes qualitatively different from an equivalent bubble when the density ratio is far from unity. This has been briefly demonstrated below in Fig. 2.1, where identical cases of rising bubbles and falling droplets have been shown side by side, comparing the steady state shape and the background vorticity field, for density ratios $\rho^\star = 1.2, 3$ & 20 and with $\mu^\star = 1$. These simulations were performed in OpenFOAM in 2D at a resolution of 40 grid cells per droplet diameter, and an adaptive time stepping following the maximum Courant number criterion of $Co_{\max} = 0.25$. It is seen that the vorticity tends to concentrate more strongly in the lighter density fluid. As $\rho^\star$ deviates further from unity, the equivalent bubble and droplet begin to differ.

2.3. STATIONARY LIQUID DROPLETS IN VAPOR

2.3.1. SIMULATION DETAILS

We first wish to address the well-known *spurious* (or *parasitic*) currents that are known to arise in VOF and PP-LB alike, and which have been detailed before in literature [59, 60]. As a brief reminder, these are *unphysical* velocity fields that arise due to the continuum surface force implementation for modeling surface tension effects in Eulerian based multiphase flow simulations like VOF, which do not disappear with grid refinement. This is a consequence of simulating a curved interface using an orthogonal grid. In PP-LB, these arise from an insufficient isotropy of the gradient operator. The standard method of investigating spurious currents is to simulate a stationary droplet suspended in vapor, without the influence of any body forces. In such a situation, although all initial velocity fluctuations should eventually settle to zero by the effect of viscosity, very coherent velocity structures are obtained particularly neighbouring the fluid interface. We simulate

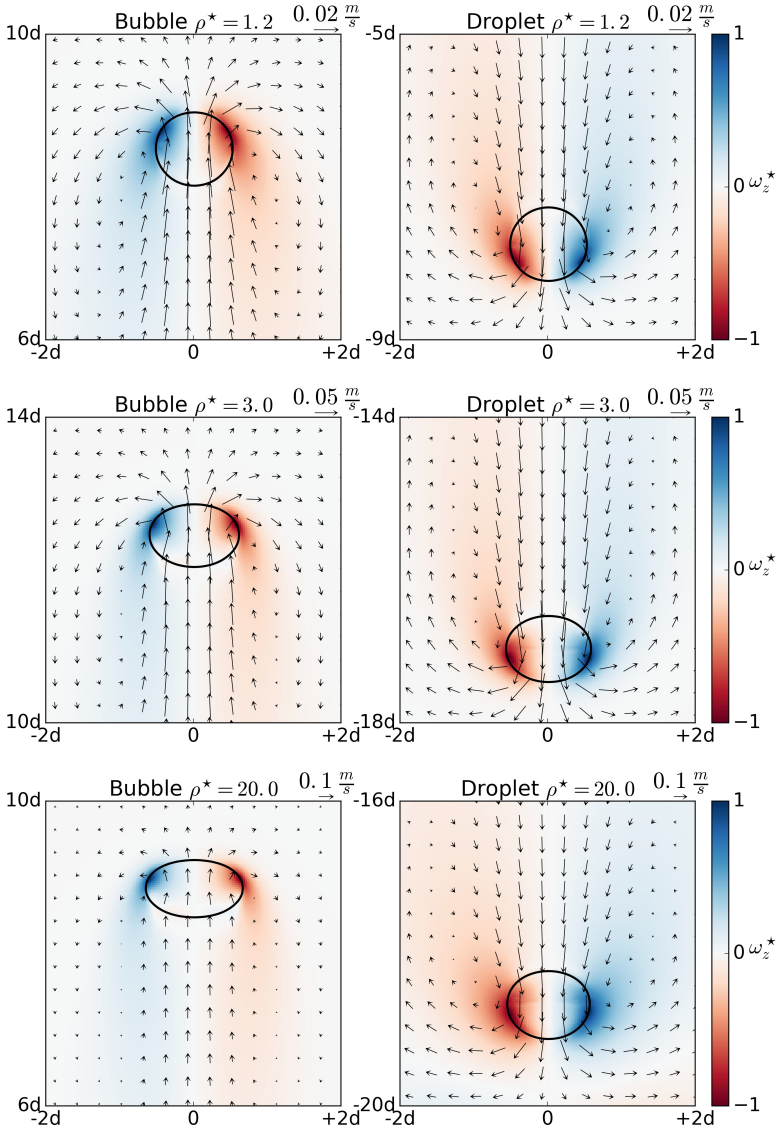

Figure 2.1: Comparison of equivalent bubble-droplet pairs for density ratio $\rho^\star = 1.2, 3$ & 20, shown along with the normalized vorticity field $\omega_z^\star = \omega_z / |\omega_z|_{\max}$ at steady state. In these cases, the bubble is seen to deform more than the droplet, while the droplet generates more intense and longer trailing vorticity fields. As the density ratio gets farther from unity, the bubble-droplet pair begins to drastically differ. These results are obtained from simulations performed in OpenFOAM in 2D.

liquid droplets (ρ_l) suspended in vapor (ρ_v), centered in a periodic domain of 150×150 uniform orthogonal cells, with a viscosity ratio $\nu^\star = 1$ (as we use single-component LB) and increase the density ratio $\rho^\star = \rho_l / \rho_v$.

LB parameters: These simulations are performed using our in-house code. The droplet diameter is set to 60 lattice units initially, with the density inside and outside the droplet varying smoothly over 6 lattice units using a hyperbolic tan profile. These densities are initialized very close to the corresponding liquid and vapor densities found from the co-existence curve [26]. The density ratio is varied by changing the reduced temperature T_r. Two sets of simulations with $\beta = 1$ (i.e. classical multiphase PP-LB) and $\beta = 1.25$ (so-called β scheme) are performed (refer Eq. 2.3). The relaxation time $\tau = 1$, which gives a LB viscosity of $\nu = 0.16$.

OpenFOAM-VOF parameters: In VOF, the droplet diameter is initialized with a diameter of $d = 2$ [mm], at 60 grid cells per diameter, which is a sharp initial profile of α which becomes slightly diffused once the simulation begins. Surface tension values have to be provided in the VOF simulations as a parameter (refer Eq. 2.18). These are obtained from the corresponding LB simulations using the Laplace law ($\Delta p = 2\sigma/R$) at steady state, where Δp is the pressure difference between the center of the droplet and the edge of the domain. Further, three sets of simulations with OpenFOAM are performed

1. Classical VOF, i.e. without interface compression ($c_\alpha = 0$)

2. VOF with interface compression ($c_\alpha = 1$), which produces a sharp interface but increases the spurious currents as it steepens the α field gradients at the interface (Klostermann *et al.* [61] report c_α does not influence the magnitude of spurious currents much, however Hoang *et al.* [38] demonstrate that a higher c_α generates stronger spurious currents)

3. VOF with interface compression ($c_\alpha = 1$), with an added α smoothing step during calculation of the curvature, which is called *VOFsmooth* after Hoang *et al.* [38] who implemented it in OpenFOAM, based upon Lafaurie *et al.* [45]. This case is aimed to specifically demonstrate the utility of the α smoothing function, despite a compressive scheme to preserve a sharp interface.

Euler time integration (with adaptive time stepping following the limiting Courant criteria $Co_{\max} = 0.25$), with *Gauss linear* interpolation of gradient terms and *Gauss van-Leer* interpolation of the advection terms is used. *Backward* time integration was also tried, however it did not influence these results much. A single PISO loop was used with 10 corrector steps, and the tolerance criterion for convergence was kept at 10^{-7} for the pressure term and 10^{-8} for the velocity.

FLUENT-VOF parameters: The FLUENT simulations are performed for two sets of cases, the first with geometrical-reconstruction and the other with an interface compression technique similar to OpenFOAM. The residuals of velocity and momentum were kept to their default values of 10^{-5} and it was checked that the average velocity in the domain was constant at this value within a time step. Time integration performed was *first order implicit* (equivalent to the OpenFOAM *Euler* integration) - other than which is not allowed for explicit VOF in FLUENT and *least squares* interpolation for the gradient terms was used. An adaptive timestepping with a maximum timestep size of 10^{-4} [s] was used along with the same Courant criterion of $Co_{\max} = 0.25$.

2.3.2. SPURIOUS CURRENTS

Spurious velocity vectors after a long simulation time are shown for the case $\rho^\star = 3$ in Fig. 2.2 with contours of $\alpha = 0.5$ for the VOF methods implemented in OpenFOAM (FLUENT results are qualitatively similar) and for LB ($\beta = 1.25$). The normalized vorticity fields ($-1 < \omega_z^\star < 1$, red to blue, where $\omega_z^\star = \omega_z / |\omega_z|_{\max}$) have also been shown. Fig. 2.2a shows classical VOF which has a slightly diffused interface and produces only a small magnitude of spurious velocities near the interface, velocity vectors distant from the interface being almost of length zero. Fig. 2.2b shows how using interface compression ($c_\alpha = 1$) steepens the magnitude of spurious velocities, which now appear with longer vectors. Upon using VOFsmooth (Fig. 2.2c) these vectors again become smaller in magnitude, while the scheme preserves a sharp interface. Lastly, Fig. 2.2d shows the spurious velocities in LB, which after having attained a steady state do not exhibit fluctuations (unlike in VOF) and attain a very symmetric profile. Note that the overall shape and magnitude of the spurious velocity field in LB can change depending on the discretization of the force term into conservative or non-conservative forms, as has been explained by Connington and Lee [62]. These results are representative of how the velocity fields look in VOF and LB. In the VOF simulations we observe that for high $\rho^\star$ values (i.e. also high σ) the droplet can perform a random walk in the domain driven by large asymmetric spurious currents, as has also been reported in literature [38].

Since there is no steady state behaviour in the VOF simulations for the global average spurious velocity or the maximum spurious velocity magnitude, a single value is ascertained for each simulation by time averaging the maximum spurious velocity magnitude $|u|_{\max}$ between 0.2 to 1.0 [s] to get $\langle |u|_{\max} \rangle$, as shown in Fig. 2.3. It was checked that this time average is representative, as performing a similar averaging over a 10 times longer signal between 0.2 to 10.0 [s], for one of the cases, yielded a value within $2-4\%$ of the shorter time average.

Finally to compare the magnitude of these spurious velocities between different techniques, a "Spurious Reynolds number" Re_{sp} is defined as follows

$$Re_{\text{sp}} = \frac{\langle |u|_{\max} \rangle \, d}{\nu} \tag{2.28}$$

where $\langle |u|_{\max} \rangle$ is the time averaged maximum spurious velocity for the VOF simulations ($\langle |u|_{\max} \rangle$ is taken to be the steady state value for LB simulations). Re_{sp} over increasing $\rho^\star$ is shown in Fig. 2.4.

LB with $\beta = 1.25$ is seen to produce Re_{sp} 1-3 orders of magnitude lower than all VOF formulations, while the classical LB approach ($\beta = 1.0$) becomes comparable to VOF around $\rho^\star = 300$. Generally among the VOF methods, interface sharpening ($c_\alpha = 1$) in OpenFOAM increases Re_{sp} by almost an order of magnitude as compared to the classical VOF ($c_\alpha = 0$). Upon smoothing the interface during curvature calculation, Re_{sp} can be brought down an order of magnitude, and this effect is more prominent at higher density ratios. The two FLUENT VOF methods produce very similar Re_{sp} numbers, which at high density ratios remain close to the VOFsmooth values. The differences between the FLUENT and OpenFOAM results here cannot be ascribed to the difference in the tolerances used for the solvers (i.e. 10^{-8} and 10^{-5} for velocity in OpenFOAM and FLUENT respectively). This is because the minimum magnitude of the spurious currents ($\mathcal{O}(10^{-3})$) is still 100 times larger than the 10^{-5} tolerance. We performed a test with the same solver

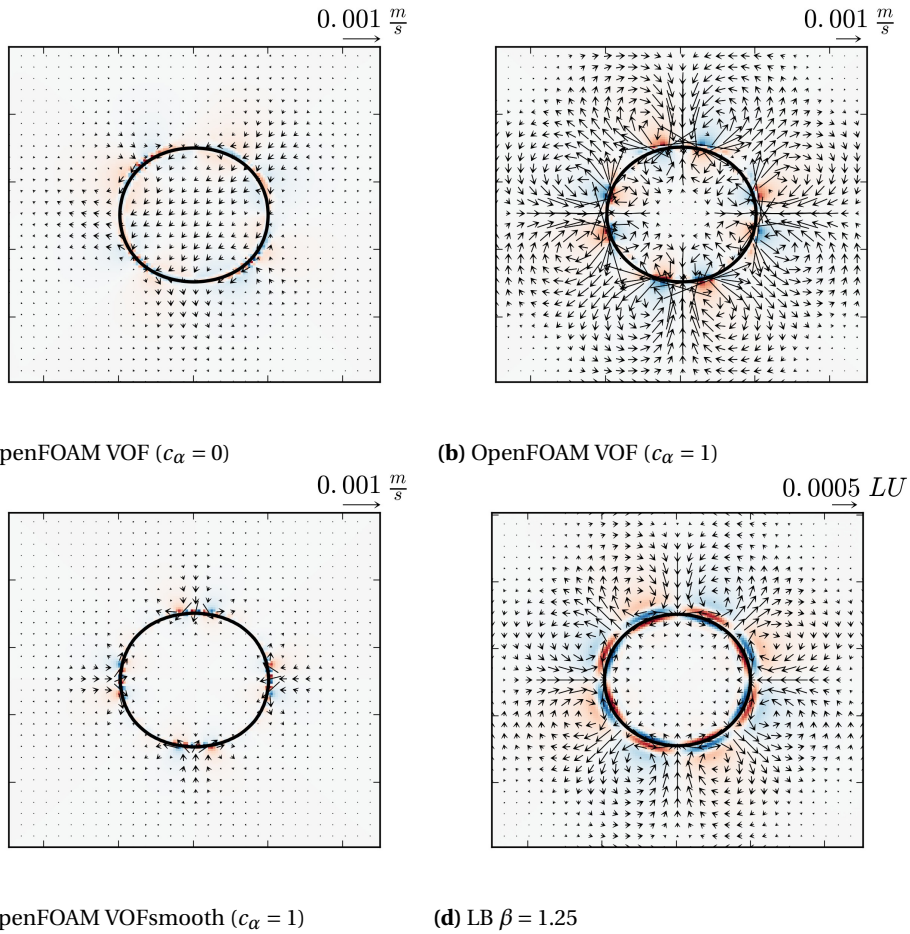

(a) OpenFOAM VOF ($c_\alpha = 0$)

(b) OpenFOAM VOF ($c_\alpha = 1$)

(c) OpenFOAM VOFsmooth ($c_\alpha = 1$)

(d) LB $\beta = 1.25$

Figure 2.2: Spurious velocity vectors for $\rho^\star = 3$ are shown for the three VOF methods implemented in OpenFOAM (FLUENT results being qualitatively similar to OpenFOAM) and for LB ($\beta = 1.25$). The normalized vorticity fields ($-1 < \omega_z^\star < 1$, red to blue, where $\omega_z^\star = \omega_z/|\omega_z|_{\max}$) have also been shown. The classic VOF method in OpenFOAM ($c_\alpha = 0$) has a slightly diffused interface and produces small spurious velocities near the interface. Using VOF with $c_\alpha = 1$ sharpens the interface while increasing the magnitude of the spurious velocity vectors. VOFsmooth with $c_\alpha = 1$ shows the utility of the α smoothing function which reduces the spurious velocities while maintaining a sharp interface. Lastly, in LB these emerge as symmetric, non-fluctuating counter rotating vortices.

in OpenFOAM for the two tolerance values of 10^{-5} and 10^{-8}, and the spurious velocity magnitudes were within 5% of each other, whereby not influencing the results in Fig. 2.4.

Due to the many differences between LB and VOF simulations, it is not possible to directly comment on why LB produces much lower spurious currents than VOF purely in terms of tolerances, numerical schemes etc. At low density ratios ($\rho^\star \sim 3-60$), where classical LB performs as well as the modified $\beta-$scheme, this difference is stark as Re_{sp}

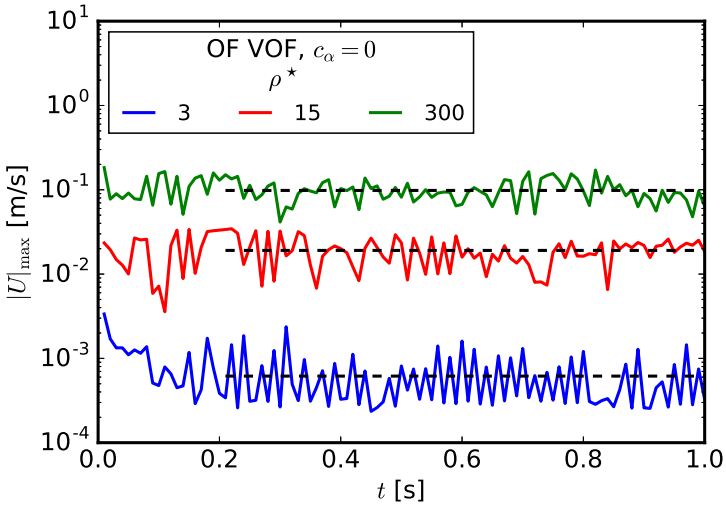

Figure 2.3: The averaging performed on the maximum spurious velocity magnitude $|u|_{\max}$ (between times 0.2 and 1.0 [s]) to ascertain a representative spurious velocity magnitude $\langle |u|_{\max} \rangle$ for VOF simulations is shown for the OpenFOAM simulations for classical VOF.

is almost 1000 times lower in LB than in VOF. This can partly be ascribed to the thicker interfaces in LB at low density ratios. Further, the non-dimensional LB units cannot be mapped to a physical set of units in this case as there are insufficient variables for a stationary droplet for a mapping. Since LB with $\beta = 1.25$ produces Re_{sp} 1000 times lower than all VOF methods, it appears better suited for simulating large density ratio flows (like air-water) at low Re - which would be difficult with VOF as spurious currents will be of the same order of magnitude or more than the physical velocity scales. Also, while simulating heat and mass transfer problems, spurious currents will increase scalar transport across the interface, where having lower spurious velocities can be a decisive advantage for a simulation technique.

In addition in LB simulations, the density ratio $\rho^\star$ and interface thickness (both of which are determined by the reduced temperature T_r used in the EOS) and β influence the magnitude of Re_{sp}, while in VOF, it is $\rho^\star$ and the value of the surface tension parameter σ. For instance in VOF, for the same value of σ (8×10^{-4} [N/m]), changing $\rho^\star$ from $\mathcal{O}(1)$ to $\mathcal{O}(100)$ only changes Re_{sp} by a factor of ~ 3, while increasing σ (from 8×10^{-4} to 2×10^{-2} [N/m], in accordance to the LB simulations) increases Re_{sp} by a factor ~ 100. Another aspect is that Re_{sp} can increase up to $2-5$ times in VOF based upon the specific choice of solvers - specially if using higher order discretization schemes (which is not shown here but was observed).

It is worthwhile to note that an alternative FVM method with an exact interface representation using body-fitted coordinates, as presented in the PROST scheme of Renardy and Renardy [63], can virtually eliminate these parasitic currents. Though such a formulation comes with its own limitations, namely a higher computational cost of re-meshing the domain at each time step along with interpolation of values to new cell faces. In PP-

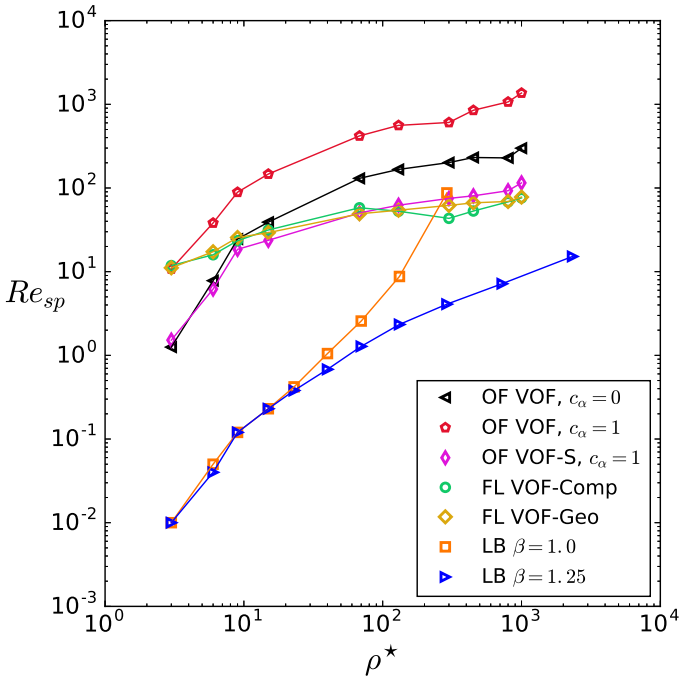

Figure 2.4: Spurious Reynolds number Re_{sp} over density ratio $\rho^\star$, for different solver cases is shown. LB with $\beta = 1.25$ produces Re_{sp} $1-3$ orders of magnitude lower than all VOF formulations. Among the VOF methods, using interface compression in OpenFOAM increases Re_{sp} by an order of magnitude as compared to classical VOF, which can be remedied by using VOFsmooth which reduces Re_{sp} significantly while maintaining a sharp interface. The FLUENT VOF methods produce very similar Re_{sp}, that are close to the VOFsmooth values for higher $\rho^\star$. Note that all these simulations were performed in 2D.

LB, upon increasing isotropy by introducing mid-range interactions, spurious velocities can be made to practically vanish as demonstrated by Sbragaglia *et al.* [64]. Such a formulation in turn breaks the ease of parallelization of the LB code, as the interactions are no longer local and successively distant lattice nodes begin to influence an otherwise compact computational molecule centered at each lattice node.

2.3.3. INTERFACE THICKNESS

Focusing on the sharpest reproducible interface, the phase indicator function α has been shown in Fig. 2.5 across the droplet interface (see schematic in the figure), for $\rho^\star = 15$ & 1000, for OpenFOAM VOF with $c_\alpha = 1$, FLUENT VOF with geometrical reconstruction and LB with $\beta = 1.25$ (in LB the density field has been normalized to a phase indicator). As a reminder, the VOF simulations are initialized with a sharp α profile, and the LB simulations start with a droplet with the interface smoothed over 6 lattice units. These interfaces then diffuse during the simulation, and the final interface thicknesses are independent of the initialization.

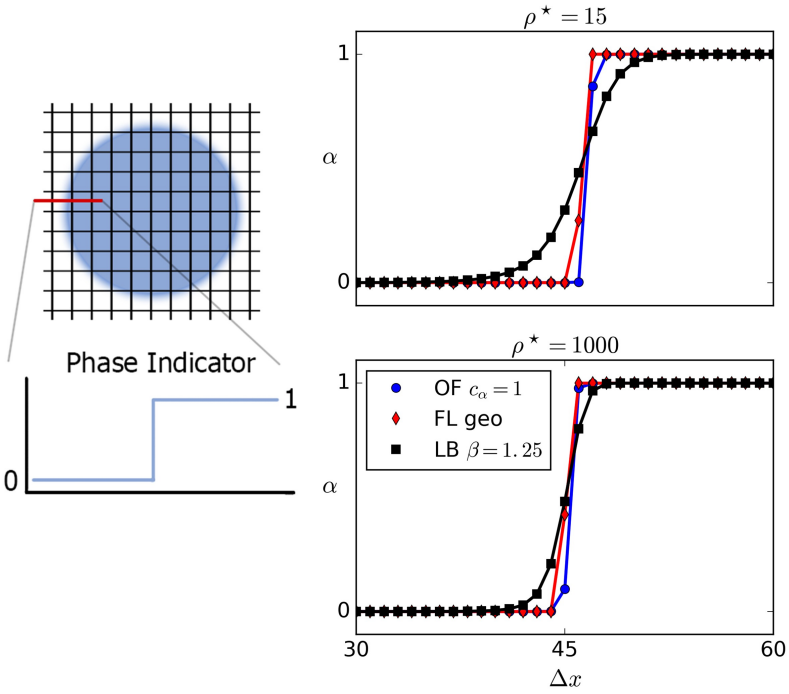

Figure 2.5: Comparison of the interface thickness at its sharpest in the stationary droplet simulations, shown as the phase indicator function α across one side of the droplet (refer schematic) for OpenFOAM VOF with interface compression ($c_\alpha = 1$), FLUENT with geometrical reconstruction and LB ($\beta = 1.25$). It is seen that FLUENT with geometrical reconstruction produces the sharpest interface, closely followed by OpenFOAM with interface compression. In LB, the interface becomes sharper with an increasing density ratio.

It is seen that FLUENT produces the sharpest interface with the geometrical reconstruction scheme, an interface of $2-3$ grid cells, closely followed by OpenFOAM with interface compression where an interface of $3-4$ grid cells is obtained, over all $\rho^\star$ values. LB produces thicker interfaces, ranging from $8-11$ lattice units for low $\rho^\star$ to $3-5$ for a higher $\rho^\star$. This $\rho^\star$ dependence comes from the pseupotential force at the interface which more strongly repels the lighter phase when $\rho^\star$ is high, and is weakly repelling for lower $\rho^\star$ values. Also, it has been shown that the interface thickness in LB is affected by the choice of the equation of state [65].

2.4. FALLING DROPLETS IN LIQUID-LIQUID SYSTEMS

2.4.1. CASE FORMULATION

Here onward, we focus on a realistic problem of a single liquid droplet, falling through a column of another immiscible liquid under gravity. We are interested in a comparison for low density ratio systems, which are highly relevant to liquid-liquid emulsion research. The cases are formulated by fixing the Eo and M numbers, which have been selected to coincide with a low Re and Eo region of the Clift map. First, a droplet is ini-

tialized in LB with an initial approximate diameter $d = 100\,\Delta x$, which is let to relax to an equilibrium value. Then, by using the Laplace law, σ is calculated. Using this value and Eo, g_{LB} is obtained. Finally, using the value of M, ν_{LB} is estimated which can be controlled by changing τ. Equivalent VOF simulations are formulated by keeping Eo and M identical to the LB simulations by varying σ and d, while keeping ρ_l, ρ_d and g constant, values of which have been listed in Table 2.1. Here onward the subscripts l, d denote the surrounding liquid and droplet liquid respectively. The five cases are listed in Table 2.2. Note that we perform these simulations for the lowest density ratio possible in our single-component PP-LB implementation, i.e. $\rho^\star = 3$, since droplets at even lower density ratios begin to dissolve under non-stationary conditions. This is because at very low density ratios, the interaction force between the phases becomes weaker in LB as phase separation is fragmented, and consequently the droplet dissolves away if it starts moving. It is worth mentioning that by choosing a low density ratio the spurious Reynolds number in VOF $\mathcal{O}(0.1)$ also remains much smaller in magnitude than the flow Reynolds number $\mathcal{O}(1-10)$.

Quantity	ρ_d	ρ_l	ν_d	ν_l	g
Units	[kg/m^3]	[kg/m^3]	[m^2/s]	[m^2/s]	[m/s^2]
Value	300.0	100.0	5.0×10^{-6}	5.0×10^{-6}	9.81

Table 2.1: Physical properties used in the VOF simulations.

Case	Eo	M	Re [23]	d [m]	σ [N/m]
1	0.98	1.75e-04	4	4.54e-04	4.12e-04
2	1.82	3.26e-04	8	5.57e-04	3.35e-04
3	2.18	5.29e-04	7	5.63e-04	2.85e-04
4	6.27	1.47e-03	13.5	8.05e-04	2.03e-04
5	3.50	9.50e-05	24	9.49e-04	5.05e-04

Table 2.2: Parameters for the five cases of a single liquid droplet falling through an immiscible liquid ($\rho^\star = 3$), along with the corresponding Re prediction by marking Eo and M on the Clift map.

2.4.2. SIMULATION DETAILS

The simulation domains with boundary conditions are shown in Fig. 2.6. The horizontal extent of our simulation domains is $8d \times 30d$ where d is the droplet diameter for the VOF simulations. This is considered sufficiently large such that the walls do not influence the velocity evolution [29, 66], given that what we wish to study is effectively a droplet freely falling in an infinite medium, i.e. to look at the droplet from a stationary frame of reference. The LB domain is larger at $10d \times 40d$, for two reasons. First is to ensure a large enough domain despite droplet expansion during the initialization phase. Secondly, our current LB implementation works with a fully periodic domain, while the VOF domains use free-slip horizontal boundaries and no-slip vertical boundaries. Since the cases we simulate have a strong left-right symmetry with no unsteady features in the droplet wake, the free-slip boundary condition should be equivalent to a

periodic boundary condition in the horizontal direction (as the horizontal extent is large enough). To minimize the influence of the vertical boundary conditions being different in VOF compared to LB, the LB domain is kept large enough in the vertical direction such that the droplet reaches terminal velocity at a sufficient distance from the bottom periodic boundary. This ensures that the droplet does not cross the boundary and its wake is captured correctly in LB.

In OpenFOAM, the PISO algorithm has been used, while the PIMPLE algorithm with residual control was also tested. FLUENT uses the SIMPLE algorithm and only the tolerances for the final residual values have to be provided, which are kept the same as in OpenFOAM at a value of 10^{-7} for pressure and 10^{-8} for velocity to consistent. Here we have changed the tolerance from its default value in FLUENT (i.e. 10^{-5}, as was used in the spurious velocity study) to 10^{-8}, as an extra precaution to eliminate any differences that may arise if these values are different. The VOF simulations use second order time integration (*backward* scheme in OpenFOAM), with *vanLeer* discretization of convective terms and *linear* interpolation of gradient terms.

The parameters used in the LB simulations are presented in Table 2.3, and these simulations are performed using the open source parallel lattice-Boltzmann Solver (Palabos-v1.5r1). The value of the reduced temperature $T_r = 0.96$, which gives a density ratio of $\rho^\star \approx 3$. The droplets are initialized with a diameter of 100 lattice units, with the density inside and outside set to 0.21 and 0.07, as obtained from the C-S coexistence curve at $T_r = 0.96$ [26]. This system is first allowed to relax to equilibrium and during this period, the droplet can expand from its original size where the magnitude of the expansion depends on the total mass in the system which needs to relax to equilibrium. Hence, this transient phase is dependent on the domain size, and if the droplet expands significantly, the horizontal and vertical extents that were chosen may be insufficient. Changing the value of β from $\beta = 1.25$ to $\beta = 1.65$ can help mitigate the droplet expansion and has been shown in the Appendix in Fig. 2.17. Thereafter, d, g_{LB} and τ are calculated and the body force is added. We perform simulations for both values of β. Note that this is specifically a problem while simulating low density ratio (or T_r close to 1) systems with single component LB. This does not occur at higher density ratios ($T_r < 0.8$), where the phase separation is strong.

Case	1	2	3	4	5
$\beta = 1.25$					
τ	0.9129	0.8503	0.8779	0.8747	0.7578
$g[\times 10^{-7}]$	0.61463	1.1383	1.3634	3.9214	2.1951
$\beta = 1.65$					
τ	0.8958	0.8753	0.9049	0.9014	0.74716
$g[\times 10^{-7}]$	0.79861	1.1601	1.3896	3.9966	2.8522

Table 2.3: LB parameters for the falling droplet cases. For these simulations, the reduced temperature $T_r = T/T_c = 0.96$ and $\rho^\star = 3$. All simulations are performed on a domain $N_x \times N_y = 1000 \times 4000$ using the parallel lattice-Boltzmann Solver (Palabos-v1.5r1).

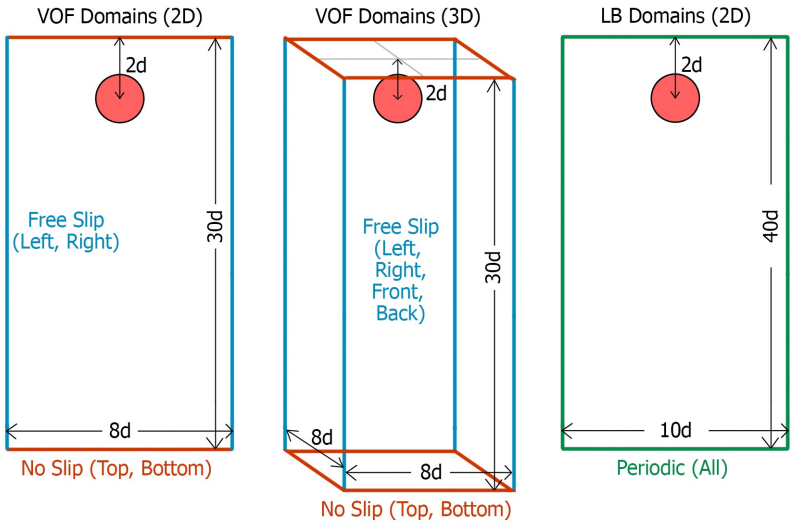

Figure 2.6: Schematic showing the computational domains and boundary conditions used in the VOF and LB simulations of a single liquid droplet falling through an immiscible liquid (with a density ratio $\rho^\star = 3$). Note that d is the droplet diameter in each case.

NOMENCLATURE

- OpenFOAM VOF simulations performed in 2D with mesh resolution of N cells per droplet diameter, $N \in \{20, 40, 80\}$, are labeled **OF2Ddx20** etc. For these simulations, we use $c_\alpha = 0.5$, to prevent interface diffusion in high Re cases, while not aggravating the spurious currents too strongly. Simulations using the VOFsmooth solver are suffixed with an 'S', Eg. OF2Ddx20S.
- OpenFOAM VOF simulations performed in 3D using dynamic mesh refinement are labeled as **OF3D**, with a suffix 'c' or 'm' for *coarse* or *medium* respectively, with 5 and 7.5 base cells per diameter and a factor 4 refinement at the interface. For our chosen simulation domain the number of grid cells is above a million for the 7.5 base cells with mesh refinement, which we do not refine further so as not to make the computational cost
- Fluent VOF simulations performed in 2D are named similar to their OpenFOAM counterparts, as **FL2Ddx20** etc.
- LB simulations were performed using the open source parallel-Lattice Boltzmann Simulator (Palabos-v1.5r1) and are labeled **LB2D**.
- When not using a suffix ('dx20', 'm' etc.), we refer to results from the finest resolution simulations.

Before we present the results, it is worthwhile to mention that we compare 2D VOF and LB simulations, along with 3D VOF, to 3D experimental results from the Clift map. The 2D droplets can be thought of as infinite fluid cylinders, without any variation in

the third direction. By balancing drag force with buoyancy, the terminal velocity can be expressed as $v_\infty = (\Delta\rho V g / 0.5\rho_c A c_D)^{1/2}$, where $\Delta\rho$, V, ρ_c, A and c_D are the density difference, volume of the droplet, density of the continuous (outer) fluid, crossectional area and coefficient of drag respectively. For the Re values in this study, the drag coefficient c_D on a (solid) cylinder and sphere are approximately 4.5 and 7 (for Case 1, $Re = 4$) and 1.8 and 2.5 (for Case 5, $Re = 24$) respectively [67]. Using these values, it can be said that the 2D VOF results will predict a velocity 25% higher than the 3D value, particularly for Case 1. Apart from this, if the flow does not consist of highly 3D features like unsteady vortices, we expect the 2D simulations to be comparable to the 3D results. Note that the internal circulation inside a droplet reduces the drag experienced by it in comparison to a solid body by almost 30% [23], so the c_D values mentioned above do not directly apply to liquid droplets, and will need a further correction factor.

2.4.3. RESULTS

The steady state Re numbers are shown together on a section of the Clift map in Fig. 2.7, where the solid black line marks the boundary between the spherical (below) and elliptical (above) shape regimes. Further, analytical solutions for the spherical and elliptical regimes (refer to Eq. 2.25 and Eq. 2.26) are shown, along with the final shapes from the OF2Ddx80 simulations for reference. This figure presents an overview of the simulations performed, also showing the small part of the falling droplet phase space that has been explored. The same is also shown in Fig. 2.8, where the cases are presented separately for additional clarity.

All techniques agree well with each other and the Clift map for Cases 4 and 5, while the spread between predictions is higher at lower Re. For VOF, this may be ascribed to a higher sensitivity of results to spurious velocities, as at low Re spurious currents may be comparable to the physical velocity. Further, the horizontal extent of the domain has a higher influence on lower Re droplets, while at higher Re values the domain edges have little influence.

We look more closely at Case 1 and Case 5, corresponding the smallest and the largest Re in this study.

CASE 1

This corresponds to the spherical region of the Clift map. The steady state droplet shapes with the velocity and normalized z-vorticity fields ($-1 < \omega_z^\star < 1$, from red to blue) are shown in Fig. 2.9, the OF3D results are plotted on a cross-section at the center of the domain. Note that these plots show only a small region around the droplet to focus on the local flow characteristics. It was checked that the velocity further from the droplet, near the domain edges, is negligible. If the domain is not sufficiently large in the horizontal direction, the velocities near the lateral walls can be significant and should be taken into account to study the falling droplet from a stationary frame of reference. The simulations produce a trailing vorticity field at steady state, with the highest concentrations outside the lower droplet region, close to the interface, clearly marking two counter rotating regions of the flow. The shapes produced are also very similar and the droplets remain mostly spherical for all solvers.

The vorticity field in LB is less intense than in VOF, but its features are similar. Some spurious vorticity regions can be seen localized near the interface which do not diffuse

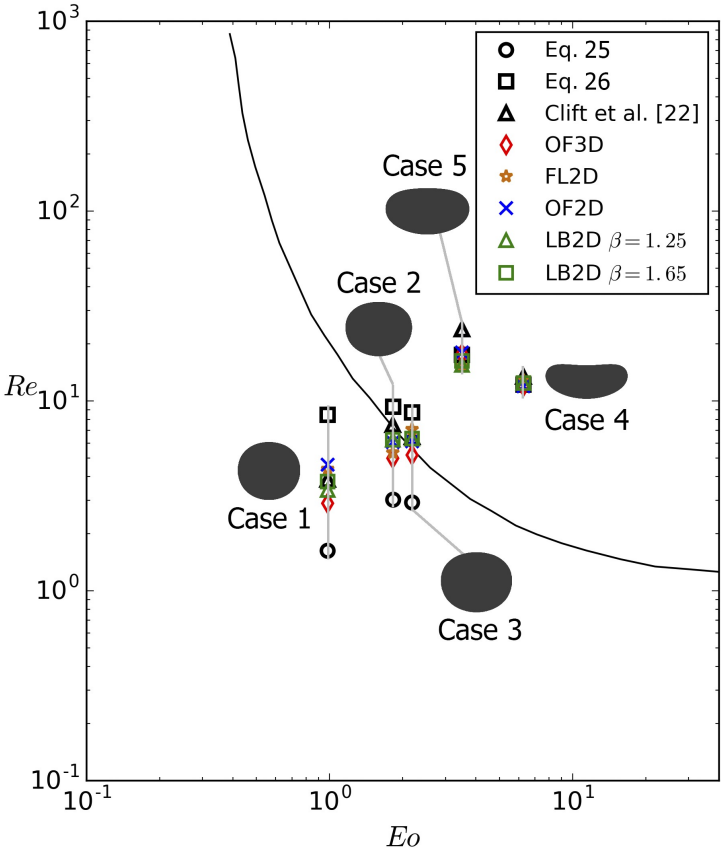

Figure 2.7: Terminal Re numbers for single liquid droplets falling through an immiscible liquid ($\rho^\star = 3$), calculated from simulations with the finest grid resolution shown with the Eo number along with the final shape from the OF2Ddx80 simulations. Results for individual cases (i.e. a fixed Eo and M number from Table 2.2) are connected with a vertical gray line, which also forks to the droplet shape for Cases 2, 3 and 5 for clarity. Lastly, the solid black curve divides the $Re-Eo$ phase-space into the spherical (below the line) and ellipsoidal (above) shape regions, and is taken from Clift *et al.* [23].

into the bulk. The spurious vorticity produced in Palabos is slightly different from the spurious vorticity in the LB simulations using our in-house code (Fig. 2.2d). This difference comes from the exact discretization of the force term in the LB equation, the effect of which has been detailed in Connington and Lee [62]. What is important here is that the spurious currents do not influence our results directly or significantly as they are symmetric and tend to cancel out. They might have an effect on the droplet shape, suppressing acute deformations, but we do not investigated that in this study.

The evolution of the Reynolds Re number of the droplet has been shown in Fig. 2.10.

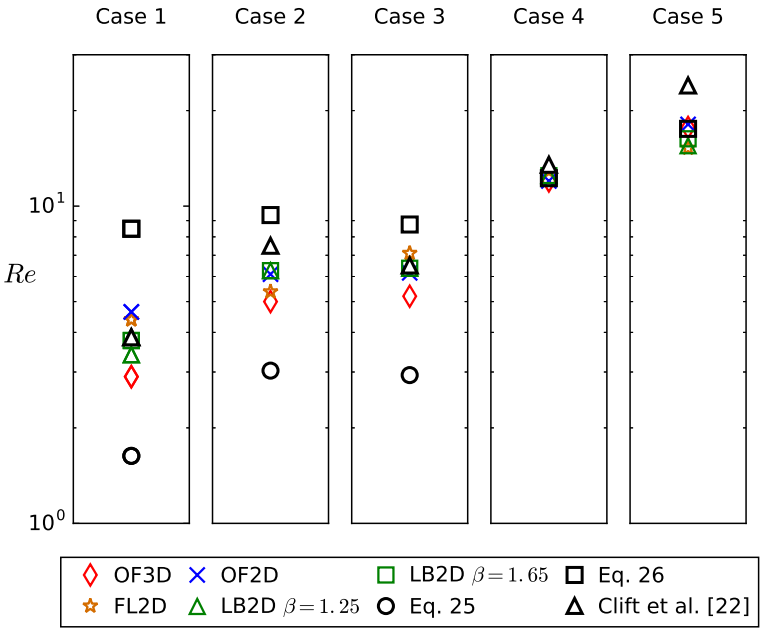

Figure 2.8: Terminal Re numbers from the different simulations shown separately for each Case listed in Table 2.2 for additional clarity. The spread between the predictions is larger at lower Re numbers, while at higher Re values all simulations agree well with each other and the Clift map. There is excellent agreement between VOF and LB results.

For calculating Re, the average velocity in the droplet region is considered as follows

$$u = \frac{\sum \alpha u_y}{\sum \alpha} \tag{2.29}$$

where $\alpha = 1$ in the droplet region and 0 outside it and u_y is the magnitude of the vertical velocity component. The evolution is shown over dimensionless time $t^\star = t/\sqrt{d/g}$ and the gray band marks the value from the Clift map with 5% uncertainty.

The 2D VOF simulations attain very similar terminal Re values, close to the 3D value extrapolated from the Clift map. The uncertainty in the results, given the magnitude of spurious Re, is expected to be around 2 – 20% for the coarse to fine mesh resolutions. Since the magnitude of spurious velocities increases from $\mathcal{O}(0.01)$ to $\mathcal{O}(1)$ from dx20 to dx80, mesh convergence of the results cannot be achieved for this case. This behaviour of OpenFOAM VOF has been observed before for flows with a low Capillary number [61]. The LB2D results are very close to the Clift map for both values of β, and the spurious currents in LB have very little influence on the droplet Re evolution. A comparison between the steady state shape for the two β values is shown in Fig. 2.19 .

OF3D under-predicts the droplet Re almost by ~ 30%. We investigated this further by performing tests on a smaller domain to reduce computational time for a representative problem. We find that compared to a uniform 3D mesh (of grid resolution equal to the finest grid size obtained upon 2 successive dynamic mesh refinements), the dynamic

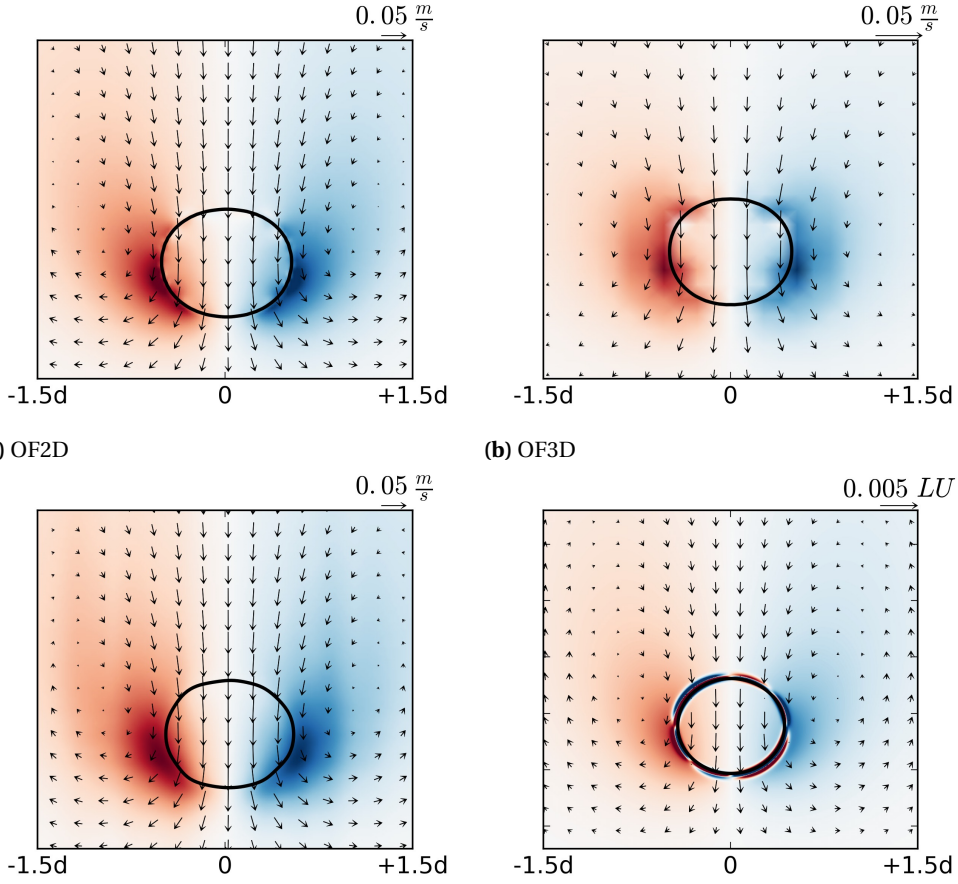

(a) OF2D **(b)** OF3D

(c) FL2D **(d)** LB2D ($\beta = 1.65$)

Figure 2.9: Steady state droplet shape with the normalized vorticity field $\omega_z^\star$ ($-1 < \omega_z^\star < 1$, red to blue, where $\omega_z^\star = \omega_z / |\omega_z|_{\max}$) is shown for Case 1, corresponding to $Re = 4$. Note that the region shown is a small part of the actual computational domain around the droplet.

mesh simulations with a coarse base mesh always under-predict the velocity. This can be ascribed to a loss in mesh orthogonality in the transition between coarse and refined mesh regions. The interpolation of values from cell center to cell faces occurs along a line that is not orthogonal to the face itself. This leads to numerical errors and can cause a different kind of spurious currents than those arising out of inaccurate curvature calculation in VOF. Further due to refinement near the interface, curvature induced spurious currents are also aggravated, and it has been reasoned by Magnini *et al.* [68] that these can be seen as capillary waves on the interface, which effectively cause a deviation from a smooth interface profile resembling a kind of surface roughness that increases drag - something we observe in the consistent underprediction of the velocity. Upon adding additional refinement criterion, for instance refinement in the droplet wake based upon a vorticity threshold, the results improve though they still do not coincide with results

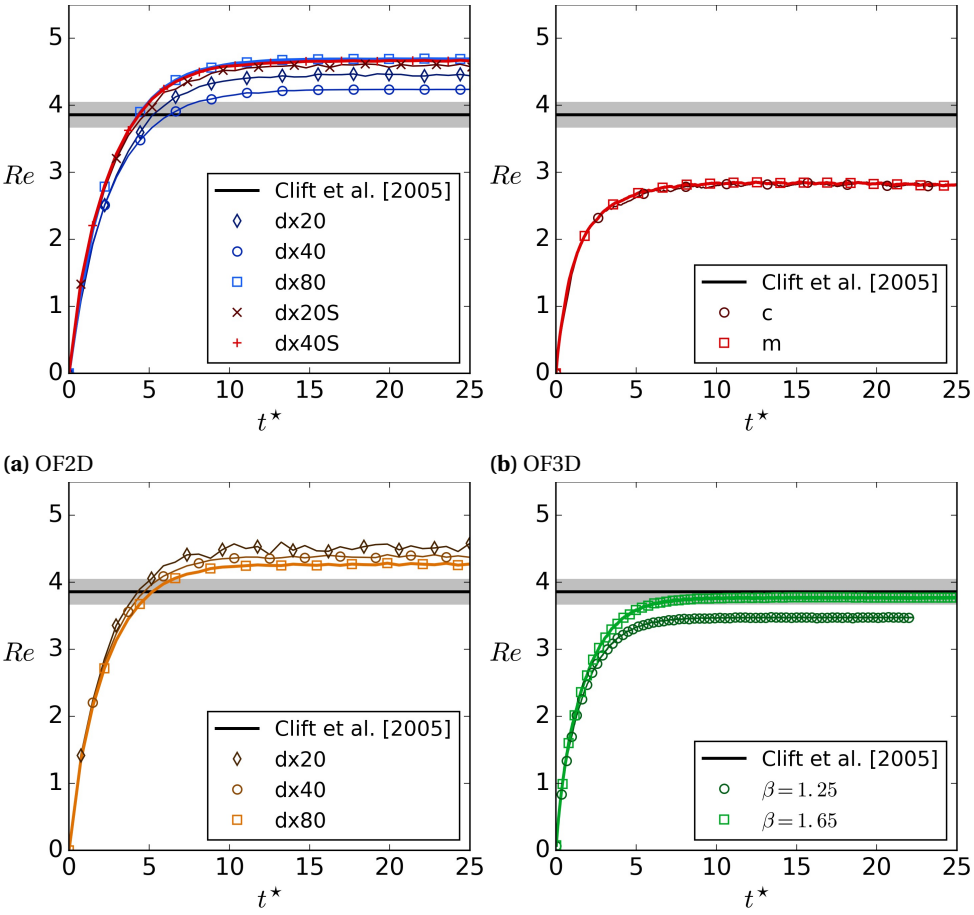

(a) OF2D

(b) OF3D

(c) FL2D

(d) LB2D

Figure 2.10: Evolution of the *Re* number for Case 1 for all simulations shown along with the value from the Clift map with 5% errorbars.

from the uniform 3D mesh.

CASE 5

This case corresponds to the ellipsoidal regime of the Clift map. The final droplet shapes along with normalized vorticity fields are shown in Fig. 2.11. It is seen that compared to the 2D VOF cases, the OF3D droplet undergoes lesser deformation, which is a consequence of the under resolved velocity field owing to a coarse base mesh. The droplet deformation is caused due to the pressure difference between high and low pressure regions around the droplet. A region of strong vorticity corresponds to lower pressure, creating a larger deforming force. Due to the lower velocity in OF3D, this pressure difference is lower, resulting in lesser deformation. The LB2D droplet does not flatten as much as the 2D VOF droplets, and in this case, the droplet shrinks slightly from its initial size.

Although we achieve a steady state here, for even higher Re numbers, moving droplets in LB can begin to dissolve away completely due to the diffused interface at low density ratios. Further, it is seen that the vorticity field in LB remains confined in the lighter phase, whereas in VOF, the vorticity field is very close to the interface and also extends to within a small region inside the droplet.

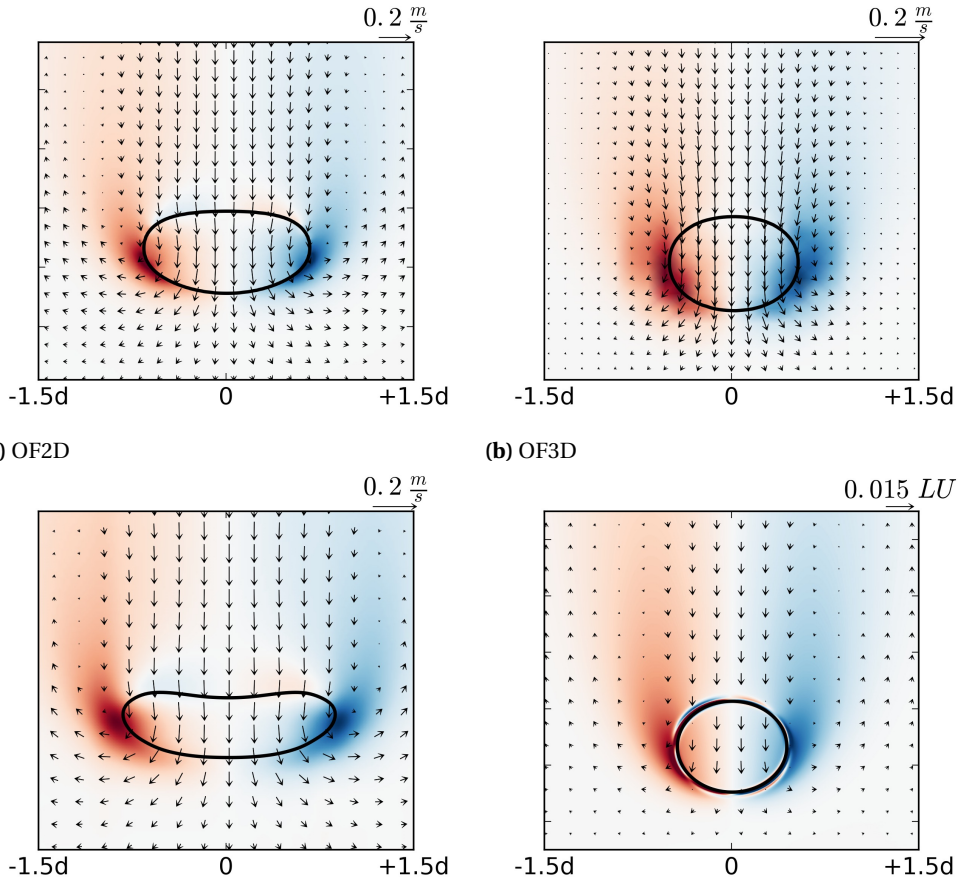

(a) OF2D **(b)** OF3D

(c) FL2D **(d)** LB2D ($\beta = 1.65$)

Figure 2.11: Steady state droplet shape with the normalized vorticity field $\omega_z^\star$ ($-1 < \omega_z^\star < 1$, red to blue, where $\omega_z^\star = \omega_z / |\omega_z|_{\max}$) is shown for Case 5, corresponding to $Re = 24$. The FL2D droplets is seen to deform the most, followed by OF2D. OF3D produces a lower deformation of the droplet, which is ascribed to an under-resolved velocity leading to a lower pressure difference between the horizontal and vertical droplet extents which acts towards deforming the droplet. The LB2D droplet does not flatten as much as the 2D VOF droplets and remains mostly spherical, and its size shrinks slightly from the initial value.

The evolution of Re numbers has been shown in Fig. 2.12. All simulations predict similar terminal Re values, though all fall below the prediction of the Clift map. Here the OF2D results were found to be within 10% of each other, as the spurious velocities

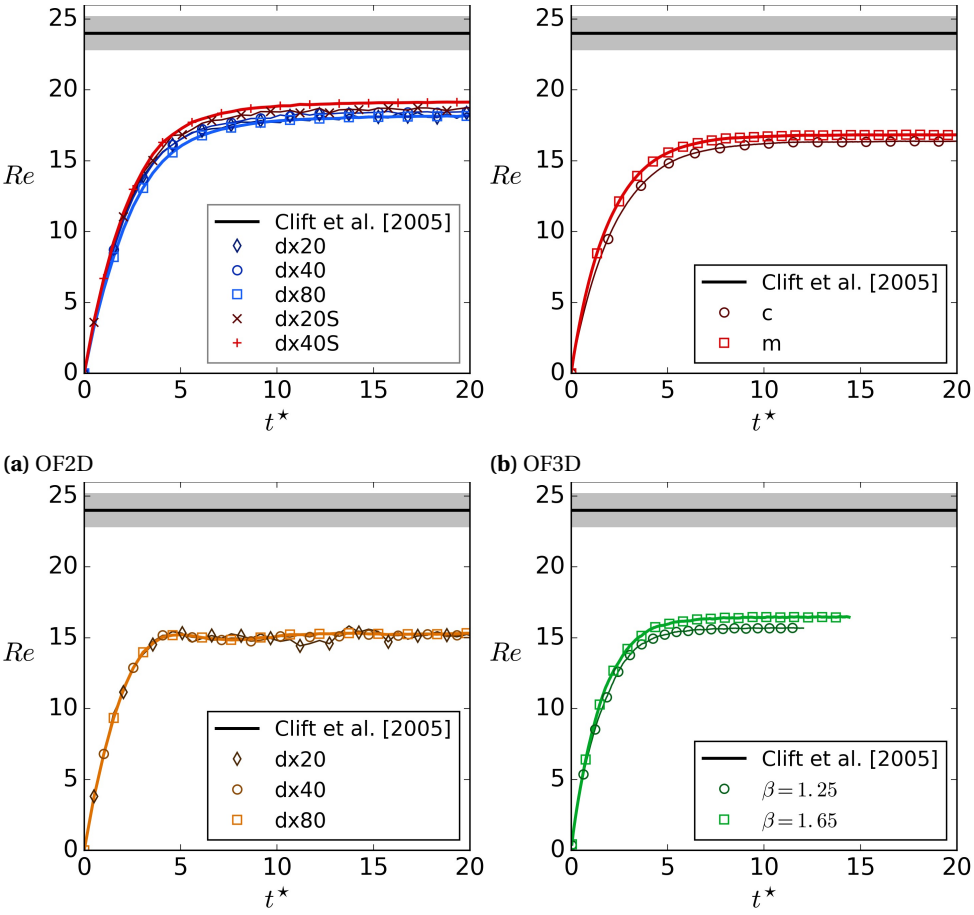

(a) OF2D **(b)** OF3D

(c) FL2D **(d)** LB2D

Figure 2.12: Evolution of Re for Case 5 for all simulations shown along with the Clift map value with 5% errorbars.

have a lower influence on the results. The terminal Re in LB for both $\beta = 1.25$ and 1.65 is smaller than the OF2D value, but comparable to the FL2D values. It was observed (not shown here) that on smaller periodic domains in LB, the droplet does not reach terminal velocity as the droplet wake becomes comparable to the domain length. Using a large enough vertical extent hence is indispensable for accurate predictions. The fact that all the simulations predict a velocity lower than the Clift map value ($Re = 24$) also might indicate that the bubble-droplet equivalence breaks down at higher Re numbers.

There are a few things worth noting regarding the results from the LB simulations. By increasing the value of β from 1.25 to 1.65, the density ratio obtained in LB deviates from the analytical solution of the selected EOS (see Fig. 2.16). Since PP-LB follows the selected EOS, large deviations from the EOS lead to unstable simulations. Therefore, the maximum value of β is limited due to the stability condition of the model. A stability

analysis shows that the simulations become unstable when g_{LB} is larger than $\mathcal{O}(10^{-5})$. This places constraints on the droplet diameter that is required for simulating a particular Re. Also since the interface width is relatively large at $\rho^{\star} = 3$ (≈ 10 lattice units), at higher Re values it can further diffuse adding to numerical inaccuracy. This can be remedied to an extent by using a larger droplet diameter, which in turn makes the domain size computationally expensive.

Lastly, we compare the deformation of the droplet which can be expressed as the standard Taylor deformation parameter $D = (L-B)/(L+B)$, where L and B are the lengths of the major and minor axes of the deformed droplet. Fig. 2.13 shows D at steady state for the different cases using simulation results from the finest mesh.

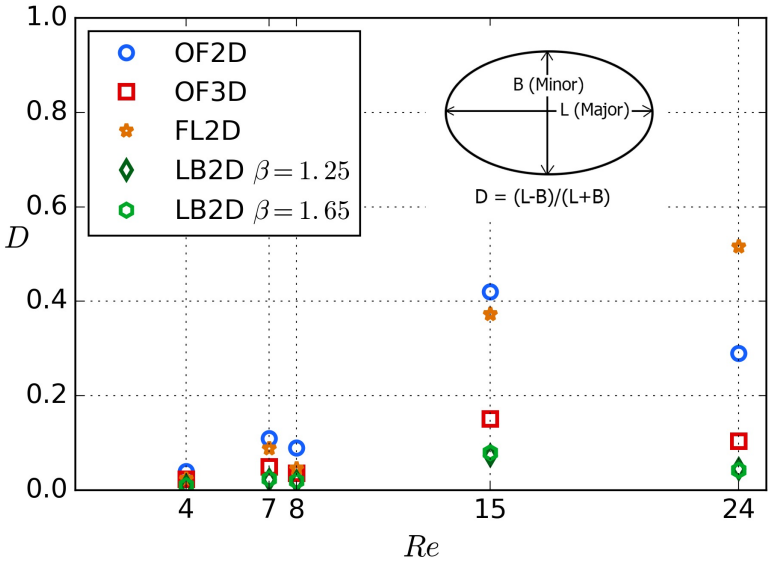

Figure 2.13: Taylor deformation parameter D at steady state for all cases.

For the cases $Re \in \{4, 7, 8\}$, the VOF simulations predict a small value of D, i.e. the droplets deform very little from their initial spherical shapes. OF3D predicts a low D for all Re numbers, which is ascribed to the under-resolved vorticity field. FL2D and OF2D predict higher deformations for $Re \in \{15, 24\}$. OF2D predicts the highest deformation for Case 4 ($Re = 15$), i.e. the case corresponding to the highest Eo. LB2D consistently predicts a low D value across all Re values. Though the Re prediction with LB turns out to be accurate, our implementation seems to be incapable of capturing droplet deformation more accurately.

2.5. DISCUSSION

It is widely held that no single flow simulation technique is universally applicable, primarily because each technique may have been developed with the view of studying a particular class of flow problems. However, it is generally also sought that a newly pro-

posed model or method be as universal as possible, i.e. to say it should be robust. Upon comparing VOF and PP-LB, we encountered several challenges unique to each method in trying to formulate a problem that can be commonly studied. We believe these points must not be overlooked, so as to better equip users with an understanding of the limitations they might face upon choosing either method. We also indicate flow regimes where either method may be better suited, along with method specific issues that have to be dealt with. Note that the following discussion draws from our investigation of low density ratio flows which are widely encountered in emulsion research, ranging from oil and gas applications to food processing and biotechnology. The same methods when applied to high density ratio multiphase flows might be faced with challenges distinct to a different flow regime, so we exercise caution while extrapolating the possible outcomes of doing so, and refrain from making overly generalized statements.

REGARDING VOF

The VOF method can be considered quite robust in that it can handle a wide range of free surface flows, without constraints on the density and viscosity ratio between the fluids or the flow Reynolds number, though extreme values will pose difficulties. As surface tension is independent of density ratio in VOF, very low density ratios like $\rho^\star \sim 1.1$ (and lower) can also be simulated as the phase fraction formulation of two fluids ensures strong immiscibility.

The computational cost in VOF increases rapidly upon using successively finer grids, particularly due to the iterative pressure and velocity solution procedure of the finite volume method, with an added transport equation for the phase indicator. Modifications like dynamic mesh refinement hence become indispensable when simulating fully three dimensional flows, but such techniques may also influence the results adversely - for instance the consistent under-prediction of terminal velocity reported in this chapter, and the additional numerical errors in interpolation of values between coarse and refined mesh regions.

For high density ratio systems at low Reynolds numbers (like falling rain droplets, or very small air bubbles in water), spurious currents can become comparable to the physical velocity scale when using the CSF implementation for the surface tension force, and classical VOF might fail to predict accurate results. Modifications like smoothing of the phase indicator field before computation of curvature, the use of body fitted coordinates or an improved surface tension force implementation will become necessary while simulating these flow regimes.

Another limitation of VOF is the time stepping method, as fully implicit schemes might not be available for transient flow solvers, as is the case with the VOF implementations in FLUENT and OpenFOAM. A crucial aspect to simulation accuracy is the residual control algorithm. In OpenFOAM, the PISO algorithm iteratively solves for velocity and pressure (*inner* correction loops), while the VOF field α is solved once per time step (at the beginning of the PISO loop). Contrarily, upon using PIMPLE (with *outer* and *inner* correction loops), the α field is corrected with ever outer loop as well. With a small enough time step and sufficient number of PISO loops, the results from PISO and PIMPLE can be similar. However, we found that some falling droplet (or rising bubble) simulations might not converge at all when using the PIMPLE algorithm, whereby PISO is the only option, and it is generally more stable and faster than the PIMPLE algorithm.

The values of the final and relative tolerances of the residuals and under relaxation factors should be carefully tested and chosen, and these can vary with the problem being simulated. In commercial software like FLUENT, the user only prescribes a final convergence criteria, which makes it easier to run simulations at the loss of full control over the solution algorithm.

REGARDING SINGLE COMPONENT PP-LB

LB is remarkably faster than finite volume based solvers (roughly 10 times when running both on a single processor for an identical problem) mainly because an iterative Poisson solver is not required, which is time consuming. Further, all computations are highly localized in classic PP-LB (i.e. when considering only nearest neighbour interactions), the advantage of this becomes immediately apparent upon parallelization of the code. The Palabos simulations on 4 million grid cells, for around 1 million iterations, were run on 24 processors and took approximately 24 hours of wall-clock time, while the finest resolution VOF simulations on 1.5 million grid cells run on 16 processors took around 10 days.

Density ratio in single component PP-LB is dependent on T_r, and simulating flows with $T_r \approx 1$ such that $\rho^\star \approx 1$ is not possible as the interface width tends to infinity when $T_r = 1$, which sets a minimum achievable density ratio. For this reason, using single-component multiphase PP-LB to simulate two immiscible liquids might not always be suitable. In this formulation, the two liquids are essentially different thermodynamic phases of the same fluid, co-existing at a prescribed sub-critical temperature (i.e. $T_r < 1$). When the density ratio is low (as in this study), the two phases are separated by a relatively thick interface and they remain miscible particularly under dynamic conditions. Owing to this, phase volumes may change over time - an artifact being small regions of the low density phase dissolving away when the droplet diameter and interface width become comparable. Note that the total mass of the fluid is conserved, only its distribution between the two phases changes. Using a multi-component formulation can help ensure stronger immiscibility between two fluid components by employing a repulsive interaction, which can also help tune surface tension more accurately.

The current LB implementation has several other limitations, for instance a minimum bound on the value of the relaxation time, where values below $\tau = 0.55$ lead to unphysical droplet expansion and wobbling, which gave inaccurate results. The value of τ also depends on the droplet size and the density ratio [26]. Increasing surface tension in the system can enable simulations at higher values of τ, however that increases the required g_{LB} and terminal velocity which should be kept in mind while modeling such a system. The value of g_{LB} is closely tied to the droplet diameter, and it increases for smaller droplets. With a stability analysis we find that simulations with $g_{\mathrm{LB}} > \mathcal{O}(10^{-5})$ become unstable, which further limits the smallest droplet size achievable - the computational domain consequently becomes large. The LB method is sensitive to the value of Re and Eo, and at relatively higher values unphysical droplet expansion or contraction is observed. With these considerations, our LB implementation was limited to low Re and low Eo cases, and several modifications like the incorporation of longer range interaction forces [64] and choosing advanced collision operators such as multiple relaxation time (MRT) [69, 70] might be necessary, along with extensive testing of parameters, to make single-component PP-LB applicable to more complex flow problems, like those

involving high density and viscosity ratios between the liquids, or high Re problems.

A general concern in LB is the maximum value of the velocity in lattice units, which should be sufficiently smaller than the lattice speed of sound (i.e. the low Mach number limit of $Ma < 0.2$). The speed of sound for the LB-EOS is $c_s = 1/\sqrt{3}$, or more generally for an arbitrary EOS $c_s^2 = \partial p/\partial \rho$. This ensures that the incompressible Navier-Stokes equations are obeyed. The error due to a non-zero Ma has been shown to be $\mathcal{O}(Ma^3)$ [71]. Lastly, it has been shown that the discrete kinetic version of the BGK equation, and notably LBM, provide semi-quantitative results [72]. Therefore, a percentage of error can be expected in classical LB modeling, the bounds of which depend upon the flow regime being simulated.

2.6. CONCLUSIONS

Multiphase flow simulations have become common tools being applied to a wide range of processes dealing with immiscible fluids. Notwithstanding, comparisons between different simulation techniques are rare and often qualitative. We have presented a quantitative comparison between an implementation of the single-component multiphase pseudopotential lattice Boltzmann method (PP-LB), which is a widely used mesoscopic technique, and the finite volume based Volume of Fluid (VOF) method. By simulating stationary and falling droplets, we compare how the methods fare for different aspects relevant to multiphase flows with a low density ratio - a regime crucial to emulsion research. The main findings are listed below.

1. A modified implementation of the LB method with the so-called $\beta-$scheme produces spurious currents $1-3$ orders of magnitude lower than all VOF implementations. This can be relevant when simulating problems involving evaporation or heat and mass transfer across interfaces, or high density ratio flows at low Re. Among the VOF methods, interface compression aggravates spurious currents while artificially smoothing the interface during curvature calculation reduces them. In VOF, spurious currents also increase with mesh refinement, and if the physical velocity and spurious velocity become comparable (for instance in our $Re = 4$ case), mesh converged results cannot be obtained.

2. In terms of computational time, LB simulations are faster than their VOF counterparts by an order of magnitude (when running comparable problems, i.e. same Re, Eo, $Nx \times Ny$ etc). The iterative Poisson solver inherent to finite volume methods makes VOF slower in comparison. LB, on the other hand, has more demanding memory requirements as it needs to store more variables per lattice node as compared to VOF (since the density f_i in LB is directional with 9 components for a D2Q9 lattice, 27 for D3Q27 etc, at every lattice node).

3. In comparing interface thickness, the FLUENT VOF with geometrical reconstruction produces the sharpest interface of $2-3$ grid cells, closely followed by OpenFOAM with interface compression ($c_\alpha = 1$). The interface width in LB remains diffuse over $5-10$ lattice units depending on the density ratio (qualitatively varying inversely).

4. The falling droplet simulations show that despite an identical case setup, the 2D results from FLUENT and OpenFOAM tend to vary slightly. For the $Re = 24$ case,

FLUENT produces a more flattened droplet with higher deformation than OpenFOAM. The differences in solutions between OpenFOAM and FLUENT derive from the different treatment of the interface (compressive scheme against an explicit geometrical reconstruction), the difference in the solution algorithm (PISO against SIMPLE) and the exact accuracy control methods. What is striking is that upon simulating a widely studied, *purely numerical* rising bubble benchmark proposed by Hysing *et al.* [73], OpenFOAM and FLUENT VOF results are found to agree well within 2% (refer to 2.A). These results were also less sensitive to the choice of discretization schemes. Hence, agreement with a numerical benchmark alone cannot be considered sufficient proof for the reliability of a solver when applied to physical problems, which calls for additional realistic benchmark studies.

5. The 3D VOF simulations using dynamic mesh refinement in OpenFOAM predict a lower terminal Re number, particularly for the $Re < 10$ cases. This is because a spherical droplet at a low flow rate experiences more drag in comparison to the 2D droplets which can be effectively considered as infinite cylinders which have a lower drag coefficient. The results are also aggravated by the coarse mesh resolution in 3D (7.5 base cells per diameter), to keep the computation cost modest. The velocity field is hence under-resolved, which also prevents the droplets from deforming for the higher Re cases as much as the 2D counterparts. More generally, results from simulations with dynamic mesh refinement have a degree of inaccuracy compared to a uniform orthogonal 3D mesh with the same resolution as the finest grid refined cell. This is due to two reasons - first the interpolation errors due to lack of orthogonality in the transition between coarse and refined mesh regions. Secondly, spurious currents are aggravated in the fine mesh region surrounding the droplet interface. These can be interpreted as capillary waves that increase the drag on the droplet by causing deviations from a smooth interface profile.

6. In LB, the droplet expands during the transient initialization phase when the densities relax to equilibrium. Several factors contribute to this, including the domain size (which corresponds to the amount of mass in the domain, refer to Fig. 2.17 in the Appendix), the strength of the pseudopotential force (given by β), and the system parameters themselves (T_r and $\rho^\star$). This is because at lower density ratios (T_r close to 1) the droplet interface is quite diffused as the phase separation is weak. This can be remedied to an extent by increasing the strength of the pseudopotential force (refer to 2.B, Fig. 2.19), also the domain size should be large enough to account for these effects. With these measures, LB is in very good agreement with VOF and the Clift map values in predicting Re. However, LB consistently underpredicts the droplet deformation, even at higher Eo values. This indicates that our current PP-LB implementation is limited to flows of low Eo and Re numbers, and several modifications to the technique are required to make it more generic and robust as compared to VOF. Lastly, while simulating dynamic multiphase problems at low density ratios using *single component* PP-LB, several precautions should be taken depending on the flow regime, as the two thermodynamic phases remain miscible.

We observe that formulating a multiphase flow problem that can be commonly studied by PP-LB and VOF is a non trivial task due to several fundamentally different aspects

of the two methods. The translation of parameters from one method to the other to keep the simulations comparable can be meticulous. Also, issues particular to each method can narrow down the operable phase space of the chosen problem considerably as we have elaborated in our Discussion section. Despite precautions and careful case formulation, we see that different numerical techniques produce different results - since the exact numerics between methods is not identical. This urges us to strongly state that such comparisons are important particularly for the formulation of newer-generation benchmark studies that detail the strengths and limitations of the increasing number of novel simulation techniques being proposed in literature.

ACKNOWLEDGMENTS

The research leading to these results has been done in cooperation with the Dutch Institute for Sustainable Process Technology (ISPT) as part of the LBM project, the Netherlands Organisation for Scientific Research (NWO) and Shell, the Netherlands. The authors would like to thank Dr. Orest Shardt (University of Limerick, Ireland) for the useful discussions and insight regarding the work.

APPENDIX

2.A. COMPARISON BETWEEN OPENFOAM AND FLUENT

We saw from our falling droplet comparison that VOF results from OpenFOAM and FLUENT are not identical. The final velocity from both methods for Case 1 ($Re = 4$) and Case 5 ($Re = 24$) are within 15%. For Case 5, the velocity evolution profiles have slightly different features (for instance an overshoot for FL2D around $t^\star = 5$, refer Fig. 2.12), and the final shape in FLUENT is more deformed than in OpenFOAM. The major difference between the two solvers is the treatment of the interface, where explicit geometrical reconstruction and an implicit compressive scheme are conceptually and numerically very different . It should be noted that the solution algorithms SIMPLE and PISO are not equivalent as well, and may also lead to differences in the solution. To investigate this further, we simulated a well established numerical benchmark for rising bubbles [73] where various multiphase techniques are tested for predicting bubble shape and velocity for two *purely numerical* 2D test cases. These are namely TC1 and TC2, formulated using parameters listed in Table 2.4. We performed the simulations for the finest mesh adopted in the study, i.e. 160 cells per bubble diameter and only show the velocity evolution here (along with the final bubble shape for reference). For comparison, we take the Hysing *et al.* [73] results as benchmark solutions, along with the results obtained by Klostermann *et al.* [61] who performed the same benchmark study using OpenFOAM to test the compressive VOF scheme.

The numerical schemes used in OpenFOAM are *backward* time integration, *vanLeer* discretization for velocity and α advection, and *linear* interpolation of gradient terms. Other parameters are kept the same as in Klostermann *et al.* [61]. The FLUENT simulations were performed with the geometrical reconstruction technique, and the schemes are the same as in Section 2.1.3.

Fig. 2.14 shows the velocity evolution of the bubble over time for TC1, where the FLUENT and OpenFOAM results are very close to each other (also, we are able to reproduce the points of Klostermann *et al.* [61] identically). Fig. 2.15 shows the velocity evolution

	ρ_1	ρ_2	μ_1	μ_2	g	σ	Re	Eo
TC1	1000	100	10	1	0.98	24.5	35	10
TC2	1000	1	10	0.1	0.98	1.96	35	125

Table 2.4: Physical properties of the two test cases formualted by Hysing *et al.* [73], for other details we refer the reader to the paper.

for TC2 and again OpenFOAM and FLUENT results are seen to be very close together until $t = 2$ [s], whereafter they differ slightly (by $\approx 1.5\%$).

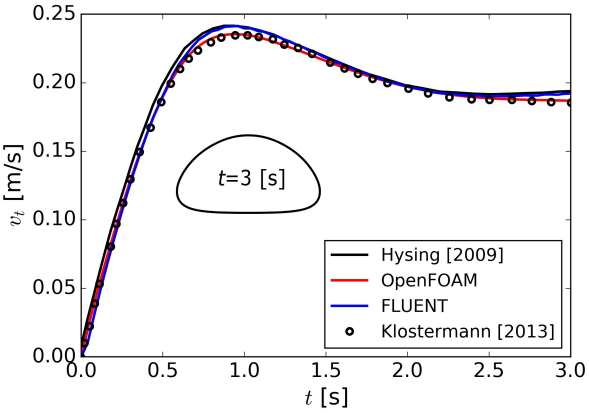

Figure 2.14: Velocity evolution for the bubble for TC1 of Hysing *et al.* [73]. The OpenFOAM and FLUENT VOF solutions are seen to be very close, and our OpenFOAM points coincide precisely with Klostermann *et al.* [61].

It appears that the VOF techniques in OpenFOAM and FLUENT agree quite well when reproducing this numerical benchmark. However, as shown in this chapter, when applied to a more generic physical problem (like the falling droplets), the transient as well as long time behaviour can be different. Though widely used to test multiphase techniques, the Hysing *et al.* [73] benchmark employs a very small domain of $2d \times 4d$, whereby the walls are very close to the edge of the bubble. This might have an influence on the bubble rising characteristics, as generally the horizontal domain width for rising bubbles is taken to be $8d - 12d$ depending on the Re, whereas the height can be anywhere between $12d - 30d$ depending on approach to steady state. This goes on to show the need for more realistic numerical benchmarks to be able to comment on the reliability of different simulation techniques - something we have attempted to do in a small way.

2.B. INFLUENCE OF β ON DROPLET SHAPE IN LB

Fig. 2.16 shows a comparison between the analytical coexistence curves for the C-S EOS and numerical results obtained with the proposed method with $\beta = 1.25$ & 1.65. It is clear that the numerical results agree well with the theoretical data over a wide range of

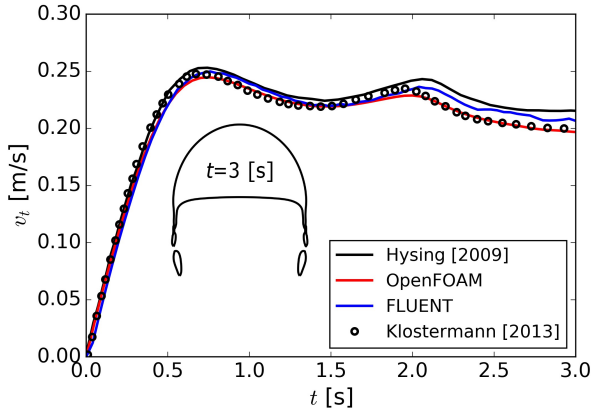

Figure 2.15: Velocity evolution for the bubble for TC2 of Hysing *et al.* [73]. The OpenFOAM and FLUENT VOF solutions are seen to be very close until $t = 2$ [s], after which they differ by roughly 1.5%, and again our OpenFOAM data points coincide precisely with Klostermann *et al.* [61].

reduced temperatures (or density ratios).

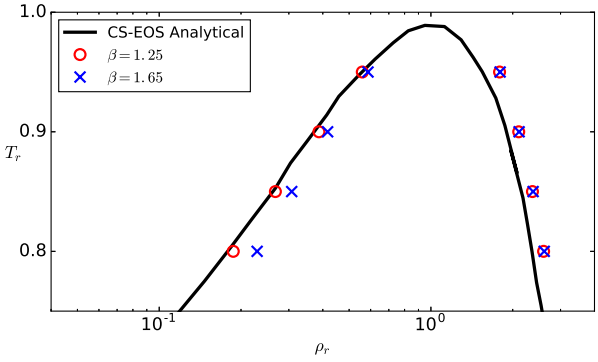

Figure 2.16: Liquid and vapor reduced density variation with reduced temperature for C-S EOS. The analytical solution is obtained from the Maxwell-rule of equal areas.

However, as discussed in the text, the LB droplets at low density ratio can undergo unphysical expansion after initialization during a small transient period when the densities relax to equilibrium. In dynamic conditions, there can be further expansion or contraction, the reason for this behaviour is that the interaction force between the phases is weak and does not constrain the initial droplet volume as it begins to falls. Further, we found the amount of expansion also depends on the total mass in the system, which depends on the domain size. This has been shown in Fig. 2.17, where a droplet is initialized with a diameter of 100 lattice units with increasing domain sizes ($N_x = N_y$), for the $\rho^\star \approx 3$ system considered in this study. The system is let to relax (up to 20000 iterations),

after which an equivalent diameter is calculated as d^{eq}, which is seen to increase with N_x significantly. The expansion can be controlled to an extent by increasing the value of β such that the pseudopotential force is stronger.

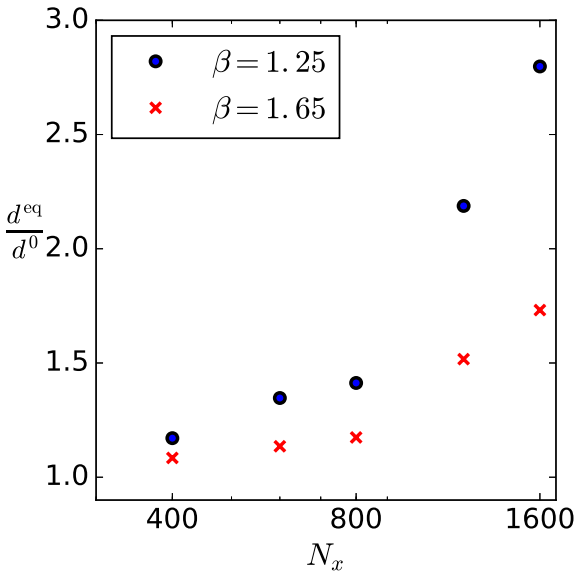

Figure 2.17: Dependence of the droplet expansion on the domain size, shown as the ratio between an equivalent droplet diameter d^{eq} calculated after a stationary droplet is let to relax for 20000 iterations, beginning from an initial diameter d^0 = 100 lattice units, for increasing domain size in lattice units where $N_X = N_y$.

A comparison of the force magnitude is shown in Fig. 2.18, which shows the interaction force along the centerline of a stationary droplet for simulations with β = 1.25 & 1.65. It can be seen that for β = 1.65, the interaction force increases slightly near the interface. Even this slight increase in interaction force influences droplet expansion significantly. It is also seen in from Fig. 2.18 that the size of the stationary droplet is smaller for β = 1.65 as compared to the case with β = 1.25.

Lastly, the final droplet shapes obtained using β = 1.25 & 1.65 for Cases 1 and 5 are presented below in Fig. 2.19. Here the shapes for both values of β are very similar, but when a similar comparison was performed on a smaller domain for these two cases, the β = 1.25 cases showed unphysical expansion and deformation. Further work is required to understand the exact behaviour depending on β and the domain size effect.

REFERENCES

[1] S. Mukherjee, A. Zarghami, C. Haringa, K. van As, S. Kenjereš, and H. E. Van den Akker, *Simulating liquid droplets: A quantitative assessment of lattice boltzmann and volume of fluid methods,* International Journal of Heat and Fluid Flow **70**, 59 (2018).

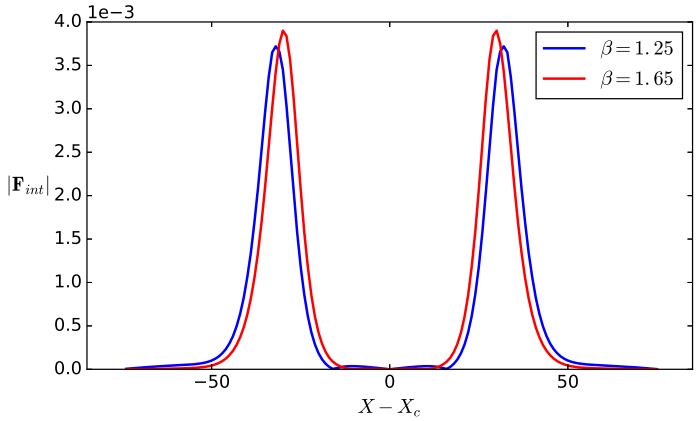

Figure 2.18: Force distribution over a diametric axis across a droplet centered at X_c for $\beta = 1.25$ and $\beta = 1.65$.

[2] A. Prosperetti and G. Tryggvason, *Computational methods for multiphase flow* (Cambridge university press, 2009).

[3] G. Tryggvason, R. Scardovelli, and S. Zaleski, *Direct numerical simulations of gas–liquid multiphase flows* (Cambridge University Press, 2011).

[4] M. Loewenberg and E. Hinch, *Numerical simulation of a concentrated emulsion in shear flow,* Journal of Fluid Mechanics **321**, 395 (1996).

[5] V. Cristini and Y.-C. Tan, *Theory and numerical simulation of droplet dynamics in complex flows—a review,* Lab on a Chip **4**, 257 (2004).

[6] S. F. Roudsari, G. Turcotte, R. Dhib, and F. Ein-Mozaffari, *Cfd modeling of the mixing of water in oil emulsions,* Computers & Chemical Engineering **45**, 124 (2012).

[7] S. Kokal *et al.*, *Crude oil emulsions: A state-of-the-art review,* in *SPE Annual Technical Conference and Exhibition* (Society of Petroleum Engineers, 2002).

[8] L. W. Lake, *Enhanced oil recovery,* (1989).

[9] R. Arshady, *Suspension, emulsion, and dispersion polymerization: A methodological survey,* Colloid & Polymer Science **270**, 717 (1992).

[10] N. Takada, M. Misawa, A. Tomiyama, and S. Fujiwara, *Numerical simulation of two- and three-dimensional two-phase fluid motion by lattice boltzmann method,* Computer Physics Communications **129**, 233 (2000).

[11] K. Sankaranarayanan, I. Kevrekidis, S. Sundaresan, J. Lu, and G. Tryggvason, *A comparative study of lattice boltzmann and front-tracking finite-difference methods for bubble simulations,* International Journal of Multiphase Flow **29**, 109 (2003).

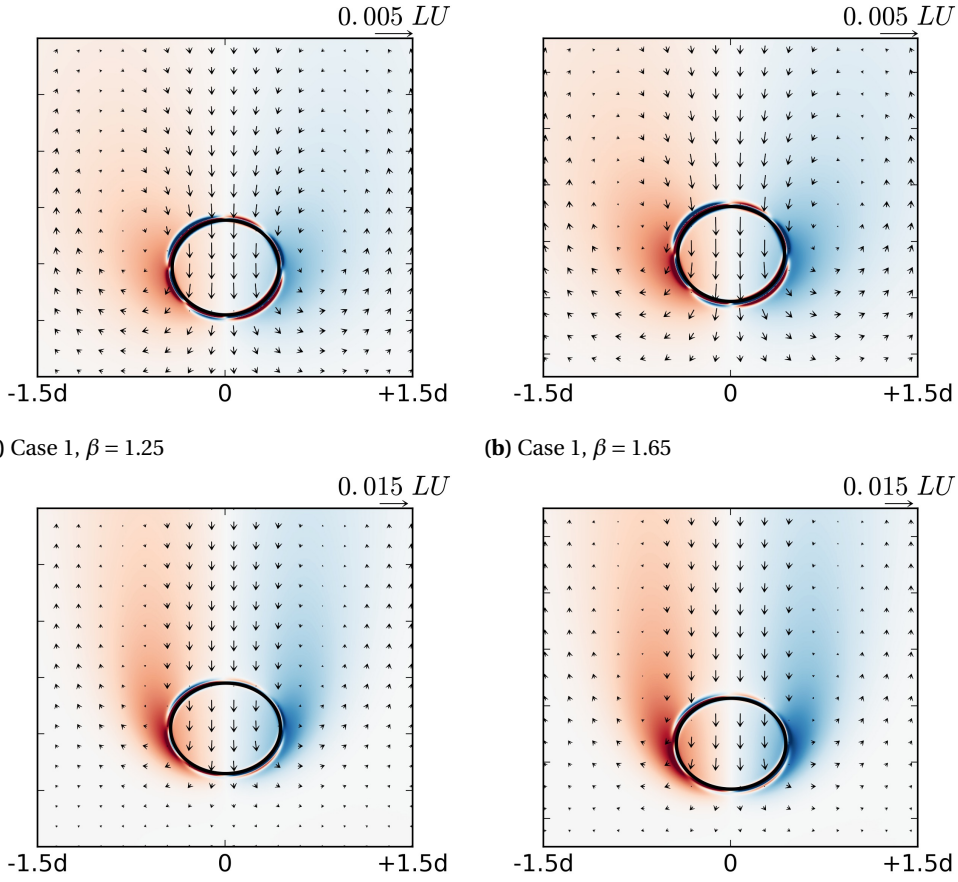

(a) Case 1, $\beta = 1.25$

(b) Case 1, $\beta = 1.65$

(c) Case 5, $\beta = 1.25$

(d) Case 5, $\beta = 1.65$

Figure 2.19: Comparison of final droplet shapes for Case 1 and Case 5 from LB2D simulations for $\beta = 1.25$ (lower surface tension and relatively higher inter-phase miscibility) and $\beta = 1.65$ (higher surface tension and low inter-phase miscibility).

[12] L. Scarbolo, D. Molin, P. Perlekar, M. Sbragaglia, A. Soldati, and F. Toschi, *Unified framework for a side-by-side comparison of different multicomponent algorithms: Lattice boltzmann vs. phase field model,* Journal of Computational Physics **234**, 263 (2013).

[13] C. W. Hirt and B. D. Nichols, *Volume of fluid (vof) method for the dynamics of free boundaries,* Journal of computational physics **39**, 201 (1981).

[14] V. R. Gopala and B. G. van Wachem, *Volume of fluid methods for immiscible-fluid and free-surface flows,* Chemical Engineering Journal **141**, 204 (2008).

[15] L. Chen, Q. Kang, Y. Mu, Y.-L. He, and W.-Q. Tao, *A critical review of the pseu-*

dopotential multiphase lattice boltzmann model: Methods and applications, International Journal of Heat and Mass Transfer **76**, 210 (2014).

[16] X. Shan and H. Chen, *Lattice boltzmann model for simulating flows with multiple phases and components,* Physical Review E **47**, 1815 (1993).

[17] X. Shan and H. Chen, *Simulation of nonideal gases and liquid-gas phase transitions by the lattice boltzmann equation,* Physical Review E **49**, 2941 (1994).

[18] S. Chen, S. Dawson, G. Doolen, D. Janecky, and A. Lawniczak, *Lattice methods and their applications to reacting systems,* Computers & chemical engineering **19**, 617 (1995).

[19] S. Chen and G. D. Doolen, *Lattice boltzmann method for fluid flows,* Annual review of fluid mechanics **30**, 329 (1998).

[20] M. R. Swift, W. Osborn, and J. Yeomans, *Lattice boltzmann simulation of nonideal fluids,* Physical Review Letters **75**, 830 (1995).

[21] P. Yuan and L. Schaefer, *Equations of state in a lattice boltzmann model,* Physics of Fluids **18**, 042101 (2006).

[22] S. Mukherjee, A. Zarghami, C. Haringa, S. Kenjereš, and H. E. Van den Akker, *A comparative assessment of lattice boltzmann and volume of fluid (vof) approaches for generic multiphase problems,* in *Proceedings of ICMF 2016 - 9th International Conference on Multiphase Flow* (2016).

[23] R. Clift, J. R. Grace, and M. E. Weber, *Bubbles, drops, and particles* (Courier Corporation, 2005).

[24] S. Succi, *The lattice Boltzmann equation: for fluid dynamics and beyond* (Oxford university press, 2001).

[25] S. Gong and P. Cheng, *Numerical investigation of droplet motion and coalescence by an improved lattice boltzmann model for phase transitions and multiphase flows,* Computers & Fluids **53**, 93 (2012).

[26] A. Zarghami, N. Looije, and H. Van den Akker, *Assessment of interaction potential in simulating nonisothermal multiphase systems by means of lattice boltzmann modeling,* Physical Review E **92**, 023307 (2015).

[27] A. Zarghami and H. E. Van den Akker, *Thermohydrodynamics of an evaporating droplet studied using a multiphase lattice boltzmann method,* Physical Review E **95**, 043310 (2017).

[28] A. Kupershtokh, D. Medvedev, and D. Karpov, *On equations of state in a lattice boltzmann method,* Computers & Mathematics with Applications **58**, 965 (2009).

[29] L. Amaya-Bower and T. Lee, *Single bubble rising dynamics for moderate reynolds number using lattice boltzmann method,* Computers & Fluids **39**, 1191 (2010).

[30] K. Sankaranarayanan, X. Shan, I. Kevrekidis, and S. Sundaresan, *Bubble flow simulations with the lattice boltzmann method,* Chemical Engineering Science **54**, 4817 (1999).

[31] K. Sankaranarayanan, X. Shan, I. Kevrekidis, and S. Sundaresan, *Analysis of drag and virtual mass forces in bubbly suspensions using an implicit formulation of the lattice boltzmann method,* Journal of Fluid Mechanics **452**, 61 (2002).

[32] H. Huang, M. Krafczyk, and X. Lu, *Forcing term in single-phase and shan-chen-type multiphase lattice boltzmann models,* Physical Review E **84**, 046710 (2011).

[33] H. Jasak, A. Jemcov, Z. Tukovic, *et al.*, *Openfoam: A c++ library for complex physics simulations,* in *International workshop on coupled methods in numerical dynamics*, Vol. 1000 (IUC Dubrovnik, Croatia, 2007) pp. 1–20.

[34] H. Jasak, *Openfoam: open source cfd in research and industry,* International Journal of Naval Architecture and Ocean Engineering **1**, 89 (2009).

[35] S. S. Deshpande, L. Anumolu, and M. F. Trujillo, *Evaluating the performance of the two-phase flow solver interfoam,* Computational science & discovery **5**, 014016 (2012).

[36] H. Marschall, K. Hinterberger, C. Schueler, F. Habla, and O. Hinrichsen, *Numerical simulation of species transfer across fluid interfaces in free-surface flows using openfoam,* Chemical engineering science **78**, 111 (2012).

[37] A. Q. Raeini, M. J. Blunt, and B. Bijeljic, *Modelling two-phase flow in porous media at the pore scale using the volume-of-fluid method,* Journal of Computational Physics **231**, 5653 (2012).

[38] D. A. Hoang, V. van Steijn, L. M. Portela, M. T. Kreutzer, and C. R. Kleijn, *Benchmark numerical simulations of segmented two-phase flows in microchannels using the volume of fluid method,* Computers & Fluids **86**, 28 (2013).

[39] C. Bilger, M. Aboukhedr, K. Vogiatzaki, and R. Cant, *Evaluation of two-phase flow solvers using level set and volume of fluid methods,* Journal of Computational Physics (2017).

[40] E. Berberovic, *Investigation of free-surface flow associated with drop impact: numerical simulations and theoretical modeling*, Ph.D. thesis, TU Darmstadt/FG Strömungslehre und Aerodynamik (2010).

[41] H. Rusche, *Computational fluid dynamics of dispersed two-phase flows at high phase fractions*, Ph.D. thesis, Imperial College London (University of London) (2003).

[42] H. Weller, *A new approach to vof-based interface capturing methods for incompressible and compressible flow,* OpenCFD Ltd., Report TR/HGW/04 (2008).

[43] P. Bohórquez, *Study and numerical simulation of sediment transport in free-surface flow*, Tech. Rep. (University of Malaga, Spain, 2008).

[44] J. Brackbill, D. B. Kothe, and C. Zemach, *A continuum method for modeling surface tension,* Journal of computational physics **100**, 335 (1992).

[45] B. Lafaurie, C. Nardone, R. Scardovelli, S. Zaleski, and G. Zanetti, *Modelling merging and fragmentation in multiphase flows with surfer,* Journal of Computational Physics **113**, 134 (1994).

[46] M. J. Berger and J. Oliger, *Adaptive mesh refinement for hyperbolic partial differential equations,* Journal of computational Physics **53**, 484 (1984).

[47] R. I. Issa, *Solution of the implicitly discretised fluid flow equations by operator-splitting,* Journal of computational physics **62**, 40 (1986).

[48] S. Patankar, *Numerical heat transfer and fluid flow* (CRC press, 1980).

[49] D. L. Youngs, *Time-dependent multi-material flow with large fluid distortion,* Numerical methods for fluid dynamics **24**, 273 (1982).

[50] O. Ubbink, *Numerical prediction of two fluid systems with sharp interfaces*, Ph.D. thesis, University of London PhD Thesis (1997).

[51] M. K. Tripathi, K. C. Sahu, and R. Govindarajan, *Why a falling drop does not in general behave like a rising bubble,* Scientific reports **4** (2014).

[52] M. K. Tripathi, K. C. Sahu, and R. Govindarajan, *Dynamics of an initially spherical bubble rising in quiescent liquid,* Nature communications **6** (2015).

[53] J. Hadamard, *Mouvement permanent lent d'une sphere liquide et visqueuse dans un liquide visqueux,* CR Acad. Sci **152**, 1735 (1911).

[54] W. Rybczynski, *On the translatory motion of a fluid sphere in a viscous medium,* Bull. Acad. Sci., Cracow, Series A **40** (1911).

[55] H. D. Mendelson, *The prediction of bubble terminal velocities from wave theory,* AIChE Journal **13**, 250 (1967).

[56] Z. Zapryanov and S. Tabakova, *Dynamics of bubbles, drops and rigid particles*, Vol. 50 (Springer Science & Business Media, 2013).

[57] J. Han and G. Tryggvason, *Secondary breakup of axisymmetric liquid drops. i. acceleration by a constant body force,* Physics of Fluids (1994-present) **11**, 3650 (1999).

[58] W. J. Dahm, C. M. Scheil, and G. Tryggvason, *Dynamics of vortex interaction with a density interface,* Journal of Fluid Mechanics **205**, 1 (1989).

[59] D. J. Harvie, M. Davidson, and M. Rudman, *An analysis of parasitic current generation in volume of fluid simulations,* Applied mathematical modelling **30**, 1056 (2006).

[60] X. Shan, *Analysis and reduction of the spurious current in a class of multiphase lattice boltzmann models,* Physical Review E **73**, 047701 (2006).

[61] J. Klostermann, K. Schaake, and R. Schwarze, *Numerical simulation of a single rising bubble by vof with surface compression,* International Journal for Numerical Methods in Fluids **71**, 960 (2013).

[62] K. Connington and T. Lee, *A review of spurious currents in the lattice boltzmann method for multiphase flows,* Journal of mechanical science and technology **26**, 3857 (2012).

[63] Y. Renardy and M. Renardy, *Prost: a parabolic reconstruction of surface tension for the volume-of-fluid method,* Journal of Computational Physics **183**, 400 (2002).

[64] M. Sbragaglia, R. Benzi, L. Biferale, S. Succi, K. Sugiyama, and F. Toschi, *Generalized lattice boltzmann method with multirange pseudopotential,* Physical Review E **75**, 026702 (2007).

[65] Q. Li and K. Luo, *Thermodynamic consistency of the pseudopotential lattice boltzmann model for simulating liquid–vapor flows,* Applied Thermal Engineering **72**, 56 (2014).

[66] J. Hua and J. Lou, *Numerical simulation of bubble rising in viscous liquid,* Journal of Computational Physics **222**, 769 (2007).

[67] L. Janssen and M. Warmoeskerken, *Transport phenomena data companion* (VSSD Delft, The Netherlands, 2006).

[68] M. Magnini, B. Pulvirenti, and J. Thome, *Characterization of the velocity fields generated by flow initialization in the cfd simulation of multiphase flows,* Applied Mathematical Modelling **40**, 6811 (2016).

[69] D. d'Humières, *Multiple–relaxation–time lattice boltzmann models in three dimensions,* Philosophical Transactions of the Royal Society of London A: Mathematical, Physical and Engineering Sciences **360**, 437 (2002).

[70] M. E. McCracken and J. Abraham, *Multiple-relaxation-time lattice-boltzmann model for multiphase flow,* Physical Review E **71**, 036701 (2005).

[71] D. O. Martinez, W. H. Matthaeus, S. Chen, and D. Montgomery, *Comparison of spectral method and lattice boltzmann simulations of two-dimensional hydrodynamics,* Physics of Fluids **6**, 1285 (1994).

[72] M. Sbragaglia and S. Succi, *A note on the lattice boltzmann method beyond the chapman-enskog limits,* EPL (Europhysics Letters) **73**, 370 (2005).

[73] S.-R. Hysing, S. Turek, D. Kuzmin, N. Parolini, E. Burman, S. Ganesan, and L. Tobiska, *Quantitative benchmark computations of two-dimensional bubble dynamics,* International Journal for Numerical Methods in Fluids **60**, 1259 (2009).

3

MODELING SURFACTANT LADEN EMULSIONS WITH PP-LB

Simulations of surfactant-laden emulsions remain an exception owing to their complexity. We present, using the pseudopotential lattice Boltzmann method, a technique to simulate liquid-liquid systems with a slightly soluble surfactant. All components are modeled as non-ideal fluids, and the surfactant is repelled by the two liquid components which makes it concentrate around interfaces. We ignore orientation effects of the surfactant molecules, long range interactions and electric fields. Investigating the extensive parameter space spanning the various interaction strengths, system temperatures and component densities, we show equilibrium surface tension reduction for a stationary droplet up to 15% *following Langmuir-isotherm like behaviour emerging from simplified pseudopotential interactions. The model is insufficient to simulate coalescence inhibition which requires an additional mechanism. One proposed method is varying the liquid-liquid interaction strength locally as a function of the surfactant density, which causes arrested phase segregation along with spontaneous droplet breakup similar to the formation of microemulsions. Finally, the model is applied to pendent droplet formation, comparing clean and surfactant-laden systems. The addition of the surfactant greatly alters the probability distribution of droplet radii after formation, and a larger number of smaller droplets are found - an effect of the reduced surface tension due to surfactants. One of the major drawbacks of the model is the non-trivial dependence of the output system state on each input parameter - most of which cannot be varied independently and better control of the system requires additional testing*[1] .

This chapter has been published in the *AIChE Journal*, 2019 [1], as a joint first author with Ir. P. Berghout.

[1] This is being currently performed at the Bernal group in University of Limerick by Dr. A. Safdari and Dr. M. Pourtousi, where they further elaborate the model behaviour along with testing it for surfactant laden droplet breakup in simple shear flow.

3.1. INTRODUCTION

During the last two decades or so, computer aided process engineering tools have started playing an important role in designing, debottlenecking and optimising both individual process devices and complete process plants. Part of this development is due to the evolution of Computational Fluid Dynamics (CFD) for both single-phase and multi-phase systems including various transport processes and chemical reactions. This, along with computational power rocketing according to Moore,s law [2] has made massively parallel simulations possible, bridging the gap between detailed flow dynamics and designing for large-scale equipment.

Despite the diverse advances in the development of flow simulation techniques, conventional Finite Volume (FV) based solvers, introduced as early as the 1970s (see Patankar and Spalding [3]), still dominate the field to an extent that virtually all commercial CFD software is rooted in FV. Much to its disadvantage, the chemical engineering community seems to keep overlooking the promises of the lattice Boltzmann (LB) method, a strong alternative to FV.

LB is a mesoscopic approach to continuum fluid mechanics, which can be used to simulate flows obeying the Navier-Stokes equations at a fraction of the computational cost of FV, particularly for (massively) parallel flow simulations. Eggels [4] and Derksen and Van den Akker [5, 6] introduced the LB technique into the realm of engineering fluid mechanics. The result was a long series of papers reporting about LB based Large Eddy Simulations (LESs) in various flow devices. Most of these simulations, as well as some Direct Numerical Simulations (DNSs) – see [7, 8] – were simply impossible using the conventional FV technique (on the platforms of the time and under the pertinent conditions).

Multiphase simulation methods can be broadly classified as Euler-Euler or Euler-Lagrangian methods. In the Euler-Euler method, fluids and particles are all treated as continua and are represented by their respective volume fractions at each grid cell of the simulation. These simulations do not resolve phase interfaces. Euler-Lagrangian methods, confined to dilute particle systems, track the individual particles which can be either point particles or finite sized. In the case of RANS-based simulations or LESs, the flow between these particles is not resolved. DNS simulations, such as Ten Cate *et al.* [9] for solid particles in a turbulent liquid flow, and Derksen and Van Den Akker [10] for a turbulent emulsion, do resolve the flow between the particles. LB also emerges as a robust technique for simulating multi-phase flows, at par with FV based solvers [11–13]. While particle laden flows like fluidized beds, suspensions and colloids have their own dedicated LB models exploiting immersed boundary conditions for reproducing the detailed interaction of fluid and moving and revolving particles [9, 14–17], we will focus here on liquid-liquid systems.

3.1.1. EMULSIONS

This chapter aims at simulating the hydrodynamic behaviour of emulsions which are crucial to various industries, ranging from cosmetics, biotechnology, and food processing to the oil and gas industry. Most (FV) simulations of dense droplet systems incorporate Population Balance modeling [18] which relies heavily on empirical relations drawn from experimental data. Though useful, this method suffers from the strong limitations of experimentally studying emulsions, due to their highly three-dimensional

spatio-temporal flow characteristics around evolving interfaces; in addition, emulsions are inherently opaque to optical measurement techniques. Here, the unprecedented details unraveled by flow resolving simulation techniques can be telling.

Due to their dense droplet population, emulsions have a multitude of interfaces separating the two liquids, and the stability of these interfaces is crucial to the stability of the emulsion - i.e., if they rupture leading to droplet coalescence, the two fluids would entirely separate. Emulsion stability is greatly altered by the presence of surfactants, which are surface active molecules preferentially adhering to interfaces. For instance, in enhanced oil recovery, steam is often used to mobilize the oil, which can cause emulsification facilitated by the presence of naturally occurring [19] or artificially added surfactants [20]. Surfactant stabilized emulsions are also used to transport highly viscous crude oils, whereafter these emulsions need to be destabilized to separate the oil and water phases [21].

Surfactant induced phenomena include drag enhancement on droplets, inhibition of coalescence, modification of interfacial boundary conditions, and Marangoni flow due to (flow induced) surface tension gradients. None of these effects are present in the commercial multiphase flow solvers, while various academic attempts have been made to account for these as shall be described below. While it is rare to encounter pure fluids in real life, it is exceedingly difficult to turn numerical fluids impure. Bridging the divide between real fluid mixtures and simulations is the main goal of the research described in this chapter which focuses on LB based detailed simulations of emulsions allowing for deformation, coalescence and break-up of droplets while accounting for surfactants.

Simulating surfactant dynamics along with hydrodynamics is a complex problem, aggravated by the fact that the surfactant adsorption and desorption kinetics occurs at the microscale. Ionic surfactants interact directly with the electric double layer formed at the interface, also called the *Debye layer*, the thickness of which is $\mathcal{O}(10^{-10} - 10^{-7}\ m)$ [22]. Surfactants can also form complex aggregates like micelles and lamellae above a critical concentration. These phenomena at the microscale can influence the dynamics of droplets and bubbles, which can be of the scale $\mathcal{O}(10^{-6}\ m)$ in emulsions, or of larger scales around $\mathcal{O}(10^{-3} - 10^{-1}\ m)$ in bubble columns. These scales, when dealing with a physically relevant flow, are separated by $8-10$ orders of magnitude. This poses an immense difficulty that has to be overcome when simulating such systems. Prior research has sought to resolve this by making reductionist assumptions regarding the nature of a surfactant, limiting its essential features. After all, simulating surfactant molecules explicitly while resolving flow is not feasible, nor necessary if surfactant behaviour is aptly modeled when one is solely interested in the macroscopic hydrodynamics. Below we briefly highlight some work done in this direction.

3.1.2. FV BASED TECHNIQUES

Among the FV based techniques, Stone and Leal [23] and Eggleton *et al.* [24] used a boundary integral method to study the breakup of a single surfactant-laden droplet. Several studies employed the Volume of Fluid (VOF) method with an insoluble surfactant confined to the interface, see e.g. Renardy *et al.* [25], Drumright-Clarke and Renardy [26], James and Lowengrub [27], Martin and Blanchette [28]. Xu *et al.* [29] followed a similar approach with the Level-Set (LS) method, also used recently by De Langavant *et al.* [30] and applied to sheared droplet breakup. Other methods include the front tracking

for interfacial and bulk surfactant transport [31], and the arbitrary-Euler-Lagrangian approach for interface tracking by Dieter-Kissling *et al.* [32] applied to droplet formation in the presence of surfactant mixtures. These techniques are well suited for the particular problems being studied, and can give very accurate predictions.

The domain of single droplet dynamics, however, is far from the typical systems encountered in emulsion research. Further, there is no simple extrapolation from the idealized problems studied here to dynamic multiple droplet flows. The constant interface tracking and reconstruction used in these methods becomes challenging once multiple bubbles and droplets are simulated, more so when they can undergo coalescence and breakup, when these techniques become prohibitively expensive and complicated, if not completely unfeasible. We do not discredit these techniques at all, for they can very accurately simulate single droplets, even at very high density and viscosity ratios. However, when looking at realistic emulsions, the capabilities offered by LB far outweigh the FV state-of-the-art.

3.1.3. LB BASED TECHNIQUES

A few LB techniques have also been introduced, and these seem more aptly suited for simulating emulsions than the FV techniques as shall become evident. In the Pseudo-Potential (PP) LB model, introduced by Shan and Chen [33, 34], adding molecular interactions between particle distributions at the meso-scale can simulate spontaneous phase separation. Many researchers embarked on this concept with the view of describing two-phase systems [35], also in our research group [36–38]. Since the multiple interfaces do not need to be tracked, captured and/or reconstructed, this PP-LB method is computationally very attractive [13].

Contrary to the bottom-up PP method, there is the top-down free-energy method for simulating multiphase flows in LB [39, 40]. Simulations using this approach start with a free-energy functional with the intended thermodynamics, which is then used to derive other physical quantities, making these methods thermodynamically consistent by definition [41]. This method has the advantage that certain properties like surface tension and interface width can be pre-defined. A drawback is that the method has been found to be almost three times more computationally expensive than other comparable LB methods [42].

Focusing on emulsion like systems with two immiscible fluid components, Chen *et al.* [43], Nekovee *et al.* [44] introduced a multi-component PP-LB approach where the surfactant is incorporated as a third additional component, coupled to an idealized point dipole. The dipole moment and surfactant distribution both follow the LB streaming and collision algorithm. The surfactant concentration, however, is of the same order as the other fluids, which is not always the case in physical systems. Using this model, Nekovee *et al.* [44] go on to confirm arrested phase segregation for high resolution 2D simulations upon the addition of an active surfactant. They also observe the formation of lamellae above the critical micellar concentration (CMC), not seen in past simulations, which they ascribe to the inclusion of the dipole orientation in their model. Skartlien *et al.* [45] demonstrated the dynamic surface tension behaviour of this model and show how the parameters can be tuned to resemble a physical surfactant like *Exxsol D80* and *Span 80*.

Furtado and Skartlien [46] derived the free energy form of the Chen *et al.* [43] model

from underlying kinetic theory principles. Including short and long range interactions, they also exhibit an inhibition of coalescence. Note that coalescence inhibition alone can also be simulated without surfactants using alternate techniques (like charge on the droplets [47] or mid-range repulsive interaction forces [48]), but Marangoni flows cannot. Skartlien *et al.* [49] used this model to study surfactant stabilized emulsions in a quasi-turbulent field which is induced by the conversion of surface energy to kinetic energy in phase segregation and Skartlien *et al.* [50] investigated droplet size distribution in weakly turbulent surfactant laden emulsions. Free-energy method based models to simulate surfactant stabilized dispersions have also been proposed. Lamura *et al.* [51] used a Ginzburg-Landau based model to show the spontaneous formation of lamellae in surfactant laden oil-water systems due to surface tension reduction. A similar approach was used by Van der Sman and Van der Graaf [52] to show Ward-Tordai like kinetics of surfactant adsorption. This method was further developed by Tóth and Kvamme [53] to show slowed down phase segregation due to the presence of surfactants, and applied to oil, water and asphaltene systems [54]. A thorough review of models for ionic surfactants has been presented by van der Sman and Meinders [55], which also gives a model taxonomy, distinguishing between Eulerian and Lagrangian approaches, with the various ways of simulating surfactants with different degrees of complexity that have been developed so far.

A lot of the studies using the Chen *et al.* [43], Nekovee *et al.* [44] model have focused on the formation of exotic gyroidal structures, complex aggregates and emergent behaviour in ternary systems [56–60], which makes the model quite unique. However, the model has not been used for a wide range of multiphase flow problems where surfactant laden simulations find application. Its complexity and the wide associated parameter space perhaps obscure its utility, whereby arises the need for simplification.

In this chapter, we propose the simplest method to incorporate soluble surfactants in a two fluid mixture by implementing a doubly repelled third surfactant component. We retain surfactant effects like surface tension reduction, and present an analysis through the corresponding parameter space. Our approach combines several other PP-LB developments, making it easy to simulate a wide range of density ratios $\mathcal{O}(1-10^3)$, different viscosity ratios between the fluids and the surfactant (which has been recently demonstrated to be an important parameter [61]), and a possibility of extension to multiple surfactants and components if required. There are several differences between our model and those suggested previously in literature [46, 53, 55, 58], apart from that we use the pseudopotential method while the latter employ the free-energy method. First, we ignore the dipole orientation of the surfactant (and consequently aggregate-like behaviour). Further, we simulate realistic fluids by modeling the components using non-ideal equations of state. This approach allows for a wider range of density ratios between components, which shall allow for simulations of surfactant laden droplets and bubbles. We also propose modifications to our simplified surfactant model that can help simulate more complex surfactant behaviour like the spontaneous formation of microemulsions which has not been presented before using LB.

3.2. NUMERICAL METHOD

3.2.1. THE LATTICE-BOLTZMANN METHOD

In this study we employ the lattice Boltzmann method (LBM), first proposed in their seminal paper by McNamara and Zanetti [62]. The Boltzmann equation, with a simplified collision term (BGK [63]), is discretized up to second order in time, space and momentum, and consequently solved on a lattice that comprises the discretization of space D and momentum Q in i and j directions respectively, and which is named D_iQ_j. The velocity space is reduced to a finite number of discrete values (i.e. Q_j), and one must have sufficient velocity directions to obey the conservation laws. Yet, for a very wide range of two-dimensional flows, a 9 velocity set is sufficient to recover the macroscopic hydrodynamics, and 19 velocities in three-dimensions [41].

Since the Boltzmann equation solves for the particle distribution function, it falls within the mesoscopic compendium of fluid solvers. Consequently, it is well suited to bridge the gap between the microscopic particle scale and the macroscopic continuum scale of fluid flow by invoking mesoscopic particle interactions. This makes modeling multiphase flow phenomena conceptually simple, as with the Pseudopotential method (described shortly), and phenomena like spontaneous phase segregation, bottom-up surface tension effects and evolving interfaces are automatically captured. The spatio-temporal locality of the computations involved makes the method easily parallelizable over distributed computational units unlike conventional finite volume based solvers where distant units need to communicate for the pressure and velocity coupling of an iterative Navier-Stokes solver. Given these factors, the LB method has gained widespread popularity over the past decades, for both single phase and multiphase flows [35, 41].

The LB equation reads

$$f_i^\sigma(\mathbf{x}+c\mathbf{e}_i\Delta t, t+\Delta t) - f_i^\sigma(\mathbf{x},t) = \frac{1}{\tau^s}(f_i^{\sigma,eq}(\mathbf{x},t) - f_i^\sigma(\mathbf{x},t)) + S_i^\sigma \tag{3.1}$$

where f_i^σ is the particle (or *density*) distribution function for some component σ in the discrete velocity direction i. The lattice speed c is defined as $c = \Delta x/\Delta t = 1$, implying constant kinetic energy for all equal mass particles and τ is the lattice relaxation time towards local equilibrium. S_i^σ is a source term which incorporates body forces. Most simulations in this chapter were carried out on a $D2Q9$ lattice, employing the standard 9 lattice velocities in 2 dimensions, $\mathbf{e}_i$, as defined below

$$\mathbf{e}_i = \begin{cases} (0,0), & i = 0 \\ (\cos\left[\frac{(i-1)\pi}{2}\right], \sin\left[\frac{(i-1)\pi}{2}\right])c, & i = 1,2,3,4 \\ \sqrt{2}(\cos\left[\frac{(i-5)\pi}{2}+\frac{\pi}{4}\right], \sin\left[\frac{(i-5)\pi}{2}+\frac{\pi}{4}\right])c, & i = 5,6,7,8 \end{cases} \tag{3.2}$$

The $D3Q19$ simulations similarly utilize the standard 19 velocity 3D lattice, which can be found described in Krüger *et al.* [41]. The discretized equilibrium distribution function follows from a multiscale expansion in the incompressible (low Mach number) limit of the Maxwellian [64]:

$$f_i^{\sigma,eq} = w_i\rho_\sigma\left\{1 + \frac{\mathbf{e}_i\cdot\mathbf{u}_\sigma}{RT} + \frac{(\mathbf{e}_i\cdot\mathbf{u}_\sigma)^2}{2(RT)^2} - \frac{\mathbf{u}_\sigma^2}{2RT}\right\} \tag{3.3}$$

The weight factors are $w_0 = 4/9$, $w_{1\to4} = 1/9$ and $w_{5\to8} = 1/36$. ρ_σ is the component density and follows from the zeroth moment of the distribution function:

$$\rho_\sigma = \sum_i f_i^\sigma \tag{3.4}$$

$\mathbf{u}_\sigma$ is the bare component velocity [41] and follows from the first moment of the distribution function:

$$\rho_\sigma \mathbf{u} = \sum_i \mathbf{e}_i f_i^\sigma + \frac{F_i \Delta t}{2} \tag{3.5}$$

where F_i is the force term. The lattice viscosity is related to the lattice relaxation time by

$$\nu = c_s^2(\tau - 1/2) \tag{3.6}$$

where the pseudo-sound-speed $c_s = \sqrt{RT}$ has the value $1/\sqrt{3}$ for the $D2Q9$ lattice. Details regarding the derivation of these quantities can be found in Succi [65].

3.2.2. MULTICOMPONENT MULTIPHASE (MCMP) MODELING

Various multiphase and multicomponent models have been proposed within the LB framework [34, 66, 67]. In this chapter, we make use of the Pseudopotential (PP) LB model. This is a bottom-up approach, where multiphase hydrodynamics emerges from particle interactions based on a mean field inter-particle force. Characteristic parameters of multiphase systems like interfacial tension and the density ratio of coexisting phases, naturally emerge from the interaction between the respective fluid components. This obviates the usual requirement of solving additional equations to capture or track the interface as one has to with traditional finite volume methods like the Volume of Fluid, Level-Set etc, and the method can be made thermodynamically consistent [68].

In this chapter we simulate three components, which are labeled as α, the high density liquid, β the low density liquid, and s the surfactant. In general, the total force $\mathbf{F}$ on a component σ is the sum of the intra-component force $\mathbf{F}^{\sigma\sigma}$ (which is based upon an equation-of-state) and a sum of inter-component repulsion forces $\mathbf{F}^{\sigma\overline{\sigma}}$ that can be interpreted as the force on σ due to $\overline{\sigma}$. Together these can be written as

$$\mathbf{F}^\sigma(\mathbf{x}, t) = \mathbf{F}^{\sigma\sigma}(\mathbf{x}, t) + \sum_{\overline{\sigma}\neq\sigma} \mathbf{F}^{\sigma\overline{\sigma}}(\mathbf{x}, t) \tag{3.7}$$

(for instance $\mathbf{F}^\alpha = \mathbf{F}^{\alpha\alpha} + \mathbf{F}^{\alpha\beta} + \mathbf{F}^{\alpha s}$). The inter-component interaction force $\mathbf{F}^{\sigma\overline{\sigma}}$ takes the classical Shan-Chen form [33]

$$\mathbf{F}^{\sigma\overline{\sigma}}(\mathbf{x}, t) = -G_{\sigma\overline{\sigma}}\phi_\sigma(\mathbf{x}, t)c_s^2 \sum_{i=0}^{N} w(|\mathbf{e}_i|^2)\phi_{\overline{\sigma}}(\mathbf{x} + \mathbf{e}_i\Delta t, t)\mathbf{e}_i \tag{3.8}$$

where we sum over the nearest neighbors ($i = 0 \rightarrow 8$). Here ϕ is the pseudopotential function, and we use the component density as ϕ, while other definitions are possible. Further, $c_s^2 = 1/3$ is the lattice speed of sound, and G is the interaction strength. This force is incorporated in the source term in Eq. 3.1. Note that its magnitude should not be disproportionately large, which can lead to numerical instabilities, as its upper bounds are set roughly by the magnitude of the component densities which comprise the left hand side of Eq. 3.1.

	α	β	s
α	$G_{\alpha\alpha}$	$G_{\alpha\beta}$	$G_{\alpha s}$
β	$G_{\beta\alpha}$	$G_{\beta\beta}$	$G_{\beta s}$
s	$G_{s\alpha}$	$G_{s\alpha}$	G_{ss}

Table 3.1: The 6 intra-component and inter-component interaction strengths coupling the three components to each other. The exact choice of the intra-component interaction strengths, $G_{\sigma\sigma}$, is not important as the term cancels out following Eq. 3.10 and 3.11, with the only requirement that it be negative to keep the argument of the square root positive, hence these is fixed to -1.0. The inter-component interaction strengths $G_{\sigma\bar{\sigma}} > 0$.

Table 3.1 gives the different interaction strengths, where a negative value gives attraction between the two components (miscibility), whereas a positive value gives repulsion (immiscibility). The surfactant is repelled by both the fluid components, and consequently is driven towards the interface. This is a highly simplified picture of the interaction of a surfactant with the two fluids. In reality, each surfactant molecule has a finite length, with a hydrophilic head and a hydrophobic tail, and it is this amphiphilic nature that drives it to seek out fluid interfaces. At a mesoscopic level, surfactants are treated as point particles, where it would seem that both fluids repel the surfactant. This approach does allow simulation of surfactants collecting at the interfaces, and reducing surface tension of the droplets as will be demonstrated. Finite size effects like steric repulsion, or formation of and interaction with electric double layers are not taken into account in the model yet. We further ignore the orientation of these molecules, also linked to the finite surfactant molecule sizes, which can lead to charge based repulsion between approaching surfactant laden interfaces. This simplified model can be used to successively incorporate features that can simulate more complex effects that are currently out of scope. We want to emphasize that the different components stream and collide on their own respective lattices. Such, there is no excluded volume effect, and the components only interact by means of the interaction force.

We keep the concentration of the surfactant three orders of magnitude lower than the liquid densities. This is because in real systems, the surfactant volume fraction is very low compared to the liquid components in the entire domain. Only at the interfaces, the surfactant can have high volume fractions, even close to 1 at high surfactant loading. A higher average surfactant density in the domain can also cause the surfactant to also form droplets, which is not desired. However, a very low surfactant density introduces another caveat. The liquid-to-surfactant forces (i.e. $\mathbf{F}^{s\alpha}, \mathbf{F}^{s\beta}$) which are based upon the liquid densities become much larger than the counter acting intra-component hard-sphere like repulsion modeled in the non-ideal EOS. To overcome these instabilities, a factor S is used to scale the liquid-to-surfactant forces, as done by Skartlien *et al.* [45], which makes the total force on the surfactant

$$\mathbf{F}^{s} = \mathbf{F}^{ss} + \frac{1}{S}\left(\mathbf{F}^{s\alpha} + \mathbf{F}^{s\beta}\right) \tag{3.9}$$

Note that this scaling factor can effect momentum conservation as pair-wise momentum between the liquids and surfactant is not conserved when $S \neq 1$. However, in this chapter all simulations are performed on fully periodic domains, due to which the sum of all inter-particle interactions cancels out such that global momentum is conserved, which

was found to be true for all S values used in this chapter. Alternatives to the scaling factor would be using a higher surfactant density (while somehow avoiding the formation of surfactant droplets), or using the surfactant distribution to influence other parameters of the simulation, as will be discussed in the section on coalescence inhibition under results.

The intra-component interaction force, $\mathbf{F}^{\sigma\sigma}$, is calculated by means of the β-scheme [69].

$$\mathbf{F}^{\sigma\sigma}(\mathbf{x},t) = -\beta G_{\sigma\sigma}\Psi_\sigma(\mathbf{x},t)c_s^2\sum_{i=0}^{N} w(|\mathbf{e}_i|^2)\Psi_\sigma(\mathbf{x}+\mathbf{e}_i\Delta t,t)\mathbf{e}_i - \frac{1-\beta}{2}G_{\sigma\sigma}\sum_{i=0}^{N} w(|\mathbf{e}_i|^2)\Psi_\sigma(\mathbf{x}+\mathbf{e}_i\Delta t,t)^2\mathbf{e}_i \tag{3.10}$$

With the proper choice of the weighting parameter β, the spurious velocities occurring at curved interfaces can be reduced significantly [68]. For this research we set the weighting factor β to 1.25, as suggested by Zarghami *et al.* [68].

Phase separation is achieved by implementing the Carnahan-Starling (CS) equation of state (EOS). The interaction term then becomes

$$\Psi_\sigma = \sqrt{\frac{6}{G_{\sigma\sigma}}\left(\rho_\sigma RT\frac{1+b_\sigma\rho_\sigma/4+(b_\sigma\rho_\sigma/4)^2-(b_\sigma\rho_\sigma/4)^3}{(1-b_\sigma\rho_\sigma/4)^3}-a_\sigma\rho_\sigma^2-\rho c_s^2\right)} \tag{3.11}$$

where a_σ and b_σ are respectively the repulsion and attraction parameters, characteristic of the different fluid components, and are set to $a = 0.4963R^2T_c^2/p_c$ and $b = 0.18727RT_c/p_c$, R is the universal gas constant and here set to 1 [68], and T_c and p_c are respectively the critical temperature and the critical pressure of the component of interest. For $T > T_c$, only one phase exists, while for $T < T_c$, two phases coexist with a density ratio determined by the reduced temperature $T_r = T/T_c$, where the corresponding liquid and vapor densities can be calculated by means of the Maxwell construction. The physical temperature is kept the same for all components by ensuring $T = T_c^\sigma \times T_r^\sigma$ has the same value.

The force is implemented in the source term S_i^σ in Eq. 3.1 using the exact differencing method (EDM) [70], given as follows

$$S_i^\sigma = f_i^{eq}\left(\rho,\mathbf{u}+\frac{\mathbf{F}^\sigma\Delta t}{\rho}\right)-f_i^{eq}(\rho,\mathbf{u}) \tag{3.12}$$

The pressure in the system is calculated as a sum of the individual fluid component contributions based upon their EOS, and the non ideal contributions due to inter-component interactions [71].

$$P = c_s^2\sum\rho_\sigma+\frac{1}{2}c_s^2\sum G_{\sigma\sigma}\Psi_\sigma^2+\frac{1}{2}c_s^2\sum_{\sigma\neq\overline{\sigma}}G_{\sigma\overline{\sigma}}\phi_\sigma\phi_{\overline{\sigma}} \tag{3.13}$$

Note that all quantities in this study are non-dimensional, though when simulating flow problems they can be mapped to physical units by keeping some non-dimensional

numbers (such as a Reynolds number) constant. Such a mapping was presented in Mukherjee *et al.* [13] for simulations of falling droplets. Lastly, we have used the massively parallel, open source lattice-Boltzmann solver Palabos in this study [72].

3.3. RESULTS

3.3.1. VALIDATION

To validate our computer code and numerical model, we perform two sets of simulations. In the first study, we validate the thermodynamic consistency of a single component multiphase system when simulated by means of the Carnahan-Starling EOS. Within a (square) periodic box, a droplet of component α is initialized as a diffused circular region defined as

$$\rho(x,y) = \frac{\rho_l + \rho_v}{2} + \frac{\rho_l - \rho_v}{2}\left[\tanh\left(2\frac{\sqrt{(x-x_i)^2+(y-y_i)^2}-R_0}{W}\right)\right] \tag{3.14}$$

where $W = 6$ is the interface thickness, R the droplet radius, ρ_l and ρ_v are the densities of component α in the liquid and vapor phases respectively. The domain size is $N_x = N_y = 601$ and $x_i = y_i = 301$ is the position of the center of the droplet. The respective values of the initial densities inside and outside the droplet are estimated from the Maxwell curve. The Maxwell curve dictates the coexisting densities for a component at a given reduced temperature T_r. The EOS parameters are $a = 1.0$ and $b = 4.0$, and the weighting parameter β of the β-scheme is 1.25.

All stationary droplet simulations have been performed for 20,000 iterations, to ensure that equilibrium is attained. After the reaching equilibrium, the liquid and vapor densities corresponding to inside and outside of the droplet are shown in Fig. 3.1 for various T_r values. At high T_r, where the strength of the phase separation is only moderate, we find excellent agreement with the Maxwell curve. For lower reduced temperatures, our numerical results start to deviate from the analytical curve, however only slightly. The lowest reduced temperature we can obtain is $T_r = 0.4$, with $\rho^\star = \rho_l/\rho_v = O(10^3)$. The thickness of the interface varies from roughly 8-3 lattice units [lu] as T_r is reduced from 0.96 to 0.4. These results are identical to recent literature [13, 68].

Next, we add an ideal lighter component β to validate the multicomponent, multiphase model with the Laplace law (Eq. 3.15). A stationary droplet of the non-ideal heavy component α, suspended in a quiescent lighter ideal component β is simulated in a periodic 2D domain. The initial densities for component α are $\rho_l = 0.45$, $\rho_v = 0.00007$, initialized using Eq. 3.14. Component β is uniformly initialized with density, $\rho = 0.00025$. Further, $T_r^\alpha = 0.52$, $\beta = 1.0$, $a = 1.0$ and $b = 4.0$. Note that the presence of component β strongly affects the phase separation of component α, such that for the same reduced temperature T_r, we find a different ρ_l/ρ_v internally within α, as compared to Fig. 3.1.

After the system has come to a steady state, we calculate the pressure difference between the center of the droplet and the edge of the domain. This is successively done for five different droplet radii R, plotted in Fig. 3.2. Here R is taken to be the radius of the contour level defined by $\rho_\alpha/2$, which is a point that lies inside the diffused interface at about half the interface width. It could also be defined as the distance between the center of the droplet and the point where $\rho_\alpha = \rho_\beta$. The exact position of R is uncertain anyhow by about half the interface thickness δ_{int} (while δ_{int} for a droplet of radius 50 [lu]

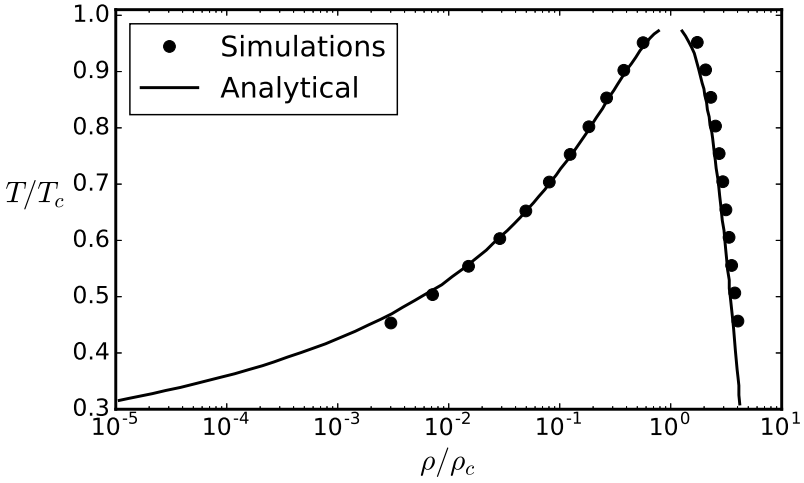

Figure 3.1: Analysis of thermodynamic consistency of the model by comparing simulation results to analytical solution of the Maxwell coexistence curve, that gives the two fluid densities existing together at a given reduced temperature.

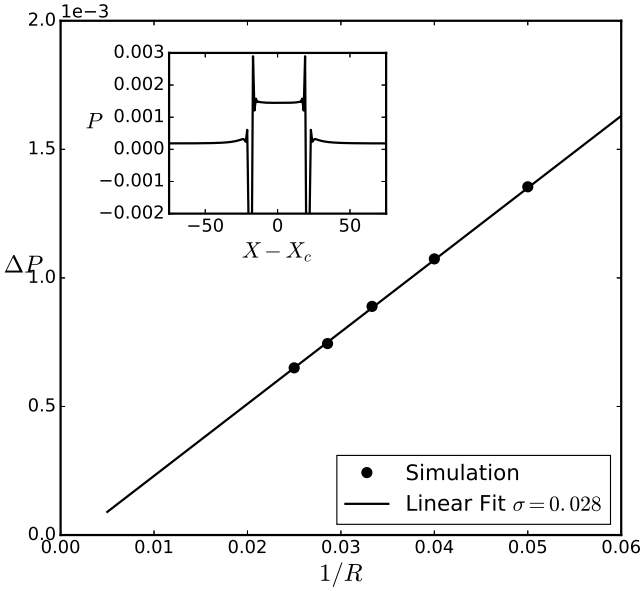

Figure 3.2: Laplace law validation for a multicomponent system is shown where ΔP is the pressure difference between the center of the droplet and the edge of the domain. Surface tension is the slope of the linear fit to ΔP over $1/R$, and is found to be σ = 0.028. The inset shows a typical pressure profile (calculated using Eq. 3.13) across the droplet diameter as indicated.

could be around 5 – 10%). The inset in Fig. 3.2 shows the pressure profile along a diametric line across the droplet. The jumps seen in the pressure profile at the interfaces are due to the local definition of P in Eq. 3.13, and can be remedied by employing the extended pressure tensor given by Sbragaglia and Belardinelli [73]. We observe a clear linear increase in ΔP with $1/R$, where the slope of the line gives the value of surface tension, and an axis cut-off close to the origin, indicating a convincing agreement with the Laplace law, Eq. 3.15.

$$\Delta P = \frac{\sigma}{R} \tag{3.15}$$

3.3.2. ADDITION OF THE SURFACTANT

The surfactant component s is now introduced, which is repelled by both liquid components α and β. The values of $G_{\alpha s}$ and $G_{\beta s}$ are chosen such that the repulsive force on the surfactant from both liquids is equal, which is ensured by maintaining $G_{\alpha s}/G_{\beta s} \approx \rho_\beta/\rho_\alpha$. The miscibility of the surfactant in either fluid can be changed by altering this ratio. All simulations in this section are performed in 2D on a 200×200 periodic lattice, which is a smaller domain facilitating a wide exploration of the parameter space while keeping the computational cost modest. The following results do not depend on the domain size.

The droplet is initialized at the center with a radius of 30 [lu] and the surfactant is uniformly distributed throughout the domain. The liquid-liquid density ratio is chosen to be $\rho^\star_{\alpha\beta} \sim 1.44$ (where $\rho^\star_{\alpha\beta} = \rho_\alpha/\rho_\beta$) while $\rho^\star_{\alpha\beta}$ values from $\mathcal{O}(1)$ to $\mathcal{O}(1000)$ are possible, and the liquid-surfactant density ratio $\rho^\star_{\alpha s} \sim 1000$.

The EOS parameters have been fixed to the values mentioned in Table 3.2. These values are chosen such that the physical temperature of the system $T = T_c \times T_r$ is constant for all components, while T_r can vary. As we simulate a liquid-liquid system, the values of a and b for components α and β are rather similar. We did not use exactly the same values for both as we let component α undergo internal phase segregation in our modeling approach while maintaining the same temperature for all components. These values should also be considered in relation to those for the surfactant component, where a and b for component s are much larger than for α and β. This is because a larger value of b means a larger internal *hard sphere* like repulsion between surfactant molecules (due to the EOS). This is required to ensure that the surfactant does not form droplets, and in the absence of repulsive forces from components α and β the surfactant remains uniformly distributed. In the presence of repulsion, the surfactant migrates to the interface and redistributes uniformly around it. Here there is again an optimum, as a very strong

Component	a	b	T_r	T_c
α	0.0068755878	0.18727	0.8	0.01385369
β	0.007343	0.25	1	0.01108295
s	17.62311	600.0	1	0.01108295

Table 3.2: EOS parameters (refer to Eq. 3.11) for the three components that have been fixed for this parameter study. $G_{\sigma\sigma}$, the intra-component interaction parameter for each parameter, is set to -1 and $R = 1$ for all components. The physical temperature $T = T_c \times T_r$ is the same for each component i.e. they form an isothermal system.

internal repulsion (larger b) would result in a very small amount of surfactant to collect at the interface. So the EOS values were chosen by finding an optimal value for b, while a is calculated such that the temperature remains the same as for components α and β. The value of $\beta = 1.25$ in Eq. 3.10, and all fluid relaxation times τ are set to 1.

Fig. 3.3a shows the steady state density fields of the three components for a quiescent droplet, where the surfactant is seen to collect at the interface. The normalized density fields $\hat{\rho} = (\rho - \rho_{\min})/(\rho_{\max} - \rho_{\min})$ where $\rho \in \{\rho_\alpha, \rho_\beta, \rho_s\}$ show how the component densities vary across the interface and the surfactant collects between the α and β components. The interface is seen to be roughly 10 [lu] here, which is wider than it is when simulating a *pure* liquid-liquid droplet (~ 5 [lu]) using the same parameters (i.e. if we set $G_{\alpha s} = G_{\beta s} = 0$). This is due to the surfactant which accumulates between the two fluids and pushes on them. The interface region can in principle be made narrower by changing the surfactant EOS parameters such that it has a lower internal repulsion and a larger amount of surfactant can collect within a small region. It is useful, also with the view of the discussion further on, to conceptually define this ratio of internal surfactant repulsion and external liquid-surfactant repulsion as

$$R_s \sim F_{\text{internal}}/F_{\text{external}} \tag{3.16}$$

So the interface width δ_{int} could be proportional to R_s, though R_s cannot assume arbitrarily large or small values. Also note that LB being a diffused interface method, there is a minimum interface thickness (roughly $5-6$ [lu]) below which the droplet becomes unstable and can dissolve away.

Interface widening is an issue faced by all diffuse interface methods. In the multicomponent PP-LB method, a higher repulsion strength between the liquid components ($G_{\alpha\beta}$ in our case), leads to a stronger phase separation and hence sharper interfaces as well as to a higher surface tension. It is difficult to manipulate these three effects independently. Typically, one would want to have a large enough separation between the droplet radius and the interface width, i.e. the ratio $\zeta = R/\delta_{\text{int}}$ should be as large as possible, ideally more than 50 or 100. The diffuse interface in such a case can be expected to have little influence on the results. Such simulations, however, will be very computationally demanding in practice, as one also reguires a large enough separation between the droplet radius R and the domain size L. To have both the ratios R/L and ζ high is generally not feasible and one has to compromise the resolution on either or both of these. This is a crucial aspect to be considered when formulating a physical problem to be simulated with any diffuse interface method. With proper scaling of these ratios, the shortcoming of a finite interface width can be overcome to meaningfully simulate the physics. We now use this stationary droplet as a test problem to perform a parameter space investigation of our model. The results presented in this section deal with equilibrium behaviour of the model like interfacial concentrations, surface tension etc., which should not be expected to be very sensitive to ζ.

INFLUENCE OF THE LIQUID-SURFACTANT REPULSION PARAMETER $G_{\alpha s}$

The parameters $G_{\alpha s}$ and $G_{\beta s}$ determine how strongly the components α and β repel the surfactant s. They also determine the extent of immiscibility of s in α and β, and since we keep these values such that s is equally immiscible (or repelled), we discuss this effect in terms of $G_{\alpha s}$ only (while $G_{\beta s} = G_{\alpha s} \times \rho^{\star}_{\alpha\beta}$). In all simulations, we keep the value of the

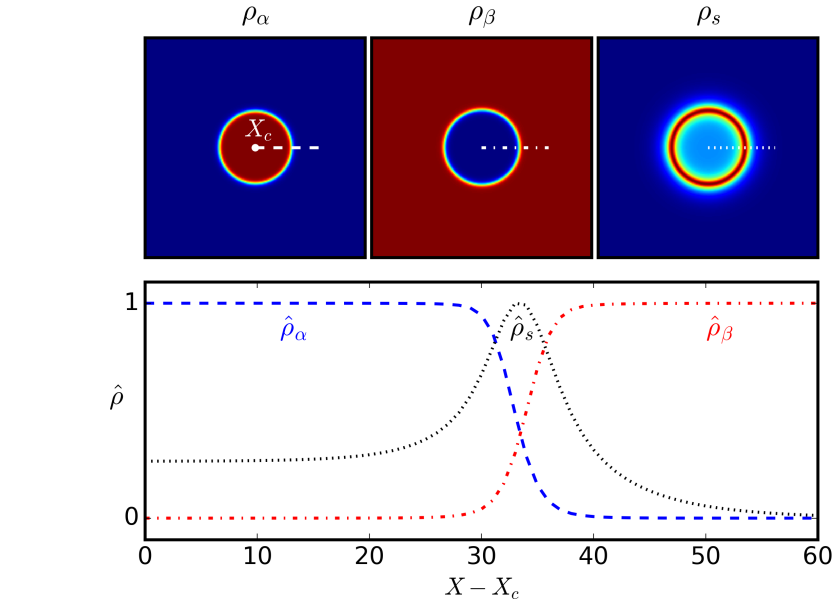

(a)

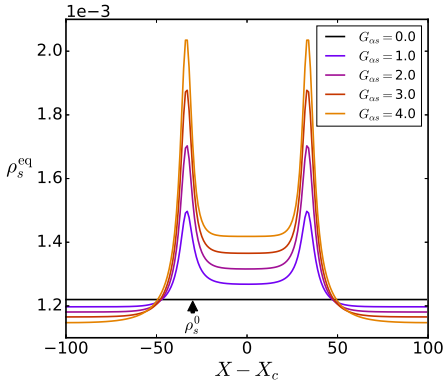

(b)

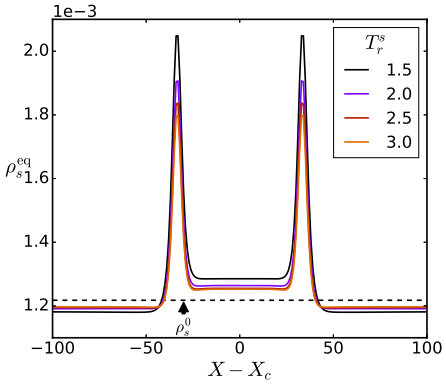

(c)

Figure 3.3: Equilibrium component densities from stationary droplet simulations are shown in: Fig. 3.3a as normalized densities in the domain and across the droplet diameter with $\hat{\rho} = (\rho - \rho_{\min})/(\rho_{\max} - \rho_{\min})$ where $\rho \in \{\rho_\alpha, \rho_\beta, \rho_s\}$. Fig. 3.3b shows the surfactant distribution for increasing values of the liquid-surfactant repulsion strength $G_{\alpha s}$ ($G_{\beta s} = 2G_{\alpha s}$ since $\rho^\star_{\alpha\beta} = 2$), where the peak concentration increases with increasing $G_{\alpha s}$ as the surfactant is more strongly repelled by both liquids. Fig. 3.3c shows the same for increasing values of the surfactant reduced temperature T_r^s, where ρ_s^{eq} decreases due to an increased internal surfactant repulsion.

liquid to surfactant force scaling parameter $S_{\alpha s} \geq 100$ (see Eq. 3.8) to ensure stability. The equilibrium surfactant concentration across a diametric line through the droplet is shown in Fig. 3.3b for increasing $G_{\alpha s}$.

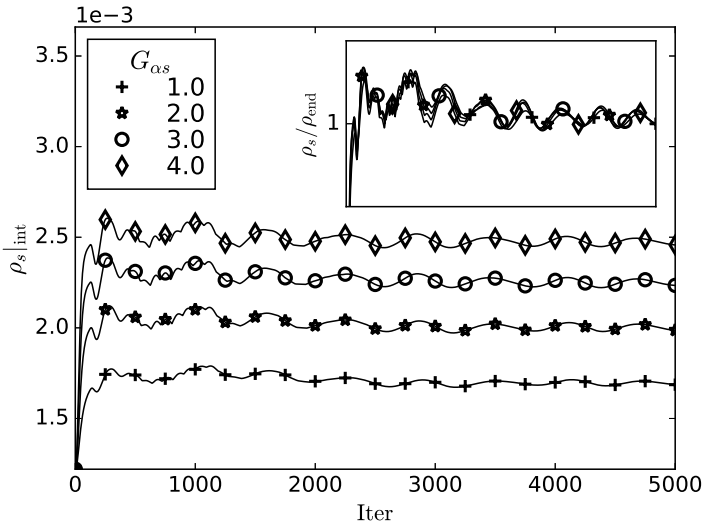

Figure 3.4: Surfactant migration to the interface increases for increasing repulsion strengths $G_{\alpha s}$, where $S_{\alpha s} = 100$ and $G_{\alpha\beta} = 0.02$. It is seen that the maximum surfactant concentration for each configuration is attained within 200 iterations. The inset shows the normalized density (also from 0 to 5000 Iter), where all cases are seen to follow the same evolution profile.

When starting with the same uniform initial surfactant concentration ρ_s^0, for increasing $G_{\alpha s}$, the equilibrium density of the surfactant at the droplet interface obtains a higher peak. The surfactant concentration outside the droplet falls to a successively lower value showing the conservation of surfactant mass in the system. The final liquid-liquid density ratio $\rho^\star_{\alpha\beta} = 1.42$ while the ratio between the repulsion strengths $G_{\beta s}/G_{\alpha s} = 1.44$. This difference reflects in the surfactant being slightly more miscible in the α component and its concentration inside the droplet increases with $G_{\alpha s}$. For larger repulsion strengths, the interface becomes slightly wider as the surfactant pushes on the two liquids more strongly. It should be noted that for each fluid configuration (i.e. liquid EOS parameters, and density ratio between α, β & s), there is a sensitive upper bound to $G_{\alpha s}$, beyond which the repulsive pseudopotential force becomes too large and simulations are unstable. Here, it is seen that around $G_{\alpha s} \sim 4.5$ the simulations become unstable (with the minimum bounds on the liquid to surfactant force scaling factor being $S_{\alpha s} = 100$ to ensure stability).

We also look into the migration of the surfactant from the bulk towards the interface in Fig. 3.4 for increasing $G_{\alpha s}$, which is done by monitoring the maximum surfactant concentration in the domain (which happens to be at the interface). Upon increasing $G_{\alpha s}$, at early times the amount of surfactant at the interface increases as the simulation proceeds. However, within around 200 iterations, the maximum concentration for each simulation is attained and the value oscillates around it until equilibrium is attained. This at

first seems counter intuitive, as increasing the force acting on the surfactant should result in its faster migration to the interface. Here two things are worth noting, first is that increasing $G_{\alpha s}$ reduces R_s (refer to Eq. 3.16), and hence a larger amount ρ_s will collect at the interface. Secondly, regarding the rate of migration of ρ_s for a stationary droplet, there is no physical timescale for interpreting the number of iterations for approach to equilibrium, and each iteration simply means a single collision and streaming step. An increasing repulsion force on the surfactant will translate to an increased change in momentum, but since velocities in LB are fixed, this change can only be achieved by streaming a larger density fraction of the surfactant within a time step. Fig. 3.4 is consistent with this reasoning, and all the cases attain their individual maximum surfactant densities after the same number of iterations. Further, the inset shows the density evolution normalized with the final density, and all the cases collapse to a single evolution curve.

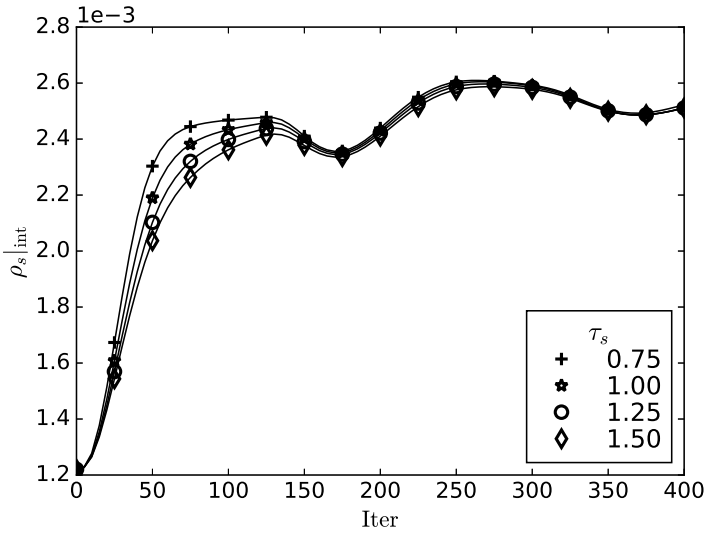

Figure 3.5: Evolution of the interfacial surfactant concentration $\rho_s|_{\text{int}}$ for varying surfactant relaxation times τ_s (related to the surfactant viscosity ν_s according to Eq. 3.6). Here $G_{\alpha\beta} = 0.02, G_{\alpha s} = 4.0$ and $S_{\alpha s} = 100$.

A last point to note here is the wiggles in the evolution profile. These are caused by the generation of pressure (sound) waves in the system due to two factors - first the relaxation of the droplet from its initialized profile to an equilibrium profile, and second the sudden addition of the surfactant repulsion forces. These wiggles completely disappear after 20000 iterations, and are present only during the initialization phase. In simulations of incompressible flow, pressure waves are undesirable, and hence these simulations must be performed over a timescale much longer than any initial transient phenomena that may be present, like approach to local equilibrium in LB. Further, it should be ensured that the flow Mach number is reasonably small (where typically $Ma < 0.1$ is desired). Once the initial phase of relaxation to equilibrium is over, any further changes in the component density distributions is due to the hydrodynamics, which proceeds over a longer timescale than the acoustic timescale. Hence our simulations do not suffer

from pressure waves.

INFLUENCE OF THE REDUCED TEMPERATURE T_r^s

Increasing the reduced temperature T_r^s for the surfactant component to values greater than 1.0 increases the internal molecular repulsion within the component, which is similar to the pressure in a gas rising when it is heated as the molecules become more energetic. At higher T_r^s, the force ratio R_s will increase, and the maximum equilibrium density of the surfactant that can collect at the interface will decrease. This is shown in Fig. 3.3c where $G_{\alpha\beta} = 0.02, S_{\alpha s} = 100$ and $G_{\alpha s} = 4.0$. To ensure that the surfactant is still at the same temperature as the other two components when $T_r^s > 1$ (i.e. the surfactant is at a supercritical temperature), the EOS parameter a is scaled with $1/T_r^s$ as $T_c = 0.3773322a/Rb$. Note that T_r^s could also be reduced to values lower than 1.0, but that could initiate internal phase segregation within the surfactant component is not desired.

Indeed, at higher T_r^s the surfactant feels a stronger internal repulsion and R_s increases, consequently a smaller amount of surfactant collects at the interface. This also leads to the interface becoming slightly narrower (as was discussed earlier after Fig. 3.3a) since a lower surfactant density has a lower repulsion strength acting on the two components on either side of the interface.

INFLUENCE OF THE SURFACTANT VISCOSITY τ_s

The surfactant viscosity ν_s, which is related to τ_s according to Eq. 3.6, has been shown to strongly influence the dynamics [61]. The surfactant concentration at a point on the interface is shown in Fig. 3.5 for varying τ_s. For the quiescent system studied here, only a slight influence is seen in the approach to equilibrium concentration, where the more viscous surfactant migrates slower. The surfactant viscosity can be expected to influence the dynamics when the characteristic time of the flow is comparable to the diffusion timescale, or for more dynamic problems like falling droplets etc. With the current setup, the viscosity ratio between components cannot have very high values, which requires further modifications to the LB method for instance as proposed by Meng and Guo [74].

3.3.3. STRENGTH OF THE SURFACTANT

The strength of a real surfactant varies greatly depending on a number of microscopic effects like the extent of ionic dissolution, adsorption of ions at the interface, et cetera [22]. So far in our modeling approach, the strength of the surfactant depends *only* on the surfactant density (ρ_s) at the interface and how strongly it repels the liquid components, which is given by the repulsion strength parameters $G_{\alpha s}$ and $G_{\beta s}$. While still keeping the discussion in terms of $G_{\alpha s}$ only, we define surfactant strength Λ as

$$\Lambda = G_{\alpha s} \sum_{\text{int}} \rho_s \tag{3.17}$$

in which the summation is carried out over the entire interface. Since the interface is diffused, we take this sum within the region bounded by two radii corresponding to the lower and upper bounds on the density of component α, given as $1.1 \times \rho_\alpha^{\min} < \rho_\alpha < 0.99 \times \rho_\alpha^{\max}$. The values 1.1 and 0.99 are somewhat arbitrary, though they accurately capture the interface width, and slightly changing these numbers does not influence the following

results. Defining Λ in this way facilitates comparison between simulations even upon varying multiple parameters.

We now investigate the equilibrium surface tension of a stationary droplet in a quiescent periodic domain for increasing surfactant strength. The surface tension is calculated using the Laplace law at steady state where $\Delta P = \sigma / R$, ΔP being the pressure difference (where P is calculated according to Eq. 3.13) between the center of the droplet and edge of the domain and R is the droplet radius. Fig. 3.6 shows the equilibrium surface tension over the strength Λ, for two cases of the clean droplet surface tension which was varied by changing the liquid-liquid repulsion strength $G_{\alpha\beta}$. Sets of simulations of varying Λ are performed by varying $0 < G_{\alpha s} < 4.0$ and $100 < S_{\alpha s} < 800$, of which only the $S_{\alpha s} = 100$ cases are shown.

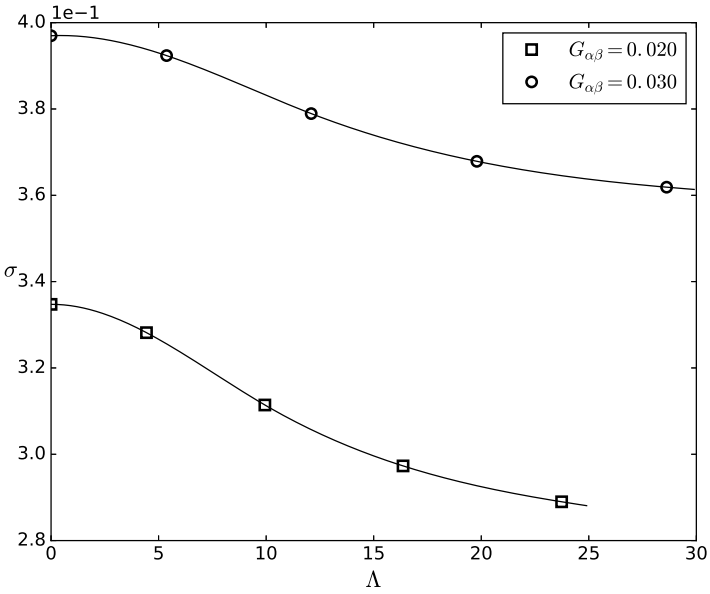

Figure 3.6: Reduction of the equilibrium surface tension σ for two cases of a clean droplet surface tension which is varied by changing the liquid-liquid repulsion parameter $G_{\alpha\beta}$. Λ is increased by varying $0 < G_{\alpha s} < 4.0$, and $S_{\alpha s} = 100$ for the cases shown.

The surface tension reduces with increasing Λ, and the two sets of simulations follow individual σ reduction curves. A maximum σ reduction of around 15% is observed. In our parameter space investigation, we varied the various interaction strengths ($G_{\alpha\beta}$, $G_{\beta s}$, $G_{\alpha s}$), the inner repulsion of the surfactant (which depends on the surfactant EOS parameters a and b, *cf.* Eq. 3.11), the reduced temperature T_r^s of the surfactant component and the surfactant viscosity ν_s. The results obtained from all these simulations are shown together in Fig. 3.7, where the y-axis shows the relative reduction in surface tension σ/σ_0 (where σ_0 is the surface tension of the clean droplet for a particular value of $G_{\alpha\beta}$), and the x-axis shows Λ.

A maximum reduction in surface tension of about 15% is achieved, and the largest value of Λ we could simulate with this model is around 25. Higher values of Λ might

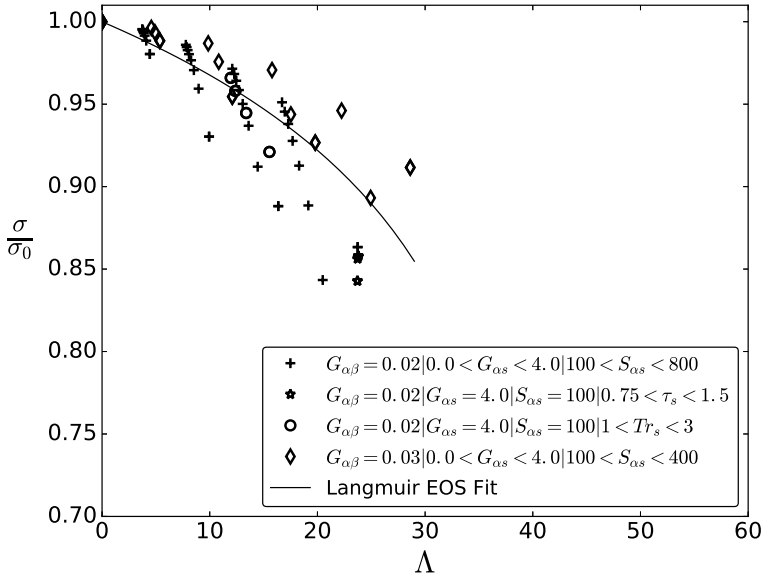

Figure 3.7: Reduction in the equilibrium surface tension σ/σ_0 for a stationary droplet over the surfactant strength Λ shown for all the cases simulated. The legend shows the range each parameter was varied over in a simulation set and the solid black line represents a Langmuir equation of state fit (refer to Eq. 3.18). Surface tension reduction seems to be spread around this curve. A larger reduction in surface tension also results in a thickening of the interface.

be possible with suitable extensions to this model which stabilize the system for higher repulsion strengths. Using the multi-range interaction method [73], a different EOS for the components or another collision operator like the MRT [75] could help achieving this, although we have not explored those possibilities in this chapter. Generally a higher reduction in σ comes at a cost of a wider interface (which goes from roughly 7.5 to 22.5 [lu]). This is a consequence of a higher concentration of the surfactant repelling the two components at the interface more strongly. The solid black line indicates a Langmuir type of fit of the form

$$\frac{\sigma}{\sigma_0} = 1 + \frac{c}{\sigma_0} RT \log\left(1 - \frac{\Lambda}{\Lambda_{\max}}\right) \tag{3.18}$$

where c is a constant fitting factor, and $\Lambda_{\max}$ is taken to be 40 for this fit. The scatter in Fig. 3.7 is due to the use of very different model parameters between cases. Upon varying just one of these parameters while keeping the remaining constant, the pertinent points follow a single curve. Using this model, a few simplified calibration simulations would be required to ascertain the particular isotherm behaviour of the parameters under consideration, as surface tension reduction emerges from simplified pseudopotential particle interactions. In alternate techniques like the free-energy method, the desired isotherm is pre-set into the model thermodynamics, which is in stark contrast to our approach.

In practice, the surfactant layer at a liquid-liquid interface has a thickness of the order of microns, and a reduction in surface tension of 50% or greater is possible. In LB, the interface is diffuse and even at its sharpest, it will be smeared over $5-7$ [lu], which

also determines the minimum thickness of the surfactant layer, and is also observed in previous work on this problem using the LB method [44, 46, 49, 50]. The interface width here should however be valued in comparison to the domain size L, and if $L \gg \delta_{\text{int}}$, theoretically the $5-7$ [lu] δ_{int} can be scaled to a small enough physical length scale. This can of course be limiting as larger domains will begin to have prohibitive computational costs, particularly in regards to memory considering a three component system.

3.4. SPINODAL DECOMPOSITION

Moving to a dynamic setting, we investigate the influence of the surfactant on spinodal decomposition [76], or phase segregation of the two fluid components. To briefly review this phenomenon, consider a single fluid component initialized in a metastable state at a sub critical temperate (or $T_r < 1.0$). Random density fluctuations are added to this component to initiate internal phase segregation where the fluid separates spontaneously into liquid and vapor states with densities determined by its EOS. The fluid initially forms localized droplet-like structures that coalesce and grow over time until the two phases are completely separated. This process, which is rather similar to Ostwald ripening in crystallization, is also denoted by the term "coarsening dynamics".

Additionally, as in our system, a second fluid component may also be present. This second component can also undergo internal phase segregation if it is modeled as a non-ideal component by being placed at a sub critical temperature (i.e. $T_r < 1.0$). Or more simply, repulsion from the first component can make the second component collect in liquid-like and vapor-like phases (the liquid and vapor densities here deviate from the Maxwell construction, as these are now formed due to the repulsive interaction with the first component, so that the bulk of the second component exists in regions where the first component exists as vapor). In our work, we model all components as non ideal. The first component, α, is allowed to undergo internal phase segregation by keeping it at $T_r < 1.0$, while the second component β and the surfactant s are kept at $T_r = 1.0$. This ensures that there are no regions in the domain where both components α and β exist in vapor phases, and a truly liquid-liquid configuration is achieved. Distinction between the terms phases and components is crucial, as a single component may exist in two phases, and yet overall the system is liquid-liquid, due to the presence of another liquid component.

Due to phase segregation interfaces emerge, and depending on the initial density of the components, either a symmetric or an asymmetric composition is achieved, the latter of which may result in nucleation or droplet phase separation based upon the initial density distribution [77]. Many studies [78–82] have reported scaling laws that give the temporal evolution of the characteristic domain length of the fluid regions growing due to coalescence over short and long times, for different binary fluid mixtures in both two and three dimensional systems. The addition of surfactants is expected to inhibit the growth rate of this characteristic domain length, which was also observed by [44].

To quantify spinodal decomposition, a commonly studied parameter is the structure factor $\hat{S}(\mathbf{k}, t)$ which is obtained by performing a Fourier transform on the instantaneous density correlation function $q(\mathbf{x}, t)$, and contains information of the evolution of various length scales in the system [43]. It is calculated as

$$\hat{S}(\mathbf{k},t) = \frac{1}{N}\left(\sum_{\mathbf{x}}\left[q(\mathbf{x},t) - \bar{q}(t)\right]e^{i\mathbf{k}\cdot\mathbf{x}}\right)^2 \tag{3.19}$$

where $q(\mathbf{x},t) = \rho_\alpha(\mathbf{x},t) - \rho_\beta(\mathbf{x},t)$ denotes the density difference between the two components at location $\mathbf{x}$ at time t, $\bar{q}(t)$ is the spatial average of q at each time step and N is the number of grid points (i.e. $N_x \times N_y$). Here $\mathbf{k}$ is a two-dimensional wavenumber, as the Fourier transform yields a two-dimensional matrix of values. To convert this to a single spatial wavenumber k, the structure factor is averaged over shells in $\mathbf{k}$ space to yield the spherically averaged quantity $\hat{S}(k,t)$ as

$$\hat{S}(k,t) = \frac{\sum_{\mathbf{k}} \hat{S}(\mathbf{k},t)}{N_{\mathbf{k}}} \tag{3.20}$$

where the sum $\sum_{\mathbf{k}}$ is over circular shells defined by $\mathbf{k} = \sqrt{k_x^2 + k_y^2}$, and $N_{\mathbf{k}}$ is the number of all k_x and k_y pairs corresponding to each $\mathbf{k}$ shell [43]. The wavenumber correpsonding to any length $\mathscr{L}$ is defined as $k = 2\pi/\mathscr{L}$. Considering the domain length to be N_x [lu] in each direction, the smallest non-zero wavenumber (largest scale) is $k_{\min} = 2\pi/N_x$, while the largest wavenumber (smallest scale) is given by $k_{\max} = 2\pi/2 = \pi$ (which is similar to a Nyquist frequency). Further, the domain growth represented by the characteristic length $R(t)$ can be calculated using the first moment of $\hat{S}(k,t)$ as

$$R(t) = 2\pi\left(\frac{\sum_k \hat{S}(k,t)}{\sum_k k\hat{S}(k,t)}\right) \tag{3.21}$$

For asymetric phase fractions of the two fluids, $R(t)$ is expected to follow a $t^{1/3}$ power law [81, 83] in the inertial regime where capillary forces are minor.

In our simulations, all three components are initialized with a uniform density field, where the density ratios are $\rho^\star_{\alpha\beta} \sim 1.44$ and $\rho^\star_{\alpha s} \sim 10^3$, $G_{\alpha\beta} = 0.02$ and $S_{\alpha s} = 100$. The denser component α is at a reduced temperature $T_r^\alpha = 0.8$ and random density fluctuations (with zero mean) are added to initiate internal phase segregation, the lighter fluid and surfactant both are kept at $T_r^\beta = T_r^s = 1$. The domain size is 512×512 [lu]. The evolution of the α component and the surfactant is shown in Fig. 3.8, for the case with $G_{\alpha s} = 4.0$. It is seen that small localized regions of the heavy component form within a short time which then coalesce and grow, while the surfactant adheres to the evolving interfaces.

Next, the structure factor $\hat{S}(k,t)$ is presented as a spectral density map in Fig. 3.9 for $G_{\alpha s} = 0.0, 2.0, 4.0$ from top to bottom. Here $\hat{S}(k,t)$ has been further normalized by the maximum value at each time step to highlight the relative growth of different scales over time.

Two distinct evolution regimes can be seen, first being a region of fast growth where within 1500 iterations small scale structures are formed and there are several contributing length scales to $\hat{S}(k,t)$, which evolve from around $k \sim 0.25$ to $k \sim 0.12$. From iteration 1500 to 10,000, a second regime of slow dynamics is observed and the system proceeds towards a dominant length scale (as is seen from the spectral density showing strongly concentrated modes, as the spread over k becomes narrower). Over longer times, it is seen that the dominant wavenumbers are more or less similar for the clean and surfactant laden cases ($k \sim 0.05 - 0.025$), with only slight variation in the evolution profiles.

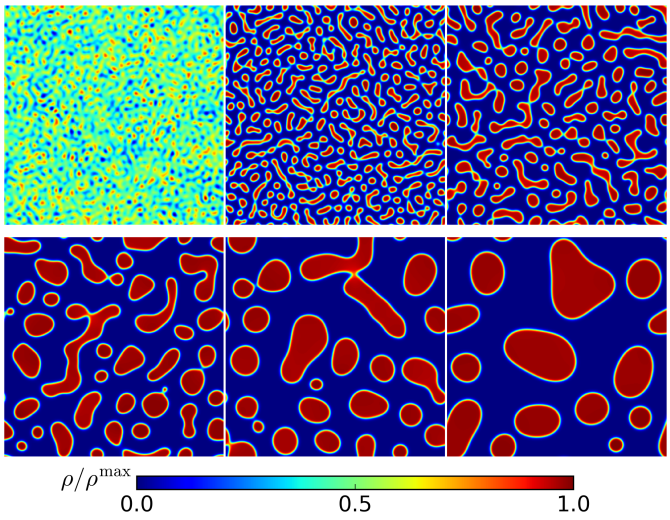

(a) Component α

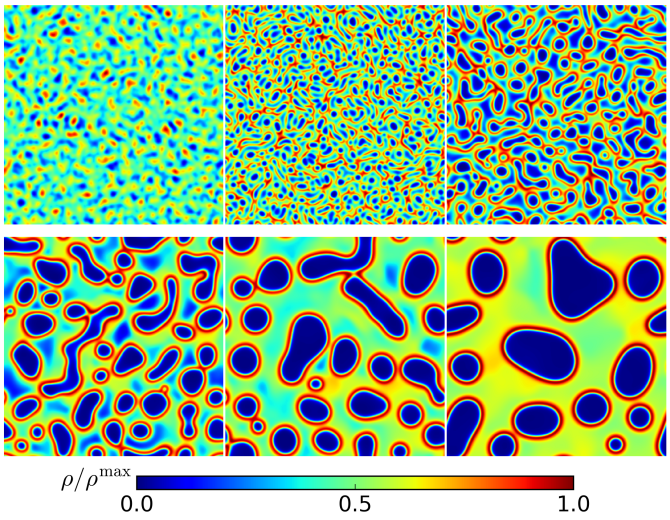

(b) Surfactant

Figure 3.8: Normalized density field of component α and surfactant s (with blue to red representing minimum to maximum value) at Iterations 100, 500, 1000, 2500, 5000 and 10,000 for phase segregation, with $G_{\alpha\beta} = 0.02$ and $G_{\alpha s} = 4.0$. The final volume fractions of α and β are 0.4 and 0.6.

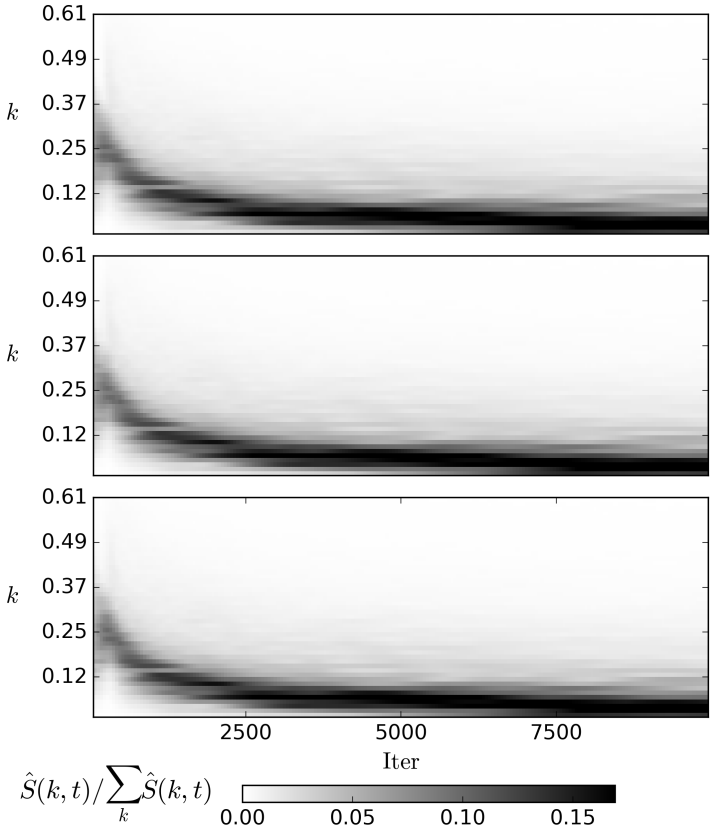

Figure 3.9: Spectral density map of the spherically averaged structure function $\hat{S}(k,t)$ (normalized by the total spectral density at each timestep $\sum_k \hat{S}(k,t)$), with the spatial wavenumber k on the $y-$axis (showing only the first 50 values out of the total 256), and the iteration number on the $x-$axis which goes from 1 to 10,000. The cases shown from top to bottom correspond to $G_{\alpha s} = 0.0, 2.0$ and 4.0. Initially the distribution peaks around $k \sim 0.25$, i.e. small dispersed droplets which then grow rapidly up to iteration 1500 to $k \sim 0.12$, after which the evolution is slow. We do not observe any influence of the surfactant on the evolution of $\hat{S}(k,t)$.

At steady state, we observe that the volume fractions of component α and β are 0.4 and 0.6 approximately, showing that our initial conditions lead to an asymmetric composition. The situation obtained is that of liquid droplets of the heavier fluid forming the dispersed phase while the lighter fluid forms the continuous medium. Upon changing the initial densities, the reverse was also observed but this has been excluded from this chapter.

Lastly, the evolution of the characteristic length $R(t)$ has been shown in Fig. 3.10 for cases with increasing $G_{\alpha s}$. No change in the expected $t^{1/3}$ exponent is found for increasing surfactant strength. Even though the highest surfactant strength reduces surface tension by 15% for a stationary droplet, this has little influence on the coalescence behaviour in a dynamic setting. This is not entirely surprising, as currently our surfac-

tant model does not contain a mechanism for explicitly shielding coalescence, which we shall shortly discuss.

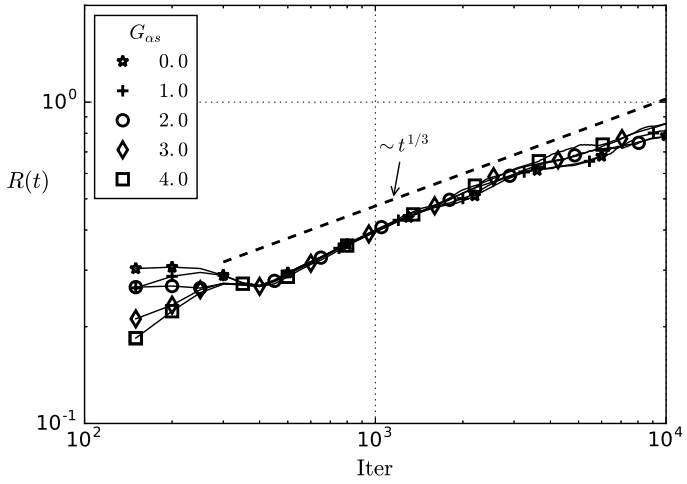

Figure 3.10: Growth of the characteristic length scale $R(t)$ for increasing $G_{\alpha s}$ is shown. No influence of an increasing surfactant strength is observed on the growth rate of $R(t)$, which follows a roughly $t^{1/3}$ scaling as reported in literature [81, 83].

One of the benefits of the LB method and our modeling approach is the ease of extension to 3D, with efficient parallelization. We extend our multi component approach to a $D3Q19$ lattice to simulate spinodal decomposition in a 256^3 three dimensional periodic domain. The same parameters as in the 2D case are taken. Fig 3.11 shows the density evolution of component α as the white contours in the column *a*, along with the surfactant density field thresholded at 75% of the maximum value in column *b*. These results correspond to the $G_{\alpha s} = 2.0$ case, while $G_{\alpha\beta} = 0.04$. The rows correspond to iterations 600, 1000 and 2000 from top to bottom. The surfactant adapts very well to the three dimensional evolving interfaces, in a decaying quasi-turbulent field which is generated by the conversion of the large initial surface energy (driven by interfacial tension) to kinetic energy (upon droplet coalescence). It is worthwhile to note the computational cost of such a simulation. The domain consists of more than 16 million lattice nodes, and the three component modeling approach with 19 velocity directions in 3D requires one to store 19×3 density distribution values (f_i^σ) at each lattice unit which in double precision amounts to around 8 Gigabytes of memory. Simulating 10,000 iterations took approximately 10 hours of wall-clock time on 24 processors. A further resolution doubling would make the memory requirements 8 times and computation time 16 times larger, soon becoming prohibitively expensive.

Fig. 3.11 column *c* shows composite density fields, with contours of component α over half the domain and the surfactant density thresholded at 75% of the maximum value at iteration 1000, for $G_{\alpha s} = 2.0$ (above) and $G_{\alpha s} = 4.0$ (below). Some qualitative difference can be seen between the two figures, particularly that the local concentrations of the surfactant are higher (a larger predominance of yellow-green regions). The

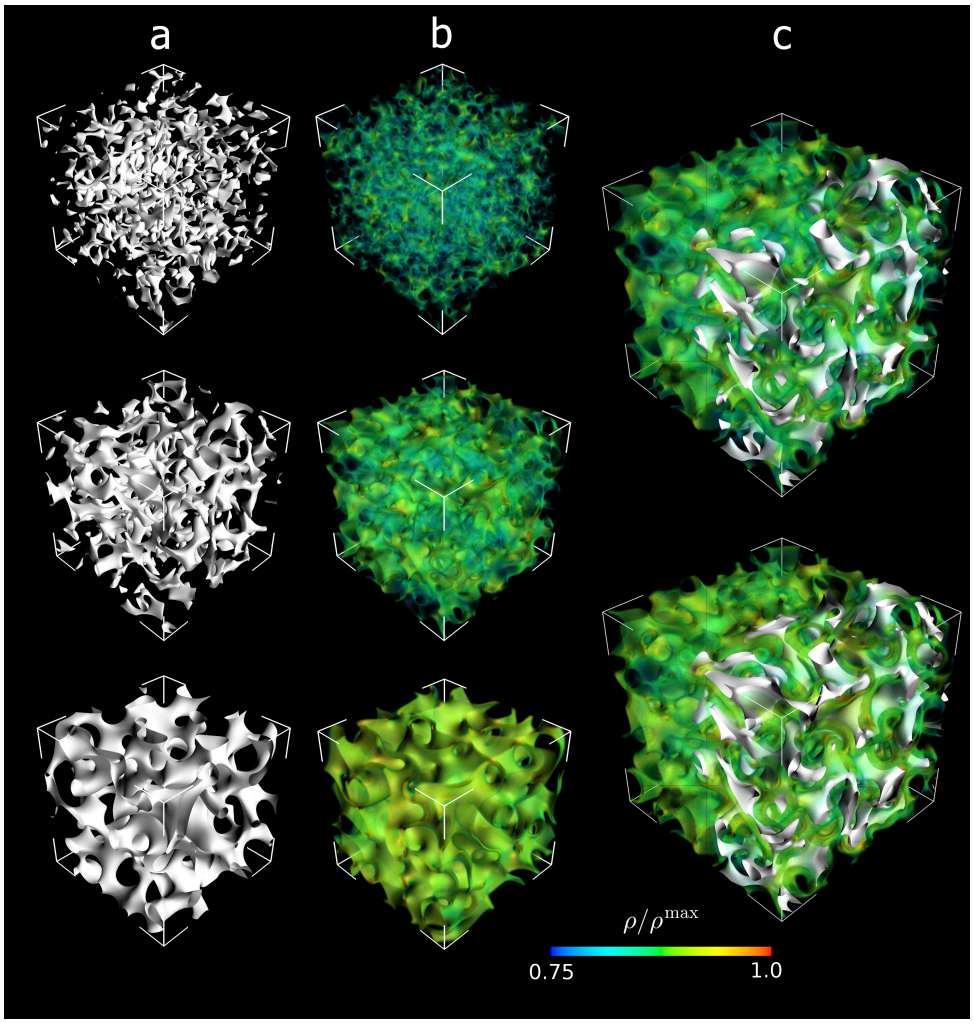

Figure 3.11: Spinodal decomposition in three dimensions is shown, with the contours of component α in column *a* and surfactant density thresholded at 75% of the maximum value in column *b*. The three rows correspond to iterations 600, 1000 and 2000. The third column, *c*, shows composite density fields: the bulk surfactant density (again thresholded at 75% of the maximum value) in the entire domain along with contours of component α (in white) in only half of the domain - all at iteration 1000. The value of $G_{\alpha s} = 2.0$ (above) and $G_{\alpha s} = 4.0$ (below).

α contours, however, are rather similar between the two cases.

3.4.1. COALESCENCE INHIBITION

Previous research on surfactant laden emulsions has included an additional aspect capable of abetting inhibition of coalescence. Chen *et al.* [43], Furtado and Skartlien [46] and Skartlien *et al.* [45] consider a dipole orientation of the surfactant that responds to

a mean field generated by surrounding dipole distributions. This might make it energetically favourable for dipoles to orient in certain manners that prevent droplet coalescence. In addition, a long range intra-component repulsive interaction force, in addition to the short range attraction has been demonstrated to shield droplets in approach from coalescing *without* the need of a surfactant component [48, 84, 85]. However, such a method does not truly represent surfactant dynamics, as it cannot give rise to Marangoni effects or modify interfacial boundary conditions.

As was seen from the spinodal decomposition studies, increasing surfactant strength did not prevent coalescence of droplets in our model. This is because despite the accumulation of the surfactant at the interface, there is no mechanism for preventing coalescence from taking place, the components α and β still repel each other to the same degree as in the absence of the surfactant, such that the resulting film drainage between approaching droplets still causes them to coalesce. Following this reasoning, we propose an extension of the current model, i.e. to make $G_{\alpha\beta}$ a function of the local surfactant density. When the surfactant now collects at the interface, it can now alter how strongly α repels β, in turn influencing the drainage of component β when two droplets of α approach each other.

We implement this in our model as

$$G_{\alpha\beta} = G^0_{\alpha\beta}\left(1 - c\left[\frac{\rho_s}{\rho_s^{\max}}\right]^p\right) \tag{3.22}$$

where $G_{\alpha\beta}$ now varies over the domain, $G^0_{\alpha\beta}$ is the maximum repulsion value (corresponding to the case when no surfactant is present), ρ_s is the surfactant density at a local lattice node which is normalized by the instantaneous maximum surfactant density anywhere in the domain $\rho_s^{\max}$. Alternatively, the surfactant density could also be normalized by a pre-fixed value that is large enough to yield a fraction between 0 and 1, though if the chosen value is too large, the dynamics would not be significantly altered, which we observed in some unreported simulations. The exponent $p = 1$ creates a linear variation in the $G_{\alpha\beta}$ profile, which might not be optimal, as immiscibility between α and β is desired to reduce more rapidly when ρ_s approaches $\rho_s^{\max}$ than when ρ_s assumes smaller values. We set $p = 3$ after some preliminary testing. Further, c sets the minimum bounds on the reduction in $G_{\alpha\beta}$, and a few values were tested whereafter we set it to $c = 0.5$. A similar treatment is done to $G_{\alpha\alpha}$ with $p = 3$ and $c = 0.1$, so as not to drastically alter the intra-component attraction in α to an extent that droplets of α begin to dissolve away. To demonstrate the influence of this technique, we redo the 2D spinodal decomposition cases presented earlier on a 512×512 domain, with $G_{\alpha s} = 2.0$, and the evolution of $R(t)$ is shown in Fig. 3.12.

The cases with varying $G_{\alpha\beta}$ and $G_{\alpha\alpha}$ show a flattening of $R(t)$ at a lower value within 5000 iterations with a clear deviation from the $t^{1/3}$ scaling, as compared to the case with constant parameters. This shows that inhibition of coalescence can be achieved, though it should be noted that varying $G_{\alpha\beta}$ and $G_{\alpha\alpha}$ also influences the surfactant density through the inter-component interactions - the dynamics is hence rather complicated. It was observed (not included in this chapter) that using larger values of c (for instance $c = 2$) can result in a change in the sign of $G_{\alpha\beta}$, whereby droplets of α can spontaneouly rip apart into smaller droplets. The growth of $R(t)$ in such simulations is also arrested in a similar way as for the case shown in Fig. 3.12. These simulations did not

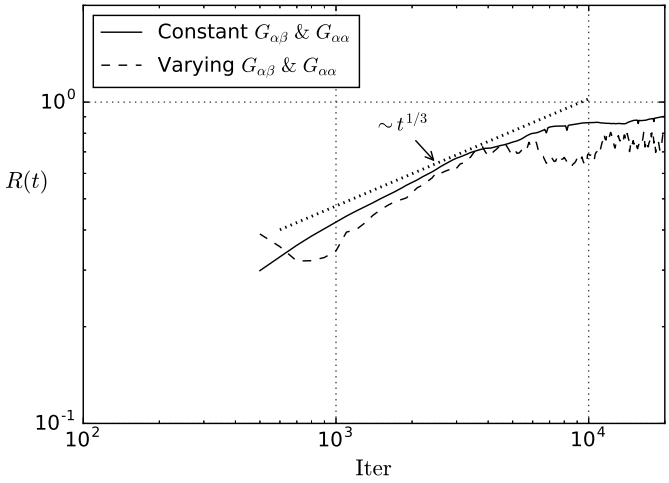

Figure 3.12: Growth of the characteristic length scale $R(t)$ for two cases of variable and constant $G_{\alpha\beta}$ and $G_{\alpha\alpha}$ values is shown. The case with varying parameters shows a clear deviation from the $t^{1/3}$ scaling, with $R(t)$ flattening at a lower value within 5000 iterations.

exhibit an approach to steady state, and the spontaneous generation of small droplets is qualitatively similar to the formation of microemulsions. Also with this modification, the force scaling factor in Eq. 3.8 is not required. The surfactant density, despite being low and interacting weakly with the other components, is sufficient information as a scalar field that is used to influence other model parameters governing miscibility. This would ensure momentum conservation in non-periodic domains as well.

3.5. DROPLET FORMATION

Finally, we apply our model to a well known multiphase flow problem, the formation of a pendent droplet, a phenomena ubiquitous in nature and many industrial processes. It involves the formation of a droplet at an aperture driven by a pressure difference (here due to the action of gravity), whereby the droplet grows under the pull of its own weight, eventually pinching off and falling away - reminiscent of a leaky faucet. This is a complex dynamical process, the crucial moment being the pinch-off, when the droplet breaks away from the reservoir fluid jet, and the process repeats until the reservoir is depleted. We simulate this for clean and surfactant laden cases, mainly focused on illustrating how the surfactant dynamics is captured by our model. Note that we do not investigate the physics here in detail - which can form a study of its own, and use this section as a preliminary demonstration.

We simulate this problem in 2D, where a pocket of a high density fluid consisting of component α in its liquid phase is initialized above an aperture. The surrounding domain is occupied by a lower density fluid β, also in its liquid phase. The density ratio between the components is $\rho^{\star}_{\alpha\beta} \sim 1.4$, while $\rho^{\star}_{\alpha\beta}$ up to $\mathcal{O}(100)$ is possible. The surfactant component is initialized uniformly throughout the entire domain, with $\rho^{\star}_{\alpha s} \sim 1000$. All

components are non-ideal and modeled by means of the CS EOS, the relevant EOS parameters being presented in Table 3.3. Because we simulate three components, we are increasingly restricted by memory limitations, and to keep computational cost modest the size of the domain is kept to $N_x \times N_y = 400 \times 900$ [lu], with the aperture placed at a height of 600 [lu] at the center of the horizontal axis, and has a size of 30 [lu] × 40 [lu] (width × height).

Once the system achieves equilibrium in a stationary configuration, a gravitational force is applied to components α and β as $\mathbf{F} = \mathbf{g}\rho_\sigma$ with $|\mathbf{g}| = 6 \times 10^{-6}$ [lu] to initiate droplet formation in the dripping regime in the absence of an imposed velocity. This strategy resembles the production of droplets by a push-mode piezoelectric Droplet-on-Demand ink jet print head. Dong *et al.* [86] describe such a drop formation process in terms of three stages: a first stage, in which the droplet gradually grows while pending, followed by a second stage of stretching and necking, after which the droplet is released and the elongated neck contracts and forms the start of a new droplet.. The domain is periodic in all directions, which ensures a continuous production of droplets, and the simulations are run for 2 million iterations, while collecting droplet statistics every 200 iterations. These simulations take roughly 48 hours of wall-clock time when run in parallel on 15 processors.

The cases simulated are presented in Table 3.4. For the "Clean" case DF1, there is no interaction between the surfactant component and the two liquid components, such that this is effectively a two component system. For the *surfactant-laden* cases, we turn on interaction between the surfactant and the fluid components, the strengths of which are presented in Table 3.4. The cases DF2 and DF3 are formulated such that the surfactant is slightly more soluble in component α and β respectively. This is to first demonstrate how such a miscibility can be achieved, as it is often found in real systems. Secondly, this alters the modification of surface tension by changing the pressure drop across the droplet interface, due to the presence of the surfactant. To the best of the authors' knowledge, this is also the first study to simulate the formation of a droplet for a multicomponent multiphase system with non-ideal fluids and a non-unity density ratio.

Fig. 3.13 shows the droplet formation process, with component α (in red) suspended in component β (in blue), for the clean case (DF1) in the top row. We observe the formation of a stretching neck that pinches off droplets which eventually fall off. The periodic boundaries of our domain in the direction of the body force causes the exiting droplets to re-enter the domain above the aperture (not shown here) and merge with the heavy fluid reservoir. The middle panel shows the same for case DF2, while the bottom panel

	α	β	s
a	0.006875	0.0073429	17.623
b	0.18727	0.25	600.0
T_r	0.8	1	1
ρ_l	7.7	5.3	0.002
ρ_v	0.05	0.05	0.002

Table 3.3: Equation of state parameters used for the droplet formation simulations. Here ρ_l and ρ_v represent the component densities in the *individual* liquid and vapor phases respectively, and are values used to initialize the simulation.

shows the surfactant density field normalized with the maximum value for DF2.

Several features here are worth noting. Qualitatively, we can see that at iteration 18,000 while the droplet is still attached to the jet for the Clean case, for the DF2 case the droplet already breaks off, which may be attributed to the reduced surface tension in DF2. Further, in the surfactant density evolution, vacuous blue regions with very little surfactant density are formed when the droplet breaks off, forming temporary surfactant *depletion* regions. Transport from the bulk and the internal surfactant repulsion replenishes these regions over time. Also, the surfactant density is higher at the trailing edge of the droplet interface, as the surfactant is swept backwards by the flow.

Around 1200 droplet formation instances have been identified during the entire simulation, which are then used to calculate the probability distribution of the equivalent droplet radii R_{eq} (found by equating the droplet area to a circle with equal area), droplet major axis L, duration between successive droplet formation instances ΔIt and the droplet center of mass position in the lateral direction X_{cm} (which shows how much the droplet oscillates from the central vertical line, where it was produced). The PDFs of these quantities are shown in the first four panels of Fig. 3.14. The PDF of r_{eq} shows that the clean case (black curve) has a strong peak at $R_{\text{eq}} = 29$. The DF2 case does not drastically alter the PDF, though the peak shifts to around $R_{\text{eq}} = 32$ which could be due to a slight thickening of the interface with the presence of the surfactant (as was also encountered in previous sections). For DF3, where the surfactant is slightly more soluble in the surrounding fluid, the peak drops significantly, and a larger number of droplets with $R_{\text{eq}} < 30$ are formed. This trend is similar for the droplet major axis L, which is the lateral extent of the droplet when it is not perfectly circular. Note that with the interface width being around 6-7 [lu], statistics below $R_{\text{eq}} = 15$ and $L = 15$ would not be meaningful.

The PDF of the interval between droplet formation shows a few interesting features of the dynamics governing the problem. For the clean case, a strong peak is seen around $\Delta\text{It} \approx 3500$, and a slightly smaller peak around $\Delta\text{It} \approx 1750$. The first one corresponds to a primary droplet break-off event, following which the depleted fluid jet retracts slightly towards the aperture due to surface tension, and it slowly begins to grow again as more fluid flows through the aperture. After some of the droplet pinch-off events following this dominant mode, there is a secondary pinch-off of a smaller droplet, which is also reflected in the PDF of R_{eq}. For the DF3 case, the PDF appears flattened as droplet formation becomes more irregular due to the intermittent presence of the surfactant (as seen in Fig. 3.13), resulting in the smaller droplets pinching off over a shorter timescale, and larger dropelts taking longer to do so.

The PDF of $X_{\text{cm}} - X_0$ normalized by the domain width W, (with X_0 the center of the domain in the horizontal direction), is very similar for all three cases, with some qualitative differences. Generally, we expect droplets to fall along the central axis without

	DF1	DF2	DF3
$G_{\alpha\beta}$	0.0085	0.0085	0.0085
$G_{\alpha s}$	0.0	4.2	4.0
$G_{\beta s}$	0.0	7.5	5.6
$S_{\alpha s}$	-	100.0	100.0

Table 3.4: Interaction strengths for the various cases.

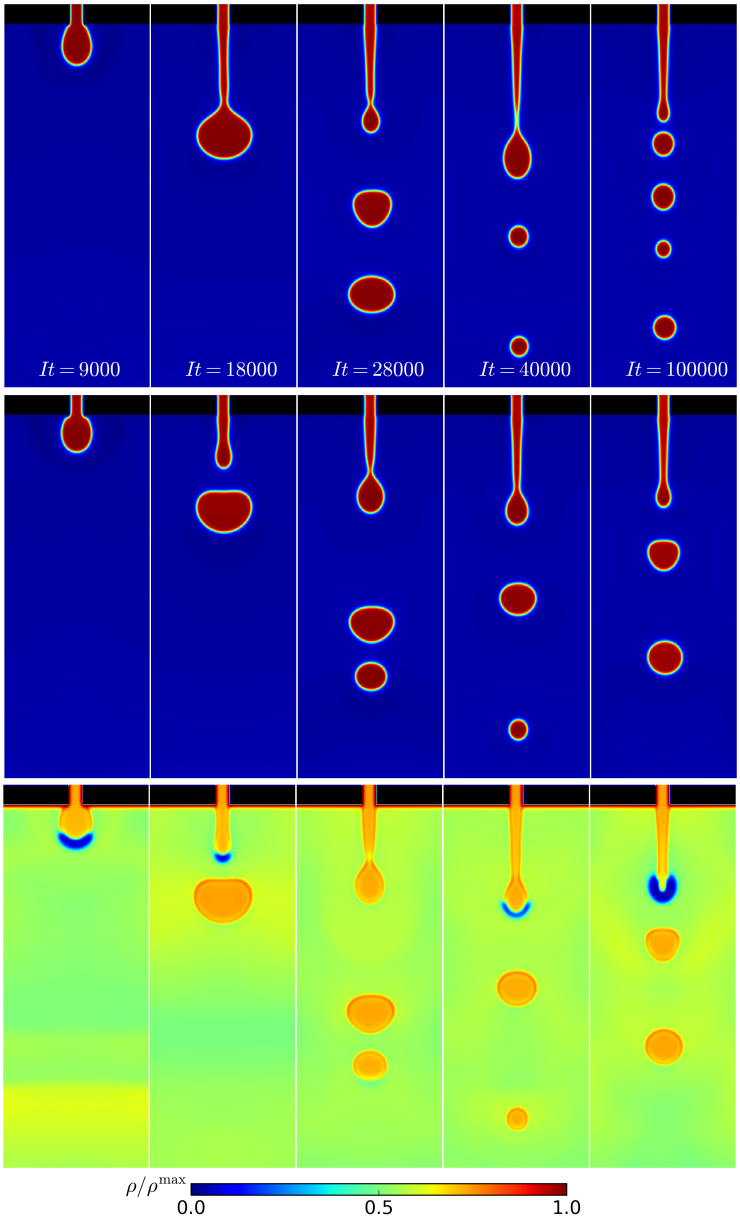

Figure 3.13: Density fields from droplet formation simulations at various time steps show the liquid α in red (β in blue) for a clean case (top row), liquid α for a surfactant laden case (middle row) and the surfactant density s (bottom row). The black bands represent the aperture. It can be seen that the surfactant laden case accelerates droplet breakup in the initial period (due to a reduction in surface tension). The surfactant is seen to closely follow the evolving interfaces, with a higher concentration at the trailing edge of the droplet.

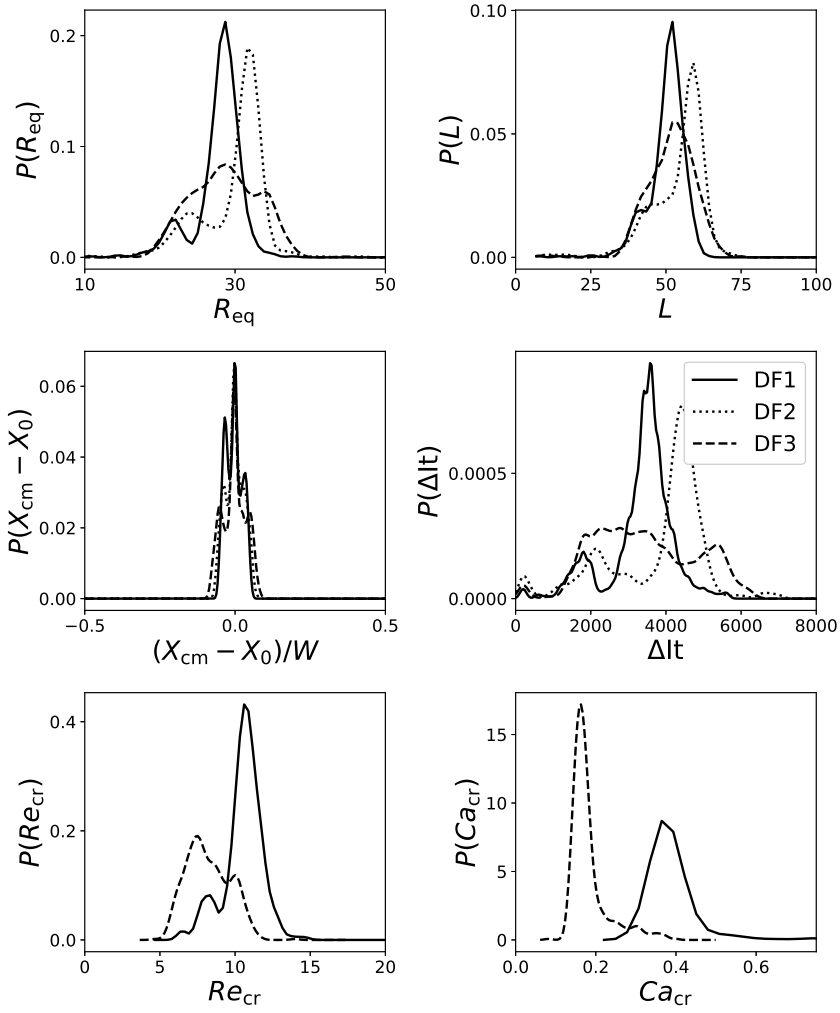

Figure 3.14: Probability distribution of the droplet equivalent radius $P(r_{eq})$, droplet major axis length L, duration between successive droplet formation events ΔIt and the droplet center of mass in the lateral direction X_{cm} is shown for the clean (DF1) and two surfactant laden (DF2,DF3) cases for the droplet formation problem in the first four panels. The bottom two panels show the critical Reynolds and Capillary number just after droplet pinch-off for DF1 and DF3, where the presence of the surfactant is seen to significantly alter the dynamics.

oscillations in the lateral direction as there is perfect symmetry across the central axis. This is true for the initial stages of the simulation (upto the formation of ≈ 150 droplets and $t < 200000\,\Delta t$). As we use vertical periodicity to ensure a continuous and steady supply of the droplet fluid, the droplets coalesce with the small reservoir above the aperture after re-entering the domain. This in turn generates some long wavelength oscillations in the free surface, which are sustained due to frequent droplet coalescence. The vertical

extent of the reservoir is not sufficiently large to completely damp these perturbations out and they later begin to weakly interact with the fluid jet at the aperture. As these free surface oscillations are not perfectly symmetrical across the central axis at longer times $t > 200000\ \Delta t$ (where even machine level inaccuracies might amplify over time due to the inherent non-linearity of the process), the liquid jet begins to swing with a low frequency and low amplitude oscillation which causes a slight spread in the center of mass location of the newly formed droplets. This could be remedied by having a much larger reservoir above the aperture, and the behaviour may be less prominent at higher density ratios where the gravitational pull will dominate any lateral lift forces. Notwithstanding, this effect is minor in our simulations, and even the maximum lateral shift ($\approx 9\%$ of W) is slightly larger than the aperture width i.e. 7.5% of W.

A critical Capillary and Reynolds number can be ascribed to the droplet just after pinch off as

$$\begin{aligned} Re_{\mathrm{cr}} &= \frac{\rho v L}{\mu} \\ Ca_{\mathrm{cr}} &= \frac{\mu v}{\sigma} \end{aligned} \tag{3.23}$$

where L is the lateral droplet extent, σ is the surface tension, and ρ and μ are the density and dynamic viscosity of component β (the surrounding fluid). Here v is taken to be the characteristic droplet velocity calculated as the mean vertical velocity inside the droplet as

$$v = \frac{\sum_{i=1}^{N} v_i}{N} \tag{3.24}$$

where i goes over all the N points comprising the interior of the droplet region. From the Fig. 3.14, it was seen that in case DF3, the droplet characteristics change more significantly as compared to the clean case. We show the PDFs of the critical Re and Ca numbers for the clean and DF3 case in the last two panels of Fig. 3.14. The surfactant significantly alters Re_{cr}, and the distribution shifts to a wider range of lower Re_{cr} values, between 6 to 10 for the DF3 case. The surfactant also shifts the peak of the Ca_{cr} PDF from a value of $Ca_{\mathrm{cr}} \approx 0.4$ to $Ca_{\mathrm{cr}} \approx 0.2$. The presence of the surfactant reduces surface tension, but also causes the formation of smaller droplets which typically have a lower fall velocity. These changes together influence Ca_{cr}, which is found to reduce here. If μ and v are kept constant, surfactant induced surface tension reduction would increase Ca. Controlling these effects individually, however, requires much more precise problem formulation and further investigation. In future work, we intend to test the model for realistic flow problems, along with validation and comparison to existing literature - which was not yet done during this developmental period and parameter space investigation we present in this chapter, as that can comprise a work unto itself.

3.6. CONCLUSIONS

We have presented a pseudopotential lattice-Boltzmann method to simulate liquid-liquid emulsions with a slightly soluble surfactant component. This is a step towards simulating realistic fluid mixtures, that are inevitably surfactant laden, while numerical simu-

lations of multiphase flows have traditionally dealt with pure fluids owing to the complexity involved in simulating surfactant dynamics while resolving fluid motion. The novelty of our work is that we use a simplified model for the surfactant in comparison to previous papers. More specifically, our approach is a simplification of the Chen *et al.* [43], Nekovee *et al.* [44] model, as we ignored orientational effects of the surfactant - an assumption we allowed ourselves to make as we did not intend to study complex aggregate behaviour attributed to dipole dynamics. We think that a simplification is also welcome as the original model is quite complex - and has hence not found widespread application. Further, we wish to see how well a simplified model compares to existing methods and what kind of physics it can simulate.

First, a single component pseudopotential LB model was validated for a non-ideal fluid component against the Maxwell reconstruction of coexisting phases. After adding a second fluid component to the system, the model was validated against the Laplace law for surface tension of a stationary droplet. While simplifying the model for the surfactant, we indeed used a slightly more complicated model for the fluids. Using non-ideal equations of state to model the fluids is a continuation of our previous work where we intend to simulate realistic fluids. Additionally, this method allows for simulating flows with a wide range of density ratios, which is not feasible with the classic Shan-Chen based models, and neither has it been reported in other work cited in this chapter.

Thereafter, a third surfactant component was added to the system in such a way that it is repelled by the two fluid components, hence aggregating at the interfaces. A parameter study was performed on a stationary, surfactant laden droplet in 2D to demonstrate the influence of varying the model parameters like the various repulsion strengths, the surfactant viscosity, EOS parameters and the reduced temperature of the surfactant. Upon defining a surfactant strength parameter Λ, surface tension reductions with respect to a clean interface up to 15% were found to vary with Λ according to, roughly, a Langmuir type of isotherm. To the best of our knowledge, we are the first to demonstrate surface tension reduction for a surfactant laden droplet following roughly Langmuir-like kinetics from purely pseudopotential particle interactions. All other models addressing this problem work with pre-set thermodynamics (where an isotherm is fixed), whereby in our approach this emerges from more fundamental interactions.

This simplistic surfactant model, despite the surface tension reduction, was found incapable of arresting phase segregation in 2D and 3D spinodal decomposition, achieving which requires an additional mechanism. We proposed varying the liquid-liquid repulsion parameter depending on the local surfactant density, which achieved this effect to some extent. Additional mechanisms like longer-range interaction forces have also been proposed in existing literature to achieve a similar effect. We also performed 3D spinodal decomposition, where the surfactant was shown to closely follow the dynamic, complex interfaces, making the model viable for future applications to more realistic droplet laden systems in 3D.

Finally, the model was demonstrated for a well-known physical problem - the formation of a pendant droplet in a liquid-liquid system for both clean and surfactant laden cases, in 2D. The density ratio simulated was $\rho^\star \approx 1.4$, as we focus on emulsion-like systems. The surfactant was capable of greatly altering the droplet distribution, abetting the formation of more numerous smaller droplets, which we ascribe to the reduced surface tension in the surfactant laden system. The critical Capillary and Reynolds number

distributions were also significantly altered. We have also found local differences in the surfactant density between the nose and rear side of pendant and falling droplets.

Our model could also be applied to simulate liquid-gas systems in the presence of a surfactant, and is one of the first studies to simulate three non-ideal fluid components. In future work, we shall investigate the currently observed surfactant effects more closely to see whether the model can simulate Marangoni flows, which remains to be ascertained. Further, we intend to more quantitatively compare our model to flow problems, like shear induced breakup of surfactant laden droplets and droplets in turbulent flows.

3.7. ACKNOWLEDGMENTS

The research leading to these results has been done in cooperation with the Dutch Institute for Sustainable Process Technology (ISPT) as part of the LBM project, the Netherlands Organisation for Scientific Research (NWO) and Shell, the Netherlands. The authors would like to thank Dr. Orest Shardt (University of Limerick, Ireland) for some insightful discussions on this work.

REFERENCES

[1] S. Mukherjee, P. Berghout, and H. E. Van den Akker, *A lattice boltzmann approach to surfactant-laden emulsions,* AIChE Journal **65**, 811 (2019).

[2] R. R. Schaller, *Moore's law: past, present and future,* IEEE spectrum **34**, 52 (1997).

[3] S. V. Patankar and D. B. Spalding, *A calculation procedure for heat, mass and momentum transfer in three-dimensional parabolic flows,* International journal of heat and mass transfer **15**, 1787 (1972).

[4] J. G. Eggels, *Direct and large-eddy simulation of turbulent fluid flow using the lattice-boltzmann scheme,* International Journal of Heat and Fluid Flow **17**, 307 (1996).

[5] J. Derksen and H. Van den Akker, *Parallel simulation of turbulent fluid flow in a mixing tank,* in *High-Performance Computing and Networking* (Springer, 1998) pp. 96–104.

[6] J. Derksen and H. E. A. Van den Akker, *Large eddy simulations on the flow driven by a rushton turbine,* AIChE Journal **45**, 209 (1999).

[7] W. Van Wageningen, D. Kandhai, R. Mudde, and H. E. A. Van Den Akker, *Dynamic flow in a kenics static mixer: An assessment of various cfd methods,* AIChE Journal **50**, 1684 (2004).

[8] J. Gillissen and H. E. A. Van den Akker, *Direct numerical simulation of the turbulent flow in a baffled tank driven by a rushton turbine,* AIChE Journal **58**, 3878 (2012).

[9] A. Ten Cate, J. J. Derksen, L. M. Portela, and H. E. A. Van Den Akker, *Fully resolved simulations of colliding monodisperse spheres in forced isotropic turbulence,* Journal of Fluid Mechanics **519**, 233 (2004).

[10] J. Derksen and H. E. A. Van Den Akker, *Multi-scale simulations of stirred liquid–liquid dispersions,* Chemical Engineering Research and Design **85**, 697 (2007).

[11] D. H. Rothman and S. Zaleski, *Lattice-gas models of phase separation: interfaces, phase transitions, and multiphase flow,* Reviews of Modern Physics **66**, 1417 (1994).

[12] R. Scardovelli and S. Zaleski, *Direct numerical simulation of free-surface and interfacial flow,* Annual review of fluid mechanics **31**, 567 (1999).

[13] S. Mukherjee, A. Zarghami, C. Haringa, K. van As, S. Kenjeres, and H. E. A. Van den Akker, *Simulating liquid droplets: a quantitative assessment of lattice boltzmann and volume of fluid methods,* International Journal of Heat and Fluid Flow (almost accepted) (2017).

[14] A. Ladd and R. Verberg, *Lattice-boltzmann simulations of particle-fluid suspensions,* Journal of statistical physics **104**, 1191 (2001).

[15] R. Van der Sman, *Simulations of confined suspension flow at multiple length scales,* Soft Matter **5**, 4376 (2009).

[16] N. Deen and J. Kuipers, *Direct numerical simulation (dns) of mass, momentum and heat transfer in dense fluid-particle systems,* Current Opinion in Chemical Engineering **5**, 84 (2014).

[17] A. J. Ladd, *Lattice-boltzmann methods for suspensions of solid particles,* Molecular Physics **113**, 2531 (2015).

[18] D. Ramkrishna, *Population balances: Theory and applications to particulate systems in engineering* (Academic press, 2000).

[19] I. Layrisse, H. Rivas, S. Intevep, and S. Acevedo, *Isolation and characterization of natural surfactants present in extra heavy crude oils,* Journal of Dispersion Science and Technology **5**, 1 (1984).

[20] I. M. Banat, *Biosurfactants production and possible uses in microbial enhanced oil recovery and oil pollution remediation: a review,* Bioresource technology **51**, 1 (1995).

[21] S. Kokal *et al.*, *Crude oil emulsions: A state-of-the-art review,* in *SPE Annual Technical Conference and Exhibition* (Society of Petroleum Engineers, 2002).

[22] M. J. Rosen and J. T. Kunjappu, *Surfactants and interfacial phenomena* (John Wiley & Sons, 2012).

[23] H. Stone and L. Leal, *The effects of surfactants on drop deformation and breakup,* Journal of Fluid Mechanics **220**, 161 (1990).

[24] C. D. Eggleton, T.-M. Tsai, and K. J. Stebe, *Tip streaming from a drop in the presence of surfactants,* Physical review letters **87**, 048302 (2001).

[25] Y. Y. Renardy, M. Renardy, and V. Cristini, *A new volume-of-fluid formulation for surfactants and simulations of drop deformation under shear at a low viscosity ratio,* European Journal of Mechanics-B/Fluids **21**, 49 (2002).

[26] M. Drumright-Clarke and Y. Renardy, *The effect of insoluble surfactant at dilute concentration on drop breakup under shear with inertia,* Physics of fluids **16**, 14 (2004).

[27] A. J. James and J. Lowengrub, *A surfactant-conserving volume-of-fluid method for interfacial flows with insoluble surfactant,* Journal of computational physics **201**, 685 (2004).

[28] D. W. Martin and F. Blanchette, *Simulations of surfactant-laden drops rising in a density-stratified medium,* Physical Review Fluids **2**, 023602 (2017).

[29] J.-J. Xu, Z. Li, J. Lowengrub, and H. Zhao, *A level-set method for interfacial flows with surfactant,* Journal of Computational Physics **212**, 590 (2006).

[30] C. C. De Langavant, A. Guittet, M. Theillard, F. Temprano-Coleto, and F. Gibou, *Level-set simulations of soluble surfactant driven flows,* Journal of Computational Physics **348**, 271 (2017).

[31] M. Muradoglu and G. Tryggvason, *A front-tracking method for computation of interfacial flows with soluble surfactants,* Journal of computational physics **227**, 2238 (2008).

[32] K. Dieter-Kissling, H. Marschall, and D. Bothe, *Direct numerical simulation of droplet formation processes under the influence of soluble surfactant mixtures,* Computers & Fluids **113**, 93 (2015).

[33] X. Shan and H. Chen, *Lattice boltzmann model for simulating flows with multiple phases and components,* Phys. Rev. E **47**, 1815 (1993).

[34] X. Shan and H. Chen, *Simulation of nonideal gases and liquid-gas phase transitions by the lattice boltzmann equation,* Phys. Rev. E **49**, 2941 (1994).

[35] L. Chen, Q. Kang, Y. Mu, Y.-L. He, and W.-Q. Tao, *A critical review of the pseudopotential multiphase lattice boltzmann model: Methods and applications,* International Journal of Heat and Mass Transfer **76**, 210 (2014).

[36] M. Kamali, S. Sundaresan, H. E. A. Van den Akker, and J. Gillissen, *A multicomponent two-phase lattice boltzmann method applied to a 1-d fischer–tropsch reactor,* Chemical engineering journal **207**, 587 (2012).

[37] M. Kamali, J. Gillissen, H. E. A. Van den Akker, and S. Sundaresan, *Lattice-boltzmann-based two-phase thermal model for simulating phase change,* Physical Review E **88**, 033302 (2013).

[38] A. Zarghami, N. Looije, and H. E. A. Van den Akker, *Assessment of interaction potential in simulating nonisothermal multiphase systems by means of lattice boltzmann modeling,* Phys. Rev. E **92**, 023307 (2015).

[39] M. R. Swift, W. Osborn, and J. Yeomans, *Lattice boltzmann simulation of nonideal fluids,* Physical review letters **75**, 830 (1995).

[40] E. Orlandini, M. R. Swift, and J. Yeomans, *A lattice boltzmann model of binary-fluid mixtures,* EPL (Europhysics Letters) **32**, 463 (1995).

[41] T. Krüger, H. Kusumaatmaja, A. Kuzmin, O. Shardt, G. Silva, and E. M. Viggen, *The Lattice Boltzmann Method* (Springer, 2017) pp. 297–329.

[42] L. Scarbolo, D. Molin, P. Perlekar, M. Sbragaglia, A. Soldati, and F. Toschi, *Unified framework for a side-by-side comparison of different multicomponent algorithms: Lattice boltzmann vs. phase field model,* Journal of Computational Physics **234**, 263 (2013).

[43] H. Chen, B. M. Boghosian, P. V. Coveney, and M. Nekovee, *A ternary lattice boltzmann model for amphiphilic fluids,* sProceedings of the Royal Society of London A: Mathematical, Physical and Engineering Sciences **456**, 2043 (2000).

[44] M. Nekovee, P. V. Coveney, H. Chen, and B. M. Boghosian, *Lattice-boltzmann model for interacting amphiphilic fluids,* Phys. Rev. E **62**, 8282 (2000).

[45] R. Skartlien, K. Furtado, E. Sollum, P. Meakin, and I. Kralova, *Lattice–boltzmann simulations of dynamic interfacial tension due to soluble amphiphilic surfactant,* Physica A: Statistical Mechanics and its Applications **390**, 2291 (2011).

[46] K. Furtado and R. Skartlien, *Derivation and thermodynamics of a lattice boltzmann model with soluble amphiphilic surfactant,* Physical Review E **81**, 066704 (2010).

[47] O. Shardt, S. K. Mitra, and J. Derksen, *Simulations of charged droplet collisions in shear flow,* Chemical Engineering Journal **302**, 314 (2016).

[48] M. Sbragaglia, R. Benzi, L. Biferale, S. Succi, K. Sugiyama, and F. Toschi, *Generalized lattice boltzmann method with multirange pseudopotential,* Phys. Rev. E **75**, 026702 (2007).

[49] R. Skartlien, B. Grimes, P. Meakin, J. Sjöblom, and E. Sollum, *Coalescence kinetics in surfactant stabilized emulsions: Evolution equations from direct numerical simulations,* The Journal of chemical physics **137**, 214701 (2012).

[50] R. Skartlien, E. Sollum, and H. Schumann, *Droplet size distributions in turbulent emulsions: Breakup criteria and surfactant effects from direct numerical simulations,* The Journal of chemical physics **139**, 174901 (2013).

[51] A. Lamura, G. Gonnella, and J. M. Yeomans, *A lattice boltzmann model of ternary fluid mixtures,* EPL (Europhysics Letters) **45**, 314 (1999).

[52] R. Van der Sman and S. Van der Graaf, *Diffuse interface model of surfactant adsorption onto flat and droplet interfaces,* Rheologica acta **46**, 3 (2006).

[53] G. I. Tóth and B. Kvamme, *Analysis of ginzburg-landau-type models of surfactant-assisted liquid phase separation,* Physical Review E **91**, 032404 (2015).

[54] G. I. Tóth and B. Kvamme, *Phase field modelling of spinodal decomposition in the oil/water/asphaltene system,* Physical Chemistry Chemical Physics **17**, 20259 (2015).

[55] R. van der Sman and M. Meinders, *Mesoscale models of dispersions stabilized by surfactants and colloids,* Advances in colloid and interface science **211**, 63 (2014).

[56] N. González-Segredo and P. V. Coveney, *Self-assembly of the gyroid cubic mesophase: lattice-boltzmann simulations,* EPL (Europhysics Letters) **65**, 795 (2004).

[57] N. González-Segredo and P. V. Coveney, *Coarsening dynamics of ternary amphiphilic fluids and the self-assembly of the gyroid and sponge mesophases: lattice-boltzmann simulations,* Physical Review E **69**, 061501 (2004).

[58] P. V. Coveney and P. W. Fowler, *Modelling biological complexity: a physical scientist's perspective,* Journal of The Royal Society Interface **2**, 267 (2005).

[59] J. Chin and P. V. Coveney, *Chirality and domain growth in the gyroid mesophase,* in *Proceedings of the Royal Society of London A: Mathematical, Physical and Engineering Sciences*, Vol. 462 (The Royal Society, 2006) pp. 3575–3600.

[60] J. Harting, G. Giupponi, and P. V. Coveney, *Structural transitions and arrest of domain growth in sheared binary immiscible fluids and microemulsions,* Physical Review E **75**, 041504 (2007).

[61] A. Ponce-Torres, J. M. Montanero, M. A. Herrada, E. J. Vega, and J. M. Vega, *Influence of the surface viscosity on the breakup of a surfactant-laden drop,* Phys. Rev. Lett. **118**, 024501 (2017).

[62] G. R. McNamara and G. Zanetti, *Use of the boltzmann equation to simulate lattice-gas automata,* Phys. Rev. Lett. **61**, 2332 (1988).

[63] P. L. Bhatnagar, E. P. Gross, and M. Krook, *A model for collision processes in gases. i. small amplitude processes in charged and neutral one-component systems,* Phys. Rev. **94**, 511 (1954).

[64] R. R. Nourgaliev, T. N. Dinh, T. G. Theofanous, and D. Joseph, *The lattice boltzmann equation method: Theoretical interpretation, numerics and implications,* Int. Multiphase Flow, J , 117 (2003).

[65] S. Succi, *The Lattice Boltzmann Equation: For Fluid Dynamics and Beyond*, Numerical Mathematics and Scientific Computation (Clarendon Press, 2001).

[66] X. He, X. Shan, and G. D. Doolen, *Discrete boltzmann equation model for nonideal gases,* Phys. Rev. E **57**, R13 (1998).

[67] A. Mazloomi M, S. S. Chikatamarla, and I. V. Karlin, *Entropic lattice boltzmann method for multiphase flows,* Phys. Rev. Lett. **114**, 174502 (2015).

[68] A. Zarghami, N. Looije, and H. E. A. Van den Akker, *Assessment of interaction potential in simulating nonisothermal multiphase systems by means of lattice boltzmann modeling,* Phys. Rev. E **92**, 023307 (2015).

[69] S. Gong and P. Cheng, *Numerical investigation of droplet motion and coalescence by an improved lattice boltzmann model for phase transitions and multiphase flows,* Computers & Fluids **53**, 93 (2012).

[70] A. Kupershtokh, D. Medvedev, and D. Karpov, *On equations of state in a lattice boltzmann method,* Computers & Mathematics with Applications **58**, 965 (2009), mesoscopic Methods in Engineering and Science.

[71] L. Chen, Q. Kang, Q. Tang, B. A. Robinson, Y.-L. He, and W.-Q. Tao, *Pore-scale simulation of multicomponent multiphase reactive transport with dissolution and precipitation,* International Journal of Heat and Mass Transfer **85**, 935 (2015).

[72] B. Chopard, D. Lagrava, O. Malaspinas, R. Ouared, J. Latt, K.-O. Lovblad, and V. Pereira-Mendes, *A lattice boltzmann modeling of bloodflow in cerebral aneurysms,* in *V Eur Conf Comput Fluid Dyn ECCOMAS CFD*, Vol. 453 (2010) p. 12.

[73] M. Sbragaglia and D. Belardinelli, *Interaction pressure tensor for a class of multicomponent lattice boltzmann models,* Physical Review E **88**, 013306 (2013).

[74] X. Meng and Z. Guo, *Multiple-relaxation-time lattice boltzmann model for incompressible miscible flow with large viscosity ratio and high péclet number,* Physical Review E **92**, 043305 (2015).

[75] D. d'Humières, *Multiple–relaxation–time lattice boltzmann models in three dimensions,* Philosophical Transactions of the Royal Society of London A: Mathematical, Physical and Engineering Sciences **360**, 437 (2002).

[76] J. W. Cahn, *On spinodal decomposition,* Acta metallurgica **9**, 795 (1961).

[77] H. Tanaka, *Hydrodynamic interface quench effects on spinodal decomposition for symmetric binary fluid mixtures,* Physical Review E **51**, 1313 (1995).

[78] E. D. Siggia, *Late stages of spinodal decomposition in binary mixtures,* Physical review A **20**, 595 (1979).

[79] S. Koch, R. C. Desai, and F. F. Abraham, *Dynamics of phase separation in two-dimensional fluids: spinodal decomposition,* Physical Review A **27**, 2152 (1983).

[80] T. Rogers, K. Elder, and R. C. Desai, *Numerical study of the late stages of spinodal decomposition,* Physical Review B **37**, 9638 (1988).

[81] W. Osborn, E. Orlandini, M. R. Swift, J. Yeomans, and J. R. Banavar, *Lattice boltzmann study of hydrodynamic spinodal decomposition,* Physical review letters **75**, 4031 (1995).

[82] N. González-Segredo, M. Nekovee, and P. V. Coveney, *Three-dimensional lattice-boltzmann simulations of critical spinodal decomposition in binary immiscible fluids,* Physical Review E **67**, 046304 (2003).

[83] J. Chin and P. V. Coveney, *Lattice boltzmann study of spinodal decomposition in two dimensions,* Physical Review E **66**, 016303 (2002).

[84] G. Falcucci, G. Bella, G. Shiatti, S. Chibbaro, M. Sbragaglia, and S. Succi, *Lattice boltzmann models with mid-range interactions,* Communications in computational physics **2**, 1071 (2007).

[85] S. Chibbaro, G. Falcucci, G. Chiatti, H. Chen, X. Shan, and S. Succi, *Lattice boltzmann models for nonideal fluids with arrested phase-separation,* Phys. Rev. E **77**, 036705 (2008).

[86] H. Dong, W. W. Carr, and J. F. Morris, *An experimental study of drop-on-demand drop formation,* Physics of fluids **18**, 072102 (2006).

4

A STRUCTURAL VIEW OF TURBULENCE

"Big whorls are streams, potential,
surrounding mild curls generate them.
Small whorls are lonely whirlwinds,
yet, experts tend to venerate them."

The concept of flow 'structures', though ill defined, has fed the imagination of turbulence researchers for almost a century. Referred variously to as 'eddies' and 'vortices', these entities have remained elusive to definition and characterization, and yet been at the core of many theories, for instance the famous 'turbulence cascade' of Richardson [1]. Intriguingly, ample evidence has been gathered for the existence of these structures, their dynamics and interactions in different representational spaces and flow decompositions (for instance Fourier/Wavelet domains, POD etc.). Yet, in the real physical space where these structures were originally envisioned, they have not been amenable to characterization. Most studies, further, employ techniques based upon the velocity gradient tensor, all of which being point criteria, may not reflect spatially finite, non-point structures in the velocity field. The lack of tools to identify instantaneous, spatial structures in turbulence fields, coupled with the confounding superposition of scales that obfuscate coherent flow regions, aggravates the situation. In this study we propose new coherence measures, inspired by a generalization of the correlation tensor, which suitably identify distinct regions of high kinetic energy and high enstrophy. By further utilizing the Helmholtz decomposition of the velocity field, these coherent structures are disentangled from their state of superposition. This paradigm allows us to identify the regions of the vorticity field which generate, in a Biot-Savart sense, two distinct flow types (as summarized in the epigraph). This study sheds new light on the organization of turbulence fields, hinting perhaps at a more 'emergent' picture of turbulent flows, where the permeating intermediate background vorticity generates most of the flow field, rather than a strict 'hierarchy' of large scales generating smaller scales.

This chapter is to be submitted to the *Journal of Fluid Mechanics*, 2019.

4.1. INTRODUCTION

"Structure" in a field can be defined as a certain distribution of the properties of the field in a region, characterized by a small number of parameters, which can be described (deterministically) in a "simple way". For instance, in a velocity field, swirling motion can be considered as a kind of structure, which brings to mind examples such as a tornado, cyclone or a simple bathtub vortex. The concept of structure in flow fields immediately also invokes the notion of "coherent motion", one interpretation of which is: regions of the flow that have a certain spatial pattern (for instance a swirling motion). This idea of structure can also be understood by considering its opposite, i.e. a structure-less field, which mathematically may be defined as random.

The structure in a general field, and in particular in a velocity field, can be the result of (arbitrary) choices in constructing the field and of the (intrinsic) dynamics of the field. For example, the addition of a translation or a rotation generate a "coherent motion" that is not related with the intrinsic dynamics of the velocity field. The pattern of the field at infinity can be seen as the result of arbitrary choices, and it can be "removed", in order to obtain patterns associated with the (intrinsic) dynamics of the field. In classical Newtonian mechanics, this is equivalent to observing motion with respect to the "distant stars". The use of correlation and Helmholtz decomposition concepts allows the generalization of these ideas. The spatial correlation of the field over a sphere with an infinite radius can be made zero by performing an opposite transformation in the field (eg. a translation or a rotation). From a Helmholtz decomposition perspective, this is equivalent to making the generalized Biot-Savart contribution of the infinity-field (far-field contribution from "large distances") equal to zero.

Turbulent flows have been found to be very rich in structure across different representational spaces, so much so that turbulence has been held synonymous to structure [2]. Moreover, turbulent flow fields are intriguing due to the superposition of structure and randomness across scales; its uncovering and characterizing has garnered profound interest over the past decades. In describing velocity field structures in turbulence, a key idea often used, albeit ill-defined, is that of the "eddy", which also refers to coherent regions of swirling motion. The superposition of eddies (or coherent motion across all scales) has served as the conceptual background upon which most of turbulence theory has been built [3, 4]. How these coherent structures arise across all scales, and what they look like, however, is not fully known. In this paper, we are interested in finding out whether the finite-sized spatial structures comprising turbulent flow fields can be identified and isolated in the vector spaces where they arise. Further, we are interested in considering instantaneous structures which are continuously produced and destroyed, and are not the result of averaging ensembles of the flow field. These structures may range from the largest, energy containing scales on one end, which according to a conventional "cascade" perspective, *drive* the turbulence dynamics, to structures at the small scales associated with the dissipation of kinetic energy. In this framework, it should be noted that the smallest scales are merely a *consequence* of the turbulence dynamics, and are hence not dynamically significant in determining the overall flow [2].

There have been various approaches aimed at identifying coherent structures in different contexts that are prevalent in the turbulence literature. Most widely used are techniques based upon the velocity gradient tensor $A_{ij} = \partial u_i / \partial x_j$ and its symmetric (S_{ij}) and skew-symemtric (Ω_{ij}) parts. For instance [5] define a criterion (called λ_2) based on

the eigenvalues of the local pressure Hessian which is related to S_{ij} and Ω_{ij}. [6] used the second and third invariants (Q and R) of A_{ij}, originally used to characterize the topology of point flow patterns [7], and [8] used the strain acceleration tensor along fluid trajectories. [9] use a wavelet decomposition to identify coherent and incoherent vorticity structures, [10, 11] studied statistically emerging lower dimensional attractors, while others have extensively studied Lagrangian structures crucial for material transport [12–14]. Non-linear equilibrium solutions have also been classified as exact coherent structures [15–17]. [18] studied spatio-temporally coherent vortical structures, while [19] and [20] investigated the structure of strong vorticity (worms) in homogeneous, isotropic turbulence and [21] showed their large-scale spatial organization.

These (and many other) studies and techniques have greatly informed our understanding of coherent structures in turbulence. However, the basic concepts of a hierarchy of coherent structures (as invoked for instance in the [1] cascade), or the energetic interaction of eddies [22] and eddy breakup, have remained intractable in the physical spaces where these ideas were first envisioned. Some of these, to the contrary, have been well described in the wavelet and spectral decomposition of turbulence fields [23, 24]. Part of this disconnect is due to the lack of tools designed to identify instantaneous spatial structures which may be driving these processes. The other issue is extracting these structures from their obfuscating scale superposition to study their form and dynamics. In order to address these issues we use correlation concepts and Helmholtz decomposition concepts. These concepts allow us to remove artificial velocity patterns associated with the arbitrary choices in constructing the velocity field (eg. frame of reference) and to identify and extract flow structures from the turbulence field. We deal with incompressible, homogeneous, isotropic turbulence, with a zero mean velocity, hence the removal of a velocity pattern associated with an "artificial frame of reference" is not an issue. We approach the concept of coherent structures arising in incompressible, homogeneous, isotropic turbulence with a focus on the following key aspects:

1. **Finite structure size** - We consider a "coherent motion" or an "eddy" to be a finite, spatial structure, that represents a unit of coherent motion. It must hence have a spatial form, that is to say, it cannot be completely irregular. Coherence, in this context, becomes almost synonymous to correlation, as an ordered spatial structure must comprise of a neighbourhood of vectors that are strongly correlated (either positively or negatively). Here it becomes important to highlight the distinction from *point-criterion* used for educing structures, which are based on the velocity gradient tensor (or derivatives thereof, like Q, R etc.). These techniques describe point structures, reasoning from the Taylor expansion perspective of the velocity field in the infinitesimal neighbourhood of each point in the flow field. Structures in the flow field, however, are *finite regions* of spatio-temporal order, and may not necessarily be related to velocity gradients at individual points within the field. In this study, we identify coherent structures in velocity and vorticity spaces, by developing "correlation" measures that are designed to seek out their particular spatial forms.

2. **Instantaneity** - Spatial structures in turbulence vector fields exist instantaneously, and are not consequences of statistical or averaging procedures. In fact, a structure will have an entire lifecycle, from generation until destruction (driven by the

dynamics of the Navier-Stokes equations). While ignoring the temporal evolution of the structures, in this work we limit ourselves to identifying structures in instantaneous realizations of turbulence fields, hence considering only the geometry of structures and not their kinematics or dynamics.

3. **Disentanglement of structures** - The complexity of turbulence fields is due to the superposition of structures, which makes it difficult to extract and study an individual structure. According to the generalized Biot-Savart rule, which follows from the Helmholtz decomposition of the velocity field, a localized velocity region is generated by the integrals of quantities associated with the gradients of the velocity. This includes both the *near-field* and the *far-field* contributions. The Biot-Savart rule provides a paradigm for *disentangling* structures, where the gradient field can be conditionally sampled based upon suitable criteria, and the contribution of these regions to a local, finite velocity structure can be isolated. We use this method to identify regions of the velocity gradient field which 'generate'—in a Biot-Savart sense—a particular velocity structure.

The tools developed in this study, namely a set of generalized correlation measures, along with velocity reconstruction using the Biot-Savart law, allow us to look at turbulence fields from a different perspective. They enable us to identify the structure of high kinetic energy and high enstrophy regions. The Biot-Savart reconstruction, further, reveals the distribution of the vorticity contributions in the generation of the velocity field. This paves the way for studying the interplay between the different components of turbulence, when considered as a dynamical system comprised of interacting structures. Our results point towards a novel description of turbulence, in particular, regarding the emergence of flow organization.

The layout of the paper is as follows. We begin by proposing different instantaneous coherence measures in section 4.2, which are designed to identify simple structures, based upon a generalization of the correlation tensor, along with correlations associated with the Biot-Savart law in section 4.3. These correlations are first applied to canonical flows in section 4.4, where some of their features are highlighted. In section 4.5, the correlations are applied to homogeneous, isotropic turbulence flow fields, where the particular flow structure of the large (energy containing) and small (enstrophy containing) scales are identified. These results are shown to be essentially similar to those obtained upon using a reference dataset in appendix 4.A. In section 4.5.6 we perform the Biot-Savart decomposition of the flow structures to show that the vorticity composition of the velocity field structures, following which we end with the conclusions of this study.

4.2. GENERALIZED CORRELATION

Correlation, in its most general form, can be interpreted as the relation between one region of phase-space with another, the two regions and their relation (most often taken to be, but not limited to, *linear*) being defined based upon certain rules when viewed from another fixed region of observation. This can be expressed as the relation between $\mathscr{R}_1(\mathscr{S}_1,\mathscr{T}_1)$ and $\mathscr{R}_2(\mathscr{S}_2,\mathscr{T}_2)$ as viewed from $\mathscr{R}_o(\mathscr{S}_o,\mathscr{T}_o)$, as illustrated in figure 4.1. Here $\mathscr{S}$ denotes a bounded region in phase-space (which could, for instance, be the velocity or momentum when considering fluid flow, or could comprise other phase-space variables) and $\mathscr{T}$ denotes a set of time slices in the entire world-line of the system's evolution

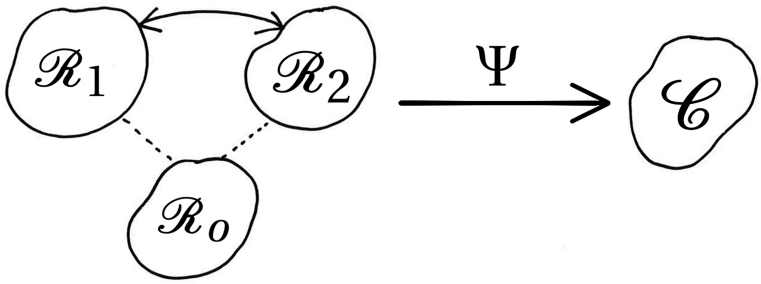

Figure 4.1: Correlation between generalized regions $\mathscr{R}_1$ and $\mathscr{R}_2$ as observed from $\mathscr{R}_o$ (where each region is defined by a surface $\mathscr{S}$ in phase-space over individual time-sets $\mathscr{T}$). Using a function Ψ, these regions are mapped onto a correlation space producing a region shown here as $\mathscr{C}$.

(which in most simple cases is a single instance of time for each region, as used in the usual two-time correlation). Based upon a set of rules given by any function Ψ, defined over $\mathscr{S}_1, \mathscr{S}_2, \mathscr{S}_o, \mathscr{T}_1, \mathscr{T}_2, \mathscr{T}_o$; the phase-space can be mapped to a correlation space $\mathscr{C}$, with appropriate dimensions, based upon the definition of Ψ.

The usual two-point correlation tensor defined for turbulent flows can be seen as a simplification of this generalized definition. We first explain this via analogy, and then re-define the two-point correlation at a higher level, to contain more information, starting with its usual definition, which is given as

$$\mathscr{R}_{ij}(\mathbf{r},t) = \left\langle u_i(\mathbf{x},t)\, u_j(\mathbf{x}+\mathbf{r},t) \right\rangle \tag{4.1}$$

where $\mathscr{R}_{ij}$ is an instantaneous measure of the spatial correlation between velocity components, and $\langle\cdot\rangle$ denotes ensemble averaging. This is done by sampling $\mathscr{R}_{ij}$, at different positions $\mathbf{x}$ and times t, for different values of the spatial separation $\mathbf{r}$. For homogeneous, isotropic turbulence, ensemble averaging is equivalent to spatial averaging, and this procedure gives an average measure of the correlation as a function of the radial distance $r = |\mathbf{r}|$ alone, regardless of the orientation of the $\mathbf{r}$ vector. As the choice of $\mathbf{r}$ itself is arbitrary and spans all directions of space, the velocity components u_i are considered along three orthogonal directions which can be given as $\mathbf{e}_1 \parallel \mathbf{r}$, $\mathbf{e}_2 \perp \mathbf{r}$ and $\mathbf{e}_3 \perp (\mathbf{r}, \mathbf{e}_2)$. This yields the three correlation functions $f(r)$ (longitudinal), $g_1(r)$ and $g_2(r)$ (transverse) respectively, which can be integrated over r to get integral lengths, after normalizing $\mathscr{R}_{ij}(\mathbf{r},t)$ with $\left\langle u_i(\mathbf{x},t)\, u_j(\mathbf{x},t) \right\rangle$.

Now, first, in comparison to the general correlation defined earlier, each instantiation of the correlation $\mathscr{R}_{ij}$ is defined between two points separated by $\mathbf{r}$, hence the regions $\mathscr{S}$ are reduced to points. Secondly, the point of observation $\mathscr{S}_o$ coincides with the first region $\mathscr{S}_1$, and it is related to the second region (i.e. also a point) $\mathscr{S}_2$, which is separated from $\mathscr{S}_1$ by $\mathbf{r}$. This is done at time t, hence the regions are also defined at the same time instance and the time-set $\mathscr{T}$ also reduces to a single instant. The function Ψ is defined over the velocity phase-space (u_i, u_j, u_k) as the product $u_i(\mathbf{x},t)\, u_j(\mathbf{x}+\mathbf{r},t)$, hence, it produces a tensor with 9 components. Note that if the velocities u_i and u_j are further considered at different times, one would arrive at the two-point two-time correlation (and $\mathscr{T}$ would be different time instances).

To make $\mathscr{R}_{ij}$ more general, instead of employing the ensemble or spatial averaging

mentioned above, an individual correlation function can be calculated at each point $\mathbf{x}$. Further, instead of looking at spatial separation r alone (i.e. averaging $\mathscr{R}_{ij}(\mathbf{r})$ over different realizations of $\mathbf{r}$), it can be defined as a function of the direction while looking around from a point. In 3D space, this direction can be specified by two angles (and with only one angle in 2D) i.e. the azimuthal angle α and an elevation angle β, which gives the direction vector $\mathbf{r}_{\alpha\beta}$ (i.e. a vector $\mathbf{r}$ which points along the direction specified by α and β, looking around from a point $\mathbf{x}$). Hence, the more generalized form of the correlation tensor can be written as $\mathscr{R}_{ij}(\mathbf{x},\mathbf{r}_{\alpha\beta},t)$, which is a function of seven scalar variables, namely, x, y, z, t, r, α and β, where x, y and z are the Cartesian components of $\mathbf{x}$ and r is the length of $\mathbf{r}_{\alpha\beta}$. It can be expanded to the matrix form, omitting time dependence t, to yield

$$\mathscr{R}_{ij}(\mathbf{x},\mathbf{r}_{\alpha\beta}) = \begin{bmatrix} u_i(\mathbf{x})u_i(\mathbf{x}+\mathbf{r}_{\alpha\beta}) & u_i(\mathbf{x})u_j(\mathbf{x}+\mathbf{r}_{\alpha\beta}) & u_i(\mathbf{x})u_k(\mathbf{x}+\mathbf{r}_{\alpha\beta}) \\ u_j(\mathbf{x})u_i(\mathbf{x}+\mathbf{r}_{\alpha\beta}) & u_j(\mathbf{x})u_j(\mathbf{x}+\mathbf{r}_{\alpha\beta}) & u_j(\mathbf{x})u_k(\mathbf{x}+\mathbf{r}_{\alpha\beta}) \\ u_k(\mathbf{x})u_i(\mathbf{x}+\mathbf{r}_{\alpha\beta}) & u_k(\mathbf{x})u_j(\mathbf{x}+\mathbf{r}_{\alpha\beta}) & u_k(\mathbf{x})u_k(\mathbf{x}+\mathbf{r}_{\alpha\beta}) \end{bmatrix} \tag{4.2}$$

This contains a lot of information, which needs to be reduced for practical reasons. So, instead of considering the entire $\mathscr{R}$ matrix, we work with one of its invariants, the trace, which is written as

$$\mathrm{tr}\left(\mathscr{R}_{ij}(\mathbf{x},\mathbf{r}_{\alpha\beta})\right) = u_i(\mathbf{x})u_i(\mathbf{x}+\mathbf{r}_{\alpha\beta}) + u_j(\mathbf{x})u_j(\mathbf{x}+\mathbf{r}_{\alpha\beta}) + u_k(\mathbf{x})u_k(\mathbf{x}+\mathbf{r}_{\alpha\beta}) \tag{4.3}$$

This is also the dot product between the velocities at points $\mathbf{x}$ and $\mathbf{x}+\mathbf{r}_{\alpha\beta}$, if we retain a fixed i, j, k basis, independent of the vector $\mathbf{r}_{\alpha\beta}$

$$\mathrm{tr}\left(\mathscr{R}_{ij}(\mathbf{x},\mathbf{r}_{\alpha\beta})\right) = \mathbf{u}(\mathbf{x})\cdot\mathbf{u}(\mathbf{x}+\mathbf{r}_{\alpha\beta}) \tag{4.4}$$

A further reduction can be performed by integrating this quantity along directions specified by $\mathbf{r}_{\alpha\beta}$ to associate an integral length $L_{\alpha\beta}(\Lambda)$ along each direction as

$$L_{\alpha\beta}(\mathbf{x},\Lambda) = \int_0^\Lambda \mathbf{u}(\mathbf{x})\cdot\mathbf{u}(\mathbf{x}+\mathbf{r}_{\alpha\beta})\mathrm{d}\mathbf{r} \tag{4.5}$$

The generalized correlation is hence reduced to a two-dimensional manifold around each spatial location $\mathbf{x}$, as illustrated in Fig. 4.2, the shape of which is a function of the integration length Λ. The size of this surface is a measure of the extent of correlation, or *coherence*, across the central point in every direction around it over a distance Λ.

These manifolds can be calculated for any velocity field, by binning the angles α and β into discrete increments. However, given that we shall utilize numerical datasets, the resolution of these angles will depend significantly upon the resolution of the data, where high resolution simulations will be required to accurately describe even a smaller subset of angles. The complexity of calculating this for the entire velocity field over a domain of N^3 will be N^6 (i.e. roughly N^3 dot products for each point, for each value of Λ). For further simplicity, and with the view to identify structures in the flow, we instead consider $L_{\alpha\beta}(\mathbf{x},\Lambda)$ along three orthogonal i, j, k axes (where i, j, k themselves are arbitrary, but orthonormal, bases), to reduce the manifold $L_{\alpha\beta}(\mathbf{x},\Lambda)$ to a *pseudo*-vector

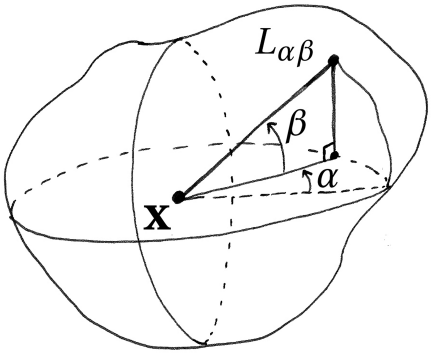

Figure 4.2: A correlation surface around point **x**, defined by a length $L_{\alpha\beta}$ found by integrating $\mathscr{R}_{ij}(\mathbf{x}, \mathbf{r}_{\alpha\beta})$ upto distance Λ along a direction specified by the angles α (azimuth) and β (elevation).

$\mathbf{L}(\mathbf{x}, \Lambda)$, which can be summarized as

$$\mathbf{L}(\mathbf{x},\Lambda) = \begin{bmatrix} L_x(\mathbf{x},\Lambda) \\ L_y(\mathbf{x},\Lambda) \\ L_z(\mathbf{x},\Lambda) \end{bmatrix}, \quad \text{where} \quad L_i(\mathbf{x},\Lambda) = \int_{-\Lambda}^{\Lambda} \mathbf{u}(\mathbf{x}) \cdot \mathbf{u}(\mathbf{x}+\mathbf{r}_i)\mathrm{d}r \tag{4.6}$$

where $i \in \{x, y, z\}$ varies along the three spatial directions. This quantity is a pseudo-vector, since it does not change sign if the coordinate axes is reversed. This follows naturally from the fact that the original quantity $L_{\alpha\beta}(\mathbf{x}, \Lambda)$ was a function of the direction, as well as the integration length, whereas **L** only depends on the limits of integration along a particular axis. This correlation can be expected to yield large values when (i) the local flow streamlines are *parallel* to each other, i.e. well-aligned (such that $\mathbf{u}(\mathbf{x})$ and $\mathbf{u}(\mathbf{x}+\mathbf{r}_i)$ are similar) and (ii) when the local magnitude of the field is high. This above definition of **L** does not include an implicit normalization which, for instance, could be achieved by dividing $L_i(\mathbf{x}, \Lambda)$ by the integral of the kinetic energy along the i direction, within the limits $-\Lambda < x_i < \Lambda$. The current definition is expected to identify regions of the flow which contain both structural organization (in the manner of parallel streamlines), and a large field magnitude. Normalizing the correlation can allow identifying regions with structural organization alone, while disregarding the field magnitude. Different forms of the correlation can hence be defined, to educe different aspects of structural organization. For the present study, we do not normalize the correlation definitions. A slightly different way of constructing the **L** correlation can be

$$\mathbf{L^s}(\mathbf{x},\Lambda) = \begin{bmatrix} L^s_x(\mathbf{x},\Lambda) \\ L^s_y(\mathbf{x},\Lambda) \\ L^s_z(\mathbf{x},\Lambda) \end{bmatrix}, \quad \text{where} \quad L^s_i(\mathbf{x},\Lambda) = \int_{0}^{\Lambda} \mathbf{u}(\mathbf{x}-\mathbf{r}_i) \cdot \mathbf{u}(\mathbf{x}+\mathbf{r}_i)\mathrm{d}r \tag{4.7}$$

with the main difference being that in the definition of $\mathbf{L^s}$, the correlation function along an axis is constructed by the dot product between velocity pairs equidistant from **x**, symmetrically, along a given axis (hence the notation $\mathbf{L^s}$ for **L**-symmetric). This correlation is also expected to yield high values when the flow streamlines are parallel (or

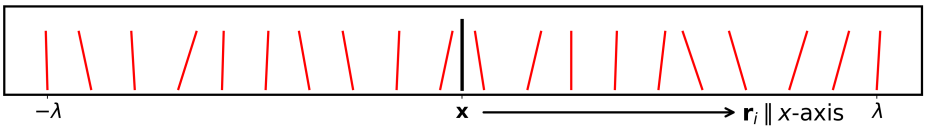

(a) In the **L** correlation, the velocity at point **x** is correlated to the velocities between points $-\Lambda < \mathbf{r}_i < \Lambda$.

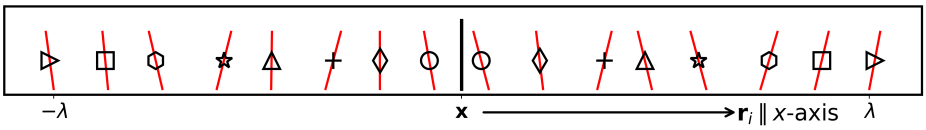

(b) In the $\mathbf{L^s}$ correlations, velocity pairs equidistant from the point **x** are correlated, between $0 < |\mathbf{r}_i| < \Lambda$. These pairs are marked by the same symbol.

Figure 4.3: Schematic of the **L** and $\mathbf{L^s}$ correlations shown along the x direction.

anti-parallel) in the $\Lambda-$neighbourhood, although, this definition can be expected to be more sensitive to the symmetries in the field. These two definitions are illustrated in figure 4.3.

The idea above can be applied to any vector field. In particular, correlation pseudo-vectors $\mathbf{G}(\mathbf{x},\Lambda)$ and $\mathbf{G^s}(\mathbf{x},\Lambda)$ can be calculated for the vorticity field, which are then given as

$$\mathbf{G}(\mathbf{x},\Lambda) \quad \text{where} \quad G_i(\mathbf{x},\Lambda) = \int_{-\Lambda}^{\Lambda} \boldsymbol{\omega}(\mathbf{x})\cdot\boldsymbol{\omega}(\mathbf{x}+\mathbf{r}_i)\mathrm{d}r \tag{4.8}$$

and

$$\mathbf{G^s}(\mathbf{x},\Lambda) \quad \text{where} \quad G^s_i(\mathbf{x},\Lambda) = \int_{0}^{\Lambda} \boldsymbol{\omega}(\mathbf{x}-\mathbf{r}_i)\cdot\boldsymbol{\omega}(\mathbf{x}+\mathbf{r}_i)\mathrm{d}r \tag{4.9}$$

The **G** correlation is expected to yield high values in regions where (i) the *vorticity streamlines* are parallel to each other (well-aligned) and (ii) where the value of the vorticity (or enstrophy, which is ω^2) is high. These regions of high vorticity magnitude are related to the smaller scales of turbulence, and correspond to the long intermittency tails of the vorticity distribution (i.e. $\omega \gg \omega'$ where $\omega' = \langle\omega^2\rangle^{1/2}$). The $\mathbf{G^s}$ correlation is the vorticity field equivalent of $\mathbf{L^s}$, and is expected to be more sensitive to the symmetries in the vorticity field. It has been shown that strong vorticity forms clusters of the size of the inertial range [21]. These structures are highly intermittent and significantly influence particle dispersion and scalar mixing due to the high acceleration generated around them [25, 26]. Although, it is not usually emphasized that these structures are a *consequence* of the turbulence dynamics, and are not responsible for driving the turbulence dynamics, which is governed by the larger scales [2].

The correlations defined so far consider the velocity and vorticity fields separately, however, other correlations can be defined which use both these fields, exploiting the relation between the velocity and vorticity. By definition, the vorticity $\boldsymbol{\omega}$ is defined as $\boldsymbol{\omega} = \nabla\times\mathbf{u}$. The velocity field, in turn, can be reconstructed from the vorticity field using

the Biot-Savart law. This serves as an important tool to identify as well as disentangle structures, and is briefly reviewed below.

4.3. BIOT-SAVART RECONSTRUCTION AND ASSOCIATED CORRELATIONS

We start with the Helmholtz decomposition which states that a twice continuously differentiable vector field, which for an infinite region is regular at infinity, can be expressed as the sum of an irrotational and a solenoidal vector field. Applied to the velocity field $\mathbf{u}$, this can be written as

$$\mathbf{u} = \nabla\phi + \nabla \times \psi \tag{4.10}$$

The scalar (ϕ) and vector (ψ) potentials relate to the divergence ($\nabla\cdot\mathbf{u}$) and curl ($\boldsymbol{\omega} = \nabla\times\mathbf{u}$), satisfying the conditions

$$\nabla^2\phi = \nabla\cdot\mathbf{u} \tag{4.11}$$

$$\nabla^2\psi = -\boldsymbol{\omega} \tag{4.12}$$

Eq. 4.10 can be written as the generalized Biot-Savart formula (for details refer to, for example, [27]), by writing out the form of the scalar and vector potentials as

$$\nabla\phi = \frac{1}{4\pi}\int_V \frac{(\nabla\cdot\mathbf{u})\,\mathbf{r}}{|\mathbf{r}|^3}dV' - \frac{1}{4\pi}\int_S \frac{(\mathbf{n}\cdot\mathbf{u})\,\mathbf{r}}{|\mathbf{r}|^3}dS' \tag{4.13}$$

$$\nabla\times\psi = \frac{1}{4\pi}\int_V \frac{\boldsymbol{\omega}\times\mathbf{r}}{|\mathbf{r}^3|}dV' - \frac{1}{4\pi}\int_S \frac{(\mathbf{n}\times\mathbf{u})\times\mathbf{r}}{|\mathbf{r}|^3}dS' \tag{4.14}$$

where $\mathbf{r}$ is the position vector from a particular point in the volume V (or the surface S), to the point where the Biot-Savart integral is being evaluated. In both eq. 4.13 and eq. 4.14, the first term represents the contribution from the potential in the volume V (i.e. the *near-field* contribution), while the second term represents a surface integral over the bounding region S (which includes the *far-field* contributions, from the surface up to infinity). The surface integrals, for large V (or periodic domains) converge to a constant: this constant can be made equal to zero by adding a constant to the velocity field; i.e. by choosing the "appropriate frame of reference" (the frame of reference eliminates the contribution from the infinity-field). Further, the first term in eq. 4.13 is also zero when considering incompressible flows (as we do in this study), since $\nabla\cdot\mathbf{u} = 0$ due to the continuity condition. This reduces the generalized Biot-Savart relation to that valid for incompressible flows, which is given simply as

$$\mathbf{u}(\mathbf{x}) = \frac{1}{4\pi}\int_V \frac{\boldsymbol{\omega}\times\mathbf{r}}{|\mathbf{r}|^3}dV' \tag{4.15}$$

The above integral allows a way to disentangle flow structures by isolating the contributions from different vorticity regions to a local velocity structure. For instance, *local* and *non-local* vorticity contributions can be separated using this paradigm, or the vorticity field can be conditionally sampled to identify the contribution of different vorticity levels in generating a local structure.

Note that even though far-field vorticity contributions (the surface integrals in eq. 4.13 and eq. 4.14) may be absent, the volumetric region can also be split into an isolated

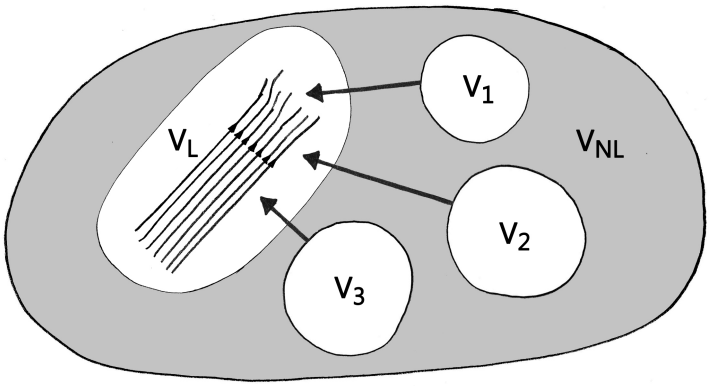

Figure 4.4: Schematic of a Biot-Savart reconstruction of the velocity field in a region V_L, from three isolated non-local regions V_1, V_2 and V_3. When the region V_L has negligible vorticity of its own, the flow generated the region by the non-local vorticity contributions is a potential flow which can be given by the gradient of a potential Ψ.

local region (V_L), surrounded by the *non-local* region (V_{NL}) which essentially behaves as a *far-field*. This leads to the consequence that if the local region has negligible vorticity within V_L, while the non-local region V_{NL} *induces* a flow within V_L, then it must be a *potential flow*. This means that the local flow in V_L can be described by the gradient of a harmonic function Ψ as $\mathbf{u}_L = -\nabla\Psi$, while $\nabla\cdot\nabla\Psi = 0$. The non-local contributions from V_{NL} *cannot* generate vorticity within the local region V_L (as illustrated in figure 4.4). A last feature to note regarding the Biot-Savart law is the rapid decay (of $1/r^2$ over a distance r) of the vorticity contribution, which means that a small, isolated vorticity region cannot extend its influence over a large distance beyond its immediate neighbourhood.

4.3.1. CORRELATIONS RELATED TO THE BIOT-SAVART LAW

Ideas associated with the Biot-Savart law can be used to define different correlations in order to identify, extract and disentangle structures associated with the relation between the velocity and vorticity fields. In regions of strong vorticity associated with swirling-flow, the Lamb vector i.e. $\boldsymbol{\omega}\times\mathbf{u}$ yields high values. Although, this is again a *local* quantity. We propose a correlation which utilizes this idea and extends it to a *non-local* form, where the vorticity at a point $\mathbf{x}$, is correlated with the velocity at point $\mathbf{x}+\mathbf{r}_i$, leading to a pseudo-vector $\mathbf{H}(\mathbf{x},\Lambda)$ which can be written as follows

$$\mathbf{H}(\mathbf{x},\Lambda) \quad \text{where} \quad H_i(\mathbf{x},\Lambda) = \int_{-\Lambda}^{\Lambda} \left(\frac{\boldsymbol{\omega}(\mathbf{x})\times\mathbf{r}_i}{|\mathbf{r}_i|} \right) \cdot \mathbf{u}(\mathbf{x}+\mathbf{r}_i)\mathrm{d}r \tag{4.16}$$

The above correlation has a flavour of the Biot-Savart law, and it allows correlating the contribution of the *local* vorticity to its neighbouring velocity field with the *global* vorticity contribution to the same, since the velocity $\mathbf{u}(\mathbf{x}+\mathbf{r}_i)$ can be seen as an integral result of the global vorticity field. Note that with the above definition, $\mathbf{H}(\mathbf{x},\Lambda)$ will tend to be *orthogonal* to $\boldsymbol{\omega}$, as H_x (i.e. H along the $x-$direction) will have a high magnitude when the vorticity is large and orthogonal to the $x-$direction.

Since the vorticity at a point generates flow, in a Biot-Savart sense, in the plane *orthogonal* to the vorticity vector, a more natural correlation definition is proposed which takes into account this fact. This is done by correlating the vorticity along a particular direction, say x, to the flow in the orthogonal plane, i.e. yz. At each point, a velocity field is generated using the $x-$vorticity (i.e. ω_x) in the orthogonal $yz-$plane, along perimeters of circles of radius $0 < r \leq \Lambda$. These velocity vectors are calculated with a simplification of the Biot-Savart construction, i.e. by taking the cross product of vorticity with unit vectors in the orthogonal plane ($\mathbf{r}_{yz}/|\mathbf{r}_{yz}|$) as done for the previous $\mathbf{H}$ correlation. This is illustrated in figure 4.5 where the ω_x vorticity component generates the velocity field shown in blue (solid lines), while the *real* velocity field generated from the global vorticity contributions is shown in red (dashed lines). To correlate these two velocity fields, only the *direction* of the velocity vectors is important (while their magnitudes only change the amplitude of the final correlation). The $\mathbf{H^p}$ correlation (for $\mathbf{H}-$*planar*) is calculated as the integral of the dot product between the vorticity generated velocity vectors (blue) and the real velocity (red), over the lengths $\mathscr{L}(r)$ of rings of radius $0 < r < \Lambda$. Since the length of the rings increases proportionally with the radius r, the integral over each ring is further divided by r (i.e. $|\mathbf{r}_{yz}|$) to give an average correlation at a distance r, though other definitions can be used without loss of generality. This correlation is given by

$$\mathbf{H^p}(\mathbf{x},\Lambda) \quad \text{where } H_x^p(\mathbf{x},\Lambda) = \int_0^\Lambda \frac{1}{|\mathbf{r}_{yz}|} \oint_{\mathscr{L}(r)} \left(\frac{\omega_x(\mathbf{x}) \times \mathbf{r}_{yz}}{|\mathbf{r}_{yz}|} \right) \cdot \mathbf{u}(\mathbf{x}+\mathbf{r}_{yz}) \, \mathrm{d}l \, \mathrm{d}r \tag{4.17}$$

while H_y^p and H_z^p are similar. Evidently, this correlation is more computationally expensive to calculate, as three planar regions need to be considered for each point in space. This requirement can be relaxed by sampling the rings $0 < r \leq \Lambda$ with a chosen frequency, i.e. using every n-th ring as $r \in \{n, 2n, 3n, \ldots\}$.

4.4. CORRELATIONS APPLIED TO SIMPLIFIED CANONICAL FLOWS

4.4.1. ONE-DIMENSIONAL FIELDS

We begin by testing these correlations on simplified flows, starting with Oseen vortices, which can be defined by a tangential velocity field and a vorticity field, given as

$$u_\theta(r) = \frac{\Gamma}{2\pi r}\left[1 - \exp\left(-\frac{r^2}{4\nu t}\right)\right] \tag{4.18}$$

$$\omega_z(r) = \frac{\Gamma}{4\pi\nu t}\exp\left(-\frac{r^2}{4\nu t}\right) \tag{4.19}$$

where r is the radial distance from the vortex core, Γ is the circulation, ν is the fluid viscosity, t is a certain time instance. The Oseen vortex comprises a small core region in solid body rotation, within which the velocity increases radially as $u_\theta \propto r$ to its maximum value. Beyond this is a potential flow region (where ω_z is nearly zero) and $u_\theta \propto 1/r$. Wen add a noise ψ to the velocity field given by eq. 4.18, this additional noise term is superposed on the velocity field to generate a "structure immersed in noise". The vortex has a certain 'reach', which depends on the amplitude of ψ, and is defined as the distance beyond which $\psi > u_\theta$. The vorticity of the Oseen vortex is calculated in Cartesian coordinates as $\omega_z = \nabla \times \mathbf{u} = \partial v/\partial x - \partial u/\partial y$, due to the addition of the noise to the velocity field.

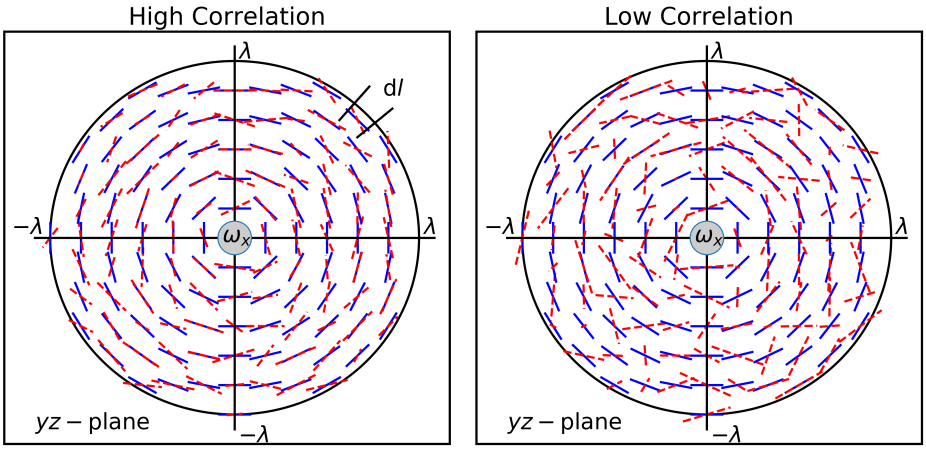

Figure 4.5: A schematic of the $\mathbf{H^p}$ correlation. The ω_x vorticity is used to generate a velocity field in the $yz-$plane (shown in solid-blue lines), which is correlated with the real velocity field (dashed-red lines) within a circular region of radius Λ. The correlation is integrated around rings ($\mathrm{d}l$ elements) and then along the radial direction ($\mathrm{d}r$). The correlation will be strong when the local vorticity dominates in producing the velocity field in its neighbourhood (left), and low when the local velocity field is not associated with the central vorticity (right).

We generate two Oseen vortices, with centers separated by a distance greater than the typical reach of either vortex and larger than the size of the vortex sub-structure. We further consider only the one-dimensional velocity field along the line connecting the centers of the two vortices. This field, hence, consists of a large periodic structure, with two smaller structures (which are two counter-rotating Oseen vortices). This creates a pattern of symmetries and anti-symmetries in the velocity and vorticity fields.

The parameters used to generate the velocity field, which is assumed to be periodic over a length of $N_x = 500$, are $\Gamma = 10$, $\nu = 2.0$ and $t = 2.0$; all quantities being presented in arbitrary units. The vortices are placed with their centres at 150 and 350, with a core region extending over 5 units on either side of the centres. Uniformly distributed random noise ($-1 < \psi < 1$), scaled to an amplitude of 1% of the maximum velocity magnitude has also been added to the velocity, which makes the velocity of the vortices in the potential flow region reduce to within 2.5% of the maximum value within 100 units outside of the 'larger structure'. The region in between the two 'sub-structures' has a velocity which is $\sim 10\%$ of the maximum value, due to the interaction between the two vortices, which can be seen in the top panel of figure 4.6. The middle and bottom panels of figure 4.6 show $\mathbf{L}$ and $\mathbf{L^s}$ respectively (which here have only a $x-$component), with the integration length spanning the entire length of the velocity field, i.e. $\Lambda = N_x/2$. A few features of the correlation profiles point at the nature of the current definitions, as well as the importance of the choice of Λ. First, $\mathbf{L}$ is found to have a shape similar to the function itself, with a sign change. If we consider the definition of $\mathbf{L}$, it is the correlation (here "product") between the value of the function at a point and its integral over a length, hence if either of the two is zero, the correlation becomes zero. Therefore, the correlation will

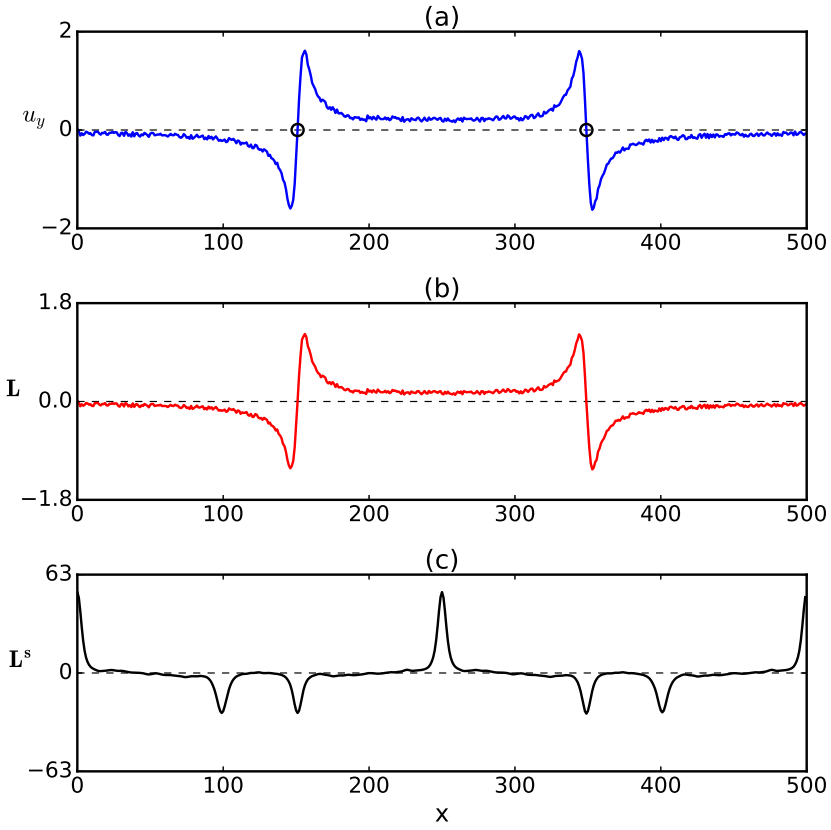

Figure 4.6: (a) A one-dimensional velocity field comprising a larger structure composed of two smaller sub-structures (i.e. two Oseen vortices, with their centers marked with circles). Correlations calculated for this field are shown in panels (b) **L** and (c) $\mathbf{L}^{\mathbf{s}}$, obtained by integrating over $\Lambda = N_x/2$, which spans the entire length of the signal.

have significant or large values, where the function itself has significant or large values, and the structure of the function (i.e. its symmetries and/or anti-symmetries) does not make its integral small. When the function is the sum of several "basis functions" (in this case two "pure" Oseen vortices and a "noise function"), the correlation also involves the "product" between a "basis function" and the integral of another "basis function", so, even if the structure of each of the "basis functions" has a small integral (i.e. if **L** of each basis function is small), **L** of the total function is not necessarily small. In the particular case presented here, the integral of the "pure" function is finite due to the interaction between the velocity fields of the two vortices, forming the larger structure, along with the integral of the "noise", which is itself a "noise". Hence, the **L** correlation has the same

shape as the velocity field itself. Mathematically, this can be essentially seen as

$$\begin{aligned}\mathbf{L} &= \int_{-\Lambda}^{\Lambda} [u(\mathbf{x}) + \psi(\mathbf{x})] \cdot [u(\mathbf{x}+\mathbf{r}_i) + \psi(\mathbf{x}+\mathbf{r}_i)] d\mathbf{r}_i \\ &= [u(\mathbf{x}) + \psi(\mathbf{x})] \cdot \int_{-\Lambda}^{\Lambda} [u(\mathbf{x}+\mathbf{r}_i) + \psi(\mathbf{x}+\mathbf{r}_i)] d\mathbf{r}_i \\ &= [u(\mathbf{x}) + \psi(\mathbf{x})] \cdot \left(\int_{-\Lambda}^{\Lambda} u(\mathbf{x}+\mathbf{r}_i) d\mathbf{r}_i + \int_{-\Lambda}^{\Lambda} \psi(\mathbf{x}+\mathbf{r}_i) d\mathbf{r}_i \right)\end{aligned} \tag{4.20}$$

where ψ is the additional "noise" term. If either $\int u$ or $\int \psi$ are non-zero, $\mathbf{L}$ will retain a similar form as u. Interestingly, even for a velocity profile which leads to $\int u = 0$ (i.e. the integral of the "pure" basis function), the additional noise term breaks the overall symmetries and anti-symmetries, such that $\mathbf{L}$ becomes non-zero, and shape of the velocity field u can be extracted. If the noise is removed from the velocity field, and the vortices are placed sufficiently far from each other such that $\int u = 0$, $\mathbf{L}$, indeed, goes to zero for $\Lambda = N_x/2$ (not shown here).

$\mathbf{L^s}$, in figure 4.6(c), shows different features, starting with a central peak around $x = 250$, which is exactly between the two counter-rotating vortices. Although the velocity around this position is small, $\mathbf{L^s}$ attains a large value since the velocity field is essentially mirrored around this point, hence being perfectly correlated (with only the noise values being different between the mirrored halves). At the core of the two vortices ($x = 150$ and $x = 250$), $\mathbf{L^s}$ shows a large negative peak, since the velocity field on the left and right of these points is anti-correlated up to the reach of each vortex. The part of $\mathbf{L^s}$ in the region outside of the larger structure (i.e. approximately $x < 100$ and $x > 400$), is a repetition of the $\mathbf{L^s}$ profile in the center (i.e. $150 < x < 350$) due to the periodicity of the velocity field and the integration length spanning the entire signal length ($\Lambda = N_x/2$).

Figure 4.7 shows the correlations for a similar velocity field, now integrated over a length of $\Lambda = 35$, which corresponds approximately to the size of the sub-structures (i.e. the individual vortices). This is because within a distance of 35 units from the center of each vortex, the velocity reduces to roughly 10% of its maximum value (note that a slightly lower or higher Λ does not change the results significantly). The $\mathbf{L}$ and $\mathbf{L^s}$ profiles show a few similarities and differences. First, the general shape of the two correlations is similar. While $\mathbf{L}$ goes to zero at the vortex cores, where the velocity is close to zero, $\mathbf{L^s}$ yields strong negative peaks because the velocity is strongly anti-correlated across the core region. In the potential flow regions of the two vortices, both $\mathbf{L}$ and $\mathbf{L^s}$ yield positive correlation values, reflecting that the flow vectors are well aligned in these regions, in the manner of parallel streamlines. $\mathbf{L^s}$ does not identify the 'larger structure' in this case, since the larger structure has a lengthscale larger than the integration length of the correlation. This shows the important of the choice of Λ in identifying larger or smaller symmetries and asymmetries of the vector fields. When these correlations are applied to the vector fields of turbulence in a later section, we shall discuss the choice of Λ at length to ascertain its influence on identifying coherent regions.

Note that it is not only the length of integration Λ, but also the lower and upper limits of integration which determine the symmetries and structures being identified. For instance, eq. 4.7 can be changed to instead find non-local structures between lengths $\Lambda_1 < \mathbf{r}_i < \Lambda_2$, while looking around from point $\mathbf{x}$, as follows

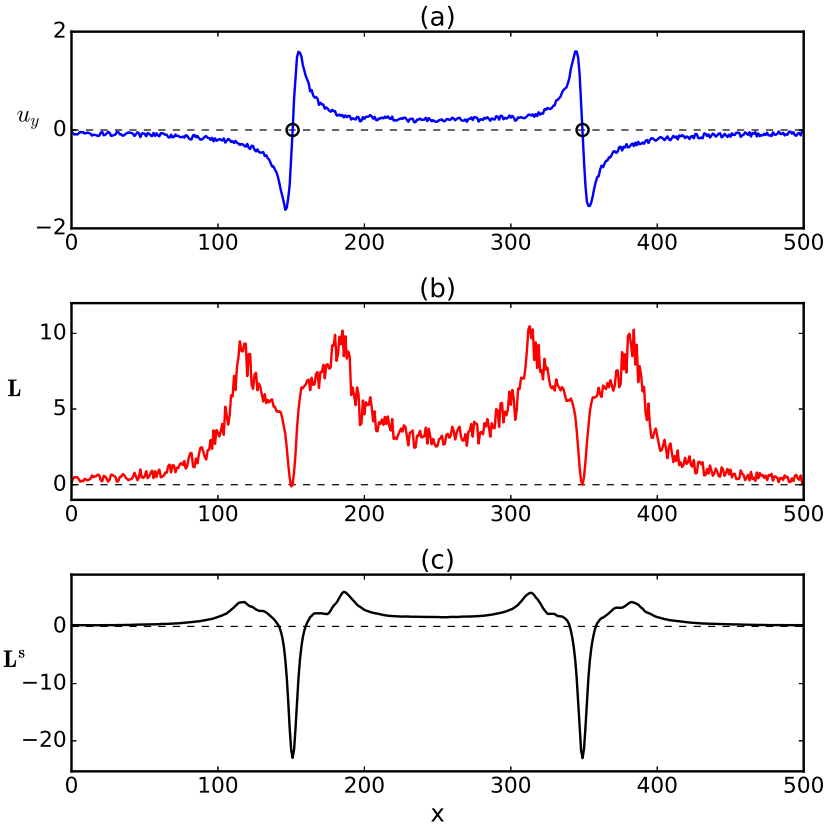

Figure 4.7: Correlations (b) **L** and (c) $\mathbf{L^s}$ calculated for an integration length of $\Lambda = 35$, which spans the approximate size of the individual 'sub-structures', i.e the two counter-rotating Oseen vortices. Here, **L** and $\mathbf{L^s}$ have a similar shape overall, while $\mathbf{L^s}$ yields strong negative values in the vortex core region across which the flow is strongly anti-correlated. Both the correlations yield positive values in the potential flow regions of the two vortices, showing that the flow vectors in these regions are well aligned.

$$L_i^s(\mathbf{x}, \Lambda_1, \Lambda_2) = \int_{\Lambda_1}^{\Lambda_2} \mathbf{u}(\mathbf{x} - \mathbf{r}_i) \cdot \mathbf{u}(\mathbf{x} + \mathbf{r}_i) \mathrm{d}r \tag{4.21}$$

Recalling the generalized correlation definition, this change in the limits of Λ is essentially defining $\mathscr{S}_1$ and $\mathscr{S}_2$ as finite regions going from $x \in [x_0 + \Lambda_1, x_0 + \Lambda_2]$ and $x \in [x_0 - \Lambda_2, x_0 - \Lambda_1]$ respectively, while the region of observation $\mathscr{S}_o$ is x_0. One example of this is shown in figure 4.8, with $\Lambda_1 = 75$ and $\Lambda_2 = 125$. These integration limits are such that, when $\mathscr{S}_o$ corresponds to the middle of the larger structure in the velocity field (i.e. at $x = 250$), Λ_1 and Λ_2 span across most of the vortex regions. The $\mathbf{L^s}$ profile, consequently, shows a strong peak in between the two vortices, resulting from the larger structure comprising the two counter-rotating vortices. These particular limits of integration

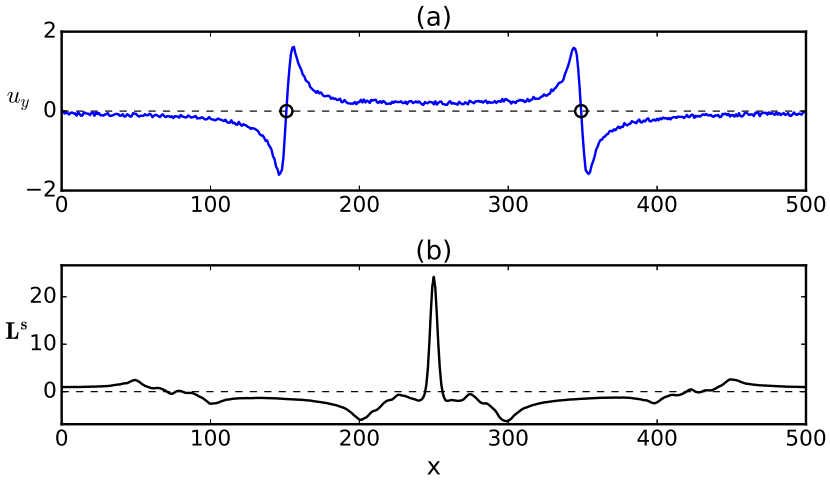

Figure 4.8: $\mathbf{L^s}$ correlation integrated from $\Lambda_1 = 75$ to $\Lambda_2 = 125$ shows how non-local symmetries can be identified by varying the limits of integration.

do not identify any significant larger symmetries, as observed from other x locations.

Figure 4.9 shows correlations $\mathbf{G}$ and $\mathbf{G^s}$, which are the vorticity field equivalents of $\mathbf{L}$ and $\mathbf{L^s}$, integrated over $\Lambda = N_x/2$, to span the entire length of the periodic velocity field. The $\mathbf{G}$ correlation remains mostly zero throughout, with small, noisy fluctuations. This is because, unlike the velocity field, which yields a finite value for $\int u$ when integrated over $\Lambda = N_x/2$ due to the interaction between the two vortices and the non-zero contribution from the integral of the noise term $\int \psi$, $\int \omega$ remains nearly zero since the vorticity is localized at the core of the two vortices, and has the same magnitude but opposite sign, the only contribution here is from the non-zero integral of the noise term which breaks the uniformity of the vorticity field. The $\mathbf{G^s}$ correlation has a very similar behaviour to $\mathbf{L^s}$, yielding a large negative peak at the middle of the larger structure ($x = 250$), since the vorticity field at the core of the two structures is anti-correlated. It also shows smaller, positive peaks at the core of the vortices ($x = 150$ and $x = 250$), where the vorticity vectors are aligned in the same direction. The $\mathbf{G^s}$ profile is also repeated due to the periodicity of the signal and the large integration length, similarly to the $\mathbf{L^s}$ profile in figure 4.6.

Figure 4.10 shows the $\mathbf{G}$ and $\mathbf{G^s}$ correlations for an integration length of $\Lambda = 35$. Again, like the $\mathbf{L}$ and $\mathbf{L^s}$ correlations in figure 4.7, both $\mathbf{G}$ and $\mathbf{G^s}$ show a very similar overall shape. Both yield a sharp positive peak at the core of the vortex regions, where the vorticity is concentrated and well aligned. The $\mathbf{G}$ correlation decays with some noise, in the potential flow regions corresponding to the two vortices. The $\mathbf{G^s}$ correlation, here, gives a sharper and less noisy profile. This is because, at the vortex core, the vorticity values to the left and right are perfectly symmetric (apart from the noise values), which gives a large correlation $\mathbf{G^s}$ value at the vortex core. Slightly moving away from the core in either direction strongly disturbs this symmetry, due to which the amplitude of $\mathbf{G^s}$ decays at a faster rate than $\mathbf{G}$. The $\mathbf{G}$ and $\mathbf{G^s}$ correlations, being fully analogous to $\mathbf{L}$ and $\mathbf{L^s}$, help in identifying high vorticity regions, where the vorticity streamlines are parallel to each

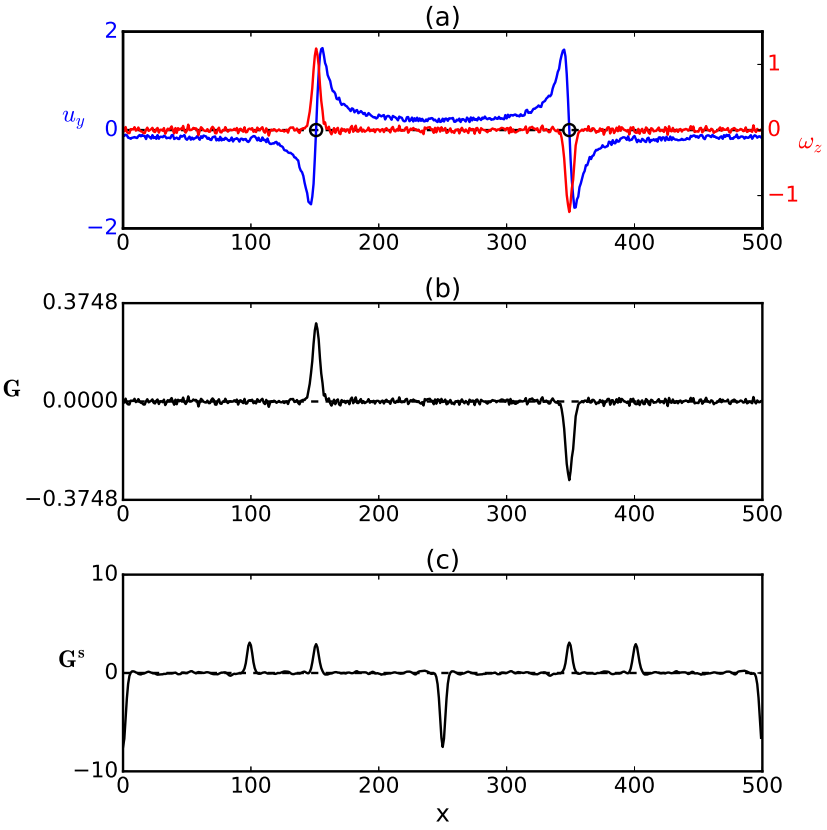

Figure 4.9: **G** and $\mathbf{G}^{\mathbf{s}}$ correlations (integrated up to $\Lambda = N_x/2$) are shown for the Oseen vortex pair. The **G** correlation remains close to zero (since $\int \omega \approx 0$ over the integration length), while $\mathbf{G}^{\mathbf{s}}$ shows a profile similar to $\mathbf{L}^{\mathbf{s}}$ in figure 4.6.

other, albeit the structure sizes are smaller than the velocity field, since vorticity remains concentrated in small spatial regions.

Finally, figure 4.11 shows the **H** correlation for the Oseen vortex pair, integrated over lengths of $\Lambda = N_x/2$ (panel b) and $\Lambda = 35$ (panel c). The form of the **H** correlation is found to be almost insensitive to the choice of Λ, while a higher Λ increases the amplitude of the correlation. This can be understood from the construction of this correlation which, in a Biot-Savart sense, is designed to identify self-induced regions of the velocity field. In this example, **H** yields large, positive values in the core region of the two vortices, since the flow around the vortex core is generated by the vorticity at the core. The independence of the choice of Λ is because the influence of the local vorticity at a point x_0 rapidly decays in space, such that at larger Λ values, the velocity field $\mathbf{u}(x_0 \pm \Lambda)$ does not depend on $\boldsymbol{\omega}(x_0)$. The larger structure in this example is induced by the sum of the two individual vortices, and is hence 'externally generated', which is why **H** remains zero in the middle of the two structures. The results are identical for the $\mathbf{H}^{\mathbf{p}}$ correlation (and

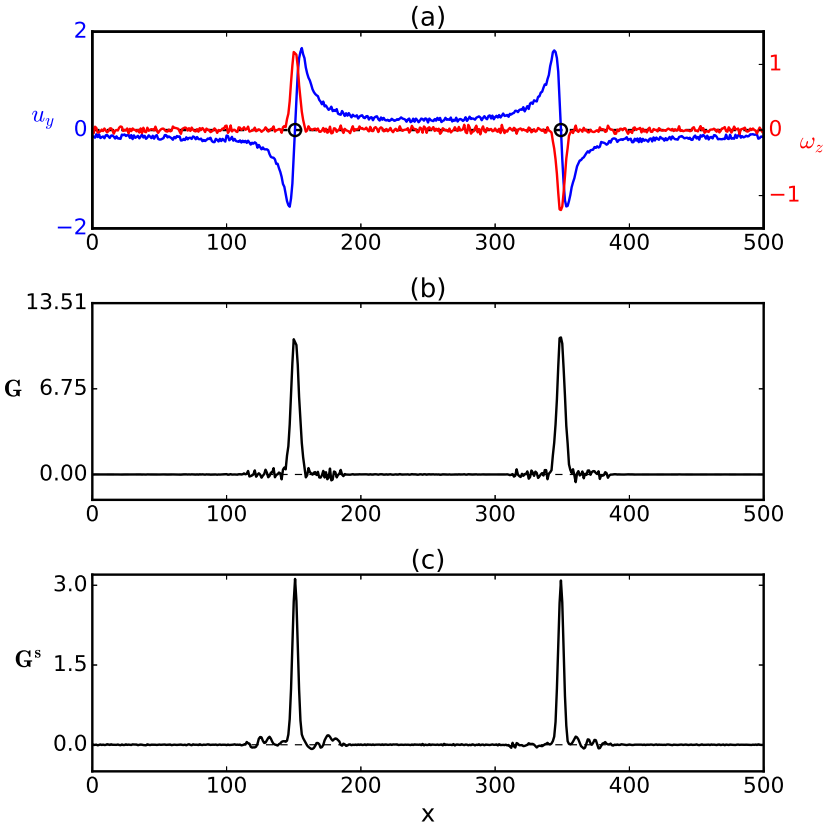

Figure 4.10: **G** and $\mathbf{G}^{\mathbf{s}}$ correlations (integrated up to $\Lambda = 35$) are shown for the Oseen vortices pair. Both correlations are similar and show a strong peak at the vortex cores, while $\mathbf{G}^{\mathbf{s}}$ has decays at a faster rate since it is more dependent on the symmetry of the vorticity field.

have hence not been additionally shown here).

4.4.2. THREE-DIMENSIONAL BURGERS VORTICES

As a final example of the correlations applied to canonical flows, we now consider a three-dimensional velocity field generated by superposing two Burgers vortices, which again generates a 'large-scale' structure comprising two smaller sub-structures. The Burgers vortex is an exact solution of the Navier-Stokes equation, consisting of a radial velocity component along with a tangential velocity, and can be constructed as

$$u_z = \kappa z, \quad u_r = -\frac{\kappa r}{2}, \quad u_\theta = \frac{\Gamma}{2\pi r}\left[1 - \exp\left(-\frac{\kappa r^2}{4\nu}\right)\right] \tag{4.22}$$

where κ represents the rate of strain, Γ the circulation and ν the kinematic viscosity. Here u_z, u_r and u_θ give velocity components in the axial, radial and tangential directions, which are converted from cylindrical to Cartesian coordinates. To isolate the vortex in

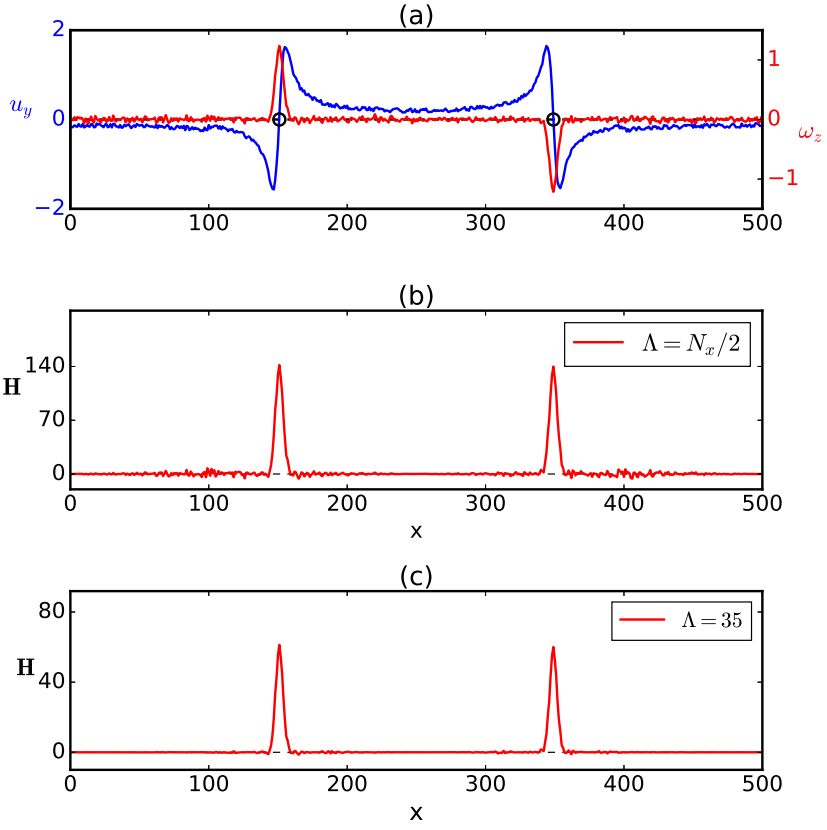

Figure 4.11: H correlation, integrated up to (b) $\Lambda = N_x/2$ and (c) $\Lambda = 35$, is shown for the Oseen vortex pair. The correlation yields strong positive peaks at the vortex cores, and this correlation definition is found to be independent of the choice of Λ (except a change in the magnitude of the correlation).

space, we multiply the velocity fields with a three-dimensional Gaussian function $\mathscr{G}$ to contain the Burgers vortex within a spherical region,

$$\mathscr{G}(x,y,z) = \exp\left[-\left(\frac{x^2+y^2+z^2}{\sigma^2}\right)\right] \tag{4.23}$$

where x, y and z are measured with the origin placed at the center of the vortex. The value of σ is chosen such that it creates a spherical region circumscribing the axial length of the vortex. This suppresses the strain regions generated by each vortex, such that the velocity field comprises primarily of two swirling-flow regions. The swirling-flow of the Burgers vortex resembles the one-dimensional Oseen vortex (as was described in Section 4.4.1), with a core in solid-body rotation where $u_\theta \propto r$, followed by a potential flow region with $u_\theta \propto 1/r$. A low amplitude uniform noise, ψ, is added to the final velocity field, over which the correlations subsequently calculated. Lastly, the vortices are also rotated at arbitrary angles with respect to the three coordinate axes, at angles $(\beta_1, \beta_2, \beta_3)$. This is done to change the orientation of the velocity field symmetries with respect to the orthogonal bases along which the correlations are calculated, to test the applicability of the correlation definitions for arbitrarily aligned structures, as will be encountered in turbulence vector fields.

We generate two vortices, on a grid of 100^3, with $\alpha = 0.1$, $\nu = 0.025$, $\Gamma = 15$ and $\psi = 0.002$ (i.e. $\sim 0.5\%$ of the maximum velocity magnitude), all quantities being presented in arbitrary units. The actual values being used here are not of importance, as we simply intend to generate a velocity field with a Burgers vortex *structure*. The resulting vortex has a core region with solid body rotation up to 5 units (grid cells), and the velocity magnitude in the potential flow region (with swirling motion) decays to approximately 40% and 10% of the maximum velocity magnitude within 15 and 30 grid cells. Both vortices are multiplied with the Gaussian function $\mathscr{G}$ generated with $\sigma = 5$. The vortices are rotated at angles $(0.6, 0.0, 0.25)$ and $(-0.45, 0.0, -0.3)$, measured in radians, around the (x, y, z) axes. These vortices are then superposed by adding their velocity fields, with their centres placed at $(40, 40, 40$ and $(70, 70, 70)$. The resulting velocity field has been shown in figure 4.12. Since the vortices are placed close to each other, their velocity fields begin to entangle and interact. However, the larger structure of the Burgers vortex pair, is distinct from the Oseen vortex pair in Section 4.4.1, and it does not have the same kind of symmetries and anti-symmetries.

Figure 4.13 shows the amplitude of all the correlations, integrated over a length of $\Lambda = 12$ for the Burgers vortex pair (while the results were found to remain qualitatively unchanged for $\Lambda = 15$ and 20, which only causes a change in the magnitude of the correlations). The features of the correlation fields strongly reflect the behaviour of their one-dimensional analogues as was presented for the Oseen vortex pair. First, panels (a) and (b) show the $\mathbf{L}$ and $\mathbf{L^s}$ correlations. The correlation regions are well aligned with the axes of the vortices, and have a size comparable to the extent of the swirling-flow region. The $\mathbf{L}$ correlation goes to zero at the vortex core where the velocity is also zero. The $\mathbf{L^s}$ correlation yields a large correlation value at the vortex core, across which the flow is highly anti-correlated, surrounding which is a thin region of zero correlation, and an outer region of finite correlation corresponding to the potential flow region of the vortex. Both these correlations identify the swirling-flow region where the streamlines are well aligned, and locally parallel to each other. Panels (c) and (d) show the $\mathbf{G}$ and $\mathbf{G^s}$ correlations, both of which yield thin, elongated correlation profiles aligned with the axes

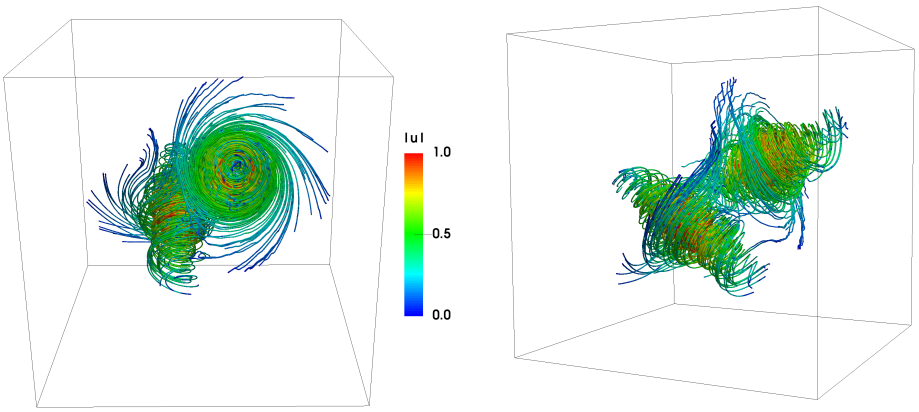

(a) View 1 **(b)** View 2

Figure 4.12: Two arbitrarily aligned Burgers vortices are shown, with isolated swirling-flow regions. The velocity streamlines show that the two vortices begin to 'interact' (where the velocity magnitude has been normalized to between 0 and 1). The edges of the cubes shown here run from $\{x, y, z\} \in [10, 90]$.

of the vortices, while the $\mathbf{G^s}$ correlation is sharper. This again reflects that, at the core of the vortices, the vorticity vectors are well aligned. Panels (e) and (f) show $\mathbf{H}$ and $\mathbf{H^p}$, which also yield strong correlation profiles at the cores of the vortices, aligned with the vortex axes. This is because the swirling velocity field is associated with the vorticity at the vortex core region.

All these features of the different correlations coincide with their one-dimensional analogues, showing that the correlation definitions are adept at identifying typical velocity and vorticity field patterns, also when arbitrarily aligned with respect to axes along which the correlations are calculated. Note that for higher integration lengths, i.e. $\Lambda \sim N_x/2$, the correlations also begin to recognize non-local symmetries (as for instance in figure 4.6 and figure 4.9), which has not been additionally shown here since we choose to focus only on local structures in the turbulence vector fields.

4.5. CORRELATIONS APPLIED TO HOMOGENEOUS, ISOTROPIC TURBULENCE

After applying the correlations to canonical flows, we now study how these ideas fare for real, turbulence vector fields. A turbulence velocity field is considered, typically, to have structure across multiple scales, while the vorticity field mainly comprises smaller scale structures. These fields, further, are highly complex and irregular. Applying the correlations to instantaneous field snapshots, as obtained from direct numerical simulations of homogeneous, isotropic turbulence, reveals their potential and possibilities, along with limitations, in educing structures. In this section, we begin with a brief description of the simulation method used to generate the turbulence data. Since the correlations yield "pseudo-vector" fields containing information about the structure of the flow, we first

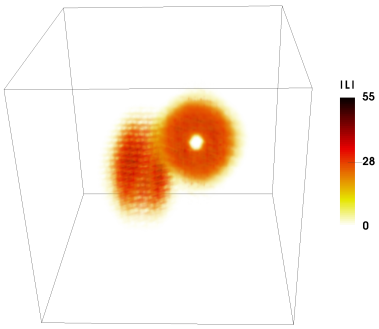

(a) **L**-correlation

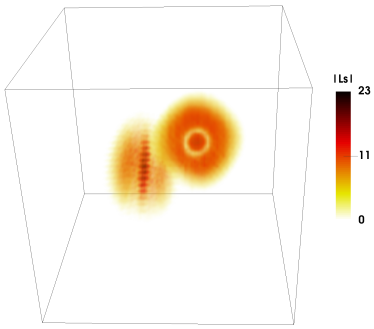

(b) $\mathbf{L}^{\mathbf{s}}$-correlation

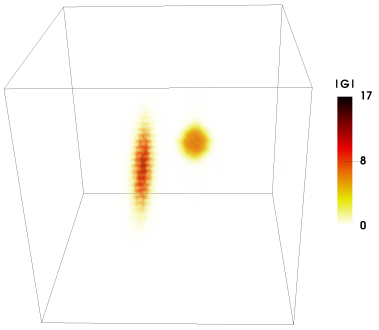

(c) **G**-correlation

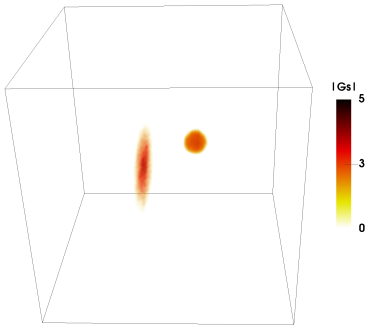

(d) $\mathbf{G}^{\mathbf{s}}$-correlation

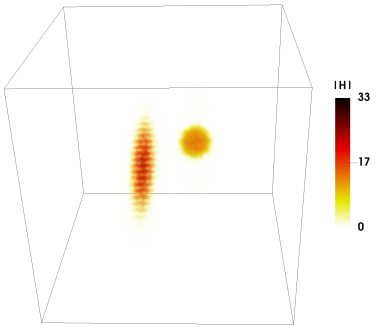

(e) **H**-correlation

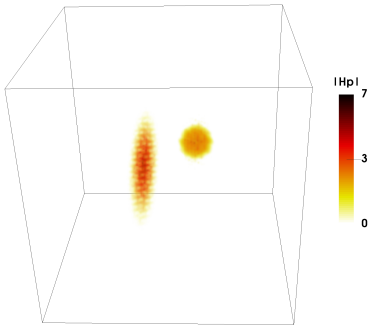

(f) $\mathbf{H}^{\mathbf{p}}$-correlation

Figure 4.13: Amplitude of all correlations calculated for the two Burgers vortices are shown for view 1, which gives a simultaneous look at the axis of one vortex and the core region of the other. The edges of the cubes shown here run from $\{x, y, z\} \in [10, 90]$.

describe how the correlation fields look qualitatively in comparison to the vector fields they are based on, i.e. the velocity and the vorticity field. We also describe the statistics of the correlation fields, like the PDFs, CDFs, spectral characteristics and their spatial organization.

4.5.1. SIMULATION DETAILS AND DATASET

For this study, we use a dataset from DNS simulations of homogeneous, isotropic turbulence, for which the Navier-Stokes equations with a body force **F** (as given below) are solved numerically

$$\frac{\partial \mathbf{u}}{\partial t} + (\mathbf{u}\cdot\nabla)\,\mathbf{u} = -\frac{\nabla p}{\rho} + \nu\nabla^2\mathbf{u} + \frac{\mathbf{F}}{\rho} \tag{4.24}$$

$$\nabla\cdot\mathbf{u} = 0 \tag{4.25}$$

Turbulence is generated in a periodic box by means of low wavenumber forcing, which is divergence-free by construction and is concentrated over a range of Fourier modes. It is of the form given by [28], and has properties similar to that devised by [29] and [30]; which can be written as

$$\begin{aligned} F_x &= \textstyle\sum_{k=k_a}^{k_b} \rho A(k)\left[\sin(2\pi k y + \phi_y(k)) + \sin(2\pi k z + \phi_z(k))\right] \\ F_y &= \textstyle\sum_{k=k_a}^{k_b} \rho A(k)\left[\sin(2\pi k x + \phi_x(k)) + \sin(2\pi k z + \phi_z(k))\right] \\ F_z &= \textstyle\sum_{k=k_a}^{k_b} \rho A(k)\left[\sin(2\pi k x + \phi_x(k)) + \sin(2\pi k y + \phi_y(k))\right] \end{aligned} \tag{4.26}$$

The forcing is stochastic (white noise) in time, which is achieved by varying each $\phi(k)$ randomly, and the force is distributed over a small range of wavenumers, given by $k_a \leq k \leq k_b$ (for this study we fix $k_a = 1, k_b = 8$), and the amplitude $A(k)$ of each of these wavenumbers is a Gaussian distribution in Fourier space, centered around a central forcing wavenumber k_f, given as

$$A(k) = A\exp\left(-\frac{\left(k-k_f\right)^2}{c}\right) \tag{4.27}$$

where c sets the width of the distribution ($c = 1.25$ here), and A is the forcing amplitude. We solve equations 4.24 and 4.25 with a standard lattice-Boltzmann (LB) solver, incorporating the turbulence forcing as per equation 4.26. This method has been used before for simulating homogeneous, isotropic turbulent flows of various kinds [28, 30–33].

The simulation is performed in a periodic box of size $(2\pi)^3$ resolved over N^3 grid points along each direction, all units being dimensionless, hence resolving a range of wavenumbers from $k = 2\pi/N$ (i.e. largest scale of length N [lu]) to $k = 2\pi/2 = \pi$ (i.e. the smallest scale of length 2 [lu]). Since we simulate homogeneous, isotropic turbulence, by definition all physical quantities are fluctuating and do not have a mean value, i.e. $\mathbf{u} = \mathbf{u}'$ and $\boldsymbol{\omega} = \boldsymbol{\omega}'$. The Kolmogorov scale is defined as $\eta \sim \left(\nu^3/\epsilon\right)^{1/4}$ where ν and ϵ are the kinematic viscosity and energy dissipation rate respectively. We adhere to the criterion for a DNS, as given by [34], i.e. $k_{\max}\eta > 1$. The Taylor microscale is calculated as

$$\lambda = \left(\frac{15\nu u'^2}{\langle\epsilon\rangle}\right)^{1/2} \tag{4.28}$$

N^3	k_f	ν	u'	ω'	$\langle E_k \rangle$	$\langle \epsilon \rangle$	λ	Re_λ	η	τ_k
256^3	2	0.0047	0.034	0.0103	1.8×10^{-3}	5.0×10^{-7}	13	95	0.67	97

Table 4.1: Simulation details, with all quantities presented in dimensionless lattice units [lu], average kinetic energy per unit mass $\langle E_k \rangle = \left(\sum_k E(k)\right)/N$, and the average rate of energy dissipation per unit mass $\langle \epsilon \rangle = (\sum_k 2\nu k^2 E(k))/N$.

where u' is the root-mean-square velocity. The average rate of energy dissipation $\langle \epsilon \rangle$ is calculated as $\langle \epsilon \rangle = \nu \langle \omega^2 \rangle = \sum_k 2\nu k^2 E(k)/N^3$, where $\langle \omega^2 \rangle$ is the average enstrophy and $E(k)$ is the kinetic energy spectrum. Note that the enstrophy $\omega^2 = \boldsymbol{\omega} \cdot \boldsymbol{\omega}$ is analogous to the turbulence kinetic energy $E_k = \mathbf{u} \cdot \mathbf{u}/2$. For homogeneous, isotropic turbulence, since $u' = v' = w'$, we have $E_k = 3u'^2/2$ or $u' = \sqrt{2E_k/3}$. The root-mean-square vorticity, ω', is obtained as $\langle \boldsymbol{\omega} \cdot \boldsymbol{\omega} \rangle^{1/2}$. In general, E_k and ϵ (apart from ν) are average measures of u' and ω', respectively. The large eddy turnover timescale is given as $T^\star = \mathscr{L}/u'$, where $\mathscr{L}$ is the forcing lengthscale given as $\mathscr{L} = N/k_f$. Using λ, the Taylor Reynolds number is calculated as

$$Re_\lambda = \frac{u'\lambda}{\nu} \tag{4.29}$$

and the Kolmogorov timescale is given as

$$\tau_k = \left(\frac{\epsilon}{\nu}\right)^{-1/2} \tag{4.30}$$

The turbulence simulation (parameters given in 4.1) is performed for a fluid initially at rest, to which the turbulence force is applied. After a brief transient duration, turbulence becomes well developed and attains a statistical steady-state, i.e. the balance of power input and energy dissipation. The simulation is then run for several additional large eddy timescales ($\sim 20 - 30T^\star$), during which around ~ 20 field snapshots are retained for analysis, all separated by $50\tau_k$, to give converged statistical results.

Figure 4.14 shows the evolution of $\langle E_k \rangle$ and $\langle \omega^2 \rangle$ for the simulation T1. Both quantities attain their steady-state values within a short transient phase, $\sim 100\tau_k$, after which they continue to oscillate around their temporal mean values. Beyond $100\tau_k$, turbulence is well developed, with a separation of scales. The temporal intermittency of $\langle E_k \rangle$ further manifests in the temporal intermittency of $\langle \omega^2 \rangle$, which has been attributed to some form of a turbulence cascading dynamics [28, 35].

Figure 4.15 shows a snapshot of the turbulence kinetic energy E_k and enstrophy ω^2 fields, as 3D volume renderings and planar cross-sections, from simulation T1 at $500\tau_k$. Typical features of the kinetic energy and enstrophy can be seen, where the kinetic energy is distributed over a range of length scales (which correspond to the inertial range), and shows a general large-scale organization (which also relates to the energy injection scale) with irregular structures across multiple scales. Enstrophy (and vorticity in general) is concentrated at the smaller scales, in spatially intermittent tube-like structures, also called "worms".

Figure 4.16 shows the probability and cumulative distribution functions (PDFs and CDFs, respectively), of the three velocity and vorticity components. These profiles have been obtained using 20 field snapshots, all separated by $50\tau_k$. Figure 4.16(a) shows that

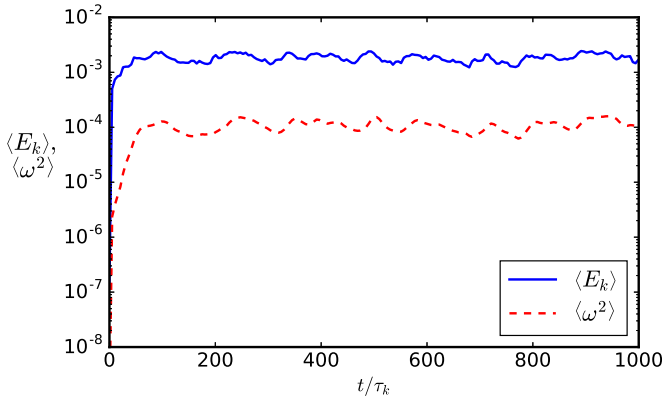

Figure 4.14: Evolution of the averaged turbulence kinetic energy $\langle E_k \rangle$ and averaged enstrophy $\langle \omega^2 \rangle$. Both quantities attain a steady-state value, reflecting a developed turbulence state.

the velocity components follow a Gaussian distribution (shown as the dashed line), and that the velocity fluctuations are not extreme (here they range from $-4 < u_i/u_i' < 4$). Figure 4.16(b) shows the CDFs of the velocity components, where 65% and 97% of the velocity has a magnitude below u_i' and $2u_i'$, respectively. Extreme values of the velocity, around $|u_i| > 3u_i'$ occupy a very small fraction of the total velocity field. Similarly, figure 4.16(c) and figure 4.16(d) show the PDFs and CDFs of the vorticity components. The PDFs show the typical long-tail distribution of vorticity, which is highly non-Gaussian. The extent of these tails gives a measure of the intermittency in the vorticity field, where increasingly extreme values can occur with a low probability. The CDFs of the vorticity show that most of the vorticity field has a low value, with 70% and 95% of the field below ω_i' and $2\omega_i'$. In this regard, the vorticity field has a similar composition as the velocity field, the difference being that the vorticity can also assume much more extreme values (even $\sim 18\omega_i'$ in this case).

It is important to note here that the vorticity field can be classified into a few "ranges", which can be done in different contexts. The first classification, which is usually adopted, is based on the amplitude and structure of the vorticity field, where the vorticity is divided into "low-vorticity", "moderate-vorticity" and "high-vorticity" ranges, as proposed by She *et al.* [19, 36]. According to their classification, "high-vorticity" ($\omega \gg \omega'$), which occupies a very small fraction of the volume, forms vorticity streamlines that are well-aligned, while the velocity field in the vicinity of these structures has a spiral, swirling motion. "Moderate-vorticity" ($\omega > \omega'$), on the other hand, was found to be less organized, whose structure was described as "sheet-like" and "ribbon-like". "Low-vorticity", at the level of the root-mean-square value ($\omega \sim \omega'$ and $\omega < \omega'$), which occupies most of the volume, was found to form random vortex lines with no apparent structure. Another way to classify the vorticity field, which is more relevant for our work, is to consider the organization of the vorticity field, along with its Biot-Savart contribution in generating the velocity field. In this classification, there is a "strong-vorticity" range which is organized as parallel vorticity streamlines with swirling-flow in the vicinity, similar to the "high-vorticity" range of She *et al.* [19]. This range forms the skirts of the vorticity PDF,

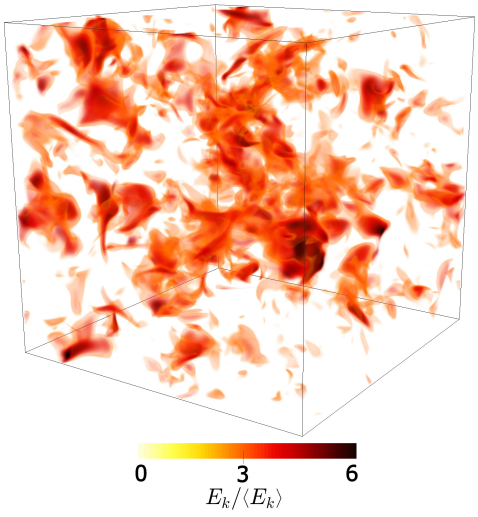

(a)

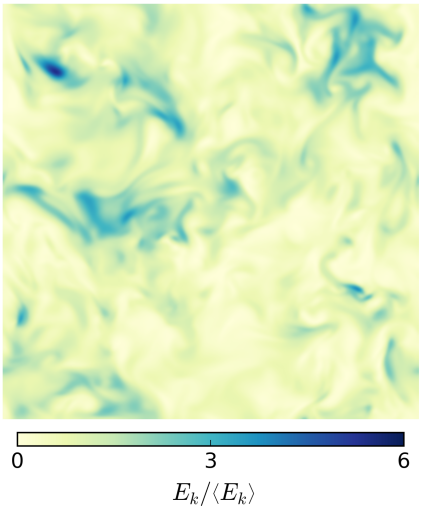

(b)

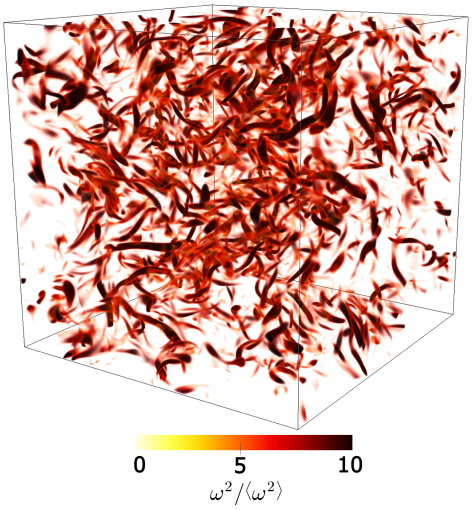

(c)

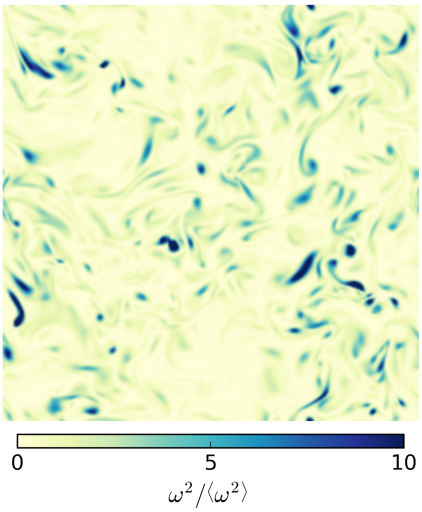

(d)

Figure 4.15: Snapshots of turbulence fields, when the flow is fully developed (at $t = 500\tau_k$), show qualitative features of the kinetic energy E_k and the enstrophy ω^2. Panel (a) shows a 3D volume rendering (at a resolution of 256^3) of the E_k field, which contains large-scale, irregular structures that permeate a part of the volume. Panel (b) shows a 2D cross-section of the E_k field (at a resolution of 256^2) at an arbitrary plane of the 3D simulation domain. Panel (c) shows a volume rendering of the ω^2 field, which is markedly different from the E_k field, as enstrophy is concentrated at the smaller scales, forming tube-like structures (also called "worms"). Panel (d) shows a planar cross-section of ω^2, which shows that most of the field has low values, interspersed with small regions of concentrated enstrophy. Both the fields have been normalized with their respective volume averaged quantity, i.e. $\langle E_k \rangle$ and $\langle \omega^2 \rangle$.

and appears most dominantly in the field due to its large amplitude (while occupying a very small fraction of the volume). We classify the rest of the vorticity field, which has a weaker organization, as the "background-vorticity". This range occupies the bulk of the volume, and can hence have a significant contribution in the Biot-Savart generation of the velocity field. The "background-vorticity", further, is divided into an "intermediate" and a "weak" range, based upon the level of Biot-Savart contribution. The range of vorticity that significantly contributes to the Biot-Savart generation of the velocity field is termed "intermediate", while the "weak" vorticity has a negligible contribution.

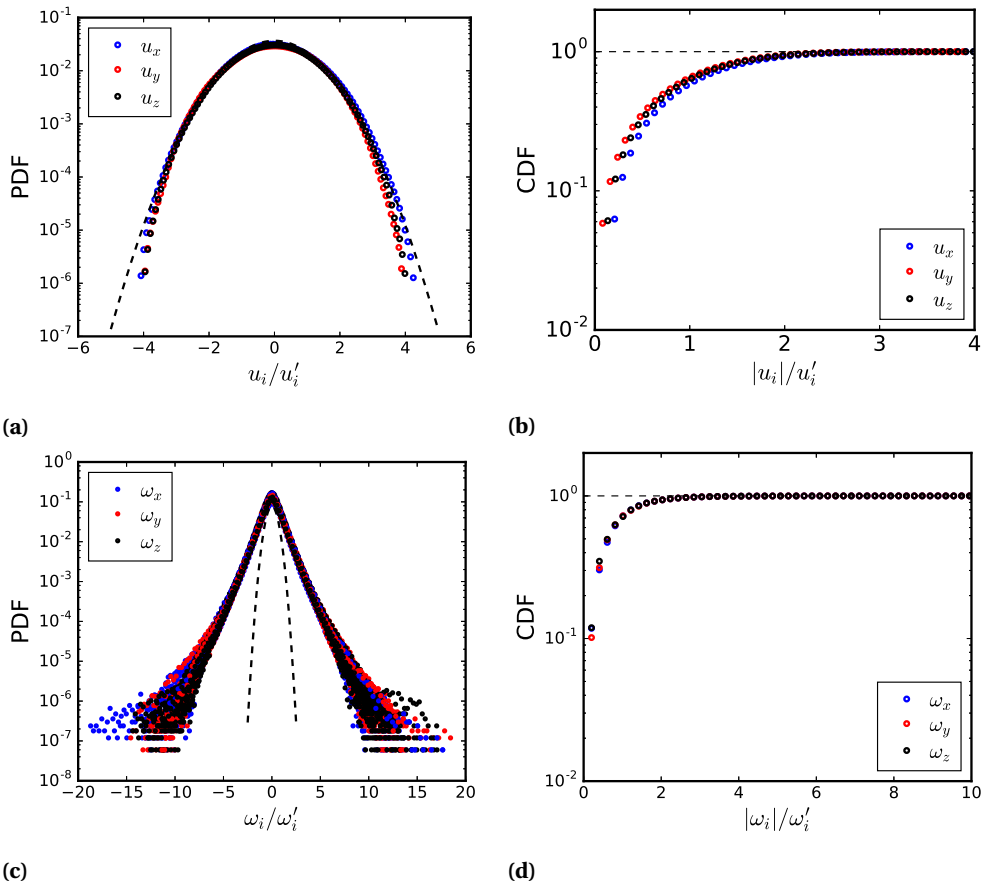

Figure 4.16: Probability and Cumulative distribution functions (PDF and CDF), shown for the three velocity and vorticity components. The dashed line in panels (a) and (c) show a typical Gaussian distribution.

The spectra of kinetic energy and enstrophy are calculated using the three-dimensional Fourier transform $\hat{\phi}_{\mathbf{k}}$ of the velocity and vorticity fields, respectively. The three-dimensional spectra are spherically averaged over wavenumber shells $k \in [k-1/2, k+1/2]$ where $k =$

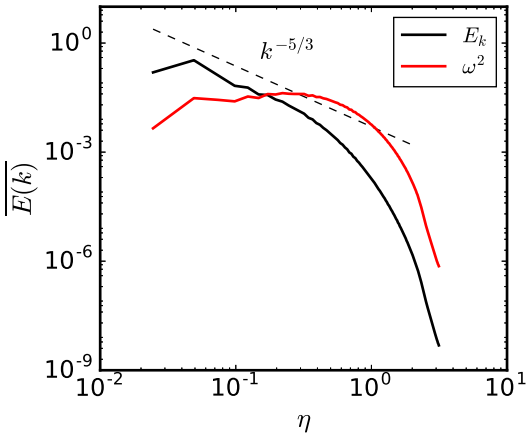

Figure 4.17: Time-averaged, one-dimensional power spectra are shown for the kinetic energy and enstrophy fields. The spectra is further normalized as $\overline{E(k)} = E(k)/\sum_k E(k)$.

$\sqrt{\mathbf{k}\cdot\mathbf{k}}$ to give one-dimensional spectra over the scalar wavenumber k as follows

$$\phi(k) = 4\pi k^2 \frac{\sum_k |\hat{\phi}_{\mathbf{k}}|^2}{\sum_k 1} \tag{4.31}$$

These one-dimensional spectra are further time averaged over 20 samples separated by $50\tau_k$ to give time-averaged spectral characteristics. Lastly, the spectrum $\phi(k)$ is normalized as $\overline{\phi(k)} = \phi_k/\sum_k \phi(k)$ to facilitate comparison of different quantities, as we are mainly interested in the relative distribution of energy over wavenumber. Figure 4.17 shows the E_k and ω^2 spectra, where E_k exhibits a well developed inertial range, which follows the $k^{-5/3}$ spectral scaling, while the enstrophy spectra has a small, positive slope, with a broad peak at higher wavenumbers.

4.5.2. QUALITATIVE AND STATISTICAL FEATURES OF THE CORRELATION FIELDS

The correlations are calculated for the snapshot of the data presented in figure 4.15, for an integration length of $\Lambda = \lambda$. Each correlation vector field $\boldsymbol{\psi}$ is normalized by its respective root mean square (rms) value ψ' which is calculated as $\psi' = \langle \boldsymbol{\psi}\cdot\boldsymbol{\psi}\rangle^{1/2}$, where $\langle . \rangle$ denotes ensemble averaging (which here is performed over space, to normalize the field snapshot with root-mean-square value at the same instance of time). The amplitude of a correlation field $|\boldsymbol{\psi}|$ is simply referred to as ψ (for instance H^p for $|\mathbf{H^p}|$). Each of the correlation fields have been shown separately to highlight their qualitative features, at a an arbitrary cross-sectional slice and as a three-dimensional volume rendering. The PDF and CDF of the three components of each correlation have been shown as well, which have been averaged over 18 field realizations, each separated by $50\tau_k$.

Figure 4.18 shows the **L** correlation. The cross-sectional slice in panel (a) shows that the correlation has features across various lengthscales, which are very similar to the features in the kinetic energy field (as seen in figure 4.15). Large, diffused regions of the

correlation are found to yield high values in regions of high kinetic energy. The three-dimensional rendering in panel (b) shows the spatial organization of $\mathbf{L}$, which is also similar to E_k. The PDF of the components of $\mathbf{L}$, in panel (c), shows that the correlation is positively skewed. This hints that, according to the definition of $\mathbf{L}$, both the local velocity $\mathbf{u}(\mathbf{x})$, and the velocity integral in the neighbourhood $-\Lambda < x_i < \Lambda$, have the same sign, in regions of high kinetic energy. This reflects that high kinetic energy regions comprise parallel flow streamlines, since they yield large values of $\mathbf{L}$ with a strong spatial correspondence (which shall be quantified with the subsequent analysis). The PDFs of L_i are also non-Gaussian, and do not extend over a very large range of values. Panel (d) shows the CDFs of L_i, where approximately 70% and 93% of the L_i fields are below L_i' and $2L_i'$, respectively.

Figure 4.19 shows the $\mathbf{L^s}$ correlation, which is found to have a more diffused structure than $\mathbf{L}$, while its qualitative features are similar to $\mathbf{L}$ and E_k with a high spatial correspondence. The PDFs of L_i^s, in panel (c), show that this correlation is also positively skewed, where high values of the correlation are positive. This further hints that high kinetic energy structures are parallel streamlines, which are aligned along the same direction. This is because the $\mathbf{L^s}$ correlation, by definition, yields large positive values for aligned streamlines, and large negative values for anti-parallel streamlines. The CDFs in panel (d) show that approximately 70% and 93% of the L_i^s fields are below $L_i^{s\prime}$ and $2L_i^{s\prime}$, respectively.

Figure 4.20 shows the $\mathbf{G}$ correlation, which is the $\mathbf{L}$ equivalent of the vorticity field. The planar (panel (b)) and volumetric (panel (c)) profiles of $\mathbf{G}$ are found to closely resemble the enstrophy field (as shown in figure 4.15b). The $\mathbf{G}$ field at high magnitudes also forms worm-like structures. This shows that high enstrophy regions are also composed of parallel vorticity streamlines, albeit the size of these structures is significantly smaller than regions of high E_k. The PDFs of the G_i components show that the correlation yields a long-tailed, positively-skewed distribution, similar to the positive half of the vorticity PDF (figure 4.16c). This again reflects that the vorticity streamlines are well aligned in the core of high enstrophy regions, since the product of $\boldsymbol{\omega}(\mathbf{x})$ and the integral of the vorticity in the neighbourhood $-\Lambda < x_i < \Lambda$, yields positive values, reflecting that the two quantities have the same sign. The CDFs, in panel (d), show that approximately 84% and 94% of the G_i fields are below G_i' and $2G_i'$, respectively.

Figure 4.21 shows the $\mathbf{G^s}$ correlation, which is the vorticity field equivalent of $\mathbf{L^s}$. The planar and volumetric profiles show a more 'patchy' structure in comparison to $\mathbf{G}$. This is possibly because the $\mathbf{G^s}$ correlation is sensitive to the symmetry of the vorticity field along each direction x_i, as viewed from each point of calculation $\mathbf{x}$. The PDFs in panel (c) shows that the components G_i^s have a positively-skewed distribution, although negative values of G_i^s are also relatively more prevalent than negative values of G_i. The positive-skew of the high magnitude G_i^s shows that the stronger vorticity regions have vorticity streamlines that are well aligned. The CDFs in panel (d) show that approximately 80% and 96% of G_i^s is under $G_i^{s\prime}$ and $2G_i^{s\prime}$, respectively.

Figure 4.22 shows the $\mathbf{H}$ correlation, which relates the local vorticity $\boldsymbol{\omega}(\mathbf{x})$ to the velocity field along directions x_i. The planar and volumetric $\mathbf{H}$ fields, in panels (a) and (b) respectively, closely resemble the enstrophy field in figure 4.16(b). The PDFs of the H_i components are highly positively-skewed, and have a long-tailed distribution. Together, these results show that the strong vorticity regions are associated with swirling-flow in

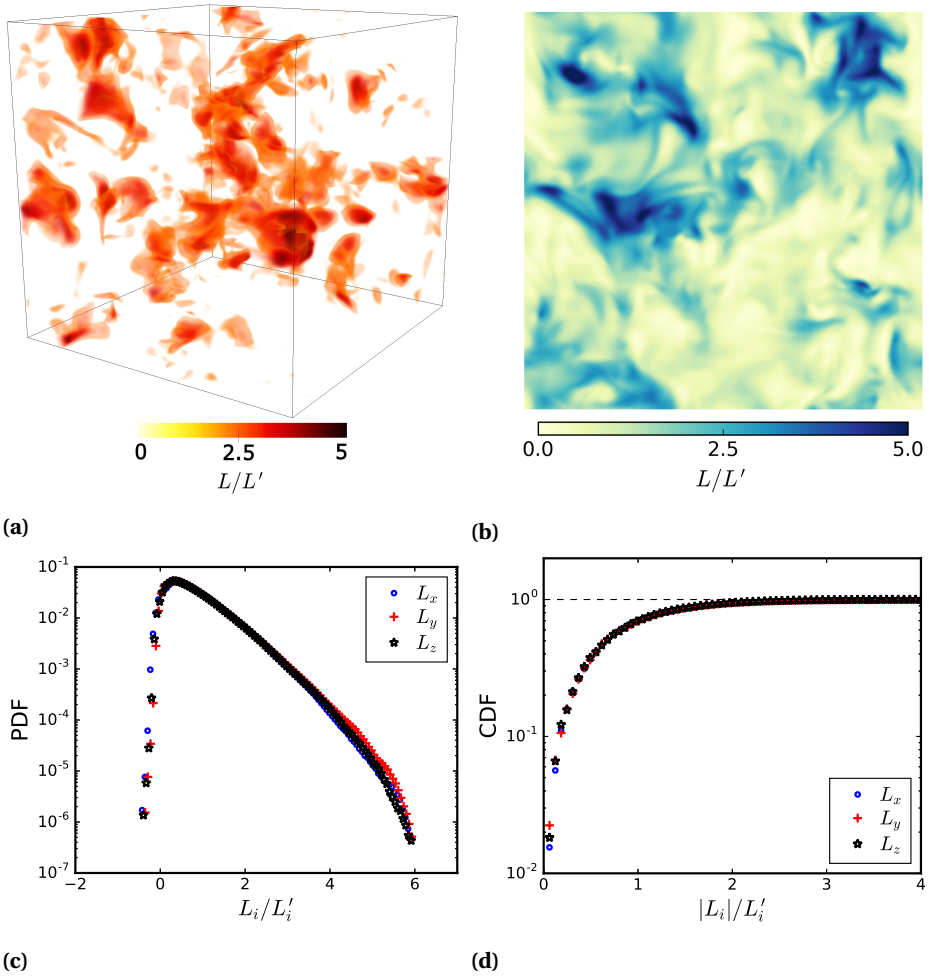

Figure 4.18: The **L** correlation is shown for a single field snapshot, at $500\tau_k$. Panel (a) shows the cross-sectional view of $L = \sqrt{\mathbf{L}\cdot\mathbf{L}}$ at an arbitrary plane, while panel (b) shows the three-dimensional field as a volume rendering. Panels (c) and (d) show the time-averaged PDFs and CDFs of the three components of **L**.

their vicinity. This is because (i) there is a strong spatial correspondence between the occurrence of strong enstrophy regions and high magnitude **H**, and (ii) the distributions of H_i show large positive values, which means that the local flow, in the $\Lambda-$neighbourhood, is well correlated with the vorticity induced flow. The CDFs of H_i in panel (d) show that approximately 82%, 94% and 99% of the H_i fields are below H_i', $2H_i'$ and $3H_i'$, respectively.

Lastly, figure 4.23 shows the $\mathbf{H^p}$ correlation, which has a very similar profile to the **H** correlation. This is expected, since the $\mathbf{H^p}$ correlation is conceptually similar to the **H** correlation. The PDFs of $H_i^{p\prime}$, in panel (c), are found to be highly positively-skewed,

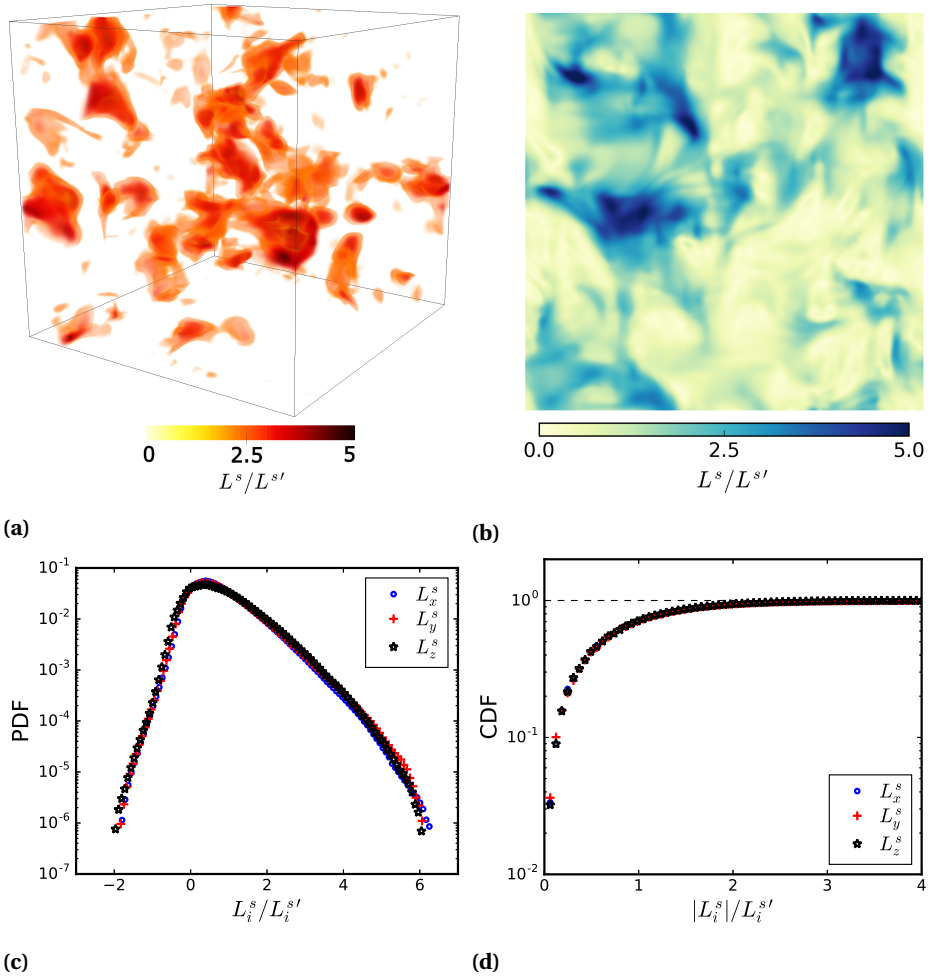

Figure 4.19: The $\mathbf{L^s}$ correlation is shown for a single field snapshot, at $500\tau_k$. Panel (a) shows the cross-sectional view of $L^s = \sqrt{\mathbf{L^s}\cdot\mathbf{L^s}}$ at an arbitrary plane, while panel (b) shows the three-dimensional field as a volume rendering. Panels (c) and (d) show the time-averaged PDFs and CDFs of the three components of $\mathbf{L^s}$.

and yield values larger than the $\mathbf{H}$ correlation. The form of the PDFs of H_i^p, however, is almost identical to the H_i, the difference being that, due to the nature of the definitions, H_x^p is similar to H_z (which is because $\mathbf{H^p}$ is designed to align parallel to the local vorticity vector, while $\mathbf{H}$ aligns orthogonal to it). Most of the high enstrophy structures ($\omega^2 > 5\langle\omega^2\rangle$) in figure 4.15(b) coinciding with regions of high H^p ($H^p < 5H^{p\prime}$) in figure 4.23(a), hints that strong enstrophy (or vorticity) regions are invariably associated with swirling motion in the orthogonal plane. The CDFs of H_i^p show that roughly 86%, 94% and 97% of the fields are within $1H_i^{p\prime}$, $2H_i^{p\prime}$ and $3H_i^{p\prime}$, respectively.

We also applied these correlations to a reference dataset of homogeneous, isotropic

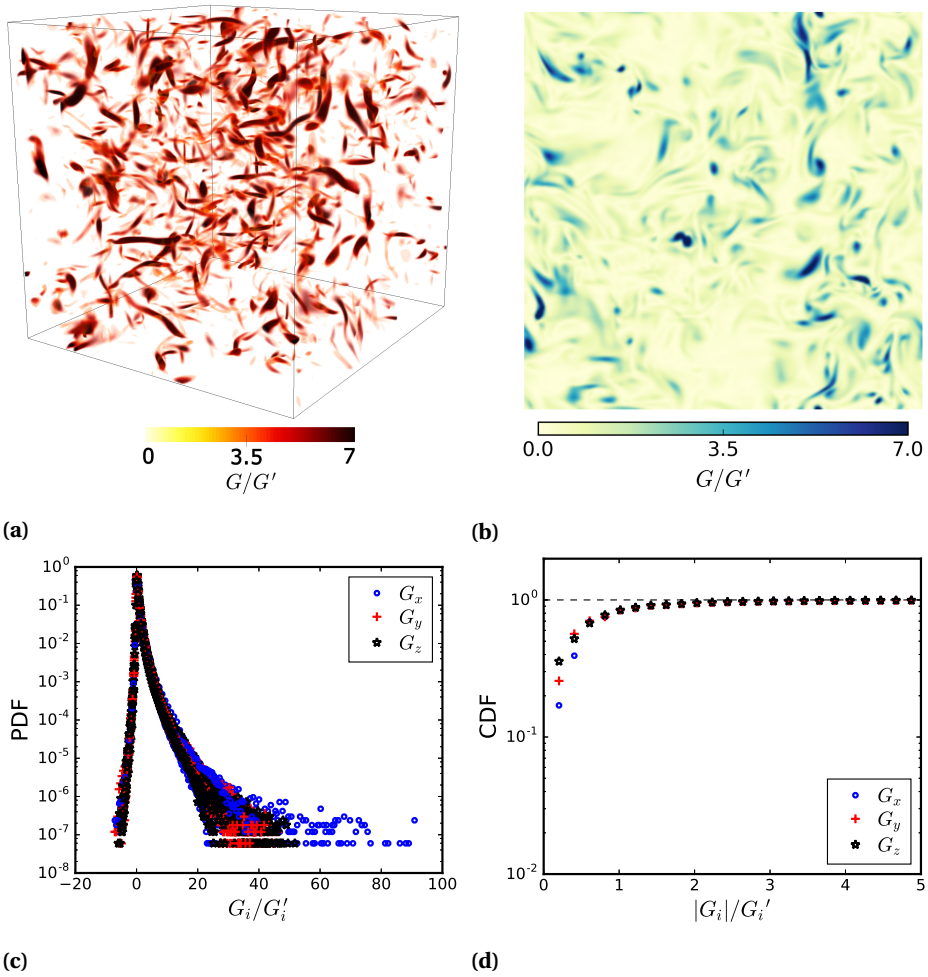

Figure 4.20: The **G** correlation is shown for a single field snapshot, at $500\tau_k$. Panel (a) shows the cross-sectional view of $G = \sqrt{\mathbf{G}\cdot\mathbf{G}}$ at an arbitrary plane, while panel (b) shows the three-dimensional field as a volume rendering. Panels (c) and (d) show the time-averaged PDFs and CDFs of the three components of **G**.

turbulence obtained from the Johns Hopkins Turbulence Databases (JHTD) [37, 38], which was generated using a pseudo-spectral method on a grid of 1024^3 at $Re_\lambda = 433$. The results are shown in Appendix 4.A; which are found to be essentially similar to those presented here, from our in-house code. We use our own numerical datasets for the remainder of this study, for our ease of accessibility and control over the data.

4.5.3. INFLUENCE OF THE CHOICE OF Λ

Before proceeding with further analysis of the correlation fields, it is important to consider the influence of Λ on the results. The obvious values of Λ that can be disregarded

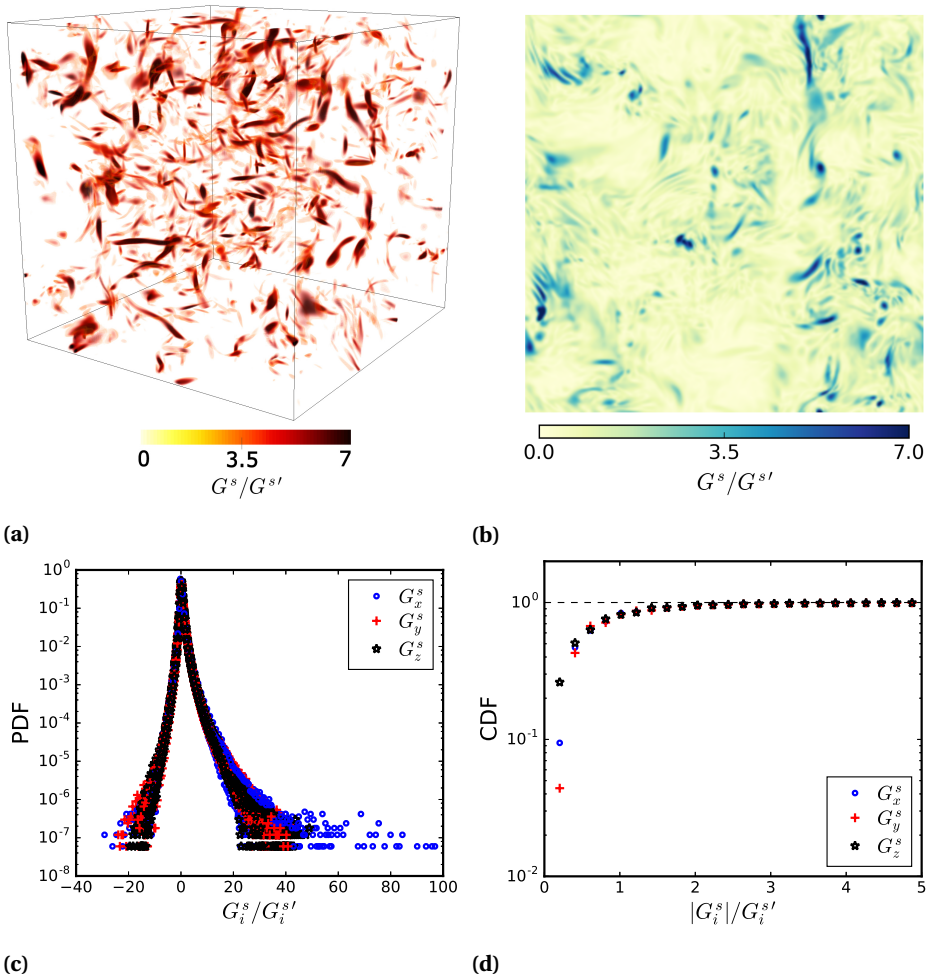

Figure 4.21: The $\mathbf{G^s}$ correlation is shown for a single field snapshot, at $500\tau_k$. Panel (a) shows the cross-sectional view of $G^s = \sqrt{\mathbf{G^s}\cdot\mathbf{G^s}}$ at an arbitrary plane, while panel (b) shows the three-dimensional field as a volume rendering. Panels (c) and (d) show the time-averaged PDFs and CDFs of the three components of $\mathbf{G^s}$.

are those extremely small or large. Too small a Λ is somewhat meaningless since we intend to capture non-local structures which have a finite physical size. On the other hand, very large values of Λ ($\sim N_x/2$) will introduce periodicity induced artifacts in the correlation fields which should be avoided. However, there is a wide range of values of Λ in $0 < \Lambda < N_x$ which are viable, and yet the results should not depend strongly on the choice of Λ.

We begin by considering the $\mathbf{L}$ correlation, which has the form

$$L_i(\mathbf{x},\Lambda) = \int_{-\Lambda}^{\Lambda} \mathbf{u}(\mathbf{x})\cdot\mathbf{u}(\mathbf{x}+\mathbf{r}_i)\mathrm{d}r \tag{4.32}$$

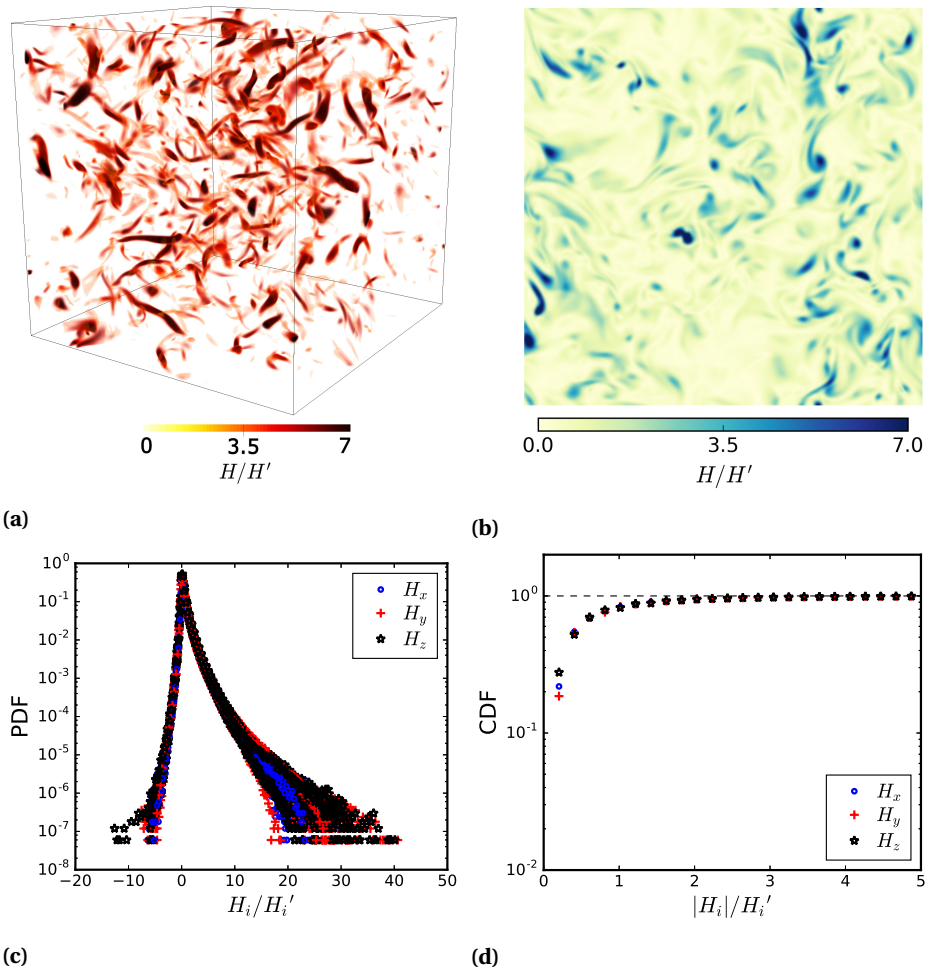

Figure 4.22: The **H** correlation is shown for a single field snapshot, at $500\tau_k$. Panel (a) shows the cross-sectional view of $H = \sqrt{\mathbf{H}\cdot\mathbf{H}}$ at an arbitrary plane, while panel (b) shows the three-dimensional field as a volume rendering. Panels (c) and (d) show the time-averaged PDFs and CDFs of the three components of **H**.

Since $\mathbf{u}(\mathbf{x})$ does not vary, it can be placed outside the integral as

$$L_i(\mathbf{x},\Lambda) = \mathbf{u}(\mathbf{x}) \cdot \int_{-\Lambda}^{\Lambda} \mathbf{u}(\mathbf{x}+\mathbf{r}_i)\mathrm{d}r$$
$$L_i(\mathbf{x},\Lambda) = 2\Lambda\,(\mathbf{u}(\mathbf{x}) \cdot \tilde{\mathbf{u}}_i) \tag{4.33}$$

where

$$\tilde{\mathbf{u}}_i = \frac{1}{2\Lambda}\int_{-\Lambda}^{\Lambda} \mathbf{u}(\mathbf{x}+\mathbf{r}_i)\mathrm{d}r \tag{4.34}$$

The **L** correlation is essentially a convolution of the velocity field **u** with the $\tilde{\mathbf{u}}$ field

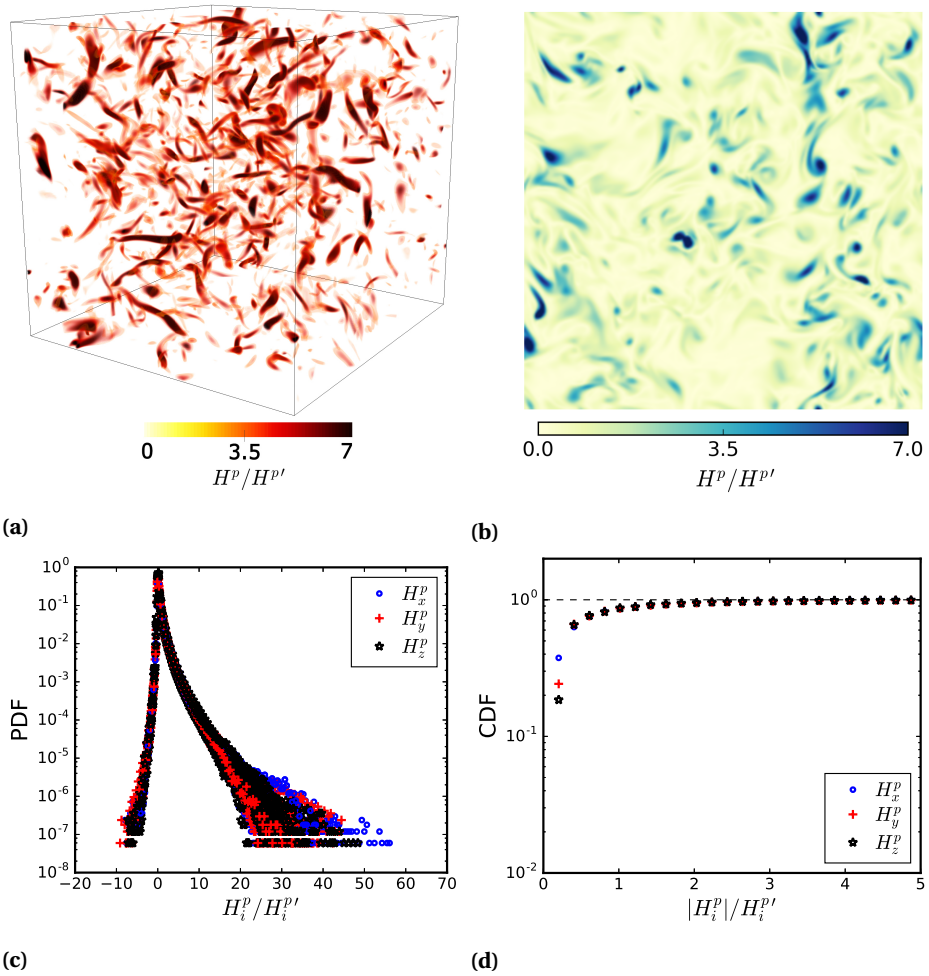

Figure 4.23: The $\mathbf{H^p}$ correlation is shown for a single field snapshot, at $500\tau_k$. Panel (a) shows the cross-sectional view of $H^p = \sqrt{\mathbf{H^p}\cdot\mathbf{H^p}}$ at an arbitrary plane, while panel (b) shows the three-dimensional field as a volume rendering. Panels (c) and (d) show the time-averaged PDFs and CDFs of the three components of $\mathbf{H^p}$.

(which is a function of Λ). Hence, if the $\widetilde{\mathbf{u}}$ field varies significantly with Λ, so will $\mathbf{L}$. In figure 4.24, snapshots of the $\widetilde{u}_z = |\widetilde{\mathbf{u}}_z|$ field are shown for a wide range of Λ/λ values, at a planar crossection from simulation T1 (at the same time instance as has been shown in figure 4.15). At very small values, $\Lambda/\lambda < 1$, the $\mathbf{L}$ field looks very similar to the E_k field, which is since the limit $\Lambda \to 0$ reduces $\mathbf{u}\cdot\widetilde{\mathbf{u}}$ to $\mathbf{u}\cdot\mathbf{u}$. The $\widetilde{u}_z$ field does not appear to change significantly for $1 \leq \Lambda/\lambda < 7$, which is also true for $\Lambda/\lambda \geq 7$, although those values of Λ begin to approach the size of the simulation domain and should be disregarded.

It is interesting that the $\widetilde{u}$ field appears to vary slowly for $\Lambda/\lambda > 1$. This can be quan-

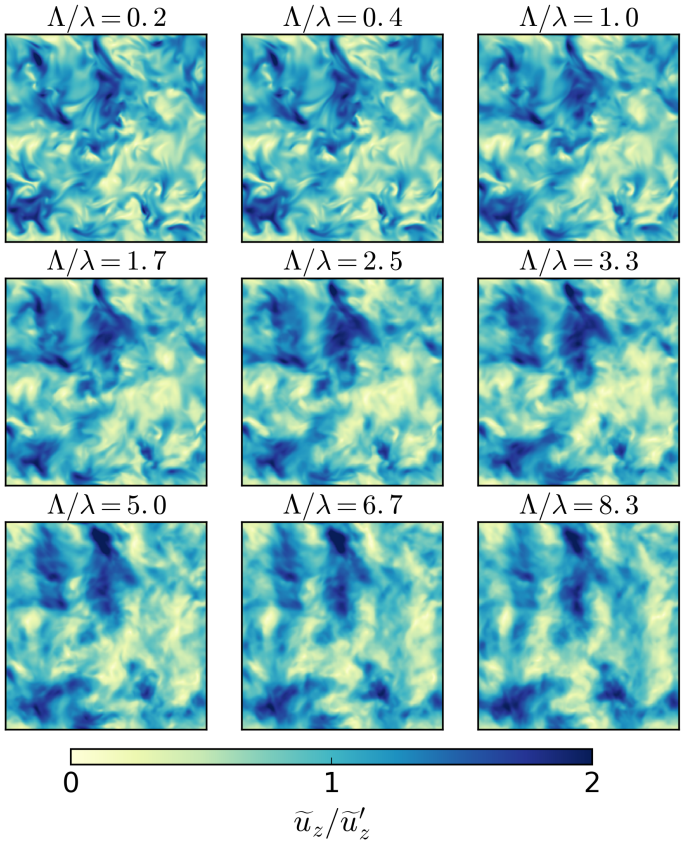

Figure 4.24: Crossectional slices of the $\tilde{u}_z$ field for varying Λ/λ.

tified by calculating

$$\frac{d\widetilde{u}_i}{d\Lambda} = \frac{|\widetilde{\mathbf{u}}_i^{\Lambda+\Delta\Lambda} - \widetilde{\mathbf{u}}_i^{\Lambda}|}{\Delta\Lambda} \tag{4.35}$$

where $|.|$ is the amplitude of the difference between the two fields. This is shown in figure 4.25 for $\widetilde{u}_x$, $\widetilde{u}_y$ and $\widetilde{u}_z$, where $\langle . \rangle$ denotes spatial averaging over the entire volumetric domain, and temporal averaging over two independent realizations for $\widetilde{u}_i$ at $t \approx 500\tau_k$ and $1000\tau_k$. The change in $d\widetilde{u}/d\Lambda$ is large for $\Lambda/\lambda < 1$. This reflects the fact that most of the fine structures in the flow are smaller than the Taylor microscale λ, and they get averaged over in the $\widetilde{u}$ fields for increasing Λ. Next, the rate of change seems to decay exponentially for $\Lambda/\lambda > 1$ (with a slope of approximately $-1/5$), which reaffirms that the $\widetilde{u}$ field varies slowly. This change of behaviour occurs via a sharp transition around $\Lambda/\lambda \approx 1$. The Taylor microscale, hence, is a good measure for the integration length of the correlations, since the results for $\mathbf{L}$ and $\mathbf{L^s}$ are not expected to vary significantly in the range $1 \leq \Lambda/\lambda < 4$. Moreover, the $\mathbf{G}$ and $\mathbf{G^s}$ correlations which identify the fine scale vorticity structures, and the $\mathbf{H}$ and $\mathbf{H^p}$ correlations which identify regions of swirling motion generated by local vorticity values, are all less dependent on the choice of Λ (provided Λ is

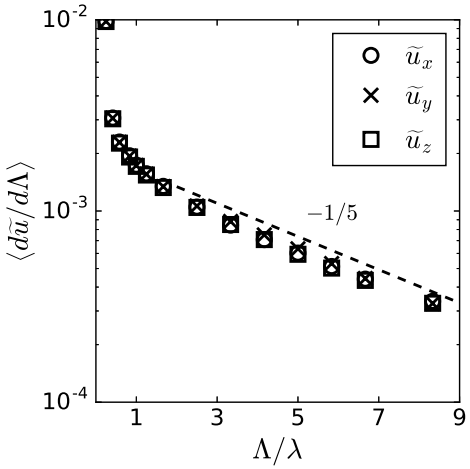

Figure 4.25: Rate of change in the $\widetilde{u}$ field with increasing Λ. Here $\langle . \rangle$ denotes spati-temporal averaging and $\widetilde{u}_i = |\widetilde{\mathbf{u}}_i|$.

large enough to identify the small-scale features). For the remainder of this study, we use $\Lambda = \lambda$ for calculating the correlations.

4.5.4. SPECTRAL CHARACTERISTICS OF THE CORRELATION FIELDS

The spectral characteristics of the three-dimensional correlation pseudo-vector fields are discussed in comparison to the kinetic energy (E_k) and enstrophy (ω^2) spectra. The correlation spectra are calculated in the same way as the E_k spectra, where the three-dimensional Fourier transforms of the correlation fields are squared and spherically averaged over wavenumber shells. The spectra have also been time-averaged over 18 realizations, each separated by $50\tau_k$. In figure 4.26, (a) $\mathbf{L}$ and (b) $\mathbf{L^s}$ spectra are found to resemble the kinetic energy spectrum, where the correlation energy is concentrated at lower wavenumbers with a peak at roughly twice the highest kinetic energy containing wavenumber. The spectral shift is explained by the definitions of these correlations, which involve a product of the velocity field with an integral of itself (i.e. $\mathbf{u}(\mathbf{x}) \cdot \int \mathbf{u}(\mathbf{x}+\mathbf{r}_i)$, in the case of $\mathbf{L}$) or an integral of velocity products (i.e. $\int \mathbf{u}(\mathbf{x}+\mathbf{r}_i) \cdot \mathbf{u}(\mathbf{x}-\mathbf{r}_i)$, in the case of $\mathbf{L^s}$). This product causes a shift in the wavenumber, in comparison to the kinetic energy spectra, which involves the square of the Fourier transform of the velocity components.

The spectra of correlations $\mathbf{G}$ and $\mathbf{G^s}$ in panels (c) and (d) of figure 4.26, respectively, are found to closely resemble the enstrophy spectrum. There is a clear shift in the spectral peak to a higher wavenumber for both cases, which is more pronounced for $\mathbf{G^s}$. This is a feature that can be related to the one-dimensional Oseen vortex pair example (see figure 4.9), where the $\mathbf{G^s}$ correlation produces a sharper profile than vorticity, since it decays at a faster rate than $\mathbf{G}$. This is because the definition of $\mathbf{G^s}$ is more sensitive to changes in the symmetry of the vorticity field. The sharper $\mathbf{G^s}$ profile, hence, leads to the formation of a peak at a higher wavenumber in the $\mathbf{G^s}$ spectrum in comparison to the enstrophy spectrum.

$\mathbf{H}$ and $\mathbf{H^p}$ correlation spectra in panels (e) and (f) of figure 4.26, respectively, are

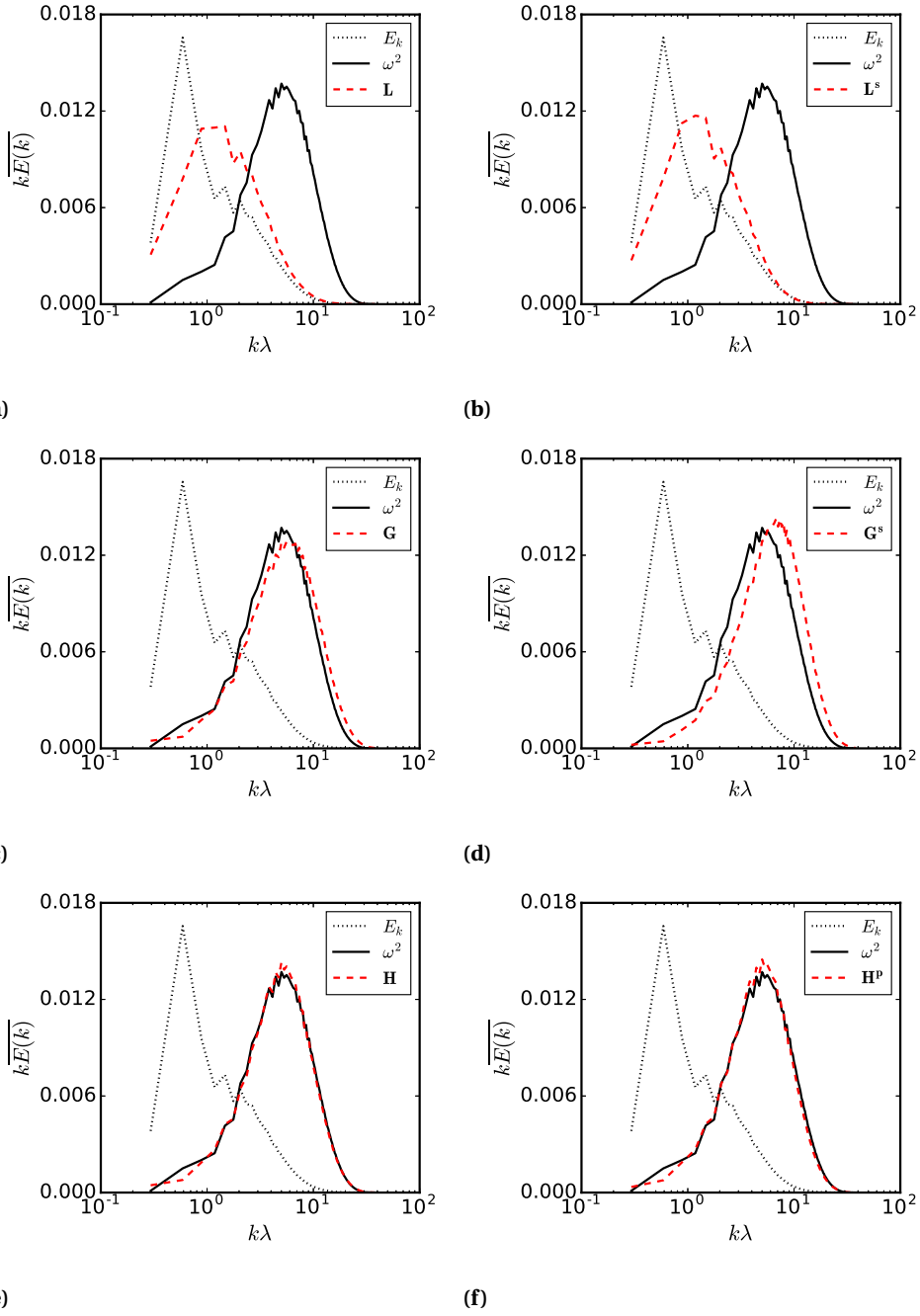

Figure 4.26: Time averaged spectra of correlation fields (a) **L**, (b) $\mathbf{L}^s$, (c) **G**, (d) $\mathbf{G}^s$, (e) **H** and (f) $\mathbf{H}^p$ shown together with the kinetic energy (E_k) and enstrophy (ω^2) spectra.

found to almost exactly follow the enstrophy spectrum. Since the enstrophy field is spatially highly intermittent, small spatial regions with high field intensities contribute most to the spectra, which gives the high wavenumber spectral peak. Since $\mathbf{H^p}$ almost coincides with the enstrophy/dissipation spectra, it reaffirms that high vorticity regions have a swirling motion (and not shear), according to what was indicated by [19]. Note that these spectra are presented for the correlation fields integrated over a length of $\Lambda = \lambda$. Changing the integration length to different values can possibly influence the spectral characteristics of the correlations.

Overall, the $\mathbf{L}$ and $\mathbf{L^s}$ correlations are found to be very similar for the turbulence fields (unlike in the canonical flows example). This shows that there are no larger symmetries/asymmetries in the velocity field, for within the integration length of $\Lambda = \lambda$. Further, $\mathbf{G}$ and $\mathbf{G^s}$ are found to be similar as well, and they have a similar spatial form to $\mathbf{H^p}$, although the definition of $\mathbf{H^p}$ is very different. For the remainder of this study, we shall focus on the $\mathbf{L}$ and $\mathbf{H^p}$ correlations, without loss of generality, since a similar analysis could be performed using the other correlations as well.

4.5.5. SPATIAL DISTRIBUTION OF CORRELATION FIELDS

The different correlation measures highlight different aspects of the flow. For instance, the $\mathbf{L}$ and $\mathbf{L^s}$ correlations, designed to identify parallel streamlines, resemble the larger scales of flow. Similarly, the $\mathbf{G}$ and $\mathbf{G^s}$ correlations identify parallel vorticity streamlines, and coincide with the smaller scales. The $\mathbf{H^p}$ correlation, also concentrated at the smaller scales, identifies regions of local swirling motion. The spatial distribution of these correlations sheds light on the distribution of coherent flow structures in physical space. In this section, we discuss the spatial distribution statistics of two of the correlations, namely $\mathbf{L}$ and $\mathbf{H^p}$, in relation to the kinetic energy and vorticity fields.

First, figure 4.27(a) shows iso-surface of $E_k = 2\langle E_k \rangle$ (shown in blue), together with iso-surfaces of $L = 2L'$ (shown in red). At the chosen threshold levels, the L regions are consistently contained within the E_k regions, reflecting the fact that increasingly higher values of the L field occupy successively smaller regions of space. This also shows that relatively higher kinetic energy $E_k \geq 2\langle E_k \rangle$ yield relatively higher L values, in the range $L \geq 2L'$. This also suggests that higher kinetic energy regions must all have parallel flow streamlines (due to the high L values they yield).

Figure 4.27(b) shows iso-surfaces of vorticity at $\omega = 3\omega'$ (in blue) together with iso-surfaces of H^p at $8H^{p\prime}$ (in red). The H^p iso-surfaces are shown at a high value to demonstrate that only a fraction of the intermediate vorticity 'worms' yield very high H^p values in their core regions. For instance, in panel (d), $H^p = 5H^{p\prime}$ iso-surfaces shown, which have a comparable size to the $3\omega'$ iso-contours in panel (b). It is found that H^p occupies equivalent or more volume than ω at low thresholds, while at increasingly higher thresholds, the H^p field occupies successively smaller fractions of the volume, as shall be quantified with the spatial statistics.

Figure 4.27(c) shows contours of E_k at $2\langle E_k \rangle$ (in blue) shown together with contours of vorticity at $\omega = 3\omega'$. It appears that high kinetic energy regions and high vorticity are *spatially exclusive* to a large extent. This spatial distribution of the two quantities may also hint at the dynamical separation between the large and small-scales of turbulence, where the larger scales *lead* the cascading dynamics, while the smaller scales are merely a *consequence* of the dynamics, as expounded by [2]. The two fields, invariably, begin to

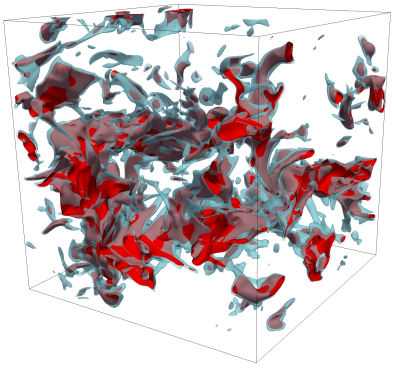

(a) Contours of the turbulent kinetic energy $E_k = 2\langle E_k \rangle$ (in blue) together with contours of $L = 2L'$ (in red).

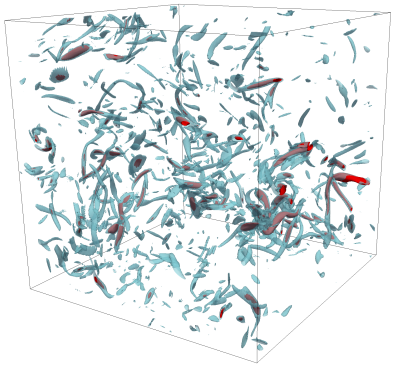

(b) Contours of vorticity at $\omega = 3\omega'$ (in blue) shown together with contours of $H^p = 8H^{p\prime}$ (in red).

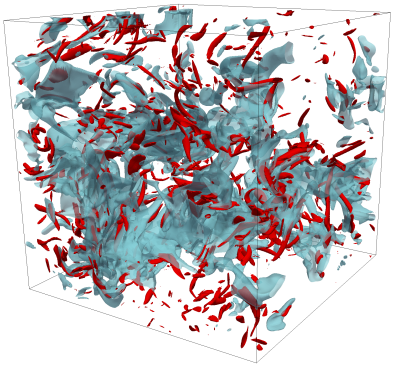

(c) Contours of $E_k = 2\langle E_k \rangle$ (blue) along with $\omega = 3\omega'$ (red) shows that these fields are spatially exclusive.

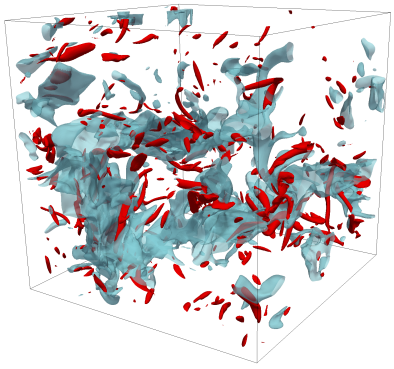

(d) Contours of $L = 2L'$ (blue) along with $H^p = 5H^{p\prime}$ (red) shows that these correlation fields are spatially exclusive.

Figure 4.27: Spatial distribution of correlations L and H^p in comparison to turbulent kinetic energy E_k and vorticity ω.

also overlap when the thresholds are lowered, and become more exclusive and distanced at higher thresholds. Lastly, panel (d) shows the distribution of correlations L and H^p, where contours of $L = 2L'$ (in blue) are shown together with contours of $H^p = 5H^{p\prime}$. Since these correlations closely resemble E_k and ω, respectively, they also remain spatially exclusive, at the chosen threshold levels.

The spatial distribution of the correlations, relative to each other and turbulence quantities like E_k and ω (as shown in figure 4.27), is quantified by the joint-PDFs of pairs of variables. The statistics are further averaged over 18 field realizations, each separated by $50\tau_k$. Figure 4.28(a) shows the joint-PDF of L and E_k. Since the two fields coincide strongly, they are highly correlated. Large values of E_k also yield large values of L. This happens because, to recall, L identifies flow regions that are comprised of velocity vectors that are (i) well-aligned and (ii) have a high magnitude. It so turns out, that regions of

high E_k are all well-aligned, and there are no regions of high E_k with disordered vectors. The slight asymmetry of the PDF towards L shows that L attains higher values, relative to L', than E_k does relative to $\langle E_k \rangle$. This asymmetry hints that an increase in E_k leads to stronger alignment of the velocity vectors, which yields higher L values. Figure 4.28(b) shows the joint-PDF of H^p and ω. The two fields are again strongly correlated, while the probability of occurrence of large-valued ω is higher than large-valued H^p. Higher values of ω are invariably associated with high H^p values, which shows that the flow around high ω regions has a swirling motion.

The relative spatial organization of E_k and ω is shown in figure 4.28(c). The two quantities reflect large-scale, inertial structures and small-scale, swirling structures, respectively. The joint-PDF shows that high values of the two quantities are mutually exclusive in space, i.e. the fields are anti-correlated. For instance, the probability of finding a high L region, which also has a high ω value, is negligible. A similar anti-correlated distribution is found for H^p and L, in figure 4.28(d). High values of H^p coincide with regions of low L, showing that swirling-flow regions do not correspond with high kinetic energy structures (as measured by L), and vice-versa.

To quantify the volume fraction and degree of spatial overlap between different fields, we construct the joint-CDFs, which are functions of the integration limits α_1, α_2, β_1 and β_2, on the fields f_1 and f_2 comprising a particular joint-PDF. This is calculated as

$$\mathrm{CDF}\left(f_1, f_2; \alpha_1, \alpha_2, \beta_1, \beta_2\right) = \int_{\beta_1}^{\beta_2} \left[\int_{\alpha_1}^{\alpha_2} \mathrm{PDF}(f_1, f_2) \, df_1 \right] df_2 \tag{4.36}$$

The CDF can directly be interpreted as the volume fraction of the region defined by the integration limits, as follows

$$\mathrm{CDF}\left(f_1, f_2; \alpha_1, \alpha_2, \beta_1, \beta_2\right) = \frac{V\left\{\left(\alpha_1 \le f_1 \le \alpha_2\right) \cap \left(\beta_1 \le f_2 \le \beta_2\right)\right\}}{V_t} \tag{4.37}$$

where V is the intersection volume where the condition $\alpha_1 \le f_1 \le \alpha_2$ and $\beta_1 \le f_2 \le \beta_2$ are both met, while V_t is the total volume. The volume fraction of a single field, within prescribed threshold limits, can also be quantified with the CDF as follows

$$\mathrm{CDF}\left(f_1, f_2; \alpha_1, \alpha_2, 0, \infty\right) = \frac{V\left(\alpha_1 \le f_1 \le \alpha_2\right)}{V_t} \tag{4.38}$$

This is because the region $0 \le f_2 \le \infty$ corresponds to the total volume V_t, hence

$$V\left\{\left(\alpha_1 \le f_1 \le \alpha_2\right) \cap V_t\right\} \equiv V\left(\alpha_1 \le f_1 \le \alpha_2\right) \tag{4.39}$$

The CDF can be used to evaluate the degree of spatial inclusivity between fields, $R(\widetilde{f_1}, \widetilde{f_2})$, which can be calculated as

$$R(\widetilde{f_1}, \widetilde{f_2}) = \frac{\mathrm{CDF}\left(f_1, f_2; \alpha_1, \alpha_2, \beta_1, \beta_2\right)}{\mathrm{CDF}\left(f_1, f_2; \alpha_1, \alpha_2, 0, \infty\right)} \tag{4.40}$$

where $\widetilde{f_1}$ and $\widetilde{f_2}$ are conditionally sampled f_1 and f_2 fields, i.e. the region $\widetilde{f_1} \equiv \alpha_1 \le f_1 \le \alpha_2$ and the region $\widetilde{f_2} \equiv \beta_1 \le f_2 \le \beta_2$. The numerator on the right hand side gives the volume fraction of the intersection region $\widetilde{f_1} \cap \widetilde{f_2}$, while the denominator gives the

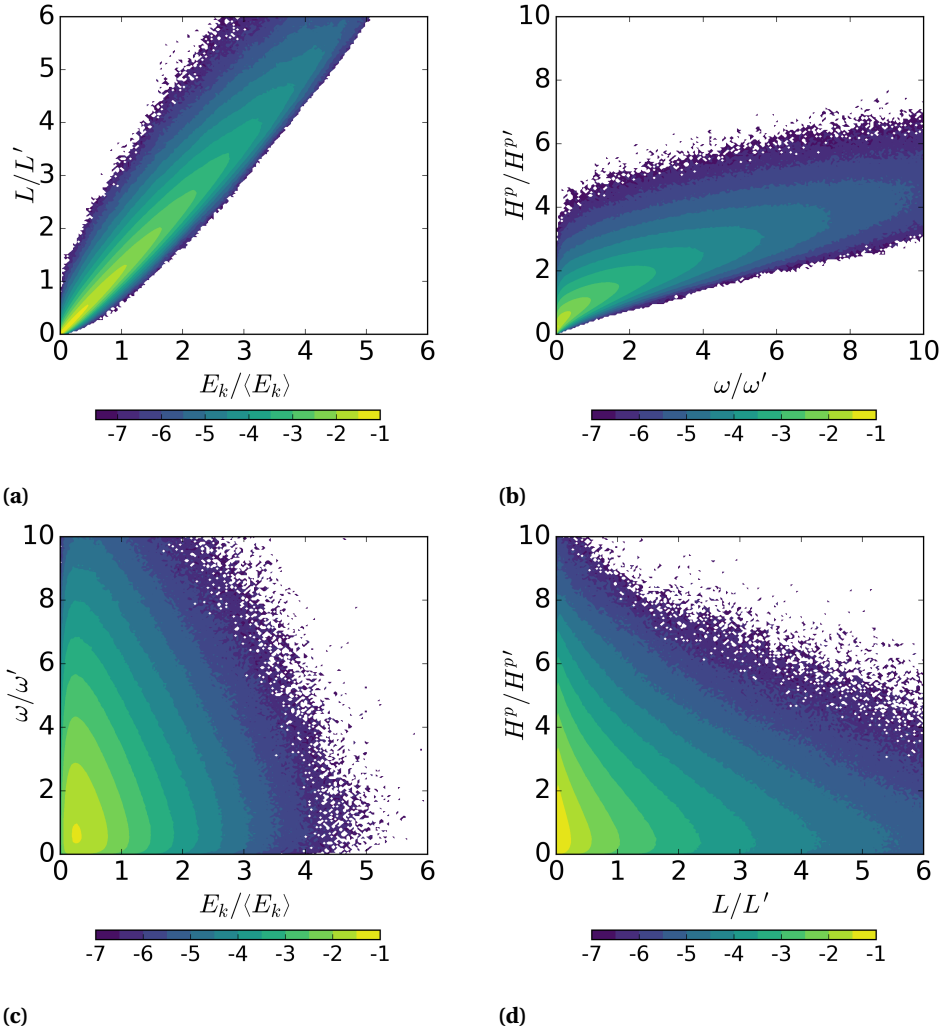

(a) **(b)** **(c)** **(d)**

Figure 4.28: Joint-PDFs of L, E_k, H^p and ω. The colors show logarithmically spaced values.

volume fraction of $\widetilde{f}_1$. Hence, the fraction denotes the degree of inclusivity of the region $\widetilde{f}_2$ in the region $\widetilde{f}_1$. Conversely, $R(\widetilde{f}_2, \widetilde{f}_1)$ gives the inclusivity of $\widetilde{f}_1$ in $\widetilde{f}_2$.

In figure 4.29(a) shows the intersection of the fields L and E_k, i.e. $R(\widetilde{L}, \widetilde{E_k})$ and $R(\widetilde{E_k}, \widetilde{L})$. The regions $\widetilde{L} \equiv L^t \leq L \leq \infty$ and $\widetilde{E_k} \equiv E_k^t \leq E_k \leq \infty$, where the thresholds L^t and E_k^t are multiples of L' and $\langle E_k \rangle$. The L field is found to remain completely enclosed within the corresponding E_k regions, since $R(\widetilde{L}, \widetilde{E_k}) = 1$, showing that higher L values occur *inside* regions of high E_k, and occupy a smaller fraction of the volume. Conversely, $R(\widetilde{E_k}, \widetilde{L})$ becomes successively smaller at higher threshold values, showing that high E_k regions occupy larger spatial regions than high L. This is also reflected in the volume fractions V_f of L and E_k, calculated as CDF$\left(L, E_k; L^t, \infty, 0, \infty\right)$ and CDF$\left(L, E_k; 0, \infty, E_k^t, \infty\right)$, respec-

tively, as shown in figure 4.29(c). At values higher than increasing threshold levels, the L field occupies smaller volume fractions in comparison to E_k. Lastly, the kinetic energy content of the thresholded L and E_k regions is shown in figure 4.29(e). Regions corresponding to $E_k \geq \langle E_k \rangle$, $E_k \geq 2\langle E_k \rangle$, $E_k \geq 3\langle E_k \rangle$ occupy 40%, 10% and 2.5% of the total volume (panel (c)), respectively, and contain 70%, 30% and 9% of the total kinetic energy. Similarly, regions corresponding to $L \geq L'$, $L \geq 2L'$ and $L \geq 3L'$ occupy 30%, 5% and 0.7% of the total volume, while containing 55%, 15% and 3% of the total kinetic energy.

Figure 4.29(b) shows the intersection of the fields H^p and ω, i.e. $R(\widetilde{H^p}, \widetilde{\omega})$ and $R(\widetilde{\omega}, \widetilde{H^p})$, where the regions $\widetilde{H^p} \equiv H^{p\,t} \leq H^p \leq \infty$ and $\widetilde{\omega} \equiv \omega^t \leq \omega \leq \infty$. The fraction of the H^p field contained inside ω regions increases at higher threshold values. This shows, first, that the H^p field occupies successively smaller spatial regions at higher thresholds. Secondly, high H^p values are invariably found *inside* high ω regions, reaffirming that strong vorticity regions contain swirling motion. This can also be seen from figure 4.28(b), where the lower bound on the value of H^p increases with ω. At low threshold values, $R(\widetilde{H^p}, \widetilde{\omega})$ is low, which shows that the H^p field at low values occupies more space in comparison to low ω. This reflected in $R(\widetilde{\omega}, \widetilde{H^p})$, which has high values at low ω. It is further confirmed in figure 4.29(d), which shows that $H^p \geq H^{p'}$ occupies 26% of the volume, while $\omega \geq \omega'$ occupies 17% of the volume. Further, the volume fraction occupied by the H^p field decays much faster than ω, when thresholded at successively higher values. Lastly, panel (f) shows that regions of $H^p \geq H^{p'}$, $H^p \geq 3H^{p'}$ and $H^p \geq 5H^{p'}$ contain 85%, 22% and 3% of the total enstrophy.

Finally, figure 4.30(a) shows the intersection of regions of high vorticity ($\widetilde{\omega} \equiv \omega^t \leq \omega \leq \infty$) with regions of low H^p ($\widetilde{H^p} \equiv 0 \leq H^p \leq H^{p'}$), i.e. $R(\widetilde{\omega}, \widetilde{H^p})$. For all instances of $\omega^t \geq \omega'$, the intersection volume of $\widetilde{\omega}$ with $\widetilde{H^p}$ goes to zero. This confirms that there are no high ω regions in the flow field that are not associated with swirling motion in their vicinity. Figure 4.30(b) shows the intersection of $\widetilde{H^p} \equiv H^{p\,t} \leq H^p \leq \infty$ with $\widetilde{L} \equiv L^t \leq L \leq \infty$, for increasing threshold values. The two fields are found to become increasingly *spatially exclusive* at higher threshold values, which can also be seen from the joint-PDFs in figure 4.28(d). This implies that high kinetic energy and strong vorticity regions are spatially isolated, which could be a consequence of the dynamical separation between high kinetic energy and strong vorticity structures.

4.5.6. FLOW STRUCTURES IN HOMOGENEOUS, ISOTROPIC TURBULENCE

In this section, we focus on answering two questions regarding flow structures that comprise a (homogeneous, isotropic) turbulent flow field. The first question is, simply put, "*What is the structure of the flow associated with (i) high kinetic energy and (ii) high enstrophy regions?*", as both these quantities pertain to different scales of the flow. High kinetic energy is concentrated at the low wavenumbers, i.e. the largest scales, while high enstrophy (or vorticity) is concentrated at the high wavenumbers, i.e. the smallest scales. It is now well known that strong vorticity regions are associated with strong swirling-flow in their vicinity [19, 20], however, the structure of the flow in high kientic energy regions is not well known and these regions are usually referred to as "large eddies" or "energy containing eddies". The tools presented in the previous sections allow us to identify and quantify the flow structures in a systematic way, and to disentangle them from the surrounding flow. This allows to determine to what extent are the structures "self-contained" (i.e. are self-generating, in a Biot-Savart sense), and to what extent they

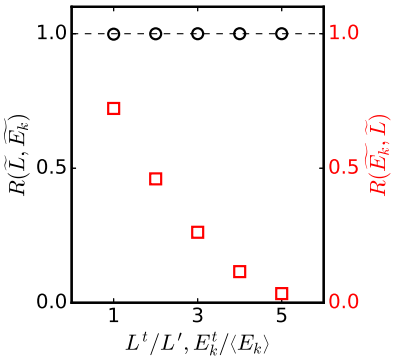

(a) Intersection volumes of $\widetilde{L}$ and $\widetilde{E_k}$.

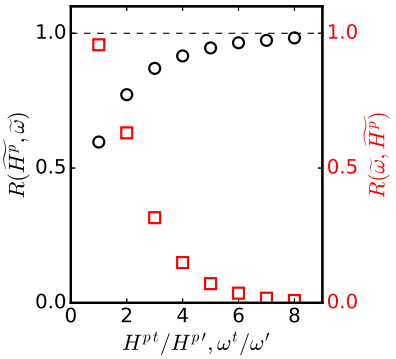

(b) Intersection volumes of $\widetilde{\omega}$ and $\widetilde{H^p}$.

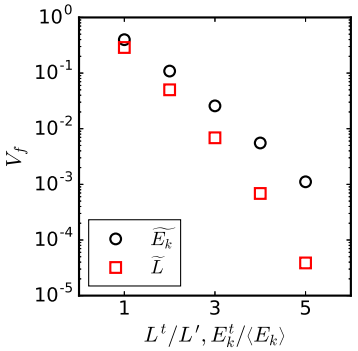

(c) Volume fraction V_f of $\widetilde{L}$ and $\widetilde{E_k}$.

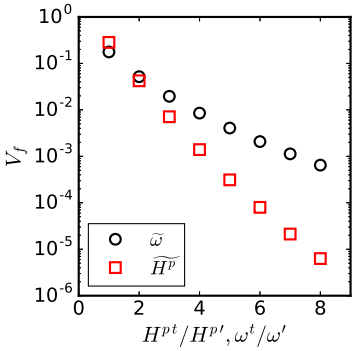

(d) Volume fraction V_f of $\widetilde{\omega}$ and $\widetilde{H^p}$.

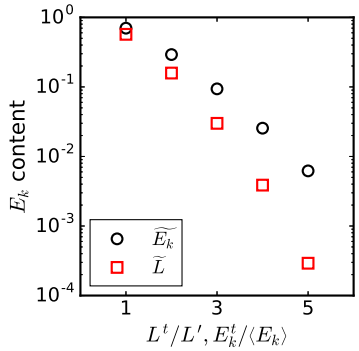

(e) Kinetic energy fraction contained in $\widetilde{L}$ and $\widetilde{E_k}$ regions.

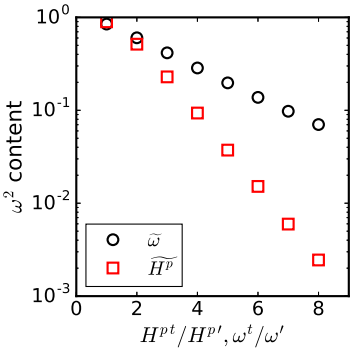

(f) Enstrophy fraction contained in $\widetilde{\omega}$ and $\widetilde{H^p}$ regions.

Figure 4.29: Statistics of intersection volumes between (a) $\widetilde{L}$ and $\widetilde{E_k}$, and (b) $\widetilde{H^p}$ and $\widetilde{\omega}$ regions, where each region $\widetilde{\psi} \equiv \psi_1 \leq \psi \leq \psi_2$. Panels (c) and (d) show the volume fractions of different thresholded regions of the fields, and panels (e) and (f) show the kinetic energy and enstrophy contents of the thresholded regions, respectively.

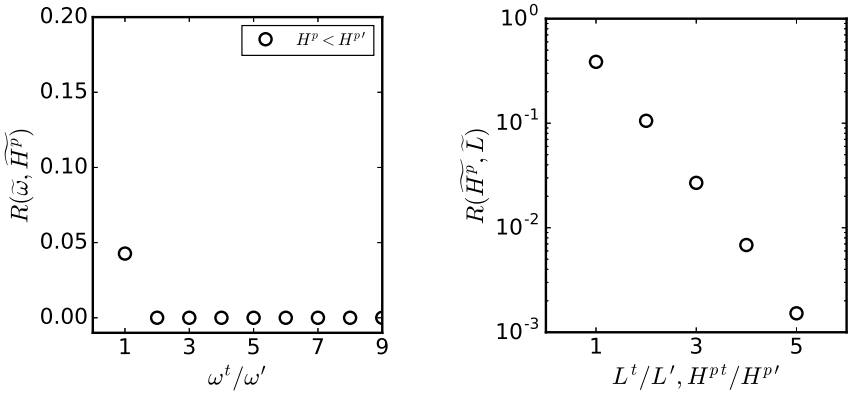

(a) Intersection volumes of $\omega > \omega^t$ with $H^p < H^{p\prime}$ regions.

(b) Intersection volumes of $H^p > H^{pt}$ and $L > L^t$ regions.

Figure 4.30: Intersection volumes of (a) high ω regions with low H^p regions and (b) high H^p regions with high L regions.

are a result of the "surrounding flow" (i.e. they are not self-generating, in a Biot-Savart sense). Closely related to this is our second question, "*What range of vorticity generates these structures in a Biot-Savart sense?*". This will reveal the vorticity composition of the different structures, possibly shedding light into the organization of the flow structures, with hints perhaps regarding the dynamics of the turbulence process.

First, we will focus on the individual flow structures, then we look at the Biot-Savart contributions from a statistical perspective. Finally, we summarize the picture that emerges from these two perspectives.

We first look at high kinetic energy (E_k) regions. Figure 4.31, panel (a) shows three individual, isolated contours of $L = 2.5L'$, which marks regions of relatively high kinetic energy. The local flow streamlines have also been shown, which have been generated from points distributed within a small region around the core of the correlation kernels. Panel (b) shows the flow streamlines alone, which clearly shows that the high kinetic energy regions comprise well aligned streamlines, with a *jet-like* structure, i.e. the local streamlines become parallel to each other. The streamlines diverge into more chaotic patterns away from the high E_k regions, showing that the coherence of the inertia containing structures is localized.

To unravel the vorticity contributions that generate high E_k structures, we first reconstruct the self-generated velocity field of these structures. This is done by applying the Biot-Savart law to the vorticity contained *inside* the $L = 2.5L'$ kernels. In this calculation, any regions overlapping with $H^p > 5H^{p\prime}$ are excluded, to generate the velocity streamlines using *only* the vorticity contained in regions of high kinetic energy (while the overlap between $2.5L'$ and $5H^{p\prime}$ regions is very small, see figure 4.28d). Panel (c) shows that the self-generated velocity field of the high E_k regions, where the streamlines have been generated using the same points and parameters as in panel (b). The self-generated flow in E_k regions is found, first, to be very weak (the self-generated velocity amplitude

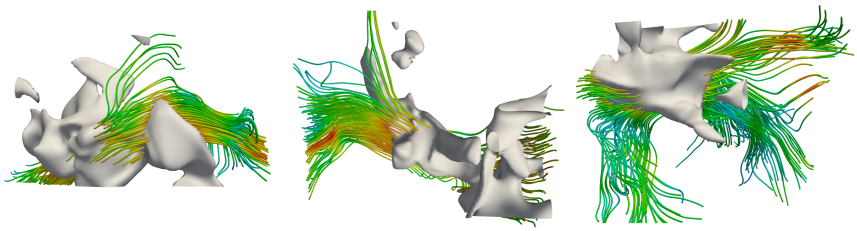

(a) Contours of $L = 2.5L'$ along with local flow streamlines.

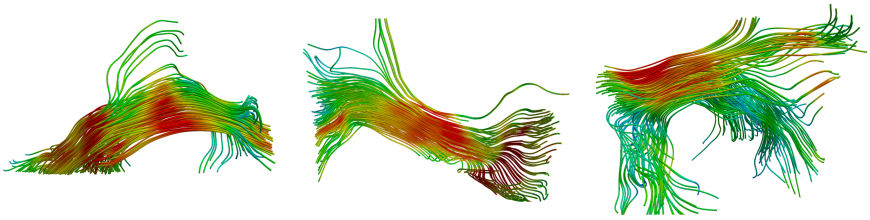

(b) Local flow streamlines.

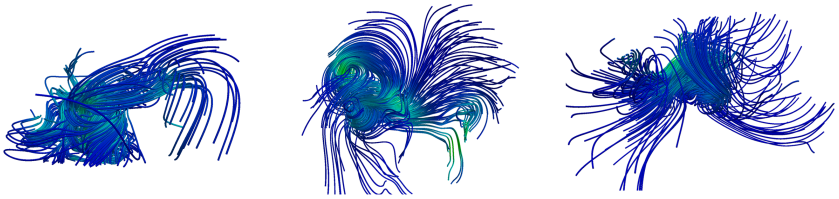

(c) Self-generated flow streamlines.

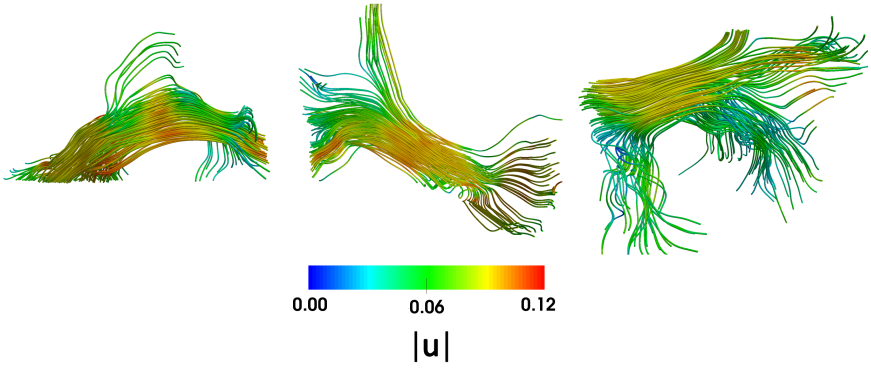

(d) Externally induced flow streamlines.

Figure 4.31: The flow structure of high kinetic energy regions is shown to be jet-like. (a) High E_k regions as identified by contours of L have been isolated, and shown together with the local flow streamlines, which have also been shown separately in panel (b). (c) The self-generated flow in high E_k regions, computed using the vorticity inside the $2.5L'$ contours (while excluding regions with $H^p > 5H^{p\prime}$). (d) The externally-induced flow field, computed using the rest of the vorticity field. The colours show the velocity magnitude $|\mathbf{u}|$ in lattice units, i.e. $\Delta x/\Delta t$.

is roughly 10 times smaller than the total velocity). Secondly, the structure of the self-generated velocity field is very different from the total velocity streamlines. These two aspects show that the self-generated velocity field in regions of high E_k contribute little to the total velocity field. Panel (d) shows the externally induced velocity field, which is calculated by applying the Biot-Savart law to the remainder of the vorticity field, i.e. all regions where $L < 2.5L'$ (while also including regions with $H^p > 5H^{p\prime}$). The externally induced velocity streamlines coincide very well with the total velocity streamlines, which shows clearly that high kinetic energy regions are *externally* induced structures (in the Biot-Savart sense), with highest contribution from the *non-local* vorticity. Note that the results are similar for slightly different levels of the L threshold used to determine the correlation kernels, i.e. $2.0 \leq L \leq 3.0$. At much lower or higher L, differences will begin to appear, which shall be subsequently discussed.

It remains to be ascertained which range of vorticity contributes most to the generation of high E_k regions. From the outset, possible contributions can come from the strong vorticity, i.e. $\omega \geq 2\omega'$, which forms the skirts of the vorticity PDF but occupies only a small fraction of the volume, and from the background vorticity, i.e. $\omega < 2\omega'$, which has a lower magnitude but permeates most of the volume. It can be argued that the weak vorticity (which is part of the background vorticity field), cannot contribute significantly to the generation of high E_k regions, since their non-local Biot-Savart contribution will be negligible. This leaves the intermediate background vorticity and the strong vorticity.

We first test the strong vorticity contribution to the generation of E_k regions. To illustrate, a single high E_k structure is shown in figure 4.32(a). The Biot-Savart velocity field is then reconstructed using multiple vorticity thresholds $\omega^t \in \{2\omega', 3.5\omega', 5\omega'\}$. Panel (b) and (c) show the velocity field generated by $\omega < \omega^t$ and $\omega > \omega^t$ regions, respectively. As ω^t increases, the flow generated by the $\omega > \omega^t$ becomes weaker in magnitude. It hence becomes evident that very strong vorticity, i.e. $\omega > 3.5\omega'$, also has a negligible contribution to the generation of the high E_k structure. The flow field in panel (a) appears to be generated mostly by the intermediate background vorticity, since the flow generated by the range $\omega < 2\omega'$ recovers most of the flow features and velocity magnitude.

This result also hints at the dynamical separation between the large-scale energy containing eddies and the small-scale swirling-flow regions. Since the small-scales arise from the decay of the larger scales, there is a temporal delay in their generation, such that the large-scales at any time will lead to strong enstrophy *after* a time delay of approximately $\Delta t \approx T^\star$, where $T^\star$ is the large-eddy timescale. This is reflected in the fact that contemporary strong vorticity regions do not generate (in a Biot-Savart sense) the larger scales of a given time instant, as the they have a dynamical origin in the past (i.e. the large-scales at $-\Delta T^\star$). Hence the Biot-Svart generation of high E_k regions, and the spatial distribution of E_k and high ω, bear imprints of the turbulence dynamics. This also supports the findings of spatial exclusivity of high kinetic energy and strong vorticity regions, see figures 4.27(c) and 4.30(b). Note that this reconstruction was performed for several different E_k regions, and the results were found to be very similar.

Similarly to the analysis of high E_k regions, we now test high vorticity (or equivalently, enstrophy) regions to ascertain the vorticity contributions in generating small-scale swirling-flow structures. Figure 4.33, panel (a) shows three instances of $H^p = 5H^{p\prime}$ regions with the local flow streamlines (which have been initiated from a collection of points distributed near the core of each correlation kernel), while panel (b) shows the

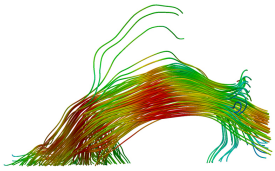

(a) An instance of a high E_k region.

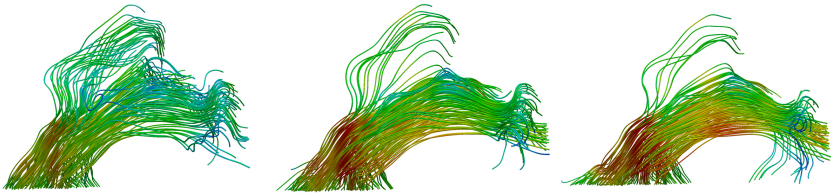

(b) Flow reconstructed using the vorticity in the range $\omega < \omega^t$, where $\omega^t \in \{2\omega', 3.5\omega', 5\omega'\}$, from left to right.

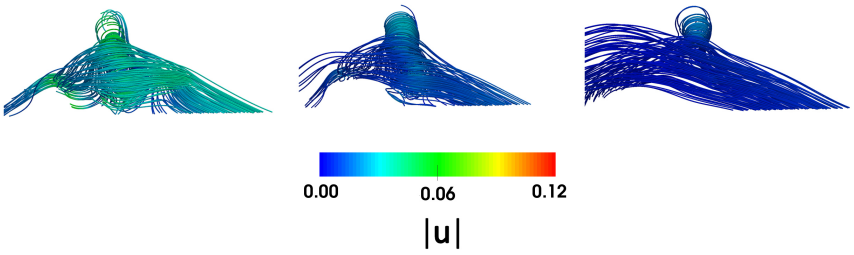

(c) Flow reconstructed using the vorticity in the range $\omega > \omega^t$, where $\omega^t \in \{2\omega', 3.5\omega', 5\omega'\}$, from left to right.

Figure 4.32: A single high E_k region has been shown in panel (a). Panels (b) and (c) show the local flow streamlines as generated by the velocity field reconstructed with the Biot-Savart law, by thresholding the vorticity as $\omega < \omega'$ and $\omega > \omega'$, respectively, where ω^t is a threshold value. The colours show the velocity magnitude $|\mathbf{u}|$ in lattice units, i.e. $\Delta x/\Delta t$.

streamlines alone. The first thing to note is that the velocity of these structures is mostly in the intermediate and low E_k range (since u is in an intermediate range). The core of these structures comprise a strongly swirling motion (as indicated by the high H^p value), while the flow decays into more disordered streamlines away from the core regions.

Panel (c) shows the self-generated velocity field, which is generated using the Biot-Savart law applied to all $H^p > 5H^{p\prime}$ regions. As expected, the self-generated streamlines show a swirling-flow, including an instance of two vortices interacting in a figure-eight velocity pattern (in panel (c), left). The self-generated velocity, distant from the core region, has a low magnitude. This shows that the strongly swirling regions influence the velocity field only within a small region of influence (due to the rapid decay of the Biot-Savart contribution). The externally induced velocity streamlines in panel (d) are at an intermediate E_k range, and closely resemble the total velocity field streamlines outside

of the core regions. This also indicates that the cutoff $H^p = 5H^{p\prime}$ is high for swirling flow regions (occupying less than 1% of the volume, see figure 4.23d). The vorticity field in the regions marked by $H^p < 5H^{p\prime}$ also contributes to the swirling-flow structures. We test this by thresholding the vorticity field at different levels, and reconstructing the Biot-Savart velocity field. This also gives a more natural indication of the vorticity range which generates swirling motion, instead of thresholding based upon the H^p field.

Figure 4.34 shows one instance of a high H^p region, with the local flow streamlines in panel (a), which have a strong swirling motion in the vicinity of the correlation kernel. We then show the Biot-Savart velocity field reconstructions obtained using $\omega < \omega^t$ and $\omega > \omega^t$, in panels (b) and (c), respectively, where $\omega^t \in \{2\omega', 3.5\omega', 5\omega'\}$. Interestingly, it is found that the flow generated by $\omega < 5\omega'$ almost completely resembles the original flow structure, showing that the contribution from $\omega > 5\omega'$ is very weak and limited to a very small region near the core of the swirling structure. Further, the flow generated by $\omega > 2\omega'$, seems to resemble the swirling flow region to a large extent, while the contribution from $\omega < 2\omega'$ is not insignificant either. This seems to suggest that the swirling flow regions are a superposition of self-generating swirls on top of a background vorticity induced velocity field, which we now quantify.

These results give a clear picture of the flow structures that together comprise turbulence fields. In summary, the high E_k regions are localized jet-like flows, which themselves contain very low levels of vorticity, and are hence externally induced structures, with dominant contributions of the intermediate vorticity field. The strong enstrophy regions are interspersed in a more or less random manner through the flow field, as they only strongly influence the flow in their immediate neighbourhood, and do not add up together, in a Biot-Savart sense, to give rise to larger structures, or those with high E_k. We also verify in Appendix 4.A that jet-like and swirling flow structures correspond to high L and high H^p regions, respectively, in the JHTD dataset.

4.6. CONCLUSIONS

In this paper, we developed mathematical tools for identifying instantaneous, spatial structures in vector fields associated with turbulent flows. We focused on structures that have a finite spatial extent, and can be found in snapshots of the vector fields (i.e. they are instantaneous). By taking coherence to mean correlation, in the context of vector fields, we began with a generalization of the correlation tensor, and introduced new correlation measures based upon certain flow types. For instance, high amplitude regions in the velocity field with parallel/anti-parallel streamlines ($\mathbf{L}$ and $\mathbf{L^s}$), high amplitude regions in the vorticity field with parallel/anti-parallel streamlines ($\mathbf{G}$ and $\mathbf{G^s}$) and swirling-flow in the vicinity of strong vorticity regions ($\mathbf{H^p}$). All these measures yield a pseudo-vector field, with three values at each point, one for each spatial direction. We tested these correlation measures against canonical flows like Oseen and Burgers vortices, and then applied them to datasets from simulations of homogeneous, isotropic turbulence. Further, reconstructing the flow field using the Biot-Savart law revealed interesting aspects regarding the vorticity contributions to the generation of velocity field structures. The main findings are summarized below:

1. We find that the velocity field has two distinct coherent flow types which characterize the high turbulence kinetic energy large-scales and the high enstrophy

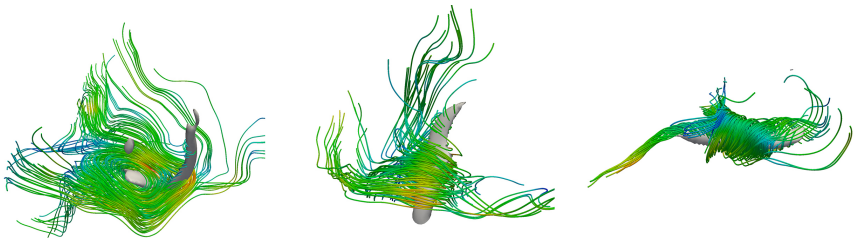

(a) Contours of $H^p = 5H^{p\prime}$ along with local flow streamlines.

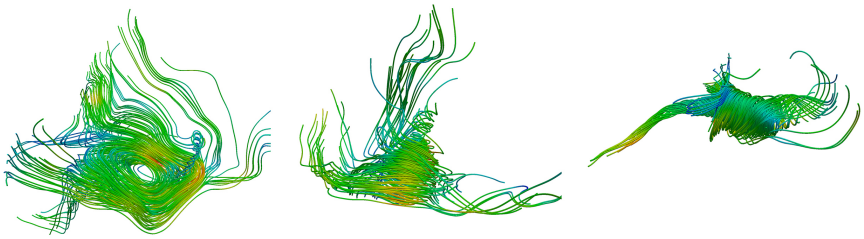

(b) Local flow streamlines.

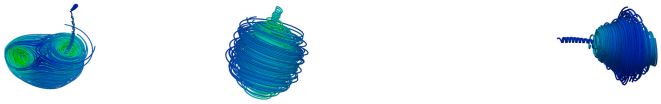

(c) Self-generated flow streamlines.

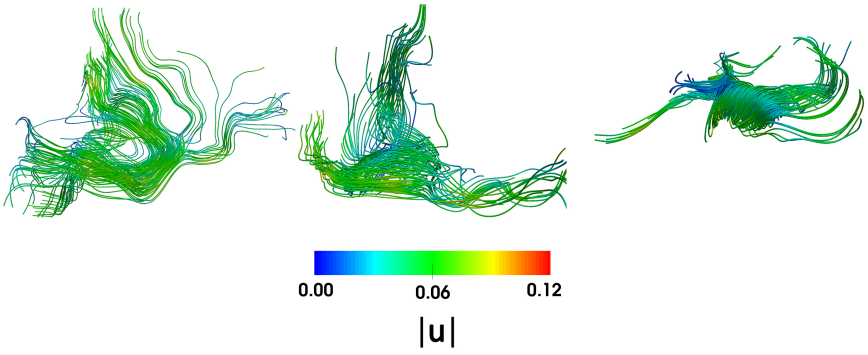

(d) Externally induced flow streamlines.

Figure 4.33: The flow around high H^p regions, which also coincide with high ω, is shown to be swirling-motion. (a) High H^p regions as identified by contours of $5H^{p\prime}$ have been isolated, and shown together with the local flow streamlines. (b) The local flow streamlines are shown separately. (c) The self-generated flow, computed using the vorticity inside the $5H^{p\prime}$ contours. (d) The externally-induced flow field, computed from the rest of the vorticity field. The colours show the velocity magnitude $|\mathbf{u}|$ in lattice units, i.e. $\Delta x/\Delta t$.

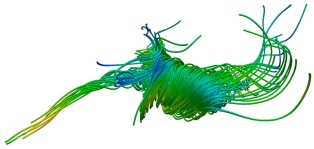

(a) An instance of a high H^p structure.

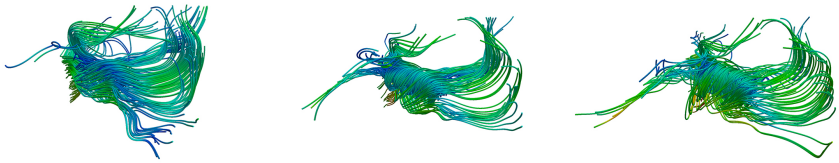

(b) Flow reconstructed using $\omega < \omega^t$, where $\omega^t \in \{2\omega', 3.5\omega', 5\omega'\}$, left to right).

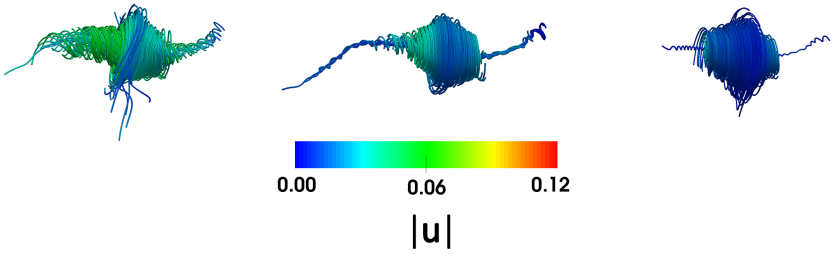

(c) Flow reconstructed using $\omega > \omega^t$, where $\omega^t \in \{2\omega', 3.5\omega', 5\omega'\}$, left to right).

Figure 4.34: A single high enstrophy region has been shown in panel (a). Panels (b) and (c) show the local flow streamlines as generated by the velocity field reconstructed with the Biot-Savart law, by thresholding the vorticity at values lower than and higher than increasing threshold values, respectively. The colours show the velocity magnitude $|\mathbf{u}|$ in lattice units, i.e. $\Delta x/\Delta t$.

small-scales.

2. Regions of high kinetic energy (E_k) are found to be locally *jet-like*. These regions yield large values for the **L** and $\mathbf{L^s}$ correlations, reflecting that (a) the flow streamlines in these regions are well aligned and (b) the velocity has a large amplitude in these regions. The joint distribution of L and E_k further shows that increasing levels of E_k lead to an increase in the flow organization as well.

3. Regions of high enstrophy (ω^2) are found to coincide with *swirling motion* in their neighbourhood, which has been shown before [19, 20, 36], while locally yielding large values for the $\mathbf{H^p}$ correlation. High ω^2 and H^p regions are both *worm-like* and small-scaled. The joint distribution of H^p and ω shows that there are no strong vorticity regions that are not associated with swirling motion in their vicinity, for the case of homogeneous, isotropic turbulence, considered in this study.

4. The statistics of the spatial organization of the correlations, viz-a-vis kinetic energy and vorticity, show that the jet-like and swirling-flow regions are spatially ex-

clusive. This hints at the dynamical separation between the high kinetic energy large scales and the high enstrophy small scales. This dynamical separation is the process of generation of high enstrophy structures from the reorganization and non-local, non-linear interactions of high kinetic energy structures. How this process is mediated is left for future work. The high enstrophy structures, in turn, are dynamically insignificant in determining the overall flow, as has also been argued in Tsinober [2].

5. The Biot-Savart reconstruction of the velocity field shows that the high E_k regions are not self-generating, as their own vorticity content is negligible. This shows that these structures are generated by non-local vorticity contributions. Conditionally sampling the vorticity field further reveals that strong-vorticity has a negligible contribution in the generation of large-scale inertial structures. This is a further hint regarding the dynamical separation between the large-scales and the small-scales. Strong-vorticity regions are spatially organized in such a manner that they remain mostly non-interacting with the remainder of the velocity field, such that they do not combine their influences to generate a large-scale structure. It is found that the background vorticity generates the high kinetic energy structures, almost entirely.

6. The structure of strong enstrophy, swirling-flow regions is found to be the result of a combination of background vorticity induced flow field and the self-induced swirling-flow. The influence of the strong vorticity regions does not extend far due to the rapid decay of the Biot-Savart contribution.

7. We find that the turbulence velocity field, including regions both of high kinetic energy and high enstrophy, is significantly generated, in a Biot-Savart sense, by the "background vorticity field" which permeates the volume, and occupies more than 90% of it. This range of vorticity corresponds to the narrow, (almost) Gaussian peak of the vorticity PDFs, while completely ignoring the long intermittency tails which correspond to extreme vorticity events. Usually, most research has focused on extreme vorticity, due to its influence on flow irreversibility, mixing and particle dispersion. It turns out that the bulk of the flow, and in particular, the kinetic energy containing regions, are completely impervious to extreme vorticity. The background vorticity can further be classified into an "intermediate" and a "weak" range, where the weak range of vorticity remains dynamically insignificant, and does not contribute much to the generation of the different flow structures.

The structural view of turbulence fields, as evident from our results, is illustrated in figure 4.35. Although our study does not explore the dynamics of structures, it seems likely that the overall organization of turbulence, along with its statistical features, emerges from the combined contribution of the permeating background vorticity. The coherence of the large, kinetic energy containing jet-like structures, is found to be a consequence of the background vorticity induced flow organization, which shows that the large inertial structures are not self-determining. Similarly, strong enstrophy structures are an outcome of the superposition of the background vorticity induced flow organization and the self-induced swirling-flow organization. In our work we did not investigate an intermediate range of coherent velocity structures (corresponding to the inertial range),

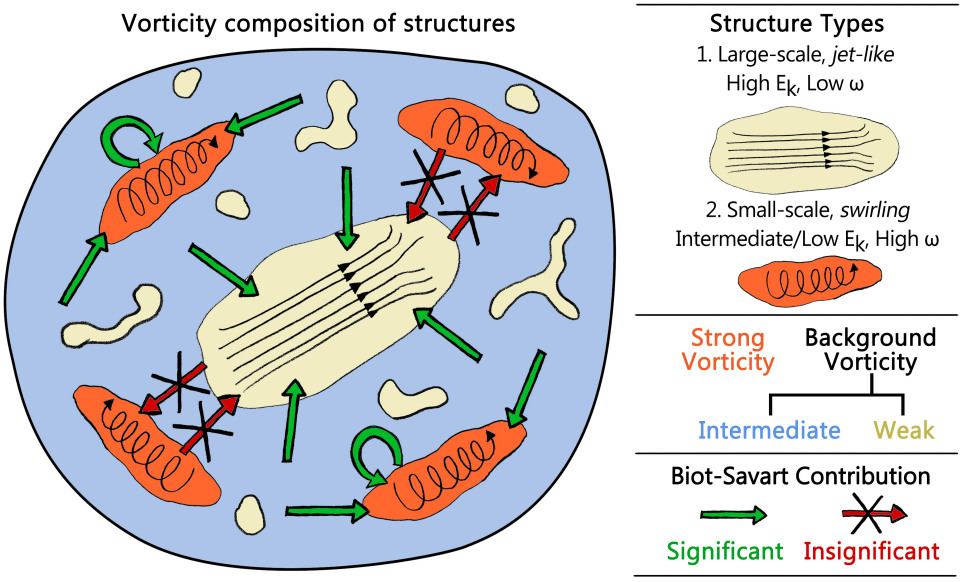

Figure 4.35: Schematic of the organization of turbulence structures along with the Biot-Savart contributions that generate them. The vorticity ranges are colour coded with strong vorticity (orange), intermediate background vorticity (blue) and weak vorticity (off white). The large-scale kinetic energy structures are *jet-like*, and do not have a significant self-generation due to their low vorticity. Their coherence is induced (in a Biot-Savart sense), almost entirely, by non-local, intermediate background vorticity contributions (shown in blue), while the contribution from strong vorticity to their generation is negligible. Strong vorticity regions have a local *swirling motion* in the velocity field. These structures are a superposition of an intermediate background vorticity generated flow and a self-induced accentuation of the swirling flow.

clearly establishing the organization of which is left for future work. The turbulence velocity field, hence, *emerges* (in the Biot-Savart sense) from the *global* vorticity field.

The traditional "cascade" perspective of turbulence dynamics explains the phenomena as being dominated by the high kinetic energy, large-scale structures, which in-turn determine the structure and generation of successively smaller scales via some eddy break-up mechanism, which goes back to the idea of Richardson [1]. Within the limits of our work, we show that turbulence can also be considered as an alternative paradigm. Instead of large scales dominating the dynamics, we find that, in a Biot-Savart sense, the large scales are themselves induced by non-local vorticity contributions. Similarly, most of the velocity field, which contains a range of "scales" (which yield the $k^{-5/3}$ spectral scaling), are also generated in a Biot-Savart sense by a permeating, intermediate range background vorticity. This view suggests that the organization of turbulence flow fields need not necessarily be a strict hierarchy, and may in-fact be a consequence of the non-local and non-linear interactions between structures dominated by the intermediate vorticity. Further investigation of the lifecycle of these velocity and vorticity structures, along with identification of the typical force-field structures that drive the dynamics (i.e. structures associated with the pressure gradient and viscous stress fields), will help illu-

minate or dispel notions regarding the existence of hierarchical coherent structures that has been expounded in different representational spaces, while having been elusive in the physical space where the phenomenon of turbulence occurs.

The tools presented in this paper (or modified versions of them) can be readily applied to identifying structures in any scalar or vector fields (not just turbulence) like pressure, strain or eigenvector distributions, electromagnetic fields, to different dimensional data-sets, or be recast as time-correlations to study the temporal nature of coherence. We believe these tools, combined with the Biot-Savart construction, open a new door into studying the dynamics of turbulence from the perspective of its constituent structures, and may pave the way towards a new structural description of turbulence organization.

4

ACKNOWLEDGEMENTS

SM would like to thank Dr. Zhao Wu (Johns Hopkins University) for providing access to the JHTD turbulence database.

APPENDIX

4.A. VALIDATION AGAINST JHTD DATASET

In this section, we apply the correlations to a reference dataset of homogeneous, isotropic turbulence from the Johns Hopkins Turbulence Databases (JHTD) [37, 38], to show that, qualitatively, the results we presented using our in-house code are similar to a different turbulence dataset. We use the forced isotropic turbulence dataset, which is a pseudo-spectral simulation performed on 1024^3 nodes, with a Taylor Reynolds number of $Re_\lambda \sim 433$ (note that our intention is not to study the effect of the different Re_λ in the reference dataset). The correlations are calculated by integrating over $\Lambda \approx \lambda$, which was shown to be a reasonable choice in section 4.5.3.

Figure 4.36 shows the kinetic energy E_k field (normalized by the mean $\langle E_k \rangle$) in panel (a) and the amplitude of the $\mathbf{L}$ correlation field (normalized by L') in panel (b). The two fields look very similar, although the L field appears more smooth with fewer fine scale structures, as was also found in our own simulations. Panel (c) shows contours of the vorticity field, and panel (d) shows contours of the H^p field, which are again very similar to our results, with the difference that the JHTD simulation is performed at a much higher Re_λ value, due to which the fine scale vorticity structures appear smaller than in our simulations.

We also verify that the structure of high kinetic energy regions and strong vorticity are similar in the JHTD dataset. Figure 4.37, panel (a) shows a single region of high kinetic energy, marked by the contour of $L = 2.5L'$ along with the local streamlines (coloured by $E_k / \langle E_k \rangle$), which have also been shown separately in panel (b). The streamlines are initialized from a spherical region of radius λ at the core of the correlation kernel, and integrated upto 10λ. The local flow structure is found to be jet-like, as the streamlines align parallel to each other in the core of the correlation contour, where E_k also assumes its maximum value. The streamlines lose their kinetic energy over distance, where they begin to become more disorganized.

Figure 4.38 shows local the flow structure in the vicinity of a $H^p = 5H^{p\prime}$ region in panel (a), along with the streamlines shown separately in panel (b). As expected, the

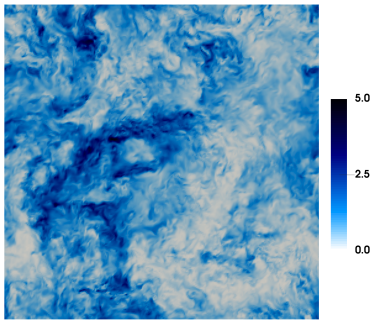

(a) E_k normalized with $\langle E_k \rangle$, shown at an arbitrary crossectional plane.

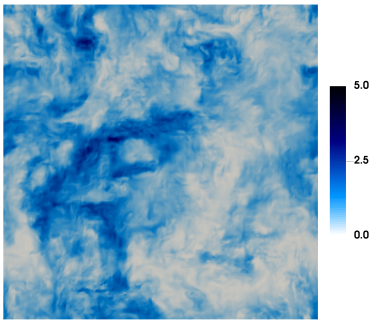

(b) Amplitude of **L** normalized with L', shown at the same crossectional plane.

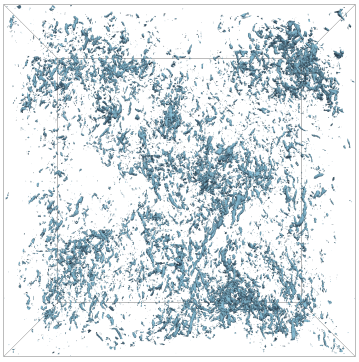

(c) Contours of $\omega = 3\omega'$.

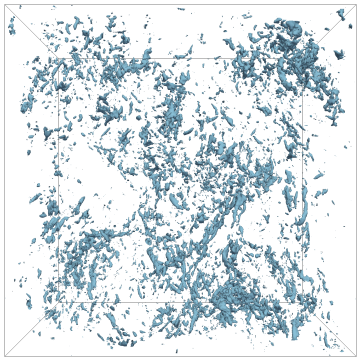

(d) Contours of $H^p = 5H^{p\prime}$.

Figure 4.36: Flow field snapshots from the JHTD isotropic turbulence dataset have been shown along with correlations **L** and $\mathbf{H^p}$. Kinetic energy E_k (a) and **L** (b) have very similar profiles, where **L** appears more smooth. The vorticity contours (c) and H^p contours (d) appear to be similar as well.

high H^p regions have a swirling motion in their vicinity and coincide with regions of high enstrophy. The streamlines show moderate to low kinetic energy values for these structures.

REFERENCES

[1] L. Richardson, *Weather prediction by numerical process,* Cambridge University Press (1922).

[2] A. Tsinober, *The essence of turbulence as a physical phenomenon*, Vol. 10 (Springer, 2014) pp. 978–94.

[3] U. Frisch, *Turbulence: the legacy of AN Kolmogorov* (Cambridge university press,

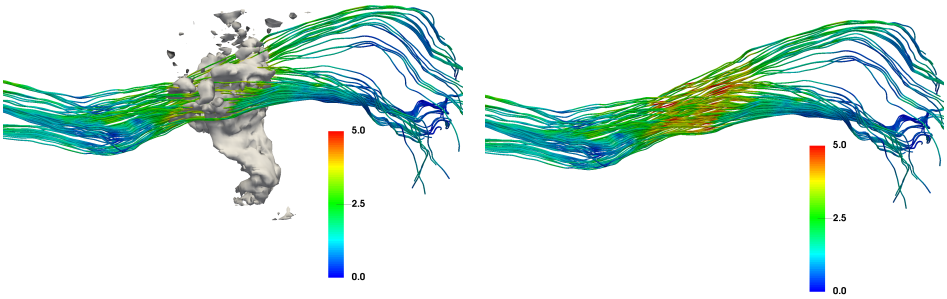

(a) A single $L = 2.5L'$ region along with local flow streamlines.

(b) Local flow streamlines shown separately.

Figure 4.37: The structure of high E_k regions in the JHTD dataset are also found to be jet-like. The streamlines have been coloured by the normalized kinetic energy $E_k / \langle E_k \rangle$.

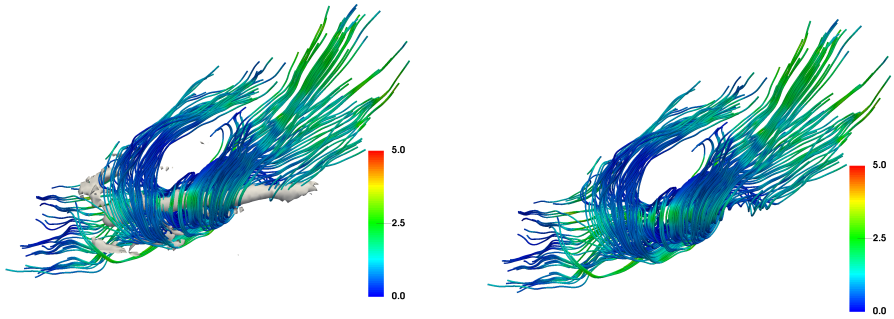

(a) A single $H^p = 5H^{p\prime}$ region along with local flow streamlines.

(b) Local flow streamlines shown separately.

Figure 4.38: The flow around high $\mathbf{H^p}$ regions is found to be swirling. The streamlines have been coloured by the normalized kinetic energy $E_k / \langle E_k \rangle$.

1995).

[4] B. Dubrulle, *Beyond kolmogorov cascades,* Journal of Fluid Mechanics **867** (2019).

[5] J. Jeong and A. Hussain, *On the identification of a vortex,* Journal of fluid mechanics **285**, 69 (1995).

[6] Y. Dubief and F. Delcayre, *On coherent-vortex identification in turbulence,* Journal of turbulence **1**, 011 (2000).

[7] M. Chong, A. Perry, and B. Cantwell, *A general classification of three-dimensional flow fields,* Physics of Fluids A: Fluid Dynamics **2**, 765 (1990).

[8] G. Haller, *An objective definition of a vortex,* Journal of fluid mechanics **525**, 1 (2005).

[9] M. Farge and K. Pellegrino, G.and Schneider, *Coherent vortex extraction in 3d turbulent flows using orthogonal wavelets,* Physical Review Letters **87**, 054501 (2001).

[10] A. Hussain, *Coherent structures and turbulence,* Journal of Fluid Mechanics **173**, 303 (1986).

[11] L. Sirovich, *Turbulence and the dynamics of coherent structures. i. coherent structures,* Quarterly of applied mathematics **45**, 561 (1987).

[12] T. Peacock and J. Dabiri, *Introduction to focus issue: Lagrangian coherent structures,* (2010).

[13] T. Peacock and G. Haller, *Lagrangian coherent structures: The hidden skeleton of fluid flows,* Physics today **66**, 41 (2013).

[14] G. Haller, *Lagrangian coherent structures,* Annual Review of Fluid Mechanics **47**, 137 (2015).

[15] F. Waleffe, *On a self-sustaining process in shear flows,* Physics of Fluids **9**, 883 (1997).

[16] F. Waleffe, *Exact coherent structures in channel flow,* Journal of Fluid Mechanics **435**, 93 (2001).

[17] K. Deguchi and P. Hall, *Canonical exact coherent structures embedded in high reynolds number flows,* Philosophical Transactions of the Royal Society of London A: Mathematical, Physical and Engineering Sciences **372**, 20130352 (2014).

[18] A. Lozano-Durán and J. Jiménez, *Time-resolved evolution of coherent structures in turbulent channels: characterization of eddies and cascades,* Journal of Fluid Mechanics **759**, 432 (2014).

[19] Z. She, E. Jackson, and S. Orszag, *Intermittent vortex structures in homogeneous isotropic turbulence,* Nature **344**, 226 (1990).

[20] J. Jiménez, A. Wray, P. Saffman, and R. Rogallo, *The structure of intense vorticity in isotropic turbulence,* Journal of Fluid Mechanics **255**, 65 (1993).

[21] F. Moisy and J. Jiménez, *Geometry and clustering of intense structures in isotropic turbulence,* Journal of fluid mechanics **513**, 111 (2004).

[22] F. Waleffe, *The nature of triad interactions in homogeneous turbulence,* Physics of Fluids A: Fluid Dynamics **4**, 350 (1992).

[23] F. Argoul, A. Arneodo, G. Grasseau, Y. Gagne, E. Hopfinger, and U. Frisch, *Wavelet analysis of turbulence reveals the multifractal nature of the richardson cascade,* Nature **338**, 51 (1989).

[24] A. Alexakis and L. Biferale, *Cascades and transitions in turbulent flows,* Physics Reports (2018).

[25] F. Toschi, L. Biferale, G. Boffetta, A. Celani, B. Devenish, and A. Lanotte, *Acceleration and vortex filaments in turbulence,* Journal of Turbulence , N15 (2005).

[26] J. Bec, L. Biferale, G. Boffetta, A. Celani, M. Cencini, A. Lanotte, S. Musacchio, and F. Toschi, *Acceleration statistics of heavy particles in turbulence,* Journal of Fluid Mechanics **550**, 349 (2006).

[27] J. Wu, H. Ma, and M. Zhou, *Vorticity and vortex dynamics* (Springer Science & Business Media, 2007).

[28] L. Biferale, P. Perlekar, M. Sbragaglia, S. Srivastava, and F. Toschi, *A lattice boltzmann method for turbulent emulsions,* in *Journal of Physics: Conference Series*, Vol. 318 (IOP Publishing, 2011) p. 052017.

[29] K. Alvelius, *Random forcing of three-dimensional homogeneous turbulence,* Physics of Fluids **11**, 1880 (1999).

[30] A. Ten Cate, E. Van Vliet, J. Derksen, and H. Van den Akker, *Application of spectral forcing in lattice-boltzmann simulations of homogeneous turbulence,* Computers & fluids **35**, 1239 (2006).

[31] A. Ten Cate, J. Derksen, L. Portela, and H. Van Den Akker, *Fully resolved simulations of colliding monodisperse spheres in forced isotropic turbulence,* Journal of Fluid Mechanics **519**, 233 (2004).

[32] P. Perlekar, L. Biferale, M. Sbragaglia, S. Srivastava, and F. Toschi, *Droplet size distribution in homogeneous isotropic turbulence,* Physics of Fluids **24**, 065101 (2012).

[33] S. Mukherjee, O. Safdari, A.and Shardt, S. Kenjeres, and H. Van den Akker, *Droplet-turbulence interactions and quasi-equilibrium dynamics in turbulent emulsions,* Journal of Fluid Mechanics **878**, 221 (2019).

[34] P. Moin and K. Mahesh, *Direct numerical simulation: a tool in turbulence research,* Annual review of fluid mechanics **30**, 539 (1998).

[35] B. Pearson, T. Yousef, N. Haugen, A. Brandenburg, and P. Krogstad, *Delayed correlation between turbulent energy injection and dissipation,* Physical Review E **70**, 056301 (2004).

[36] Z. She, E. Jackson, and S. Orszag, *Structure and dynamics of homogeneous turbulence: models and simulations,* Proceedings of the Royal Society of London. Series A: Mathematical and Physical Sciences **434**, 101 (1991).

[37] E. Perlman, R. Burns, Y. Li, and C. Meneveau, *Data exploration of turbulence simulations using a database cluster,* in *Proceedings of the 2007 ACM/IEEE conference on Supercomputing* (ACM, 2007) p. 23.

[38] Y. Li, E. Perlman, M. Wan, Y. Yang, C. Meneveau, R. Burns, S. Chen, A. Szalay, and G. Eyink, *A public turbulence database cluster and applications to study lagrangian evolution of velocity increments in turbulence,* Journal of Turbulence , N31 (2008).

5

TURBULENT EMULSION DYNAMICS

A detailed dynamical description of the underlying processes of turbulent emulsification is still lacking. Despite the widespread application of emulsions, so far our understanding of its formation has been driven by empiricism as dynamics revealing experiments remain intractable. The work of Hinze [2] and Deane and Stokes [3] still hold definitive in describing the fate of droplets in turbulence. Although much progress has been made recently in simulating turbulent multiphase flows, interface resolving turbulence simulations remain an exception to the point that only a handful of them have been performed so far [4]. In this chapter we demonstrate how existing numerical techniques (namely a pseudopotential lattice-Boltzmann scheme and a turbulence forcing mechanism) can be correctly combined to perform hitherto unreported, long and stable, fully resolved numerical simulations (in certain regions of the turbulent emulsion parameter space). We report on characteristics of dispersion formation - namely droplet size distributions, modification of turbulence due to droplets globally (i.e. kinetic energy spectra) and locally (i.e. flow topology), and the effect of turbulence intensity on the emulsion morphology. Further, we initiate discussion and exploration of the dynamics of coalescence and breakup that forms an interesting quasi-equilibrium system, which has so far never been reported. Intermittent peaks in kinetic energy were found to consistently manifest in the enstrophy and droplet number density evolution with characteristic delays in a cascade of cause and effect. These state space variables evolve into time delayed limit-cycles, with alternating coalescence and breakup dominated dynamics. Similarly, surface energy peaks were found to precede droplet breakup which gives new evidence that tip streaming and filament stretching are dominant breakup mechanisms. As simulations such as those presented here (and a few existing studies) slowly become commonplace, the burden will shift to lie on interpretation, validation and prediction. Ours is an attempt to begin pointing towards these aspects of physics resolving simulations.

This chapter has been published in the *Journal of Fluid Mechanics*, 2019 [1].

5.1. INTRODUCTION

AN emulsion consists of a dense suspension of droplets of one fluid (the dispersed phase) suspended in another fluid (the continuous phase), and is often formed due to turbulent mixing of these two immiscible fluids. Emulsions are found (both desirably and undesirably) in a wide range of industries. For instance, in food processing, diverse products depend on the stability and texture of emulsions [5]. In biotechnology, emulsions can serve as miniature laboratories where living cells can be compartmentalized into individual droplets [6]. They are also known to cause various losses in crude oil production [7], or to the contrary, enable enhanced oil recovery [8]. Emulsification, i.e. the formation of an emulsion, requires shearing of droplets which can occur both in laminar and turbulent flow conditions, although the latter may be a more common occurrence. Turbulent emulsions can be said to form a particular class of droplet laden turbulent flows where there is close interplay between turbulence and the dynamics of the dispersed phase. Accurately describing these systems hence involves an account of the dynamics of deforming interfaces, while allowing for coalescence and breakup of droplets, resolution of a range of length and time scales of turbulent flow and the possible presence of surface active agents (surfactants) that can alter the interfacial dynamics. We ignore surfactants in the present study, and focus only on emulsions formed by pure fluids.

The primary effect of turbulence on droplets during emulsification is to cause fragmentation, where an initially large connected volume of the dispersed phase is broken into smaller droplets. Under sustained turbulence, there is a supposed equilibrium between coalescence and breakup which leads to a droplet distribution around a theoretical maximum stable diameter, known as the Hinze scale [2]. This droplet distribution can be expected to follow a $d^{-10/3}$ slope (where d is the droplet diameter), which was first postulated and shown by Garrett *et al.* [9] for a different system, i.e. air bubbles in breaking ocean waves, later also confirmed by Deane and Stokes [3]. Although the emulsification process is different from the bubble dynamics in a breaking wave, both can proceed via a cascading breakup process governing the dispersed phase, which might only depend on the inertia at a given scale (which in turn may be estimated from the rate of energy dissipation in some cases). The dispersed phase influences turbulence by drawing turbulent kinetic energy (TKE) from the flow, which partially goes into the difference between the surface energy of parent and daughter droplets, while the rest is stored in the deformation of interfaces. This reduces the effective turbulent kinetic energy (TKE), which has consequences on the turbulence cascade and spectrum, noticeably at scales comparable to droplet sizes. Coalescing droplets in turn set finer flow structures into motion, where interfacial tension releases the energy stored in droplet deformations back as TKE into the flow at scales smaller than the droplet sizes [10].

LITERATURE REVIEW

In this chapter, we are interested in studying the dynamics of emulsions under continuously forced, homogeneous, isotropic turbulence. So far, most studies on emulsification have been experimental, which is because numerically simulating emulsions while resolving interfacial dynamics and turbulence has only recently become feasible. Most of these experimental results have been phenomenological and statistical, which has greatly informed our understanding of emulsification mainly regarding the formation of

droplet size distributions and emulsion stability, and has in turn aided modeling. The dynamics of emulsification, however, has remained intractable to experiments due to the difficulty of performing measurements during the emulsification process, further aggravated by emulsions being optically opaque, and interfacial dynamics being inherently three-dimensional. To fully paint the dynamical picture, one would require to measure the position of interfaces and the spatial distribution of velocity (to quantify velocity gradients), along with their time evolution. Simulations here are key, as they can reveal all these quantities in telling detail. There have been only a handful of numerical studies devoted to turbulent emulsions, some of which have been detailed in the recent review by Elghobashi [4] on DNS simulations of turbulent flows laden with droplets or bubbles. We refer interested readers to it for a general overview, while we shall discuss the current state of simulating turbulent emulsions, highlighting those aspects that we intend to address with our work.

In one of the first studies, Derksen and Van den Akker [11] simulated a turbulent liquid-liquid dispersion using a free-energy based lattice-Boltzmann (LB) method. They modeled a fluid packet as it passes by the impeller in a stirred vessel, hence experiencing a burst of turbulence, before entering a quiescent zone. They show evolution of the droplet distribution in the dispersion under first constant, and then decaying turbulence, also reporting the modification to the kinetic energy spectra at a crossover scale.

Perlekar *et al.* [12] simulated droplet breakup in homogeneous, isotropic turbulence using a pseudopotential (PP) LB method, showing that the distribution of droplet diameters has a finite width around the Hinze scale. Since Hinze's criterion does not account for droplet coalescence or coagulation, deviation from it was found at higher volume fractions. Further, droplet breakup was attributed to peaks in the local energy dissipation rate. The study reported on the method being originally incapable of attaining steady state simulations due to droplet dissolution, which was remedied by a mass correction scheme to artificially re-inflate droplets which helped maintain a steady volume fraction [13]. Later, Perlekar *et al.* [14] simulated turbulent spinodal decomposition to show coarsening arrest in a symmetric binary fluid mixture (which is compositionally similar to an emulsion, although the morphology is distinctly different). Turbulence was shown to inhibit the coarsening dynamics at droplet sizes larger than the Hinze scale.

Skartlien *et al.* [15] simulated a surfactant laden emulsion under weak turbulence ($Re_\lambda \leq 20$) using a free-energy LB method, and reproduced a $d^{-10/3}$ droplet distribution. They did not find any influence of the surfactant in altering the coalescence rates in the considered range of surfactant activities and turbulence intensities. Also using a free-energy LB method, Komrakova *et al.* [16] simulated turbulent liquid-liquid dispersions at varying volume fractions, focusing on the resolution of droplets with respect to the Kolmogorov scale. They found that droplet dissolution was a significant issue, which made it impossible to obtain a steady state droplet distribution at low phase fractions, while at higher phase fractions ($\phi > 0.2$), despite breakup, most droplets coalesce to form a single connected region with multiple smaller satellite droplets. Increasing the resolution of the Kolmogorov scale remedied droplet dissolution to some extent, and a log-normal droplet distribution was shown from transient simulations, as has been experimentally found for turbulent liquid-liquid dispersions [17, 18]. The multiphase energy spectra could not be reproduced due to spurious currents which caused unphysical energy gain at high wavenumbers, whose magnitude was found to be close to the turbulent velocity

scale u'.

In their detailed study on droplet-turbulence interaction, Dodd and Ferrante [10] simulated a large number of initially spherical droplets ($\phi = 0.05$) in decaying homogeneous, isotropic turbulence using a mass conserving volume-of-fluid method. They considered a wide range of density and viscosity ratios between the droplet and carrier fluids, and showed an enhanced rate of energy dissipation for increasing droplet Weber number (We). Introducing the TKE equations, they show that breakup and coalescence act as source and sink terms of TKE. Roccon *et al.* [19] studied the influence of viscosity on breakup and coalescence in a swarm of droplets ($\phi = 0.18$) in wall bounded turbulent flow using a coupled Cahn-Hillard Navier-Stokes solver. They report a slight drag reduction in the flow due to the presence of droplets, and show that a higher interfacial tension or droplet viscosity favours coalescence, and the number of droplets rapidly decreases to $1-10\%$ of its initial value. At low viscosity, where breakup dominates, around 50% of the droplets remain separated and their sizes follow Hinze's $\langle D \rangle \propto We^{-3/5}$ criterion.

Recently, using a mass conserving level-set method, Shao *et al.* [20] studied interface-turbulence interactions in droplet breakup simulations. They showed that vortical structures tend to align with large scale interfaces before breakup. They also show that there is a slight increase in axial straining and vortex compression upon mapping the flow topology in the presence of droplets, in comparison to single-phase turbulence.

OUR STUDY

In this study, we resolve several of the issues faced in previous work, and report new findings from direct numerical simulations of turbulent emulsions. We use the PP-LB method for a multicomponent fluid system without phase change to simulate the formation of a dispersion. PP-LB is well suited for simulating multiphase flows comprising deformable droplets due to the spontaneous formation of interfaces (emerging from simplified inter-particle repulsion forces) and naturally occurring coalescence and breakup all without the need for interface tracking or models for film drainage [21–23]. In general, different multiphase LB models have been used and validated successfully for simulating droplets and bubbles in various flow conditions of varying complexity. A few examples are simulations of binary droplet collisions and coalescence at different density ratios [24], inertial droplet collision dynamics [25–28], and droplet breakup in Stokes [29] and inertial [30] shear flows. Some examples of the PP-LB method in particular are simulations of multiple bubble dynamics [31], droplet deformation and breakup in shear flow [13, 32], droplet collision [33] and impact [34] at high Weber numbers, and droplet formation and breakup [35, 36] and gas-liquid flow [37] in micro-channels. Chen *et al.* [38] gives an extensive review of the application of PP-LB to various physical problems involving droplets or bubbles. PP-LB has been used before for simulating droplets in turbulence as well [12, 14, 39], along with the free-energy LB method [16].

However, LB comes with a caveat that due to interfaces being diffuse, coalescence is favourable when interfaces overlap. This makes the resolution of the interface width relative to droplet sizes, i.e. the Cahn number, an important criterion [40]. The diffuse interface also leads to dissolution of small droplets as has been noted before [12, 16, 41]. We show that droplet dissolution can be limited to a minor effect in certain parameter regimes, and that a mass correction scheme as used in Perlekar *et al.* [12], Biferale *et al.* [13] is not requisite for simulating droplets in turbulence while using the original PP-LB

method.

Additionally, multiphase LB simulations suffer from spurious currents (u^{sp}) which are velocities arising from anisotropy in the discretization of inter-particle forces. While it has been shown that u^{sp} can be kept small in the pseudopotential LB method [37, 42], also lower than in comparison to conventional finite volume techniques like the volume-of-fluid method [43], in the free-energy LB method they were found strong enough to dominate the multiphase kinetic energy spectra at high wavenumbers [16]. Further, in LB, the characteristic fluid velocity (here the large scale velocity $\mathscr{U}$) should be kept smaller than the lattice speed of sound c_s, such that the flow Mach number $Ma = \mathscr{U}/c_s$ is low (where traditionally $Ma < 0.3$ is considered incompressible) and hence the flow being simulated obeys the incompressible Navier-Stokes equations. Hence, the velocities should scale as $c_s > \mathscr{U} \gg u^{sp}$, which we maintain in our work.

We simulate a dispersion in a periodic box, employing a forcing scheme to generate homogeneous, isotropic turbulence. The system we consider in our numerical setup can be expected to form a *small* portion (assumed to be isotropic) of a larger process (usually anisotropic). One reason to consider isotropic turbulence is that it is the simplest form of turbulence, and is widely used as the flow condition to study the more complicated dynamics of Lagrangian objects like droplets or particles. It further allows us to compare our results with the classical scaling laws of Hinze [2], Garrett *et al.* [9], Kolmogorov [44] and Deane and Stokes [3]. The largest (i.e. energy injection) scale in our simulations is significantly smaller than the largest flow scales in an experiment. Conceptually, we expect that the energy cascade extends to much smaller wavenumbers (than present in our simulations), and what we are able to capture is the tail-end of the energy cascade - which has a small part of the inertial range transitioning into the dissipation range. Hence we have droplets at the end of the inertial range. In real physical systems, droplet dynamics will also occur in a similar range of scales (and extend into the deep dissipation range), while much larger droplet phase regions (at significantly lower wavenumbers) will not occur. The effect of droplets on the flow will then be namely extracting kinetic energy into deformations, generation of smaller scale motions via coalescence (both also corroborated by Dodd and Ferrante [10]), and the modification of local flow topology - and these aspects are what we capture in our simulations.

We particularly study the influence of varying the dispersed phase volume fraction (ϕ) and turbulence intensity (Re_λ) on the characteristics of the emulsification process and the dispersion so formed. We show the influence of the dispersed phase on the multiphase kinetic energy spectra which has not been systematically presented before, or was not possible due to the limitations of the numerical method [16]. We show that ϕ, Re_λ and the interfacial tension γ together determine the dispersion morphology, and that droplets of a particular characteristic length can be generated by varying these parameters. Investigating local flow topology, we show that the effect of the dispersed phase is significant and more pronounced than previously stated [20], with a sharp increase in vortex compression and axial straining in the droplet regions. We also present, for the first time, an analysis of the equilibrium dynamics of a droplet laden isotropic turbulent flow, showing that the system evolution in its state-space is akin to time delayed limit-cycles with alternating dominance of coalescence and breakup as the system oscillates between different dispersion morphologies.

LENGTH SCALES

Through this study we highlight a few considerations that have not been discussed in previous work and are crucial to simulating droplets in turbulence. First is numerically resolving to a sufficient degree the several length scales that govern different aspects of these simulations. Of these, a length scale central to emulsification is the maximum stable droplet diameter for a constant turbulence intensity. This was first given by Hinze [2], who expressed the critical Weber number for droplet breakup (i.e. the ratio between inertial stresses across a droplet and restoring surface tension forces) in terms of the energy dissipation rate ϵ, and is since called the Hinze scale

$$d_{\max} = 0.725(\rho^c/\gamma)^{-3/5}\epsilon^{-2/5} \tag{5.1}$$

where ρ^c and γ are the carrier fluid density and interfacial tension, respectively, and 0.725 is a fitting constant. Since the dissipation field is far from uniform and is highly intermittent, it is now accepted that the local variations in ϵ also set local Hinze scales, and an entire spectrum of droplets centered around $d_{\max}$ tends to arise. Further, deviations from the Hinze scale occur due to droplet coalescence in dense suspensions, as the original scaling was derived for dilute systems with negligible coalescence. A closely associated length scale is the interface width ζ, which in physical systems can be of the order of nanometers for micron to millimeter size droplets. However, as a limitation of our simulation technique (and every other diffuse interface method), the interface width extends over a few computational grid cells. The ratio between ζ and the droplet diameter d is termed the Cahn number $Ch = \zeta/d$ [30], and extreme values of Ch are undesirable. While we require $Ch \ll 1$, coalescence is expected to be fully suppressed in the limit $Ch \to 0$ [40, 45], and therefore the value of Ch should also be finite. Hence the relative separation between d and ζ needs to be considered.

Next, the two length scales characterizing turbulence are the energy injection scale $\mathscr{L}$ which is determined by the forcing scheme, and the smallest (or Kolmogorov) scale η which is determined by the viscosity ν and the dissipation rate ϵ. A wide separation between $\mathscr{L}$ and η means a higher Reynolds number Re, which can be expressed as $Re \approx \left(\mathscr{L}/\eta\right)^{4/3}$. A final length scale of importance in simulations is the size of the simulation domain, which along one spatial direction can be considered to be N_x, and this is generally chosen to be close to $\mathscr{L}$. As droplets will break up due to *extension* under turbulent stresses, the domain size N_x should be sufficiently larger than the maximum droplet elongation before breakup to yield meaningful results (particularly for simulations on periodic domains, where large droplets would begin to interact with images of themselves). Here a particular caveat is also the simplistic description of highly deformed droplets, where an equivalent droplet diameter $d = (6V/\pi)^{1/3}$ gives the impression of $N_x \gg d$, whereas in the form of long, slender filaments, droplets can extend across the entire domain. This can give rise to elongated droplets that remain connected due to periodicity, and this is more prone to occur at high volume fractions under weak turbulence, as for instance can be seen in Skartlien *et al.* [15].

Comparing these length scales, the required spatial separation between them for simulating droplets in the inertial range, at least from a stance of reasoning, would follow as

$$N_x \gg \mathscr{L} \gg d \gg \eta \gg \zeta \tag{5.2}$$

while $N_x > \mathscr{L}$ may also be sufficient, and most studies currently are limited to $N_x \approx \mathscr{L}$.

Also, d can vary over a range of values, extending upto $d \sim \eta$ if the Kolmogorov scale is over-resolved. Upon conceding to limitations of modeling, current simulations can at best reproduce

$$N_x > \mathscr{L} \gg d \gg \eta \approx \zeta \tag{5.3}$$

We try to maintain such a separation of scales, except that we have $\zeta > \eta$. This is a limitation of the current study, as physically the interface thickness is much smaller than any turbulence length scale. This issue is further discussed in section 5.4. Lastly, having $\eta > d$ would mean sub-Kolmogorov droplets. These droplets can also deform and breakup due to the action of viscous stresses instead of inertial stresses [4].

We begin with a description of the numerical method in section 5.2, followed by a brief validation of the turbulence forcing scheme. We then present results from turbulent emulsions in section 5.4, where first the effect of varying the volume fraction is shown in section 5.4.2, followed by a generalization of the Hinze scale in section 5.4.3. The effect of varying the turbulence intensity is shown in section 5.4.4, along with a demonstration of controlling droplet dissolution by reducing the Cahn number. Section 5.4.5 discusses the importance of sufficient resolution of the largest scales and section 5.4.6 shows the influence of the turbulence forcing wavenumber on the dispersion morphology. Finally, in section 5.5 we discuss some general results regarding emulsion dynamics, with the quasi-equilibrium limit-cycle presented in section 5.5.1, droplet-vorticity alignment in section 5.5.2 and influence of droplets on local flow topology in section 5.5.3, after which we end with the conclusions.

5.2. NUMERICAL METHOD

5.2.1. LATTICE-BOLTZMANN METHOD

Each component $\sigma \in \{\alpha, \beta\}$ obeys the standard LBGK equation with a single relaxation time which can be written as [46]

$$f_i^\sigma(\mathbf{x} + \mathbf{c}_i \Delta t, t + \Delta t) = f_i^\sigma(\mathbf{x}, t) - \frac{f_i^\sigma(\mathbf{x}, t) - f_i^{\mathrm{eq},\sigma}(\mathbf{x}, t)}{\tau^\sigma} \Delta t \tag{5.4}$$

where f_i^σ is the distribution function of component σ along the discrete velocity direction $\mathbf{c}_i$. Here τ^σ is the lattice relaxation time towards local equilibrium which relates to the macroscopic component viscosity $\nu^\sigma = c_s^2(\tau^\sigma - 1/2)$ where $c_s = 1/\sqrt{3}$ is the lattice speed of sound (the mixture viscosity is a more complex expression when the components have different τ). The equilibrium distribution $f_i^{\mathrm{eq},\sigma}$ is given by the local Maxwellian as

$$f_i^{\mathrm{eq},\sigma} = w_i \rho \left(1 + \frac{\mathbf{u}^{\mathrm{eq}} \cdot \mathbf{c}_i}{c_s^2} + \frac{\left(\mathbf{u}^{\mathrm{eq}} \cdot \mathbf{c}_i\right)^2}{2c_s^4} - \frac{\mathbf{u}^{\mathrm{eq}} \cdot \mathbf{u}^{\mathrm{eq}}}{2c_s^2} \right) \tag{5.5}$$

where w_i are the LB weights in each direction i, and $\mathbf{u}^{\mathrm{eq}}$ is the equilibrium velocity which is given as

$$\mathbf{u}^{\mathrm{eq}} = \mathbf{u}' + \frac{\tau^\sigma \mathbf{F}^\sigma}{\rho^\sigma} \tag{5.6}$$

The density of a component $\rho^\sigma = \sum_i f_i^\sigma$, and $\mathbf{F}^\sigma$ incorporates all the forces (here the inter-component interactions and the turbulence forcing), into the *common* fluid veloc-

ity $\mathbf{u}'$ between the two components which is given as

$$\mathbf{u}' = \frac{\sum_\sigma \frac{\rho^\sigma \mathbf{u}^\sigma}{\tau^\sigma}}{\sum_\sigma \frac{\rho^\sigma}{\tau^\sigma}} \tag{5.7}$$

where $\mathbf{u}^\sigma$ is the *bare* component velocity. This is calculated in its usual form

$$\mathbf{u}^\sigma = \frac{1}{\rho^\sigma} \sum_i f_i^\sigma \mathbf{c}_i \tag{5.8}$$

For details see Krüger *et al.* [46], Succi [47]. The inter-component interaction force, $\mathbf{F}^{\mathrm{SC}}$, is modeled using the method of Shan and Doolen [23], which can be written as

$$\mathbf{F}^{\mathrm{SC},\sigma}(\mathbf{x}) = -G_{\sigma\bar{\sigma}} \psi^\sigma(\mathbf{x}) \sum_{\sigma \neq \bar{\sigma}} \psi^{\bar{\sigma}}(\mathbf{x} + \mathbf{c}_i \Delta t)\, \mathbf{c}_i\, w_i \Delta t \tag{5.9}$$

5

where ψ^σ is the pseudopotential function for component σ and in this study we have chosen $\psi^\sigma = \rho^\sigma$ (while other definitions are possible). This force between the components is kept to be repulsive, hence the interaction strength parameter $G_{\sigma\bar{\sigma}}$ should have a positive value. It should be noted that the fluids remain partially miscible, and essentially the final composition consists of $\alpha-$rich and $\beta-$rich regions, while a small amount of one component remains dissolved in the other. A higher magnitude of $G_{\sigma\bar{\sigma}}$ results in lower solubility and gives rise to a higher interfacial tension. The total density of the fluid is the sum of the two fluid densities, $\rho^{\mathrm{tot}} = \sum_\sigma \rho^\sigma$, and the hydrodynamic velocity is given as $\mathbf{u} = (1/\rho^{\mathrm{tot}}) \sum_\sigma \left(\mathbf{u}^\sigma \rho^\sigma + (1/2)\mathbf{F}^\sigma \Delta t\right)$. The equation of state for this multicomponent system is [46]

$$p = c_s^2 \sum_\sigma \rho^\sigma + \frac{c_s^2 \Delta t^2}{2} \sum_{\sigma,\bar{\sigma}} G_{\sigma\bar{\sigma}} \psi^\sigma \psi^{\bar{\sigma}} \tag{5.10}$$

Lastly, the interfacial tension γ can be calculated using the Laplace law $\Delta p = 2\gamma/r$, where Δp is the pressure difference across the interface of a spherical droplet.

The simulations here have been performed on a $D3Q19$ lattice, i.e. a three-dimensional lattice with a set of 19 discrete velocity directions. Further, the lattice spacing Δx and time step Δt are both set equal to 1, and consequently all quantities are expressed in dimensionless lattice units [lu].

5.2.2. TURBULENCE FORCING

To generate and sustain turbulence in the fluid, a constant source of energy is required, which is constantly being dissipated by viscosity at the smallest scales (i.e. the Kolmogorov scales). This is done by setting the largest scales of flow into motion, and if the fluid viscosity is low enough, these large structures become unstable and give rise to successively smaller scales. One of the ways to achieve this numerically is by employing a low wavenumber spectral forcing, as given by Alvelius [48], while alternative techniques could also be used [49, 50]. This forcing was also implemented by Ten Cate *et al.* [51] in LB to simulate the response of clouds of spherical solid particles to homogeneous isotropic turbulence. A very similar form of the forcing is used by Perlekar *et al.*

[12], which is constructed directly in real space but could be made to have a similar effective spectral form as [51, 52], albeit with less control over output parameters, as we do in this study. The forcing is divergence free by construction and can be written as

$$\begin{aligned} F_x^\sigma &= \sum_{k=k_a}^{k_b} \frac{\rho^\sigma}{\rho^{\text{tot}}} A(k) \left[\sin(2\pi k y + \phi_y(k)) + \sin(2\pi k z + \phi_z(k))\right] \\ F_y^\sigma &= \sum_{k=k_a}^{k_b} \frac{\rho^\sigma}{\rho^{\text{tot}}} A(k) \left[\sin(2\pi k x + \phi_x(k)) + \sin(2\pi k z + \phi_z(k))\right] \\ F_z^\sigma &= \sum_{k=k_a}^{k_b} \frac{\rho^\sigma}{\rho^{\text{tot}}} A(k) \left[\sin(2\pi k x + \phi_x(k)) + \sin(2\pi k y + \phi_y(k))\right] \end{aligned} \tag{5.11}$$

Here each $\phi_i(k)$ is a unique random phase. Alternatively, $\phi_i(k)$ can be evolved as a stochastic process, as done in Perlekar *et al.* [12], but in our approach $\phi_i(k)$ (and hence the forcing) varies as white noise in time. This ensures that the force is not related to any timescale of turbulent motion, and is a choice also made in Ten Cate *et al.* [52]. The force is distributed over a small range of wavenumbers $k_a \leq k \leq k_b$, while the contribution of each of these wavenumbers is determined by $A(k)$ which centers the Gaussian around k_f in Fourier space, given as

$$A(k) = A \exp\left(-\frac{(k-k_f)^2}{c}\right) \tag{5.12}$$

where k_f is the central forcing wavenumber, c is a width over which to distribute the force amplitude and is set to $c = 1.25$, and A is a forcing magnitude. This method ensures that there is a dominant central wavenumber k_f (which can also be a fraction) in the forcing scheme, while neighbouring wavenumbers also contain some energy, which makes the scheme more stable [52]. Lastly, the total power input to the fluid can be written as the sum of two terms as follows

$$P = P_1 + P_2 = \frac{1}{2}\overline{f_k f_k}\Delta t + \overline{u_k f_k} \tag{5.13}$$

where the two terms are the force-force and force-velocity correlations respectively, and u_k, f_k refer to the volumetric velocity and force fields. The force-velocity correlation, P_2, should be 0 to avoid an uncontrolled growth of energy in the fluid [48], and it is achieved by varying the force term at each time step. This is computationally expensive, hence some studies [51, 52] vary the force by choosing randomly from a pre-computed set of force fields at each time step. This was found to introduce a non-zero contribution from the P_2 term, where the steady state kinetic energy was roughly 10 times larger than with a unique random force at each time step - hence in this study we adhere to the latter approach.

In the continuum (long-wavelength) limit, the PP-LB model solves the Navier-Stokes equations for the two fluid mixture with a body force (see Scarbolo *et al.* [53])

$$\rho^{\text{tot}}\left(\frac{\partial \mathbf{u}}{\partial t} + \mathbf{u}\cdot\nabla\mathbf{u}\right) = -\nabla p + \nabla\cdot\left(\mu\nabla\mathbf{u} + \mu\nabla\mathbf{u}^T\right) + \sum_\sigma \mathbf{F}^\sigma \tag{5.14}$$

where p is the pressure (refer eq. 5.10), $\mu = \sum_\sigma \rho^\sigma \nu^\sigma$ is the dynamic viscosity, and $\mathbf{F}^\sigma$ is the total force acting on component σ, which here is given as $\mathbf{F}^\sigma = \mathbf{F}^\sigma_{\text{PP}} + \mathbf{F}^\sigma_{\text{turb}}$ (i.e. the

sum of the pseudopotential contribution as given by eq. 5.9 and the turbulence contribution given by eq. 5.11). The per component continuity equation includes an additional term, i.e. the divergence of the diffusive current $\mathbf{J}^\sigma$ (as given in Scarbolo *et al.* [53]) which causes phase-segregation between the two components, and has the form

$$\frac{\partial \rho^\sigma}{\partial t} + \nabla \cdot \left(\rho^\sigma \mathbf{u}\right) = \nabla \cdot \mathbf{J}^\sigma \tag{5.15}$$

where

$$\mathbf{J}^\alpha = \frac{\rho^\alpha \rho^\beta}{\rho^{\text{tot}}} \left[c_s^2 \left(\tau - \frac{1}{2}\right) \left(\frac{\nabla \rho^\alpha}{\rho^\alpha} - \frac{\nabla \rho^\beta}{\rho^\beta} \right) - \tau \left(\frac{\mathbf{F}^\alpha}{\rho^\alpha} - \frac{\mathbf{F}^\beta}{\rho^\beta} \right) \right] = -\mathbf{J}^\beta \tag{5.16}$$

It can be seen that the turbulence force contribution to $\mathbf{J}^\sigma$ cancels out since $\mathbf{F}^\alpha_{\text{turb}}/\rho^\alpha = \mathbf{F}^\beta_{\text{turb}}/\rho^\beta$. Further, the flux of each component is negligible away from interfaces where gradients of density and the pseudopotential force vanish. The *global* continuity equation, obtained by adding individual component continuity equations, is not influenced by the diffusive current term (since $\mathbf{J}^\alpha = -\mathbf{J}^\beta$). For more details on the continuum form of the equations, refer to Shan and Doolen [23], Scarbolo *et al.* [53] and chapter 4 of Krüger *et al.* [46].

5

TURBULENCE QUANTITIES

The largest scale in the system is given by the domain size N_x, which sets the minimum wavenumber $k_{\text{min}} = 2\pi/N_x$. All other wavenumbers are integer multiples of k_{min}, with the maximum wavenumber being $k_{\text{max}} = k_{\text{min}} N_x/2 = \pi$. The smallest scale of turbulence (Kolmogorov scale) is calculated as $\eta \sim \left(\nu^3/\epsilon\right)^{1/4}$ where ν and ϵ are the kinematic viscosity and energy dissipation rate respectively. The criterion for a resolved DNS simulation is that $k_{\text{max}}\eta > 1$ [54], and the Kolmogorov scale should obey $\eta > 0.318$ [lu] [52]. We shall mention the forcing wavenumber k_f and the wavenumber bounds as multiples of k_{min} in this study. For a central forcing wavenumber k_f, the associated large scale length then becomes

$$\mathscr{L} \sim \frac{2\pi}{k_f k_{\text{min}}} = \frac{N_x}{k_f} \tag{5.17}$$

Further, the Taylor microscale is calculated as

$$\lambda = \left(\frac{15 \nu u'^2}{\epsilon} \right)^{1/2} \tag{5.18}$$

where u' is the root mean square velocity along one direction, and $u'_x = u'_y = u'_z$ in isotropic turbulence. The rate of energy dissipation $\langle \epsilon \rangle$ can be found in two ways, as $\epsilon \approx \nu \langle \omega^2 \rangle \approx \sum_k 2\nu k^2 E(k)/N_x^3$ where $\langle \omega^2 \rangle$ is the average enstrophy and $E(k)$ is the kinetic energy spectrum. Using λ, the Taylor Reynolds number is calculated as

$$Re_\lambda = \frac{u'\lambda}{\nu} \tag{5.19}$$

Lastly, the Kolmogorov timescale is given as

$$\tau_k = \left(\frac{\epsilon}{\nu}\right)^{-1/2} \tag{5.20}$$

For eddies in the inertial range with a size l, the velocity $u(l)$ and timescale $\tau(l)$ are determined uniquely by ϵ and l alone as $u(l) = (\epsilon l)^{1/3} \sim \mathscr{U}(l/\mathscr{L})^{1/3}$ and $\tau(l) = (l^2/\epsilon)^{1/3} \sim \mathscr{T}(l/\mathscr{L})^{2/3}$, where $\mathscr{L}$, $\mathscr{T}$ and $\mathscr{U}$ are the characteristic length, time and velocity of the largest eddies (with $\mathscr{T} = \mathscr{L}/\mathscr{U}$). We consider $\mathscr{U} \approx \langle E_k \rangle^{1/2}$ as the largest eddies contain most of the kinetic energy, and generally $u' < \mathscr{U}$. The characteristic velocity at a particular length scale can also be found from the kinetic energy spectrum as $u(l) \approx \sqrt{E(k_l)}$ where $k_l = 2\pi/l$.

5.3. SINGLE-PHASE TURBULENCE

We begin with a single-phase turbulence simulation to show that the forcing scheme is able to maintain a statistically stationary turbulent flow (simulation "SP" in table 5.1) and to compare it with results available in literature. A domain of 256^3 lattice nodes representing a length $(2\pi)^3$ is initialized with a uniform initial density of $\rho^\alpha = 4.0$ [lu]. The relaxation time is set to $\tau = 0.5141$ which gives a viscosity of $\nu = 0.0047$ [lu] (Perlekar *et al.* [12] use a similar value with $\tau = 0.515$), which is a low enough viscosity to sustain turbulence while still being numerically stable. The forcing is concentrated around $k_f = 2k_{\min}$ and is distributed in the range of $k = k_{\min}$ to $8k_{\min}$, and is applied from $t = 0$ to a fluid initially at rest i.e. with zero velocity. Further, $A = 0.0005$, which generates a turbulent flow with a Taylor microscale of $\lambda = 13$ [lu], $Re_\lambda = 95$, $\tau_k = 97$ [lu], $\eta = 0.7$ [lu] ($k_{\max}\eta = 2.2$) and $\langle \epsilon \rangle \approx 5 \times 10^{-7}$ [lu], which are calculated *a posteriori*. The simulation is performed for $10^5\ \Delta t$, which corresponds to $1000\tau_k$.

Figure 5.1 shows the evolution of $\langle E_k \rangle$ and $\langle \omega^2 \rangle$ which attain their steady state values around $75\tau_k$ and continue to oscillate around this value. Note that the turbulence forcing scheme is steady in the sense that it leads to the balance of energy injection and dissipation. The large scale instability itself is not steady, and the force variation in time leads to intermittency of the power input which is a standard feature of continuously forced turbulence [48, 50]. Further in figure 5.1 (see inset), the crests and troughs of the $\langle E_k \rangle$ evolution show up in the $\langle \omega^2 \rangle$ evolution with a slight delay, where the quantities have been normalized with their time averaged values over the latter 3/4th of the simulation duration). This has been observed before, and ascribed to the energy cascading mechanism [13, 55] while Tsinober [56] acknowledges this feature without invoking a cascade.

Figure 5.2 shows typical velocity and enstrophy field snapshots from a planar cross-section in the center of the domain at $500\tau_k$. The velocity field shows motions across various scales, while the enstrophy field (which is the square of the vorticity) shows typical small scale localized structures. Also note that ω^2 assumes values as much as 10 times the average $\langle \omega^2 \rangle$ (while at higher Re_λ, more extreme values are found), showing that intermittency is well reproduced in the simulations. This patchy structure of enstrophy is an important factor to consider in simulations of turbulent dispersions, as it leads to varying degrees of droplet-vorticity interactions which can in turn lead to droplet breakup.

The kinetic energy spectrum is shown in figure 5.3, along with a benchmark spectrum from the Johns Hopkins Turbulence Database [57] for a homogeneous isotropic turbulence simulation with $Re_\lambda = 433$ (on a grid of 1024^3, generated with a spectral solver). The energy $E(k)$ has been normalized by the total energy $\sum_k E(k)$, and the wavenumber is normalized to show multiples of $k_{\min}$, which is done to compare the two spectra.

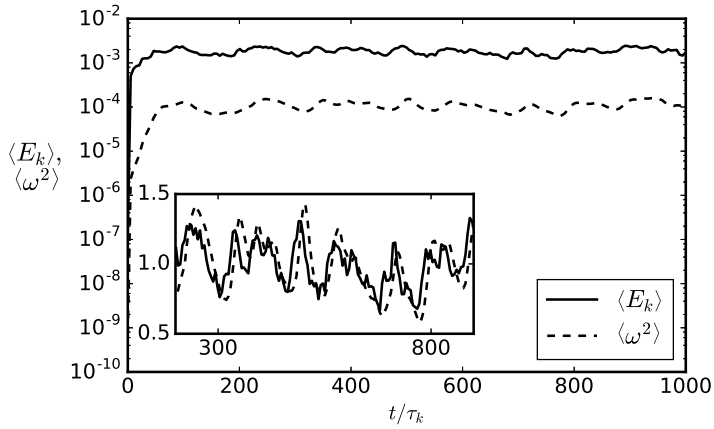

Figure 5.1: Evolution of average kinetic energy $\langle E_k \rangle$ and enstrophy $\langle \omega^2 \rangle$ in the single-phase turbulence simulation with $Re_\lambda = 95$. Both $\langle E_k \rangle$ and $\langle \omega^2 \rangle$ reach steady state confirming the balance between the energy dissipation and power input. In the inset, both profiles have been normalized by their time averaged value over the latter 3/4th of the simulation duration.

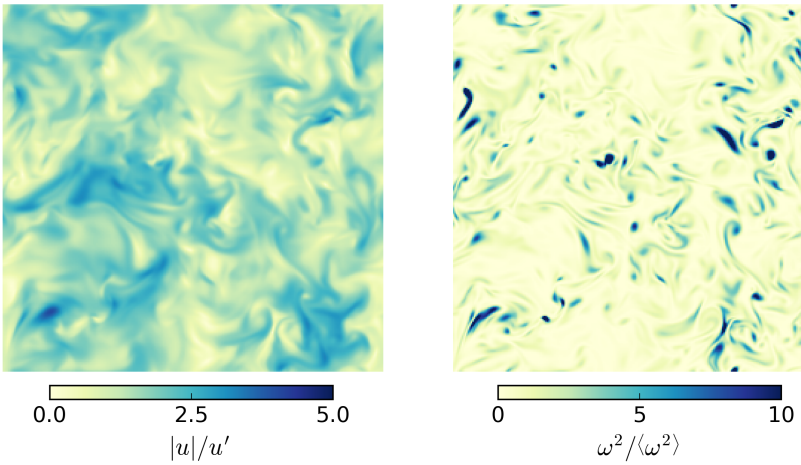

Figure 5.2: Cross-sections (at $z = N_x/2$) show snapshots of the velocity magnitude $|u|$ (left) and enstrophy ω^2 (right) at time $t = 500\tau_k$. Features typical of turbulent flow can be seen, where the velocity field shows features across several length scales while enstrophy remains localized in small scale structures.

A well developed inertial range is seen to exist, following the $k^{-5/3}$ spectral slope, which falls off around $k = 30k_{\text{min}}$ in our simulation. Lastly, in this simulation $u' = 0.034$ [lu], and since the speed of sound is $c_s = 1/\sqrt{3}$ [lu], the flow Mach number is $Ma = 0.06$ which is well within the incompressibility limit.

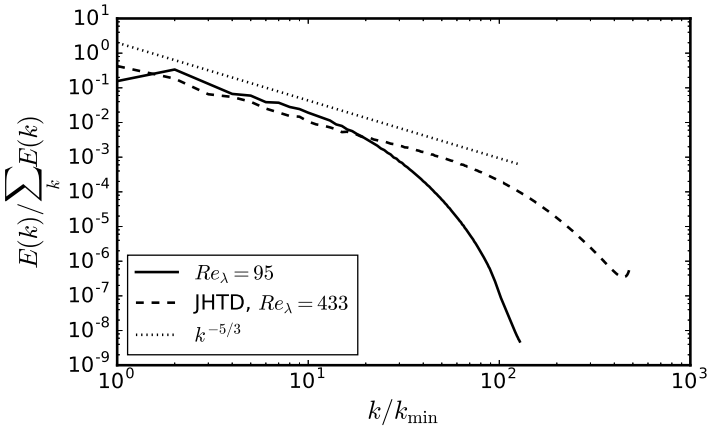

Figure 5.3: Kinetic energy spectrum for the single-phase simulation shown together with a sample spectrum from the Johns Hopkins Turbulence Database (JHTD, with $Re_\lambda = 433$). The chosen normalization is only to compare the shape of the two spectra along with a $k^{-5/3}$ inertial range scaling. The spectrum is further averaged over 20 realizations separated by $50\tau_k$.

5

5.4. TURBULENT EMULSIONS

5.4.1. SIMULATION SETUP

The turbulent emulsion simulations are initialized with two fluids, which we denote by α (the carrier fluid) and β (the droplet fluid), with a liquid-liquid density ratio $\rho_\beta/\rho_\alpha = 1$, which well represents many oil in water emulsions. For a chosen volume fraction ϕ of fluid β, a single spherical droplet (a β-rich region) is initialized in the center of the domain which is otherwise α-rich. The droplet density is denoted by ρ_β^{in}, i.e the density of β in the β-rich region, while ρ_β^{out} denotes the dissolved amount of component β in the α-rich region (i.e. the continuous phase), and likewise for component α. Further, ρ_β^{avg} is used to refer to the average density of component β in the entire domain. During the simulation, these density values can change to some extent depending on the $G_{\alpha\beta}$ parameter, though due to the symmetry of the model we have $\rho_\beta^{\text{in}}/\rho_\alpha^{\text{in}} = 1$ and $\rho_\beta^{\text{out}}/\rho_\alpha^{\text{out}} = 1$. We also keep $\nu_\beta/\nu_\alpha = 1$ (with $\nu_\alpha = \nu_\beta = 0.0047$ [lu]). Spurious velocities (u^{sp}) in these simulations have been limited to values sufficiently smaller than the physical velocity, so that their influence on the results is negligible. This was checked by performing additional quiescent simulations i.e. a droplet suspended in the continuous phase without any turbulence forcing, for both liquid-liquid repulsion strengths considered in this study (i.e. $G_{\alpha\beta}$, which leads to the interfacial tension γ). The maximum spurious current magnitude $u_{\text{max}}^{\text{sp}}$ (found only at the interface) was less than the physical velocity scale (u') by more than a factor 10, and the spurious currents decay to 10% of this maximum magnitude within 5 grid cells, while the average spurious current magnitude $u_{\text{avg}}^{\text{sp}}$ is less than u' by a factor more than 100. Given that the speed of sound in these simulations $c_s = 1/\sqrt{3}$, we maintain that $u^{\text{sp}} \ll \mathcal{U} \ll c_s$, which is in line with our recent findings for emulsion droplets simulated with PP-LB [41–43].

We carried out three sets of simulations, the details of which are mentioned in ta-

ble 5.1. In all these simulations, the turbulence force is applied starting at $t = 0$. The turbulence energy density $\langle E_k \rangle$ in an emulsion, for the same forcing amplitude, can be an order of magnitude lower than in single-phase turbulence. The Kolmogorov scale values have been calculated using the scaling $\eta \approx (\nu^3/\overline{\langle \epsilon \rangle})^{1/4}$ where $\overline{\langle \epsilon \rangle}$ is the spatio-temporally averaged dissipation rate (with $\overline{\langle . \rangle}$ denoting time averaging after the first quarter of the simulation time, during which the flow is well developed). We report η upto two decimal places that follow from this scaling. The three sets are divided as follows

- Set 1 (P1-P5): In these simulations, only the dispersed phase volume fraction has been changed (from $\phi = 0.01$ to $\phi = 0.45$). Here η is found to increase in simulations P1-P5, which is because the turbulence forcing scale $\mathscr{L}$ remains the same while Re_λ decreases, hence reducing the separation between the largest and smallest scales.

- Set 2 (T1-T5): In these simulations, the turbulence force amplitude is varied to change Re_λ (at a fixed volume fraction $\phi = 0.10$). For case T5, the interfacial tension has also been increased. Due to increasing Re_λ in these simulations, since $\mathscr{L}$ is kept constant, η is found (as expected) to decrease. An additional simulation T3R has been performed, which is equivalent to T3, but has a larger domain size ($N = 384^3$). The energy density is the same in T3 and T3R (while the other turbulence statistics turn out slightly different). This is to demonstrate the effect of the Cahn number on droplet dissolution.

- Set 3 (D1-D5): In these simulations, the domain size is increased while keeping the forcing lengthscale $\mathscr{L}$, amplitude and volume fraction ($\phi = 0.15$) fixed, which keeps the turbulence energy density (or Re_λ) fixed. An additional simulation, D5, has been performed where the turbulence intensity and volume fraction have been increased for comparison with case D4. For all cases, η remains almost constant as Re_λ is kept constant by varying $\mathscr{L}$ (so that the ratio $\mathscr{L}/\eta$ is constant). In simulation D5, Re_λ is increased fourfold in comparison to D1-D4, yet η is the same as the increase in Re_λ is achieved by the added scale separation due to a fourfold decrease in the forcing wavenumber in D5 ($k_f = 1.5$) as opposed to D4 ($k_f = 6.0$).

To study the droplet characteristics in these simulations, we segment the droplets in space (also known as clustering) by thresholding the droplet density field at a cutoff value $\rho^c/\rho_\beta^{\text{in}} = 0.57$ (which is effectively the density along the interface where $\rho^c \approx \rho_\alpha = \rho_\beta$) based on the algorithm used in Siebesma and Jonker [58]. This allows us to identify and mark all lattice points within individual droplets, which gives the droplet volume V, which in turn is used to calculate an effective diameter $d = (6V/\pi)^{1/3}$. Estimating the surface area of these droplets, which are in voxel form, requires more care. Often, the 'GNU triangulation surface' (GTS) library [59] is used in studies due to its efficient surface splitting operations (without the need for volumetric droplet segmentation). However, it was not used in this study as it did not provide a straightforward way of identifying droplets cut-off at domain edges due to periodicity (an issue implicitly resolved by our segmentation algorithm). Also, the GTS library was found to underpredict the surface area of a sphere by around 10%. Instead, we use the method proposed by Windreich *et al.* [60] (originally developed for medical MRI data) to calculate surface area directly from voxels using a look-up table which divides surface voxels into 9 classes, and each

Sim	N	ν	$G_{\alpha\beta}$	ϕ	A	k_a, k_f, k_b	γ	$\langle E_k \rangle$	$\langle \epsilon \rangle$	τ_k	Re_λ	η
SP	256^3	0.0047	-	-	0.0005	2.0	-	1.8×10^{-3}	5.0×10^{-7}	97	95	0.7
P1	256^3	0.0047	0.015	0.01	0.0005	1,2,8	0.017	2.0×10^{-4}	2.21×10^{-8}	461	51	1.47
P2	256^3	0.0047	0.015	0.06	0.0005	1,2,8	0.017	2.0×10^{-4}	2.10×10^{-8}	474	53	1.49
P3	256^3	0.0047	0.015	0.15	0.0005	1,2,8	0.017	1.7×10^{-4}	1.93×10^{-8}	493	47	1.52
P4	256^3	0.0047	0.015	0.2	0.0005	1,2,8	0.017	1.5×10^{-4}	1.75×10^{-8}	518	45	1.56
P5	256^3	0.0047	0.015	0.45	0.0005	1,2,8	0.017	1.3×10^{-4}	1.65×10^{-8}	534	39	1.58
T1	256^3	0.0047	0.015	0.10	0.00025	1,1.5,8	0.017	8.4×10^{-5}	4.90×10^{-9}	980	44	2.14
T2	256^3	0.0047	0.015	0.10	0.0005	1,1.5,8	0.017	2.4×10^{-4}	1.87×10^{-8}	502	64	1.54
T3	256^3	0.0047	0.015	0.10	0.00075	1,1.5,8	0.017	4.6×10^{-4}	4.78×10^{-8}	313	78	1.22
T3R	384^3	0.0047	0.015	0.10	0.00065	1,1.5,8	0.017	4.9×10^{-4}	3.44×10^{-8}	369	100	1.32
T4	256^3	0.0047	0.015	0.10	0.001	1,1.5,8	0.017	6.5×10^{-4}	8.36×10^{-8}	237	84	1.06
T5	256^3	0.0047	0.016	0.10	0.001	1,1.5,8	0.04	6.6×10^{-4}	7.70×10^{-8}	247	90	1.08
D1	128^3	0.0047	0.015	0.15	0.0005	1,1.5,6	0.017	1.2×10^{-4}	1.80×10^{-8}	511	34	1.55
D2	256^3	0.0047	0.015	0.15	0.0005	1,3,6	0.017	1.1×10^{-4}	1.77×10^{-8}	514	30	1.56
D3	384^3	0.0047	0.015	0.15	0.0005	2,4.5,8	0.017	1.1×10^{-4}	1.81×10^{-8}	509	30	1.55
D4	512^3	0.0047	0.015	0.15	0.0005	3,6,9	0.017	1.1×10^{-4}	1.87×10^{-8}	501	30	1.54
D5	512^3	0.0047	0.015	0.2	0.0005	1,1.5,6	0.017	4.2×10^{-4}	1.80×10^{-8}	511	118	1.55

Table 5.1: Simulation parameters for all cases. Here viscosity ν and interfacial tension γ are in lattice units [lu], along with length and time measured as multiples of Δx and Δt. The density and viscosity ratio between the components is kept at unity. The turbulence forcing is distributed over the range of wavenumbers from k_a to k_b centered at k_f. The fluid densities are initialized to $\rho^{\text{in}}_{\alpha,\beta} = 4.0$ $\rho^{\text{out}}_{\alpha,\beta} = 0.77$. The average kinetic energy $\langle E_k \rangle = (\sum_k E(k))/N$, and the average rate of energy dissipation $\langle \epsilon \rangle = (\sum_k 2\nu k^2 E(k))/N$.

class has a weighted contribution to the surface area. Using only the first 4 of these 9 classes, the area estimation error for a sphere was found to decrease to 1%, which was sufficiently accurate for our study.

5.4.2. EFFECT OF VOLUME FRACTION

We now show results from simulations with varying dispersed phase volume fractions $\phi \in \{0.01, 0.06, 0.15, 0.2, 0.45\}$ under identical turbulence forcing conditions (corresponding to P1-P5 in table 5.1). These simulations are performed for 10^5 time steps. Figure 5.4 shows the dispersion formation process at various time instances starting from the initial spherical droplet of component β shown as the iso-surfaces representing $\rho_\beta = \rho_\alpha$. The droplet begins to deform under the turbulent stresses, eventually breaking up to form a dispersion with a characteristic distribution.

Of the various volume fractions considered, $\phi = 0.06$ and 0.15 are most emulsion-like, i.e. they have a profusion of small droplets with a few large connected filaments. At $\phi = 0.01$, the dispersed phase is too dilute to be considered an emulsion, although the droplet dynamics is interesting as the number of droplets N_d and their characteristic diameters d is small, and hence most of the droplets remain dispersed with relatively few coalescence events, and when droplets do coalesce, they break up soon after. At $\phi \geq 0.2$, most of the fluid volume remains connected, which is aggravated by the enhanced coalescence inherent to diffuse interface methods [16, 19]. This in turn is due to insufficient resolution of the interface with respect to the droplet sizes [40], an effect we discuss more in depth in section 5.4.5. At higher turbulence intensity, the large connected regions can be expected to break into smaller droplets, and any coalescence will generate droplets of sizes larger than the maximum stable diameter, which will again breakup.

Before discussing further results, we first show a quantitative sample of the typical data from these simulations. In figure 5.5, the dispersed phase density ρ_β, a single velocity component u_x and a single vorticity component ω_x are shown along an arbitrary line passing through a droplet in the P4 dataset, along the $x-$axis, at time $t = 190\tau_k$. At this time, the flow is well within the fully developed turbulent regime, along with the typical dispersion morphology having been attained. The first thing to note is that the velocity and vorticity fields are sufficiently well resolved and vary uniformly, i.e. there are no severe jumps due to spurious currents near the interfaces (only a small subtle spike), which shows that the physical velocity scales dominate over the spurious velocities.

The velocity field in figure 5.5 gradually varies through the interface. This is reasonable due to the continuity of tangential stress across the interface and, we again emphasize, is inevitable due to the condition $\zeta > \eta$. Physically, this situation will not occur since the interface width is typically of the size $O(10^{-9})$ [m], and the smallest turbulent fluctuations, for micrometer sized droplets, may extend up to roughly $O(10^{-6} - 10^{-7})$ [m] (while they depend on Re_λ). The finite interface width is a limitation which will be encountered in any diffuse interface method, and which may be alleviated by adaptive mesh refinement near the interface as presented by Yu and Fan [61], or by increasing the droplet resolution while keeping the interface thickness fixed (i.e. decreasing the Cahn number Ch). The latter is done by adopting a larger simulation domain, as shown by Komrakova *et al.* [16], and it also remedies other diffuse interface artifacts, as will be subsequently discussed.

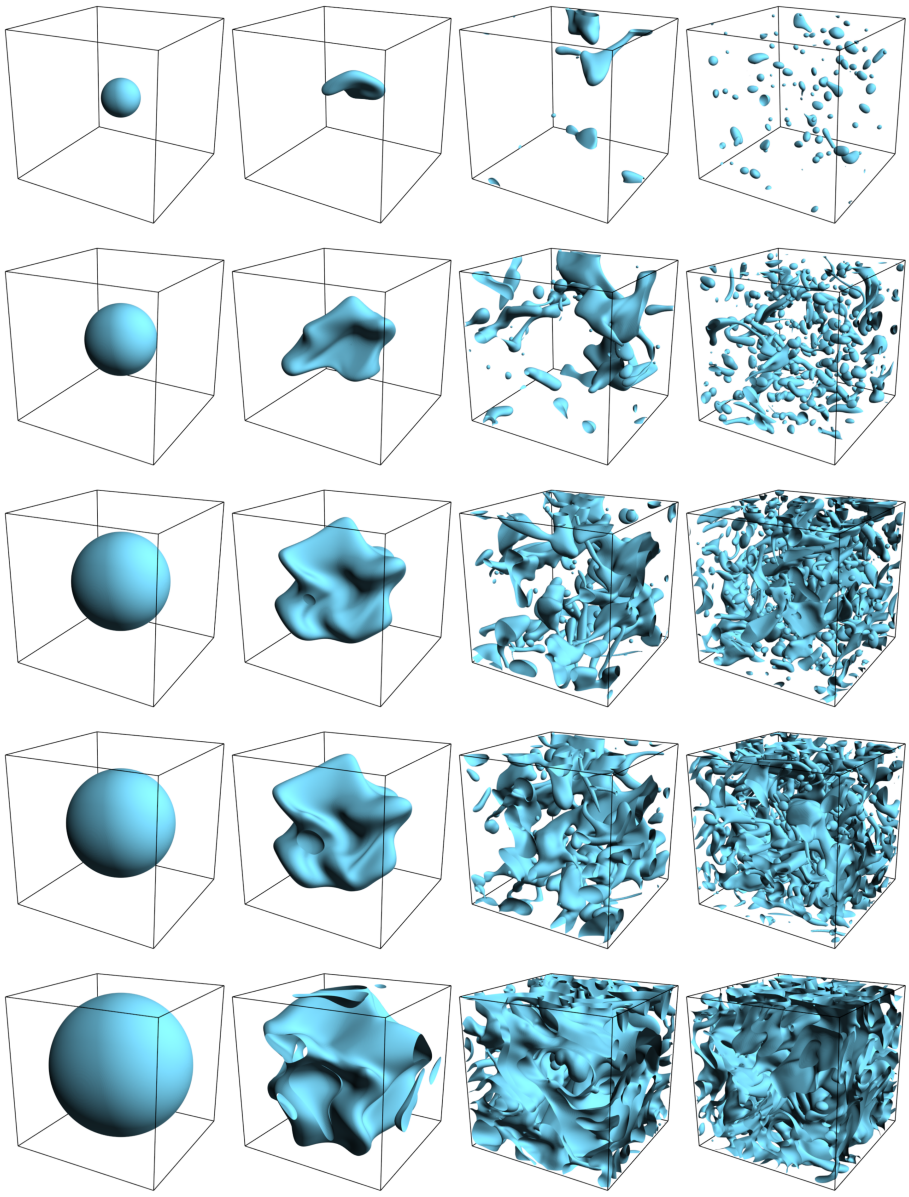

Figure 5.4: Dispersion formation under turbulence, for increasing volume fractions $\phi \in \{0.01, 0.06, 0.15, 0.2, 0.45\}$ corresponding to simulation P1-P5 in table 5.1 (top to bottom). The time instances are $t/\tau_k \approx 0, 10, 40, 100$ (left to right), and the dispersions are subjected to identical turbulence forcing.

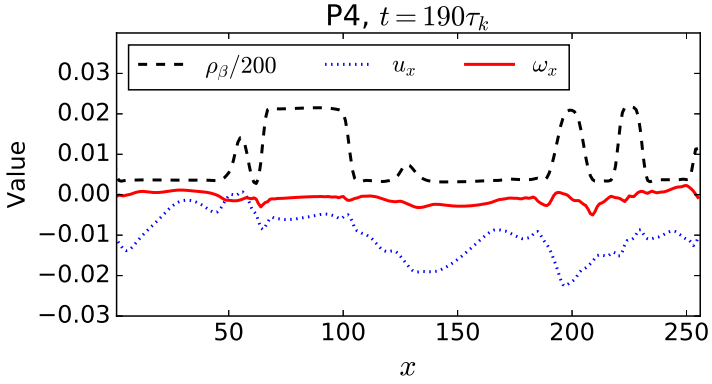

Figure 5.5: A sample of the dispersed phase density (ρ_β, scaled by a factor of 1/200), $x-$velocity (u_x) and $x-$vorticity (ω_x) are shown along an arbitrary line passing through the P4 dataset along the $x-$axis, at time $t = 190\tau_k$ when the turbulence and dispersion are fully developed.

5

PHASE FRACTION EVOLUTION

Figure 5.6 shows the evolution of the dispersed phase volume fraction ϕ normalized by the initial volume fraction ϕ_0. There is a clear decrease over time (upto around $100\tau_k$) in the relative volume fraction, beyond which the value plateaus to a level around which it continues to oscillate (this will be confirmed subsequently from simulations T1-T5 in section 5.4.4 which were performed for a five times longer duration). This relative reduction in ϕ is more pronounced at lower ϕ values (up to around 30%) than at higher ϕ (around $2-5\%$). Note that this is *not* a mass conservation issue, as the total component mass is perfectly conserved in the system, and only the amount of component β present as the dispersed phase reduces, which gets dissolved in the α-rich (continuous phase) region. This is also why the relative decrease in ϕ is strongest for $\phi = 0.01$, as the dissolution of β into the continuous phase is provided by a very low number of droplets.

The reason for the reduction in ϕ is twofold. First is the dissolution of small droplets due to a finite interface width, which is an issue inherent to most diffuse interface methods. Yue *et al.* [62] showed that there is a slow drift in the droplet density due to diffusion, which also leads to droplet shrinkage. They also show that a small droplet in a large domain is more prone to dissolution, which is reflected in figure 5.6 where the lowest ϕ simulation suffers most from droplet dissolution. This effect is also tied to the Cahn number Ch. If $Ch \sim O(1)$ (or greater), the droplet becomes unstable and is prone to dissolution. On the other hand, Shardt *et al.* [40] showed for droplet collision in shear flow that coalescence is inhibited with decreasing Ch number. In the limit of $Ch \to 0$, coalescence would cease to occur, while increasing Ch leads to coalescence at higher capillary numbers. These considerations mandate having a finite Ch number in the range $0 < Ch \ll 1$ (for all droplet sizes in the system) for achieving steady state simulations while allowing for both coalescence and breakup. The effect of Cahn number on droplet dissolution is analyzed subsequently in section 5.4.4.

The second reason for the reduction in ϕ is its sensitivity to the segmentation threshold. In appendix 5.A we demonstrate that *only* this result, i.e. the evolution of the volume fraction, depends on the choice of the segmentation threshold. Part of the droplet

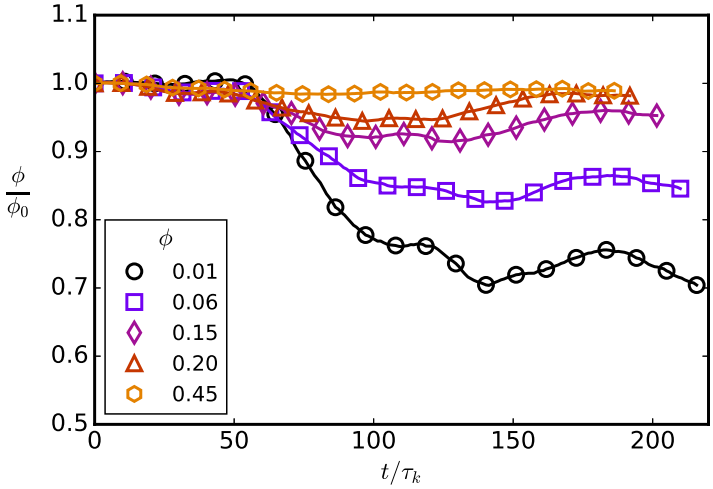

Figure 5.6: Evolution of volume fraction ϕ normalized by the initial volume fraction ϕ_0, for the same turbulence intensity across simulations. There is more droplet dissolution for lower ϕ values, while the decrease is not monotonic as new smaller droplets can be formed as well.

phase fraction goes into constituting the increased interfacial region (i.e. roughly the total surface area of all droplets S_A multiplied by the interface width ζ). Slightly varying the segmentation threshold to lower values (so that it is closer to ρ_β^{out}), the apparent volume fraction loss is reduced (which may indicate that $\rho^{\text{c}} \neq (\rho^{\text{out}} + \rho^{in})/2$), although the exact choice of ρ^{c} does not change our results. Further, the reduction in ϕ is also not monotonic, as mass of component β dissolved in the α-rich region can eventually accumulate inside other droplets.

Droplet dissolution can be a debilitating numerical issue, where for instance Perlekar *et al.* [12], Biferale *et al.* [13] had to resort to artificially inflating droplets to maintain a constant phase fraction and Komrakova *et al.* [16] reported that they could not attain steady state simulations with the free-energy LB method at low volume fractions as all droplets dissolved away into the continuous phase. In our PP-LB simulations, this issue is due to an interplay of three main factors - (i) the liquid-liquid repulsion $G_{\alpha\beta}$ which keeps the two components demixed, (ii) the turbulence intensity which breaks large droplets into smaller ones and (iii) the phase fraction which at low values makes $\rho_\beta^{\text{out}} \approx \rho_\beta^{\text{avg}}$ (i.e. at low ϕ, phase segregation can become weaker). Despite being present, droplet dissolution is limited to a minor effect in our simulations. More precisely, the PP-LB method employed in this study can be used to reasonably simulate certain regions of the turbulent emulsions parameter space where droplet dissolution is not significant. Namely, for a given turbulence intensity (Re_λ), there will be a critical lower bound on the interfacial tension γ_c such that droplets with $\gamma > \gamma_c$ can be simulated. For increasing Re_λ, γ_c would increase as well, and its exact dependence on Re_λ could be investigated by numerically mapping the phase space which is out of the scope of the current study. Similarly, there will be a lower bound on the value of ϕ, below which all droplets will dissolve due to weak phase segregation when $\rho_\beta^{\text{out}} \approx \rho_\beta^{\text{avg}}$. Considering these related effects,

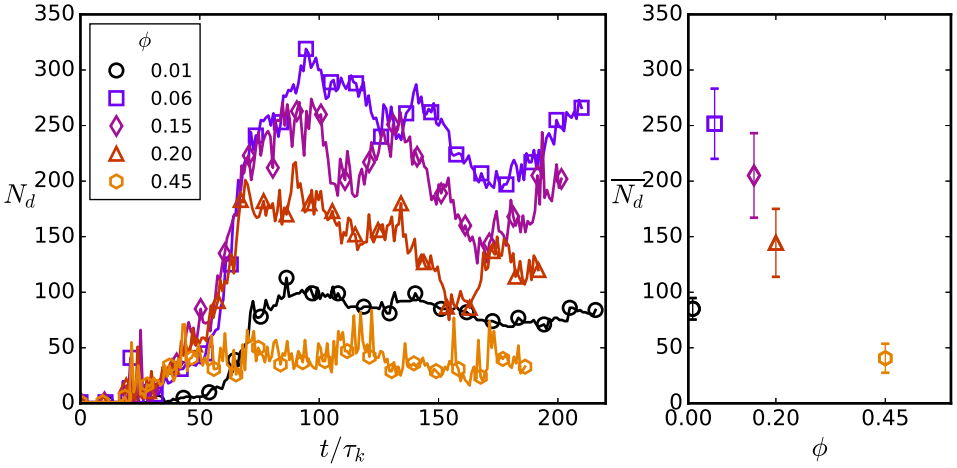

Figure 5.7: Evolution of the number of droplets (N_d) in the system, which attains its characteristic value around $75\tau_k$ and oscillates around a temporal mean. The $\phi = 0.06$ case produces the highest number of droplets (around 250), which is seen on the right panel where $\overline{N_d}$ is N_d averaged from $75\tau_k$ to $200\tau_k$, and the error bars show the standard deviation.

we restrict ourselves to a parameter range where we can attain long, stable simulations to collect meaningful statistics pertaining to the droplet coalescence and breakup equilibrium.

DROPLET NUMBER DENSITY EVOLUTION

Figure 5.7 shows the evolution of the number of droplets (N_d) in the system for varying ϕ. N_d begins to increase following the first breakup events around $25\tau_k$ and rises steadily to its characteristic value around $75\tau_k$, around which it continues to oscillate. The oscillations in N_d are indicative of competing coalescence and breakup dynamics. The falls in the N_d evolution profiles are due to coalescence events, which generate droplets of large sizes that are unstable. These droplets then break up under turbulent stresses and N_d increases again. Breakup is delayed for $\phi = 0.01$ as compared to the other cases and N_d only begins to increase around $50\tau_k$. This is because the size of initial droplet is much smaller (~ 64 [lu]) than the forcing wavelength (~ 128 [lu]), and the droplet starts to advect initially, as seen from figure 5.4. When smaller scales are generated (around $50\tau_k$, as can be seen from the enstrophy evolution in figure 5.1), the droplet begins to shear and break. The evolution of N_d does not show large fluctuations for $\phi = 0.01$ due to relatively fewer coalescence and breakup events in this case, which is because the droplets are smaller and more distant from each other than in higher ϕ cases.

Although $\phi = 0.15$ and 0.2 simulations have a larger volume of fluid β, the number of droplets generated is lower than $\phi = 0.06$. This is because of a higher propensity for coalescence in these systems which generates large connected regions and smaller satellite droplets. This is most prominently seen for $\phi = 0.45$, where N_d is even lower than $\phi = 0.01$, as most of the fluid forms extended filaments that remain connected across the periodic boundaries. Increasing the turbulence intensity can be expected to generate

more droplets at higher ϕ, and hence for a given Re_λ, there will be a specific ϕ that maximizes the number of droplets formed and hence produce a more emulsion-like droplet size distribution.

Once the turbulent emulsion achieves its 'steady-state' (albeit fluctuating), it holds no memory of the initial conditions of the dispersed phase. To demonstrate this, simulation P3 (with $\phi = 0.15$) is repeated, where instead of a single droplet, 216 smaller droplets (together also comprising $\phi = 0.15$), equally spaced on a regular lattice, are initialized. Figure 5.8 shows the droplet number density and volume fraction evolution for the two initial conditions for P3. The multiple droplet system proceeds with dominant coalescence up to $t \approx 30\tau_k$, after which breakup and coalescence begin to occur simultaneously. N_d soon reaches its typical value, similar to the single droplet initialization, and the time averaged droplet number density $\overline{N_d}$ (between $75\tau_k - 200\tau_k$, shown in the inset of the left panel) is very similar for both cases. Although not equal within the duration of these simulations, $\overline{N_d}$ can be expected to converge to the same value when averaged over a longer duration. The relative volume fraction evolution is also very similar for both initial conditions, in particular for $t > 150\tau_k$.

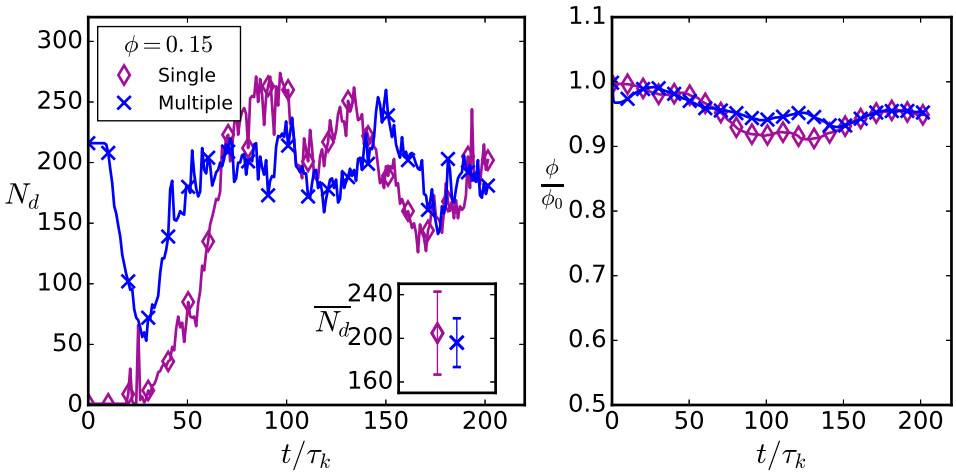

Figure 5.8: Evolution of the droplet number density N_d and the relative volume fraction ϕ/ϕ_0 is compared for different dispersed phase initial conditions for simulation P3 with $\phi = 0.15$. The 'single' case starts with one droplet of $\phi = 0.15$ while the 'multiple' case distributes the same droplet volume over 216 smaller droplets, all equally spaced. Both cases proceed to the same final state, with almost the same average morphology, and the coincidence is expected to increase over a longer simulation duration.

DROPLET SIZE DISTRIBUTION

Figure 5.9 shows the distribution of the equivalent droplet diameter $d = (6V/\pi)^{1/3}$ (where V is the droplet volume) for varying ϕ (calculated with $25000 - 35000$ droplets identified between times $75\tau_k$ to $200\tau_k$, sampled at each τ_k). Case (a) $\phi = 0.01$ shows a peak around $d/\eta \approx 10$, beyond which the distribution rapidly falls off due to the dispersion being dilute (see 4th panel in the top row of figure 5.4). Due to infrequent coalescence, large

droplets are not formed very often. This was also reflected in the N_d evolution (figure 5.7) which does not fluctuate as much as higher ϕ simulations. Cases (c) and (d) with $\phi \geq 0.15$ (and to a small extent case (b)) show two power-law regimes in the droplet distribution. The occurrence of droplets of sizes $d > d_{\max}$ (where $d_{\max}$ is the Hinze [2] scale) falls off with a $d^{-10/3}$ slope, while droplets of sizes $d < d_{\max}$ show a weak $d^{-3/2}$ slope (the latter is more prominent for case (d)).

The $d^{-10/3}$ scaling was originally postulated and shown for air bubbles in breaking ocean waves by Garrett *et al.* [9]. The scaling was derived from dimensional and mechanistic arguments (that bubble lifetimes depended on bubble sizes), with assumptions of a *purely* inertial breakup process that depends only on the turbulence intensity (determined by ϵ), and the rate of supply of the dispersed phase (i.e. volume of air entrained per volume of water per second). This led to a $d^{-10/3}$ scaling for the droplet spectrum $P(d)$, which was again verified by Deane and Stokes [3] for air bubbles above the Hinze scale in breaking waves. Deane and Stokes [3] further showed that bubble sizes below the Hinze scale follow a $d^{-3/2}$ distribution, which was also dimensionally motivated (while including surface tension effects for smaller droplets). They found the scalings to hold for a brief period before the turbulence decayed. Skartlien *et al.* [15] showed that the droplet distribution in their turbulent emulsion simulations also follows a $d^{-10/3}$ scaling, which can be expected since the power law of Garrett *et al.* [9] is valid for homogeneous and isotropic turbulence. Our results also verify that the conditions for purely inertial breakup of the dispersed phase are met in these simulations. The $d^{-3/2}$ scaling is seen upto only a few droplet sizes in the range $d < d_{\max}$ for most simulations. This is because as droplet sizes get smaller, the $Ch \to 1$ limit is reached and the droplets become unstable and prone to dissolution, which is why the distribution begins to fall off to the left of $d/\eta \approx 5$.

Also, for $\phi \geq 0.15$, a secondary peak appears at high d/η, which is due to a few large connected regions forming due to coalescence, which remain connected despite occasional satellite droplets breaking off. Such large connected regions of the droplet fluid (for instance see bottom right panel of figure 5.4) are also identified as 'droplets' in the segmentation step which considers all contiguous droplet fluid regions as individual droplets and ascribes an equivalent diameter to them. Due to the presence of these large regions, droplets in an intermediate range are less frequent, as upon formation they would soon coalesce with the larger connected region. This is first a consequence of having a high volume fraction at a lower turbulence intensity. At higher Re_λ, the large region would be unstable and hence break apart forming droplets with a range of diameters. Secondly, the formation of this larger connected region also depends on Ch. If a simulation is performed on a much larger domain for the same volume fraction $\phi = 0.20$ and turbulence intensity $Re_\lambda = 45$, due to an increased separation between d and ζ (lower Ch), coalescence would be inhibited. We estimate that that the uncertainty in determination of d is around 10%.

Further, $\eta \approx 1.5$ [lu] here and given that the interface width $\zeta \approx 5-6$ [lu], the Ch for these droplets is approximately in the range $0.03 < Ch < 1.5$. The smallest droplets that are meaningfully resolved are of the size $d \approx 12-15$ [lu]. In physical systems, small droplets are stable and can only be destroyed by coalescence. Resolving droplets in this range of diameters (where $d/\eta \sim O(1)$) will require over-resolving the Kolmogorov scale (to decrease the relative Ch), as was done by Komrakova *et al.* [16]. Lastly, the length

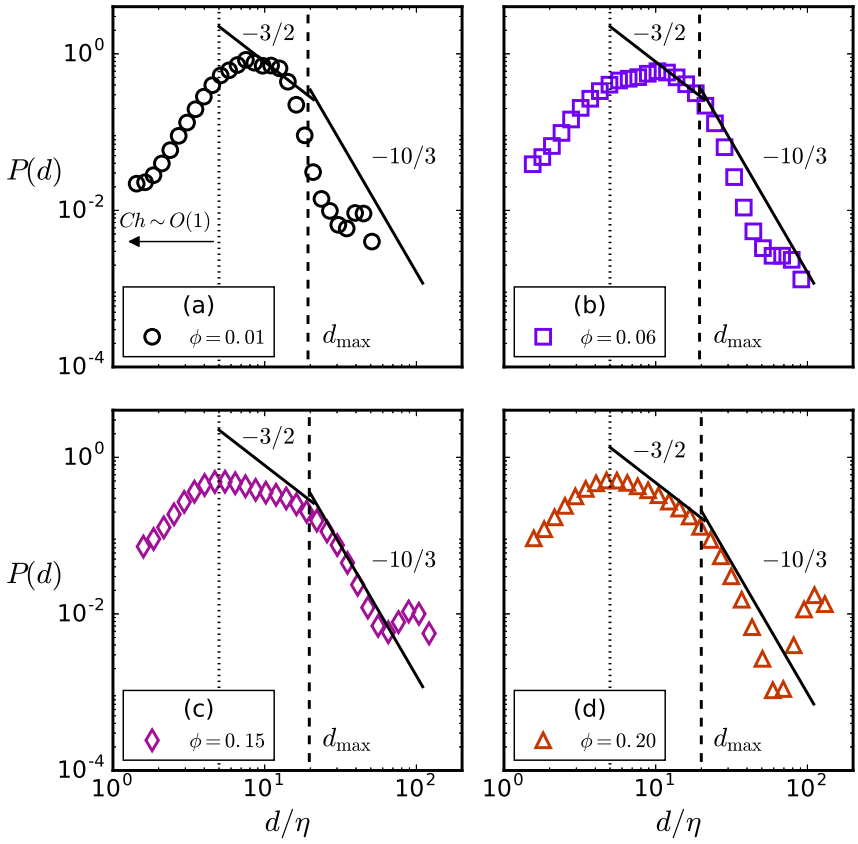

Figure 5.9: Droplet size distributions for varying volume fractions (on a 256^3 domain). Case (a) $\phi = 0.01$ shows a peak around $d/\eta \approx 10$, which rapidly falls off at higher d/η. Cases (b) $\phi = 0.06$ and (c) $\phi = 0.15$ have a wider range of droplet sizes, and the distribution follows a $d^{-10/3}$ scaling in the range $d > d_{\max}$. The distributions also weakly show a $d^{-3/2}$ scaling over some droplet sizes in the range $d < d_{\max}$ (most prominently case (d)). For $\phi \geq 0.20$, a significant secondary peak at high d/η indicates the few large connected regions that form in the periodic simulation domain, along with multiple smaller satellite droplets. The vertical dashed line shows the Hinze scale and the vertical dotted line marks the limit to the left of which the Cahn number $Ch \sim O(1)$ and droplets become unstable.

scales are ordered as $N_x > \mathscr{L} \gg d \gg \zeta > \eta$ for cases P1-P3 while $N_x > \mathscr{L} > d \gg \zeta > \eta$ for cases P4 and P5 (where due to higher ϕ, the long droplet filaments can be of length $\sim \mathscr{L}$).

MULTIPHASE KINETIC ENERGY SPECTRA

In this section, we study the wavenumber spectra of the multiphase flow field. For computing the spectra using the Fourier transform, the entire volumetric flow field including both fluid components is considered, as we intend to study the velocity variations in both the continuous and dispersed phases. This is important since there is consider-

able amount of flow inside the droplets as well, especially for large droplets with sizes in the inertial range. Using the entire volumetric flow field in our case is acceptable since the viscosity and density ratios between the fluids are exactly 1. In case of a non-unity viscosity ratio (and specially at large values), the velocity profile across a sharp interface is not smooth, as it has to satisfy the tangential stress continuity condition. The sharp change in the velocity gradient across the interface adversely affects the spectra (in the manner of a Dirac pulse added on top of a smooth field). In any diffuse interface method, the velocity profile across the interface will be smooth by definition, even when $\mu_\alpha \neq \mu_\beta$, and the velocity gradient will also vary smoothly within the width of the interface. This alleviates the situation slightly, although without remedying it. In these cases, one might have to resort to using the wavelet spectra instead [63], or use the frequency spectra from Lagrangian trajectories in the continuous phase which has been shown to improve the spectral velocity representation for turbulence with solid particles [64].

Figure 5.10 shows the kinetic energy spectra in panel (a) for the droplet laden simulations, in comparison to the single-phase turbulence simulation with identical forcing. The first effect to note is the suppression of the inertial range (i.e. deviation from the $k^{-5/3}$ law) which is seen more clearly in the compensated spectra shown in panel (b), which is an effect that has also been found previously [14]. For increasing ϕ, the spectra between $1 < k/k_f < 10$ shift away from the inertial range scaling and the single-phase spectrum, which shows that the cascading mechanism becomes weaker. This happens due to frequent coalescence at higher ϕ, which leads to the formation of larger droplets which can interact directly with larger inertial range scales, redirecting the kinetic energy from its cascading process into droplet deformations and breakup. Interestingly, the spectra pass through a single point, which is marked by the vertical line in panel (b). This point is very close to the inverse of the Hinze length scale given by $d_{\max} = 0.725(\rho/\gamma)^{-3/5}\epsilon^{-2/5}$. Since ϵ varies slightly between cases P1-P5, so does $d_{\max}$ (within 5%), which is why we indicate the length as $\sim d_{\max}$ in figure 5.10b.

Beyond the inverse Hinze scale, the higher ϕ simulations contain higher energy at the smaller scales (large wavenumbers). This is due to coalescence, which generates small scale eddies, and is more frequent at higher ϕ. Two or more droplets coalescing add kinetic energy to the flow by loss of surface energy due to a reduction in overall surface area. The $\phi = 0.01$ simulation has the lowest energy at high wavenumbers, as coalescence events are rare, and the droplet sizes are smaller, which in turn derive energy from eddies corresponding to slightly higher wavenumbers. While the spectra reflect these effects, they do not give any insight into the *direction* of the energy cascade. It would be interesting to study the effect of droplets on spectral energy transfer across scales, using the approach given by for instance Alexakis and Biferale [65], which would allow one to quantify the scale dependent cascade direction, which we leave for future work. The crossover of the multiphase spectra (for $\phi \geq 0.15$ cases) with the single-phase spectrum shows that the dissipation range has higher energy in the presence of droplets, as was also reported by Perlekar *et al.* [14]. Interestingly, Ten Cate *et al.* [51] also found such a spectral crossover at increasing volume fractions for solid spherical particles in turbulence.

Lastly, a small jump in the spectra at $k/k_f \approx 50$ is consistently seen for all cases, which corresponds precisely with the interface width in our simulations (i.e 5−6 [lu]). The extra energy there is due to the spurious currents present in the system, which are found to

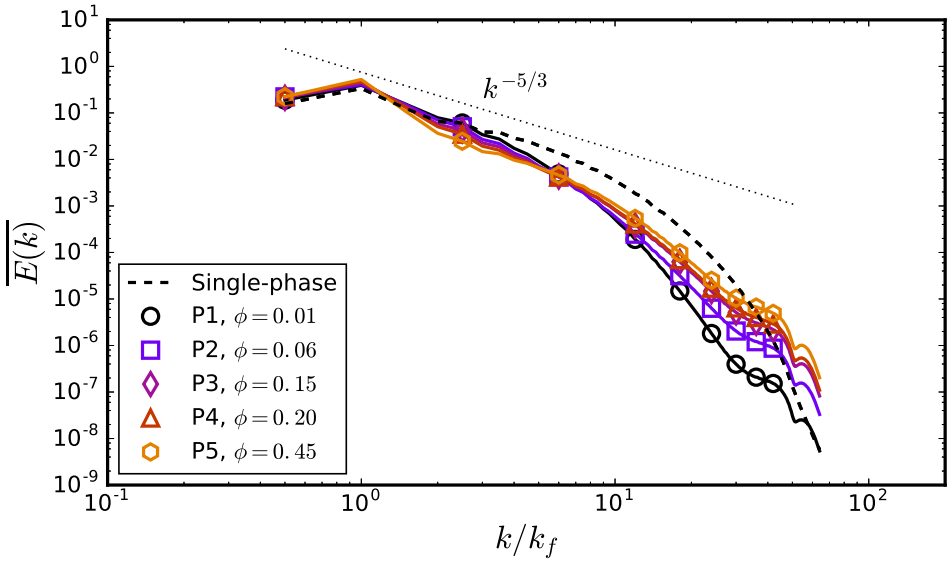

(a) Kinetic energy spectra

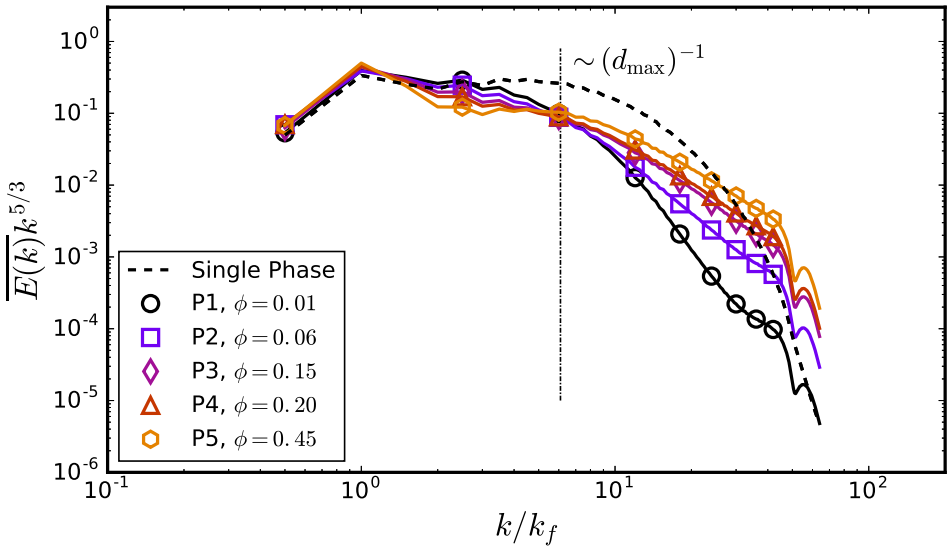

(b) Compensated kinetic energy spectra

Figure 5.10: Kinetic energy spectra are shown in panel (a), which are obtained from varying ϕ simulations i.e. P1-P5 (averaged between $75\tau_k$ and $100\tau_k$, sampled every $2\tau_k$), where $\overline{E(k)} = E(k)/\sum_k E(k)$. At higher ϕ values, the turbulence cascade is suppressed at intermediate wavenumbers (seen as deviations from Kolmogorov's $k^{-5/3}$ scaling). Panel (b) shows the compensated spectra, where the trends can be seen more clearly. At higher wavenumbers, droplet coalescence adds kinetic energy to the smaller scales, which is stronger at higher ϕ values due a higher chance of coalescence in a dense dispersion. The vertical line in panel (b) corresponds approximately to the inverse of the Hinze scale.

be much weaker than the physical velocity scales. Komrakova *et al.* [16] reported that spurious currents completely dominated the higher wavenumbers of the kinetic energy spectra in their turbulent dispersion simulations, due to which the spectra could not be well represented. Our work does not suffer from this problem, and although spurious currents are present, they do not adversely influence our results.

5.4.3. GENERALIZED HINZE SCALE AND WEBER NUMBER SPECTRA

The derivation of the Hinze scale is under the assumption of a developed inertial range, and is taken to hold for dilute suspensions without coalescence. The inertial range scaling can be found for a small range of wavenumbers for simulations P1 and P2 ($\phi = 0.01, 0.06$) which are relatively dilute, have infrequent coalescence, and contain droplets that are smaller than the largest inertial range scales. For these cases, the assumptions of Hinze [2] are reasonably well approximated.

If a large amount of the dispersed phase is present, and turbulent shear cannot overcome surface tension to cause large droplets to fragment into (on an average) smaller droplets, the droplet lengthscale can be large. At larger ϕ, coalescence becomes significant as well. In these cases, there is a deviation from the $k^{-5/3}$ inertial scaling (simulations P3-P5). This is because the large droplets can directly extract kinetic energy from the larger inertial range scales of flow into deformation and breakup energy, which in turn hinders the cascading mechanism. Whether this happens depends on the ratio of inertial to surface tension forces, i.e. the Weber number. For instance, the $k^{-5/3}$ scaling is found again for simulation T5, where $\phi = 0.10$, $Re_\lambda = 91$ and $\gamma = 0.04$. In this case, the largest droplet sizes correspond to scales in the middle of the inertial range, such that a small range of wavenumbers exhibit the $k^{-5/3}$ scaling, similar to simulation P1, which is shown in figure 5.11.

Generally, at higher volume fractions, the Hinze scale is not expected to be valid due to frequent coalescence. Even without coalescence, droplet-eddy interactions become hindered due to the presence of multiple droplets. Another lengthscale becomes important in such cases, which is the inter-droplet spacing which scales at $\Delta x \propto \phi^{-1/3} d$. Even at seemingly low volume fractions, say $\phi = 0.10$, the inter droplet spacing is of the order of two droplet radii, due to which the dilute suspension assumption breaks down. One can, however, still consider a critical Weber number at a lengthscale $d_{\max}$, such that *on average*, at larger lengthscales breakup dynamics will dominate, and at lower lengthscales coalescence will dominate. This was also the original idea of Hinze, where the critical Weber number was described using the velocity scale at length d arising from Kolmogorov's theory as $u_d \sim \langle\epsilon\rangle^{1/3} d^{1/3}$ as

$$We_{\text{crit}} = \frac{\rho u_d^2 d}{\gamma} \tag{5.21}$$

The use of $\langle\epsilon\rangle$ is merely to express the velocity at a given scale, under the condition that power input is balanced by the energy dissipation, and the inertial scales only transfer energy without dissipating it (basically the theory of Kolmogorov [44]). Since the power input is generally known, this allows estimating the typical droplet sizes that will arise in a dispersion. Since in high volume fraction simulations (P3-P5) the Kolmogorov

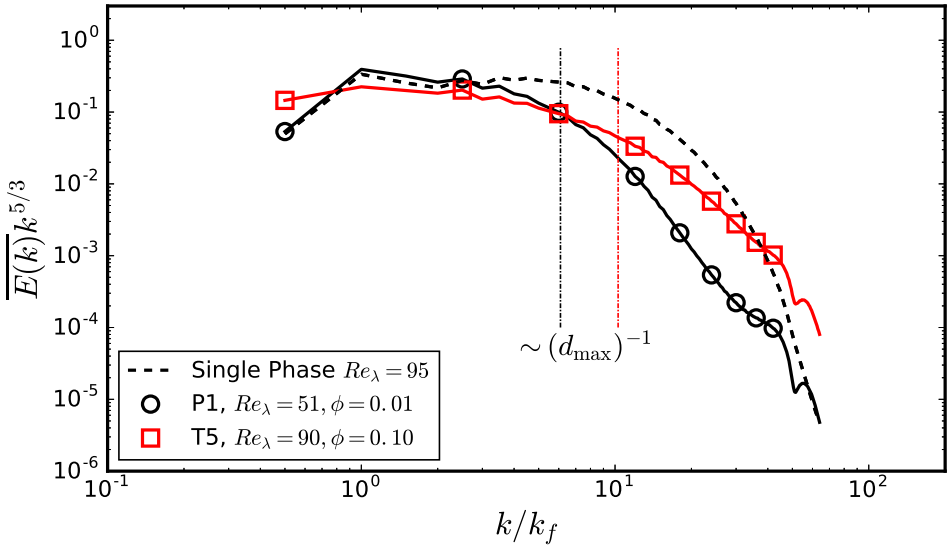

Figure 5.11: Compensated spectra for cases P1 and T5 showing the presence of an inertial range.

[44] scaling does not hold, only $\langle\epsilon\rangle$ and d alone cannot be used to determine u_d. The power input now is balanced in part by dissipation, and in part by the changes in interfacial energy, while the dynamics of the 'intermediate' (that would usually be called 'inertial') range of scales is more complex. We propose an alternate scaling to determine u_d, using the multiphase kinetic energy spectra $E(k)$, which implicitly takes into account the average velocity dynamics at lengthscale d.

The volume averaged energy spectra $\langle E(k)\rangle$ (with units L^3T^{-2}) and the droplet wavenumber $k_d = 2\pi/d$ (with units L^{-1}) can be used to determine a velocity as

$$u_d^2 \sim k_d \langle E(k_d)\rangle \tag{5.22}$$

while other combinations of k_d and $E(k_d)$ are also possible. This velocity scale can be replaced in eq. 5.21 to calculate a Weber number spectra for all k as follows

$$We(k) = \frac{\rho k \langle E(k)\rangle d}{\gamma} \tag{5.23}$$

If the critical Weber number can be found, for instance using Lagrangian tracking as done by Perlekar *et al.* [12], a generalized Hinze scale can be approximated for any form of the energy spectrum $E(k)$ that may arise in a multiphase system which does not obey the $k^{-5/3}$ scaling, and whose form may not be known *a priori*. Even if the critical Weber number is not quantifiable directly, an indication of the scale k_d at which $We \approx 1$ can be found, such that droplets at scales $k < k_d$ will be more prone to breakup, while droplets at scales $k > k_d$ will mostly coalesce. If in eq. 5.23 we plug-in the Kolmogorov energy spectrum $E(k) \sim \epsilon^{2/3}k^{-5/3}$, we get the term $k\epsilon^{2/3}k^{-5/3}d$, which gives us $\epsilon^{2/3}k^{-2/3}d \sim \epsilon^{2/3}(2\pi/d)^{-2/3}d \sim \epsilon^{2/3}d^{5/3}$ (to within multiplicative constants). Solving this equation for

d, for a known critical Weber number, yields the classical Hinze scale $d \sim (\gamma/\rho)^{3/5}\epsilon^{-2/5}$. Hence eq 5.23 can be treated as a generalization of the Hinze scale, applicable to dense and dilute suspensions alike.

In figure 5.12, the Weber number spectra as given by eq. 5.23 are shown for cases P3-P5, which were sufficiently dense suspensions for the chosen Re_λ, such that the inertial range scaling is affected by the dispersed phase. A range of wavenumbers gives $We > 1$, which should correspond to breakup dominated scales. Case P3 is shown in the inset, where we have $We = 1$ at $k/k_f = 2.5$ i.e. $k = 5$. This corresponds to a droplet scale of around $d \approx 50$ [lu]. From figure 5.9, panel (c), we see that the droplet distribution begins to fall off with the $d^{-10/3}$ slope around $d/\eta \approx 30$, which gives $d \approx 45$ [lu]. These two values are of the same order, which shows that the unstable scale prediction from the Weber spectrum well approximates the cutoff droplet scale k_d, such that in the range $k > k_d$, droplets can be expected to predominantly undergo breakup (the $d^{-10/3}$ regime), while in the $k < k_d$ range droplets are stable (the $d^{-3/2}$ regime). Deane and Stokes [3] also refer to the scale at which they observed this transition between the two scaling regimes to be the critical (Hinze) scale.

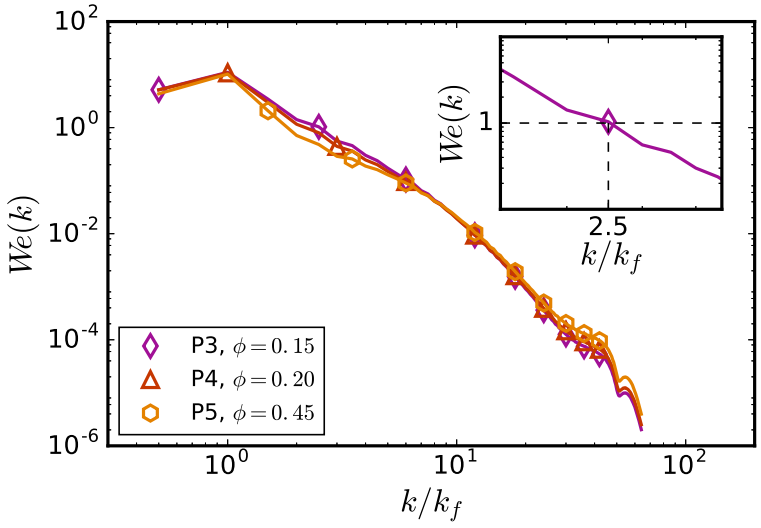

Figure 5.12: Weber spectrum $We(k)$ for cases P3-P5, along with a close look (inset) at case P3 near $We = 1$, which occurs at $k/k_f = 2.5$, which closely corresponds to the scale at which there is a transition in the droplet distribution power law slopes (panel (c) and (d) of figure 5.9).

5.4.4. EFFECT OF TURBULENCE INTENSITY

As mentioned earlier, the idea behind applying turbulence is to cause fragmentation of the dispersed phase, and the number of droplets thus formed depends upon the intensity of turbulence. We now keep the volume fraction fixed at $\phi = 0.1$ and increase the turbulence intensity by increasing the forcing amplitude. These are simulations T1-T5 in table 5.1, and are run for $t = 0.5$ million time steps each, though the simulations will have different τ_k. Figure 5.13 shows the evolution of the normalized phase fraction over time,

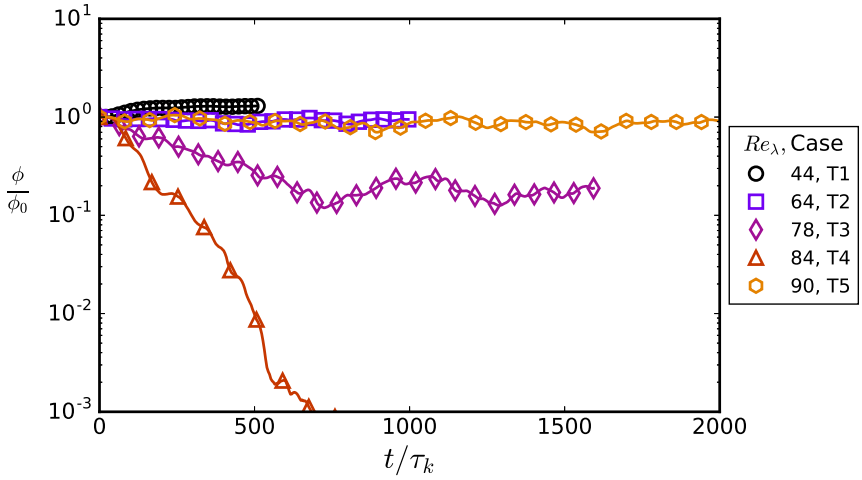

Figure 5.13: Evolution of the relative volume fraction ϕ/ϕ_0 for varying turbulence intensity simulations (cases T1-T5 in table 5.1). Increasing Re_λ causes greater droplet dissolution leading to a lower settling value of ϕ/ϕ_0. This effect limits the parameter space that can be simulated with the original PP-LB method, as shown by cases T4 and T5.

and as expected, at higher turbulence intensities (which leads to a higher Re_λ), ϕ/ϕ_0 reduces over time to an individual stable value. In case T4, all the droplets dissolve within $600\tau_k$, which shows that for this combination of parameters (refer to table 5.1), turbulence forcing undesirably outclasses the PP-LB phase segregation. The small droplets formed in this system are subsequently unstable (due to $Ch \sim O(1)$), which causes complete dissolution of the dispersed phase. Upon increasing the liquid-liquid repulsion parameter $G_{\alpha\beta}$ (hence also changing the fluid composition and dimensionless numbers that include interfacial tension, like the Weber or Ohnesorge number) in case T5, we see that for the same turbulence intensity as case T4, ϕ/ϕ_0 remains stable. This reaffirms that with the original PP-LB method certain regions of the turbulent emulsions parameter space can be simulated on a given mesh size, while in other cases (case T4 and to some degree also case T3) simulations may require additional numerical remedies like the mass correction scheme of Perlekar *et al.* [12], Biferale *et al.* [13] or an enhanced Kolmogorov scale resolution (to achieve higher Cahn numbers) as done by Komrakova *et al.* [16]. We now briefly demonstrate the latter method.

DECREASING THE CAHN NUMBER TO CONTROL DROPLET DISSOLUTION

The Cahn number for a simulation can be decreased by increasing the domain size N_x, while the turbulence intensity and energy injection scale (forcing wavenumber) are kept the same. In this case, the Kolmogorov scale η increases because the separation between the energy injection scale $\mathscr{L}$ and the dissipation scale η remains fixed, while $\mathscr{L}$ increases. Since the interface width ζ remains unchanged, and the droplet sizes d increase, ζ/d decreases. The shrinkage and dissolution of droplets occurs due to the slow diffusion process, which has a timescale $\tau_d \propto N_x^2$. Hence decreasing the Cahn number

has two effects which together reduce droplet dissolution. First is that a larger domain size leads to a higher τ_d, which can be made sufficiently larger than the flow timescale $\mathscr{T}$ such that the slow mass diffusion does not influence the results. Secondly, since on average the droplets are larger, there will be fewer small droplets that are unstable and prone to dissolution.

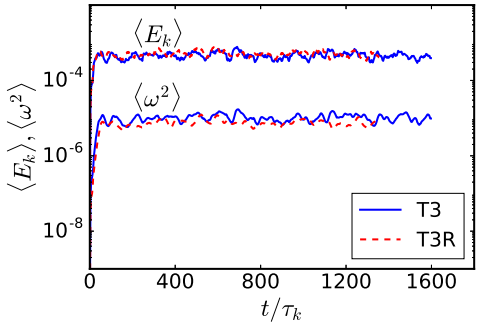

(a) Evolution of volume averaged kinetic energy and enstrophy for simulations T3 and T3R.

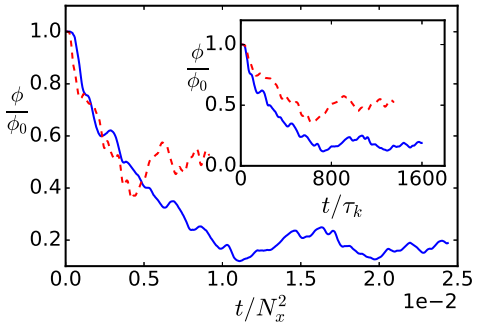

(b) Evolution of normalized volume fraction for simulations T3 and T3R.

Figure 5.14: Decreasing the Cahn number is shown to reduce droplet dissolution. Simulation T3 is performed again on a larger domain (i.e. simulation T3R), while keeping the energy density the same, as shown in panel (a). Panel (b) shows the volume fraction evolution for the two simulations. The droplet dissolution effect is lower in T3R, and the stable ϕ value is a factor 2 higher than T3. Upon scaling time with the square of the domain size, the two curves collapse for the initial droplet dissolution phase until steady state is reached. Lower droplet dissolution is an effect of increased separation between the flow timescale and component diffusion timescale (as shown in the inset of panel (b), where ϕ reduces at a slower rate for T3R).

Simulations T3 and T4 suffer most strongly from droplet dissolution, so we test how increasing the resolution of these simulations can reduce this effect. Figure 5.14 shows a comparison between simulation T3 and T3R. Panel (a) shows that the two simulations have very similar average kinetic energy $\langle E_k \rangle$ and enstrophy $\langle \omega^2 \rangle$, although $\langle \omega^2 \rangle$ is found to be slightly lower in T3R which leads to slightly higher Re_λ in T3R than in T3. This is because with the current formulation of the turbulence forcing mechanism it is not possible to exactly set the Re_λ of the simulation, and it depends on the forcing amplitude A. Despite this difference, the higher resolution of T3R leads to less droplet dissolution as seen from panel (b). Upon non-dimensionalizing time with the domain size N_x, the initial reduction in ϕ for T3 and T3R overlap, which shows that the diffusive mass redistribution occurs over a longer timescale proportional to N_x^2. In non-dimensional units, these physically long duration simulations over $1000\tau_k$ are well within 10^{-2} diffusive time units, showing that the timescale of flow is much faster. Further, T3R has a higher ϕ value at steady state, where droplet dissolution is reduced from 80% to 50%. This is an indication that fewer droplets with $Ch \sim O(1)$ are formed. The inset in panel (b) shows the evolution of ϕ over time non-dimensionalized with τ_k. The steady state ϕ is found to be achieved sooner, and at the limit of much higher resolution, diffusional mass transfer will not influence the flow. The same effect was found upon performing a refined version of simulation T4 (T4R, not shown here), where increasing the resolution

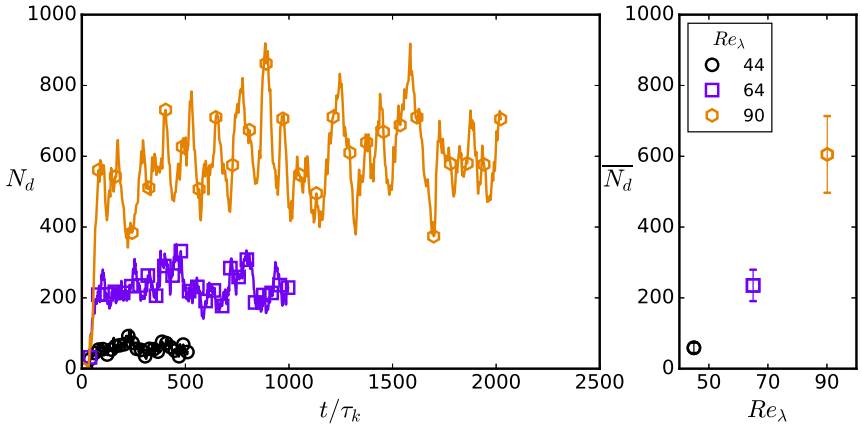

Figure 5.15: Evolution of the number of droplets (N_d) for increasing turbulence intensity, indicated by Re_λ. Increasing Re_λ leads to a larger number of droplets in the system, also widening the droplet distributions as seen from the fluctuations in the N_d evolution. $\overline{N(d)}$ is obtained by averaging $N(d)$ after steady-state conditions are reached.

from 256^3 to 384^3 reduced droplet dissolution from 100% to about 80%. We omit cases T3 and T4 from further analysis due to severe droplet dissolution.

DROPLET NUMBER DENSITY EVOLUTION

Figure 5.15 shows the evolution of the number of droplets for cases T1, T2 and T5. Increasing Re_λ increases the average number of droplets in the system (obtained by averaging N_d after steady-state conditions are reached for each simulation) from around $\overline{N_d} = 50$ for $Re_\lambda = 44$ to $\overline{N_d} = 600$ for $Re_\lambda = 90$. Further, two interesting features in the evolution of N_d can be noted. First is that the variation in N_d increases with Re_λ, which results in a larger standard deviation of $\overline{N_d}$. This also makes it possible to generate a wider distribution of droplet diameters in the system, due to higher intermittency [9]. The second striking feature is the quasi-periodic rise and fall in the droplet number concentration (with a period of around $8-10\mathcal{T}$), most distinctly seen for the $Re_\lambda = 90$ simulation (case T5). There seems to be an upper limit to the number of droplets that can be formed, which apart from constraints of resolution and maximum sphere-packing of the domain while keeping the diffuse interfaces apart, indicates also at the underlying physical mechanisms. At its peak, $N_d \approx 900$ here, a state corresponding to most droplets being rather small that cannot undergo additional breakup as they would all be well below the Hinze scale. These droplets are advected around by the flow, and they begin to coalesce when they collide, causing N_d to drop to its lower limit, where a significant number of droplets will again be larger than the Hinze scale, and they begin to break and this cycle continues. We shall revisit this feature in detail in section 5.5.1.

DISPERSION MORPHOLOGY

The dispersion morphology can be quantified with the concentration spectrum $k^2 S(k,t)$, a quantity commonly used to describe coarsening dynamics (or spinodal decomposi-

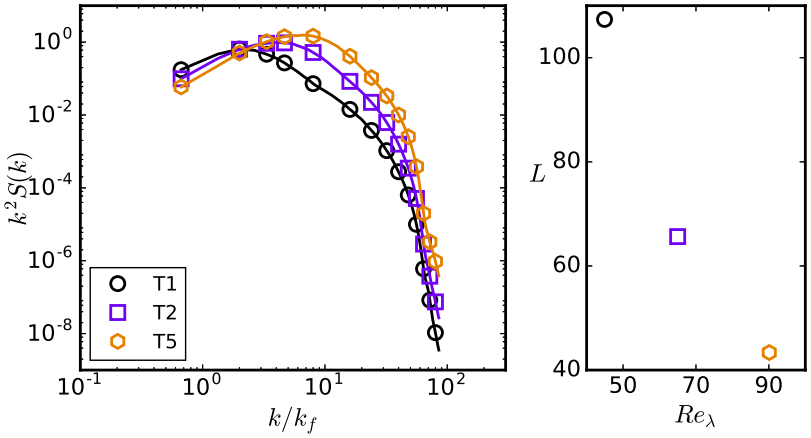

Figure 5.16: Concentration spectrum and characteristic length characterizing the dispersion morphology for increasing turbulence intensity simulations, corresponding to cases T1, T2 and T5 in table 5.1. The structure factor $S(k,t)$ was time averaged over 10 realizations separated by $\approx 50\tau_k$, and further normalized by $\sum_k S(k,t)$ to compare the relative difference in concentration at each wavelength. Increasing Re_λ generates smaller droplets which is seen in the reduction of the characteristic length.

5

tion) [14, 66]. Here $S(k,t)$ is the shell-averaged structure factor which is obtained using the Fourier transform $\hat{\phi}_{\mathbf{k}}$ of the density-density correlation function $\phi - \overline{\phi}$, where $\phi = (\rho_\alpha - \rho_\beta)$ and $\overline{\phi}$ is the mean value of ϕ. The quantity $\hat{\phi}_{\mathbf{k}}$ is shell-averaged in wavenumber space to obtain $S(k,t)$ as follows

$$S(k,t) = \frac{\sum_k |\hat{\phi}_{\mathbf{k}}|^2}{\sum_k 1} \tag{5.24}$$

Here $\sum$ denotes summation over wavenumber shells $k \in [k-1/2, k+1/2]$ where $k = \sqrt{\mathbf{k}\cdot\mathbf{k}}$. Further, a characteristic length $L(t)$ can be calculated using the first moment of $S(k,t)$ as follows

$$L(t) = 2\pi \frac{\sum_k S(k,t)}{\sum_k kS(k,t)} \tag{5.25}$$

Figure 5.16 shows the concentration spectrum for cases T1, T2 and T5. As Re_λ is increased, smaller droplets begin to dominate the system which is seen from the shift towards higher wavenumbers in $k^2S(k,t)$. This is also reflected in the time averaged characteristic length L which decreases from 100 to around 40 [lu]. Note, however, that T5 has a higher surface tension than T1 and T2, and it is together that γ and Re_λ determine the morphology of the emulsion for a given dispersed phase volume fraction.

5.4.5. EFFECT OF DOMAIN SIZE

In simulations corresponding to D1-D4 in table 5.1, we successively increase the domain size N_x while keeping the turbulent energy density the same. This essentially creates a separation between the domain size N_x and the forcing scale $\mathscr{L}$, and allows for a better resolution of the largest droplet extension before breakup. So far, studies on turbulent

dispersions have focused on maximizing the turbulence intensity which is reflected in the general proclivity for achieving higher Re_λ in DNS simulations with Lagrangian objects like particles or droplets [67]. This finds implicit justification in that Re_λ in real systems where droplets and turbulence interact is typically very high, (where $Re_\lambda = \sqrt{15Re}$ for homogeneous, isotropic turbulence). For instance, emulsification in a valve homogenizer or colloid mill can occur at $Re \sim 30000$ [68, 69], and emulsification in stirred vessels has been studied at $Re \sim 15000$ [70] - for all these situations $Re_\lambda > 500$, which is several times larger than the range considered in the current study. In periodic domain DNSs, a high Re_λ is achieved by minimally resolving the Kolmogorov scale (the $k_{\max}\eta > 1$ condition [54]), while forcing turbulence at the largest possible scales i.e. $\mathscr{L} \approx N_x$ or $k_f \approx 1 - 2k_{\min}$. This wide separation of scales manifests a high Re_λ. There are a few connected issues regarding the relative resolution of the various length scales, which is the focus of this section.

The first issue, emphasized by Komrakova *et al.* [16], is the utility of over-resolving the Kolmogorov scale ($\eta \approx 10$ as opposed to 1 [lu]), which helped remedy the rapid dissolution of droplets in their simulations. The increased resolution of η and d can also be seen as a reduction in the size of the interface ζ, i.e. an decrease in the Cahn number Ch, since the interface thickness (in terms of the *number* of lattice spacings) remains constant while smaller droplets and turbulent length scales become better resolved (i.e. they become larger relative to ζ). Droplet dissolution also depends on the relative strengths of turbulence and phase segregation (effectively the interfacial tension), as was demonstrated in section 5.4.4.

The other issue is that weak large scale forcing introduces a caveat that droplets tend to deform into long, slender filaments that stay connected across the periodic domain. The length scale of the largest droplet extension before breakup d^{ext} can become comparable to N_x, which means that breakup cannot be resolved. The dispersion then forms a complex tangled structure, which does not morphologically resemble an emulsion. This issue is aggravated by high volume fractions of the dispersed phase.

In simulations D1-D4, we increase the forcing wavenumber k_f by the same factor as the domain size N_x (while keeping the forcing amplitude A the same). The upper and lower wavenumber bounds (k_a, k_b) are also suitably adjusted to distribute the forcing over a reasonable wavenumber range (and all integer values in the range $k \in [k_a, k_b]$ are considered). This ensures that the energy density remains the same in these simulations, while larger droplet deformations (d^{ext}) can be resolved accurately. Successively increasing the domain size in this way allows separating N_x from $\mathscr{L}$. Note that doing this does not decrease Ch for droplets, as that would entail scaling $\mathscr{L}$ proportionally with N_x while weakening the forcing amplitude such that Re_λ remains constant and η is over-resolved (the approach of Komrakova *et al.* [16]). We do not additionally pursue this as droplet dissolution is not significant in most of the parameter range considered in this study.

Figure 5.17 shows the droplets in the system (volume rendered) at $400\tau_k$ for increasing domain sizes. It can be seen that the largest structures in the 128^3 domain span a significant fraction of the domain, whereas for increasing domain sizes the typical large scale structure becomes better resolved in relation to the domain size. The volume averaged droplet number density for these simulations was found to be almost identical.

The domain size limitation becomes apparent when considering the droplet distri-

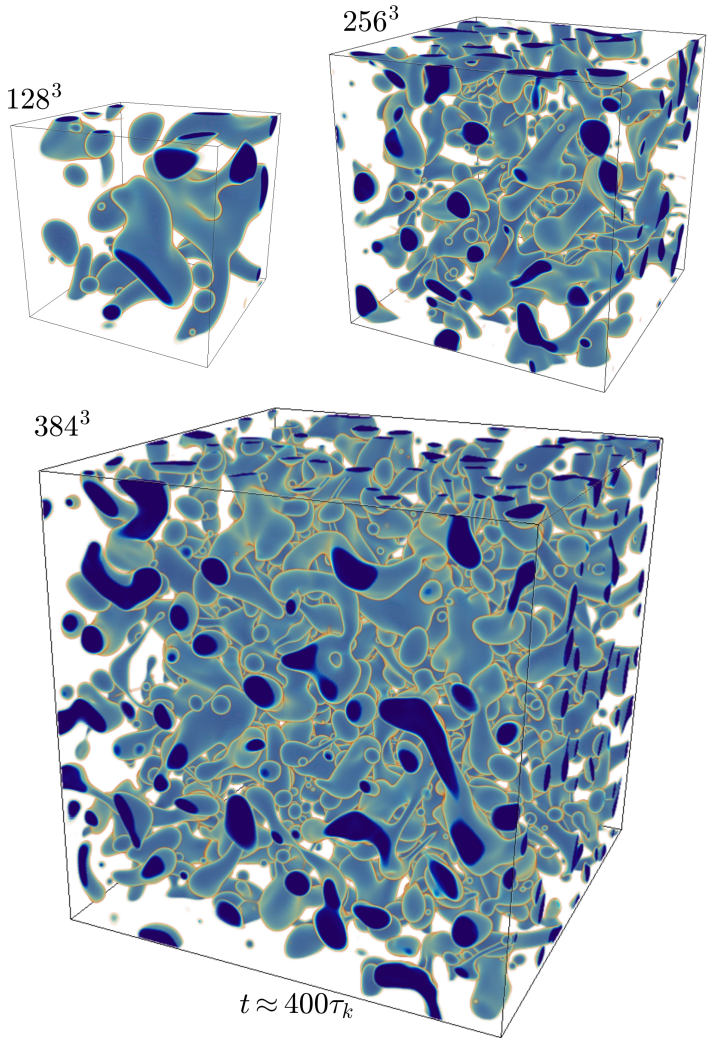

Figure 5.17: Volumetric droplet distribution for increasing domain sizes while maintaining the same energy density (power input) for cases D1, D2 and D3 with $N_x = 128^3, 256^3$ and 384^3 respectively. The resolution of large droplet extensions becomes feasible at higher domain sizes. Here dark blue to orange goes from the droplet interior to the matrix phase.

bution, as shown in figure 5.18. For the case of $N_x = 128^3$ (D1), the distribution is limited to a small region around the peak, clearly being cut off at a secondary peak emerging at higher d/η due to a lack of resolution of larger structures. This case is under-resolved, the issue made acute with the small domain size, significant ϕ and moderate $Re_\lambda \approx 30$. We include this case to emphasize that the same issue might arise in simulations with higher Re_λ and N_x of high volume fraction dispersions. Upon increasing N_x, the distribution successively assumes a longer tail which closely follows the $d^{-10/3}$ scaling for droplets larger than the Hinze scale.

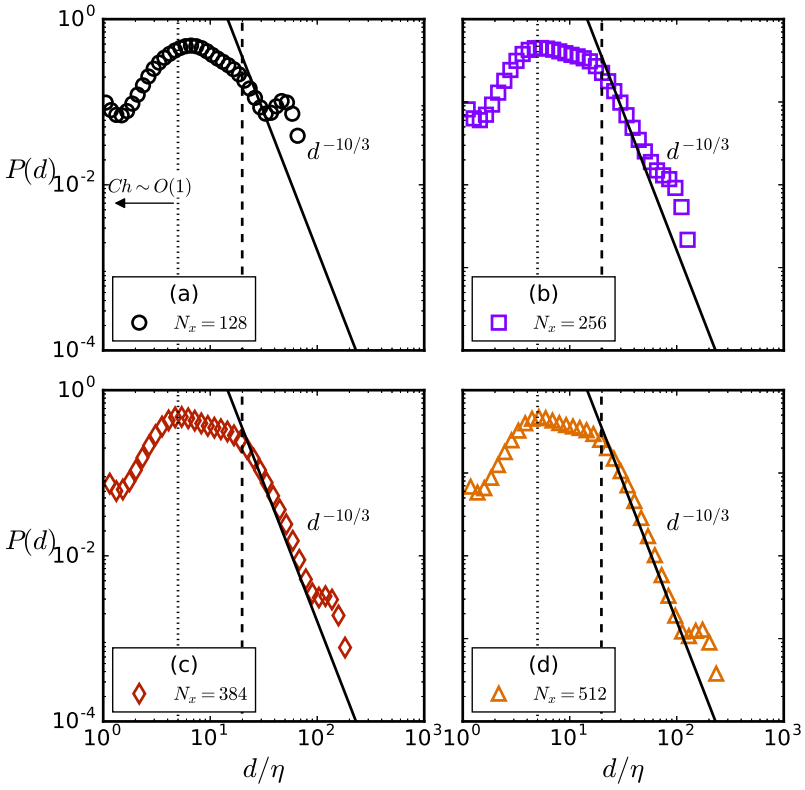

Figure 5.18: Droplet size distributions for cases D1-D4, all with $\phi = 0.15$ and $Re_\lambda \approx 30$. The total number of droplets considered between times $150 - 600\ \tau_k$ are $\approx 5000, 40000, 54000, 133000$ for $N_x = 128, 256, 384, 512$ respectively. The dashed vertical line shows the Hinze scale and the dotted vertical line marks the limit $Ch \sim O(1)$.

Figure 5.19a shows the concentration spectrum for cases D1-D4, which first reflects the proper scaling as the spectra coincide for $k/k_f \geq 1$. The importance of resolving the dominant length scales characterizing the dispersion morphology vis-à-vis the domain size N_x becomes apparent. The smallest wavenumber (largest length scale) that can be represented depends on N_x as $k_{\min} = 2\pi/N_x$. For case D1, $k_{\min}$ is very close to the wavenumber corresponding to the peak in the concentration spectrum, i.e. the dominant wavenumber k_d (or length scale N_x/k_d). If $k_{\min} \approx k_d$, two issues would tend to

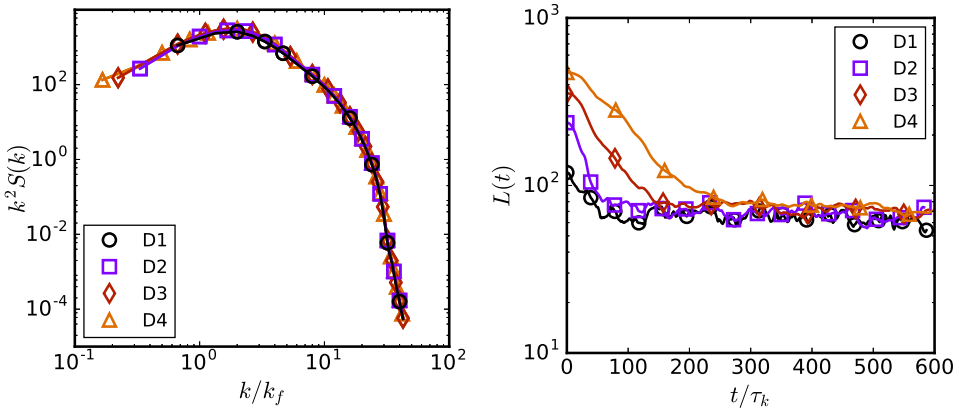

(a) Concentration spectrum

(b) Characteristic length evolution

Figure 5.19: Dispersion morphology characterized with the (a) concentration spectrum $k^2S(k,t)$ and (b) characteristic length $L(t)$ for cases D1-D4. The concentration spectrum is averaged between times $150-600\tau_k$, sampled every $4\tau_k$. The importance of separation between the domain size N_x or $k_{\min}$ and the dominant length scales characterizing the dispersion i.e. k_d or $L(t)$ is evident from the fact that these two length scales can become comparable.

arise. First is that the dominant length scale of the emulsion morphology is comparable to the domain size making its dynamics under-resolved. Secondly, this structure will strongly interact with an image of itself due to periodicity of the domain, which is undesirable. For successively larger domains, the dominant length scale does not change (due to the same energy density across simulations). Further, the separation of $k_{\min}$ and k_d is increased, which confirms that the largest structures ($\sim N_x/k_d$) are well resolved, while even larger structures (in the range of $k < k_d$) are formed but not sustained as the peak of $S(k)$ resides at k_d. The characteristic length evolution in figure 5.19b also shows that the morphology obtained for D1-D4 is similar, and that the typical length scale $L(t) \approx 80$ becomes better resolved in relation to the grid size upon increasing N_x.

5.4.6. EFFECT OF FORCING WAVENUMBER

To highlight the consequences of forcing turbulence at the largest possible scale i.e. having $\mathscr{L}$ comparable to N_x (hence maximizing Re_λ), we performed an additional simulation D5 with $k_f = 1.5k_{\min}$ and $\phi = 0.2$ to compare with D4 ($k_f = 6k_{\min}$, $\phi = 0.15$), while keeping the forcing amplitude the same, which results in $Re_\lambda = 118$ for case D5 (while $Re_\lambda = 30$ for D4). Figure 5.20 shows the typical morphology of the droplets (at a random time instance), where visibly the D4 case seems to have smaller, more spherical droplets, while D5 shows more elongated filaments. Despite the higher Re_λ, the dispersion does not comprise smaller droplets as droplet sizes depend on $\langle\epsilon\rangle$ which remains mostly unchanged. The presence of elongated filaments in D5 reflects the nature of the turbulence forcing. For a long cylindrical filament, a higher wavenumber forcing will generate more curvature variations. This would increase the possibility of filament breakup driven by Rayleigh-Plateau instabilities. A lower wavenumber forcing would generate weaker cur-

vature differences in a long filament, and the timescale of breakup of these filaments might be comparable to the timescale of the large eddies, in which case the filaments will only break when the direction of the large scale shear changes.

We further quantify the differences by calculating the droplet distribution for D4 and D5 (which have slightly different ϕ), while also comparing simulations D2 (with $k_f = 3.0$ and $Re_\lambda = 30$) and P3 ($k_f = 2.0$ and $Re_\lambda = 47$) which have the same ϕ, shown in figure 5.21. Indeed, the D5 case deviates from the $d^{-10/3}$ distribution above the Hinze scale reflecting the infrequent breakup of the long filaments that would lead to droplets in this range of sizes. This deficit of droplets shows up in a secondary peak at high d/η, which corresponds to the fewer, larger structures being sustained instead. A similar difference is seen between cases D2 and P3, where the P3 case shows a small peak at high d/η, again attributed to a lower wavenumber forcing. The same behaviour is reflected in the concentration spectrum as well between the cases (not shown here), where there is a relative increase in concentration at low wavenumbers for cases D5 and P3, although the characteristic length remains similar.

It is worthwhile to summarize the results from the domain size comparison and to draw conclusions. At modest Re_λ (< 120 in this study), the turbulence forcing wavelength and domain size influence the morphology. Having $N_x > \mathscr{L} \gg d$ (as in case D4) ensures sufficient resolution of the droplet breakup dynamics. While having $N_x \approx \mathscr{L} \gg d$ (case D5) causes the formation of longer filaments of the droplet fluid. Spatially, this causes the formation of larger droplets $d/\eta > 100$ at the cost of some intermediate droplets $20 < d/\eta < 100$, for d/η above the Hinze scale.

5.5. TURBULENT EMULSION DYNAMICS

5.5.1. A QUASI-EQUILIBRIUM (LIMIT) CYCLE

Droplet number density plots such as figure 5.15 show oscillations of N_d around a typical mean value which characterizes the dispersion morphology. So far, studies on droplets in turbulence refer to this state as a "steady state" where coalescence and breakup equilibrate. Since these oscillations can be significant (with its extreme values remaining bounded, similar to kinetic energy and dissipation), the dynamics should more accurately be called as a quasi-equilibrium (limit) cycle in the system state space comprising (1) kinetic energy $\langle E_k \rangle$, (2) enstrophy $\langle \omega^2 \rangle$, which is defined as $\langle \omega^2 \rangle = \langle \boldsymbol{\omega} \cdot \boldsymbol{\omega} \rangle$ (where $\boldsymbol{\omega} = \nabla \times \boldsymbol{u}$ is the vorticity), (3) interfacial energy $\langle E_\gamma \rangle = \langle S_A \gamma \rangle$ (i.e. the product of the total interfacial area S_A and the interfacial tension γ) and (4) the droplet number density N_d. Here $\langle . \rangle$ denotes volume averaging of the quantities. Coalescence and breakup equilibrate in a statistical sense only, while the instantaneous dynamics is governed by temporal branches of alternating dominance of coalescence and breakup. Note that the term "limit cycle" is used loosely to illustrate the dynamics, since truly closed trajectories in phase space were not found, perhaps primarily due to intermittency and non-periodicity of the numerical solutions.

A dominant mediator of droplet breakup is intense enstrophy (or dissipation ϵ). Since dissipation destroys turbulent kinetic energy, it is interesting to note that its interaction with the dispersed phase is associated with interfacial wrinkling, deformation and breakup - all mechanisms that increase the amount of surface energy in the system at the cost of kinetic energy. This excess energy, however, is still available in the flow field,

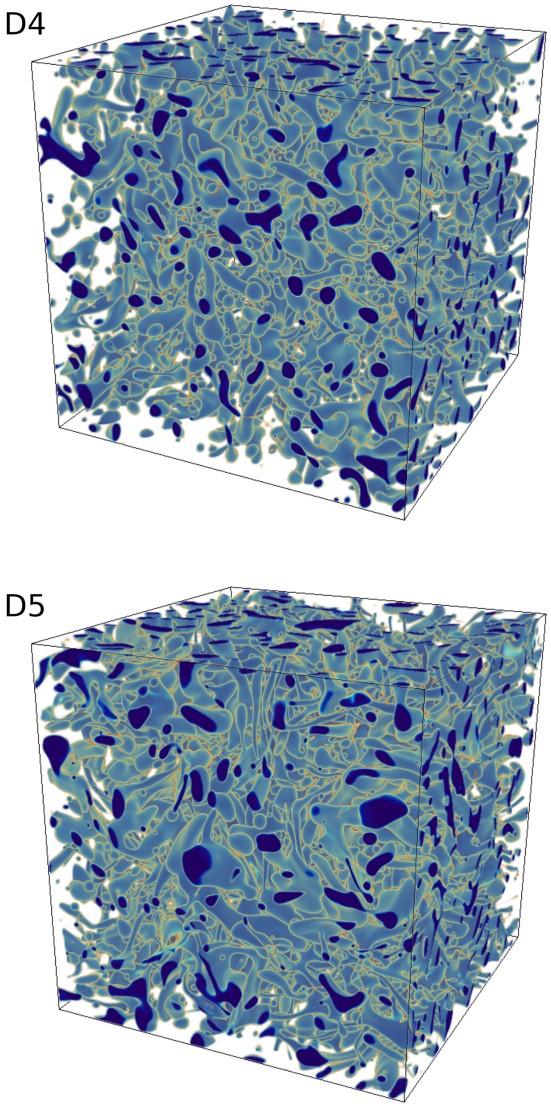

Figure 5.20: Volumetric droplet distribution for cases D4 and D5, where the forcing wavenumber is changed from $k_f = 6$ to $k_f = 1.5$, shown at $400\tau_k$. The D4 case shows a preponderance of smaller, more spherical droplets while D5 has more elongated filaments, possibly sustained due to the long wavelength of the forcing.

and true destruction of it (i.e. into heat) must be mediated via kinetic energy dissipa-

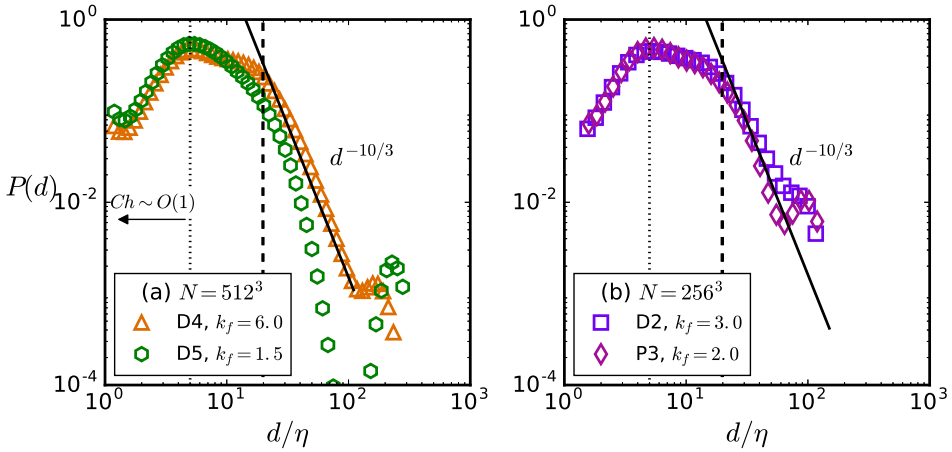

Figure 5.21: Droplet size distributions comparing (a) Cases D4 ($k_f = 6.0, \phi = 0.15, Re_\lambda = 30$) and D5 ($k_f = 1.5, \phi = 0.20, Re_\lambda = 118$), and (b) Cases D2 ($k_f = 3.0, Re_\lambda = 30$) and P3 ($k_f = 2.0, Re_\lambda = 47$).

5

tion, which occurs by the generation of smaller scales in the flow due to coalescence or damped oscillations of deformed droplet interfaces. A higher globally averaged $\langle \omega^2 \rangle$ can be expected to increase the chance of droplet breakup (as it also reduces the effective Hinze scale), and vice-versa. Hence the trends seen in the N_d evolution should reflect those in the evolution of $\langle \omega^2 \rangle$, which in turn should follow the peaks and valleys of the kinetic energy $\langle E_k \rangle$ evolution.

This hypothesis is found to be true, and is shown in figure 5.22 in the evolution of $\langle E_k \rangle$, $\langle \omega^2 \rangle$, N_d and $\langle E_\gamma \rangle$ for case T5.Here each variable has been normalized by its time average (between $50\tau_k$ and $1000\tau_k$), such that it oscillates around a mean value of 1, which is done merely to facilitate comparison between the different curves. The peaks in $\langle E_k \rangle$ (panel (a)) are found to consistently manifest in $\langle \omega^2 \rangle$ (panel (b)) with a small time delay, which are again found with a further time delay in the evolution of N_d (panel (c)). Two such instances have been marked by the three successive vertical lines than connect panels (a), (b) and (c), coinciding approximately with the local peaks of the different curves. Similarly, peaks in the evolution of $\langle E_\gamma \rangle$ (panel (d)) are found to precede peaks in N_d (panel (c)), two instances of which have also been similarly marked by vertical lines spanning the two panels of figure 5.22. This shows clearly that the droplet surface area (since here $E_\gamma \propto S_A$) is at its maximum before breakup, which hints that the droplet breakup mechanism is mainly the extension of filaments. Since droplet breakup leads to an increase in surface area - for example a spherical droplet breaking into n equal volume daughter droplets leads to an increase in surface area by a factor of $n^{1/3}$, the peak in surface area *prior* to breakup signifies that the droplet before breakup must be significantly elongated to have a larger surface area than the subsequently formed daughter droplets. This also shows that a single droplet does not break into too many daughter droplets at once, and the process is cascading, since otherwise a large number of daughter droplets will lead to higher surface areas *after* breakup, not before it. A correlation between the evolution of different variables can be calculated as

$$\mathrm{Corr}(\delta t) = \frac{\overline{\langle E_k(t)\rangle \langle \omega^2(t+\delta t)\rangle}}{\overline{\langle E_k\rangle}\,\overline{\langle \omega^2\rangle}} \tag{5.26}$$

where δt is a time lag and the overbar is a temporal average. This has been done for the different signal pairs and is shown in figure 5.23. Here $\langle \omega^2 \rangle$ is found to correlate strongly with $\langle E_k \rangle$ with a time delay of $\sim 0.3\mathcal{T}$. N_d shows a very strong correlation with $\langle \omega^2 \rangle$ at a time delay of $\sim 0.6\mathcal{T}$. Consequently, a significant correlation between N_d and $\langle E_k \rangle$ is found at $\sim 0.9\mathcal{T}$. The converse effect of droplets on turbulence can also be hinted at with this figure, where the valleys of the N_d evolution often coincide with peaks in the $\langle E_k \rangle$ evolution. This shows that when the droplet number density reduces due to coalescence, the excess surface energy is released into the flow as kinetic energy, which has been expounded by Dodd and Ferrante [10]. Since turbulence in our simulations is constantly forced (as opposed to Dodd and Ferrante [10] who simulate droplets in decaying turbulence) - the variation in $\langle E_k \rangle$ in our simulations comes from a more complex confluence of the power input as well as the droplet dynamics. The correlation of surface energy $\langle E_\gamma \rangle$ and N_d is shown in panel (c) of figure 5.23, where a weaker but certain correlation between $\langle E_\gamma \rangle$ and N_d is found with a time lag of $0.8\mathcal{T}$.

We also observed this time delayed dynamics of $\langle E_k \rangle$ and N_d for cases with different parameters like turbulence forcing amplitude and interfacial tension, although for some cases the effect was less explicit. Particularly, for weaker γ or lower Re_λ, the N_d oscillations were not as extreme as for case T5 (where turbulence intensity and interfacial tension are both relatively stronger forces), although the $\langle E_k \rangle$ and N_d correlation was found to be strong. Generally, the dynamics can be described as follows. First the large scale structures generate higher velocity gradients at the dissipation scale (which may be due to the energy cascade if such exists) with an initial time lag. This larger dissipation rate is felt by the droplets, which respond by breaking up with a further time delay, increasing the number of droplets in the system. This process (from peaks in $\langle E_k \rangle$ to peaks in N_d) was consistently found to take place with a delay of around $\sim 0.9\mathcal{T}$ across different cases, which is roughly the lifetime of the large eddies. This finding can be important for droplet dynamics models like population balance equations, where breakup kernels rely upon the instantaneous local value of ϵ. If the temporal aspect to droplet populations is important, a relaxation time should separate cause and effect which is not done currently as seen in the various models reviewed by Sajjadi *et al.* [71].

In summary, the turbulent emulsion dynamics can also be interpreted as a quasi-periodic evolution in a state space comprising $\langle E_k \rangle$, $\langle \omega^2 \rangle$, N_d and $\langle E_\gamma \rangle$. Essentially, there are two bounded extrema in the droplet number density at a given turbulent intensity for a certain set of fluid properties. These correspond to a state of low N_d which is marked by fewer, relatively large droplets. When dissipation attains a subsequent peak, several of these droplets must be larger than the instantaneous Hinze scale - which leads to accelerated droplet breakup with takes the system to its other extremum - a state marked with high N_d. Most of the droplets in this state are stable and cannot undergo further breakup. As dissipation reduces, these droplets are advected around, and due to a higher chance of droplet-droplet collisions, coalescence dominates the next part of the state-space evolution. These two states also exhibit slightly different dispersion morphologies, as illustrated in figure 5.24. The fluctuations in N_d are caused by these two phases, where

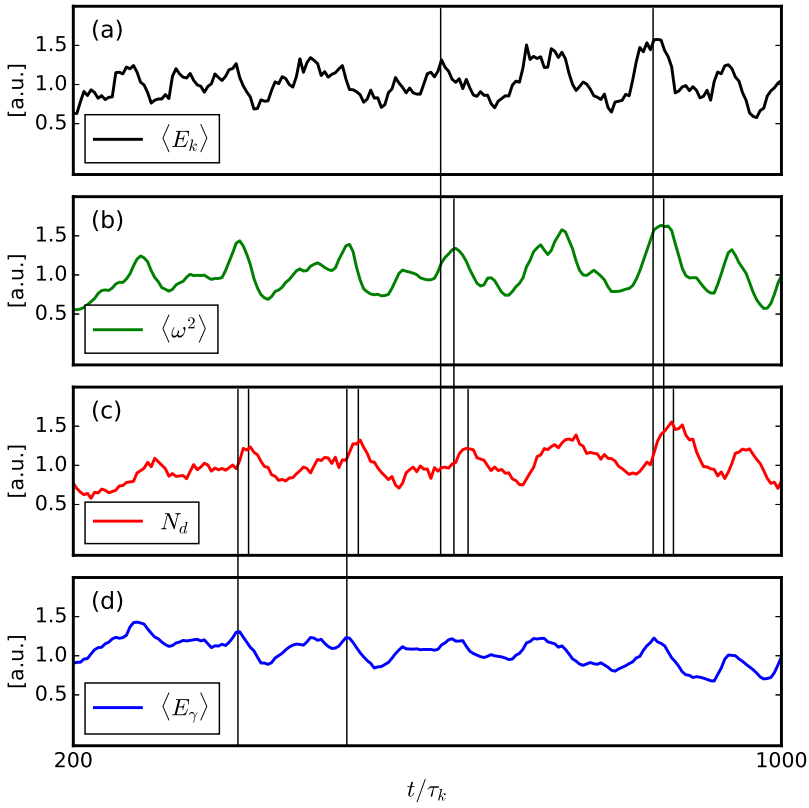

Figure 5.22: Evolution of state-space variables N_d, $\langle E_k \rangle$, $\langle \omega^2 \rangle$ and $\langle E_\gamma \rangle$ (from case T5). The $y-$axis is in arbitrary units [a.u.] for each quantity since they have been normalized by their time averaged values between $50\tau_k$ and $1000\tau_k$, to scale the fluctuations to around a mean value of 1 (to facilitate visual comparison between the different curves). In panels (a) to (c), peaks in $\langle E_k \rangle$ are shown to manifest in the $\langle \omega^2 \rangle$ evolution with a small time delay, which are then found in the N_d evolution with a further time delay, in a cascade of cause and effect. Two such instances have been shown using the vertical lines extending from panel (a) to panel (c), which approximately indicate individual sequences of cascading events. Similarly, peaks in $\langle E_\gamma \rangle$ are found to precede peaks in N_d, of which also two instances have been shown using the vertical lines between panels (c) and (d).

breakup and coalescence alternate in their dominance. In the $E_k - E_\gamma$ phase space, this can be viewed as (a somewhat erratic) evolution within a bounded region of finite E_k and E_γ. We do find signatures of this behaviour, although to more accurately describe the $E_k - E_\gamma$ phase space requires further work where the contribution from breakup and coalescence are separately accounted for and the surface area is better resolved by simulating larger droplets in weaker turbulence. It should be noted, though, that the dynamics we report would correspond to local dynamics in larger droplet laden systems like stirred vessels or in clouds. When considering these systems as a whole, the equilibrium properties may not fluctuate as much as reported here, as the local fluctuations in

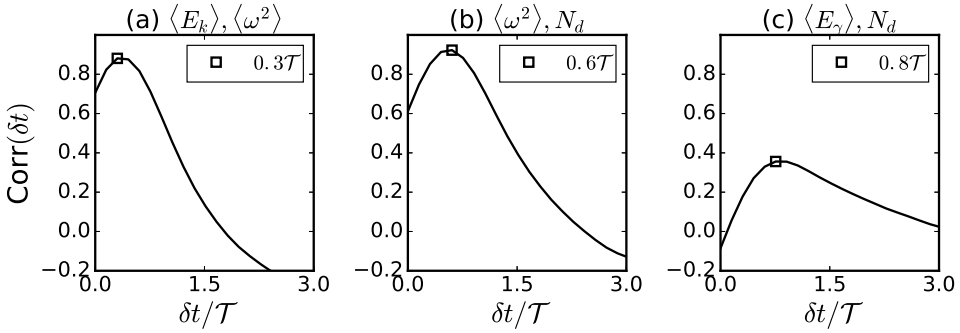

Figure 5.23: Correlation between N_d, $\langle E_k \rangle$ and $\langle \omega^2 \rangle$ for case T5. N_d consistently correlates strongly with $\langle E_k \rangle$ with a temporal delay of $0.9\mathcal{T}$, while $\langle E_\gamma \rangle$ is found to attain its maximum value *before* N_d, hinting that breakup occurs via extension of droplets into long filaments.

5

different regions of the system would cancel out.

5.5.2. VORTICITY AND INTERFACE ALIGNMENT

Figure 5.25 shows snapshots of enstrophy from a vertical cross-section of the varying ϕ simulations (P1-P4), with the droplet contours shown in black. Strong vortical regions are often found in the vicinity of the droplet interface and in the droplet wakes. There is strong interplay between the interfacial dynamics and dissipation, as strong vortical regions align with the interface [20] and cause wrinkling, and high local dissipative events can lead to droplet breakup [12].

The interplay between the vorticity vector and the interface normal can be quantified by using the distribution of the cosine of the angle between these two vectors. First, the density field ρ_β is converted to a phase indicator field $\psi = (\rho_\beta - \rho_\beta^{\text{out}})/(\rho_\beta^{\text{in}} - \rho_\beta^{\text{out}})$, such that $\psi = 1$ in the droplet region, $\psi = 0$ in the carrier fluid region, and $0 < \psi < 1$ at the interface. The typical phase indicator gradient then becomes $\nabla\psi = 1/\zeta$, and the cosine of the orientation angle is calculated where $\nabla\psi > 0.01\zeta$ (where 0.01 ensures all the interfacial region is considered while ignoring the bulk regions where $\nabla\psi = 0$ by construction) as follows

$$\cos(\theta) = \hat{\mathbf{n}} \cdot \hat{\boldsymbol{\omega}} \tag{5.27}$$

where $\hat{\mathbf{n}} = \nabla\psi/|\nabla\psi|$ gives the unit normal vector at the interface and $\hat{\boldsymbol{\omega}} = \boldsymbol{\omega}/|\boldsymbol{\omega}|$ is the normalized vorticity vector.

Using this measure, Shao *et al.* [20] showed that vorticity tends to align tangentially to droplet interfaces in turbulent flow. Here we extend their result in figure 5.26 which shows the joint probability distribution of the cosine of the orientation angle θ and the normalized vorticity vector $\boldsymbol{\omega}/\langle\omega^2\rangle^{1/2}$. The joint PDFs have been generated with statistics collected from 6 different field snapshots, evenly spaced between roughly $100-200$ τ_k. The black dashed lines mark $\omega = 0.5\langle\omega^2\rangle^{1/2}$. Stronger vorticity ($\omega > 0.5\langle\omega^2\rangle^{1/2}$) is found to be more prone to align tangentially to the interface. In this range, vorticity is associated with strong swirling motion in the plane orthogonal to the vorticity vector, which causes droplet accretion and subsequent tangential alignment of vorticity with interfaces, yielding $\cos(\theta) = 0$. Weaker vorticity ($\omega < 0.5\langle\omega^2\rangle^{1/2}$, i.e. below the black

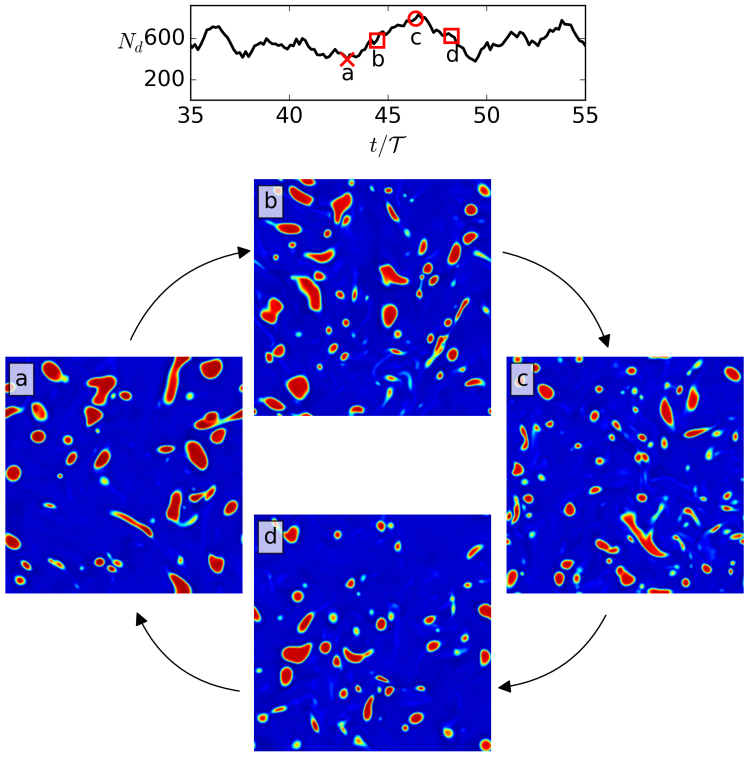

Figure 5.24: Quasi-periodic evolution of droplet morphology, cyclically visiting a typical state **'a'** marked by low N_d (and hence low $\langle E_\gamma \rangle$) and high $\langle E_k \rangle$ and state **'c'** marked by large N_d (and $\langle E_\gamma \rangle$) and low $\langle E_k \rangle$. The transition from **'a'** to **'c'** happens via a dominance of breakup shown in state **'b'**, while the return from **'c'** to **'a'** via state **'d'** happens due to dominant coalescence. These snapshots are from case T5.

dashed line) is incapable of exerting this influence on droplets, and hence exhibits a uniform random distribution of orientation angles with respect to the interfaces (as all θ values seem to occur with equal probability at a given ω).

Another explanation for this effect could be that most droplets are elongated. It is a known phenomenon that oblate objects align with the vorticity parallel to their axis, as has been shown for sub-Kolmogorov oblate particles [72] and inertial spheroids [73]. Since the elongated interfacial regions influence the joint PDF more strongly (by being more prevalent), and since there is a significant peak at $\cos(\theta) = 0$, the axial alignment mechanism seems plausible. On the other hand, spherical sub-Kolmogorov droplets would tend to spin in local shear of the deep dissipation range, and if deformed, may also tend to have orientation statistics similar to rods in turbulence [72]. This hypothesis would need to be further tested. Our orientation statistics are valid for droplets in the inertial range, and a simple extrapolation to sub-Kolmogorov droplets cannot be done.

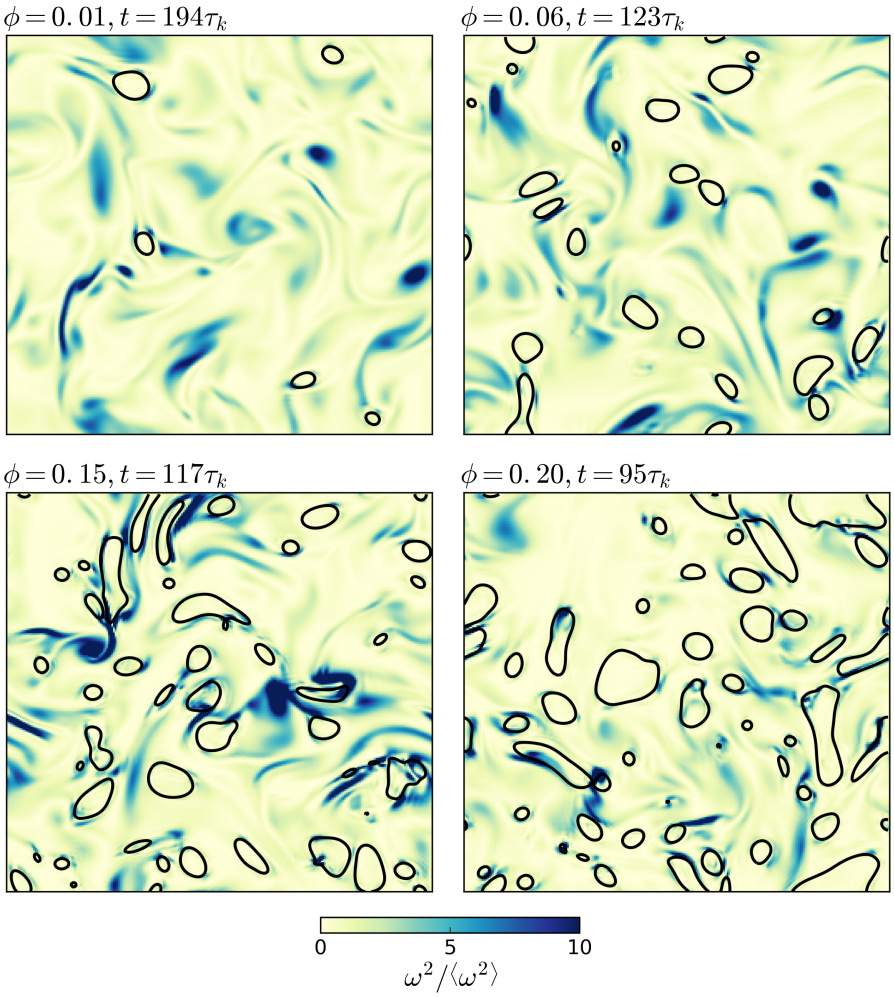

Figure 5.25: Planar cross-sections (at $z = N_x/2$) of the enstrophy field ω^2 normalized by the average enstrophy $\langle\omega^2\rangle$ along with droplet contours for varying ϕ values (cases P1-P4). These snapshots show the typical dissipation profiles with localized, intense dissipation events often concentrated around droplet interfaces or leading to droplet accretion.

5.5.3. EFFECT OF DROPLETS ON FLOW TOPOLOGY

Local flow topology is described in terms of the three invariants (P, Q and R) of the velocity gradient tensor $A_{ij} = \partial u_i/\partial x_j$, which form the coefficients of its characteristic equation

$$\lambda^3 + P\lambda^2 + Q\lambda + R = 0 \tag{5.28}$$

where $P = -A_{ii}$, $Q = -A_{ij}A_{ji}/2$ and $R = -A_{ij}A_{jk}A_{ki}/3$. For incompressible flow, $P = 0$ (i.e. the sum of the eigenvalues). In the $P = 0$ plane (or the QR-plane), turbulent flow of diverse kinds produces a teardrop-like profile for the joint probability distribution

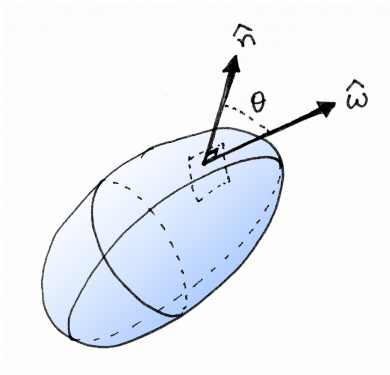

(a)

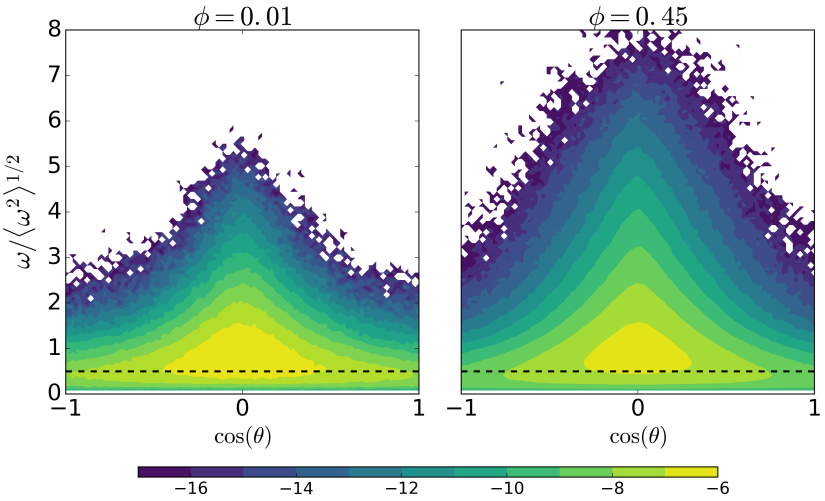

(b)

Figure 5.26: (a) Schematic of the orientation angle θ. Here $\hat{\mathbf{n}}$ is the normal unit vector to the interface and $\hat{\boldsymbol{\omega}}$ is the vorticity unit vector at that point; (b) Alignment between vorticity and the local interface normal is shown as the joint pdf of the cosine of the angle between them and the magnitude of vorticity, for the two extreme cases of $\phi = 0.01$ (simulation P1) and $\phi = 0.45$ (simulation P5), the intermediate cases being in between these two. The contour levels have been logarithmically spaced. Stronger vorticity ($\omega > 0.5\langle\omega^2\rangle^{1/2}$, above the black dashed lines) tends to align orthogonal to the interface while weaker vorticity remains randomly aligned with the interface with a more uniform distribution.

of Q and R with four distinct flow topologies that have been illustrated in figure 5.27 (adapted from Ooi *et al.* [74]). The curve $D = 27R^2/4 + Q^3 = 0$ (derivation can be found in Chong *et al.* [75]) divides the region with three real eigenvalues of A_{ij} (below, where $D < 0$) from the region with one real and a pair of complex conjugate eigenvalues (above, where $D > 0$). The most dominant flow features are stable focus stretching 'SFS' (i.e.

vortex stretching) and unstable-node/saddle/saddle 'UN/S/S' i.e. bi-axial straining [76]. 'UFC' corresponds to unstable focus compression (or vortex compression) and 'SN/S/S' is stable-node/saddle/saddle (or axial straining).

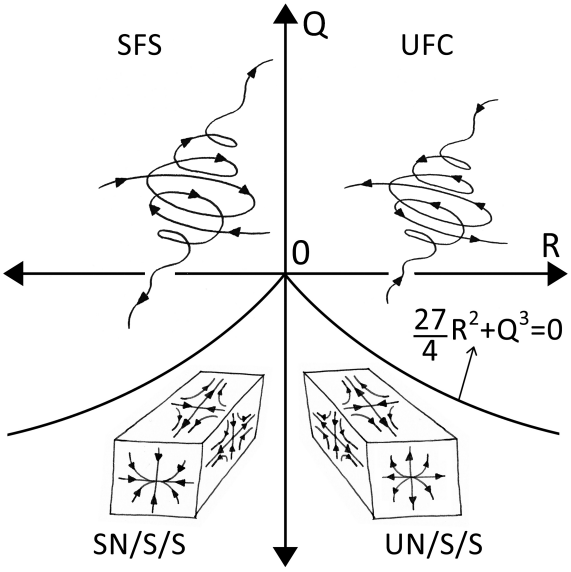

Figure 5.27: The four distinct flow topologies of turbulent flow shown in the plane of Q and R i.e. the second and third invariants of the velocity gradient tensor A_{ij}. 'SFS' is stable focus stretching, 'UFC' is unstable focus compression, 'SN/S/S' is stable-node/saddle/saddle and 'UN/S/S' is unstable-node/saddle/saddle. This figure is an adaptation from the classification in Ooi *et al.* [74].

The presence of droplets or particles which interact with the flow can modify the distribution of flow topologies, which is a modification of turbulence structure at a more local and fundamental level than for instance modifications to the kinetic energy spectrum. This has been well investigated for particle laden turbulence [77, 78] and recently shown for elastic polymers in turbulence by Perlekar *et al.* [79]. Although polymer additives are fundamentally very different from droplets, both are elastic objects, and hence they may have some similar turbulence modification effects. Recently, Shao *et al.* [20] showed a mild suppression of bi-axial straining in droplet laden turbulence upon changing the Weber number.

How droplets modify flow topology has not fully been investigated so far. Here, we first show the influence of increasing dispersed phase volume fraction on the QR profiles calculated using simulations P1-P5. Since Re_λ for these cases varies (and is almost a factor 2 lower than the corresponding single-phase turbulence simulation, see table 5.1), the normalization factor $\langle Q_w \rangle = \langle \omega^2 \rangle / 4$ [74] is calculated for each case separately. This allows us to focus on the modification of flow features alone, without comparing the magnitude of these extreme QR events. Figure 5.28 shows the QR field sampled over the entire multiphase velocity field. For case (b) $\phi = 0.01$, the profile is narrower than for single-phase turbulence, case (a), although the overall shape is similar. This might be due to the $\phi = 0.01$ dispersion being dilute, which makes coalescence infrequent.

Overall, in this case, the flow field is similar to that in single-phase turbulence, and coalescence generated smaller scale features are rare. This seems likely, as at successively higher volume fractions, cases (c) through (f), the QR profile is influenced more significantly and it tends to become more symmetric across the $R = 0$ line. This follows from an increase in the axial straining part of the flow, along with an extension of the profile into the $D > 0$ and $R > 0$ region which shows a relative increase in vortex compression as opposed to vortex stretching ($D > 0$ and $R < 0$).

Modification of the QR profile due to an increase in ϕ hints that it is a consequence of turbulence being constrained by the dispersed phase. To validate this claim, in figure 5.29 the QR profiles are shown while being sampled inside and outside the droplet regions (marked as "d" for droplet-phase and "c" for continuous-phase). This has been done for simulations D4 and D5 (which have the highest resolution, and significantly different $Re_\lambda = 30$ and 118 respectively). The QR profiles have been sampled at 5 time instances separated by $100\tau_k$. The difference between the flow topology in the droplet and continuous phase is striking, where within the droplet region QR profile seems to almost have flipped across the $R = 0$ axis.

There is a small increase in axial straining and a significant increase in vortex compression inside the droplets. A possible explanation for this effect could be the presence of interfaces surrounding droplets which behave like elastic surfaces. Vortices being stretched inside the droplets will try to elongate the droplet along the stretching axis, and this will be counteracted by interfacial tension which would instead tend to compress vortices. Since vortex compression contributes to energy dissipation [56], an enhancement of energy dissipation might also be expected inside droplets from these results (further investigation of this is left for future work). With a similar reasoning, increase in axial straining may also be an effect of surface tension. Axial strain tends to stretch droplets into prolate ellipsoids (cigar-like objects), while bi-axial strain would shape them into oblate ellipsoids (flat, pancake like objects). For equivalent strain intensity, bi-axial strain would lead to a more rapid increase in surface energy than axial strain. The increase in axial strain may hence be another consequence of droplets trying to minimize surface energy. More work is required to pinpoint the reason behind the droplet effects on flow topology. These effects, along with the alignment of elongated droplets parallel to local vorticity, can be viewed as complementary phenomena. The continuous phase QR profile remains mostly tear-drop like, with minor increase in axial straining and vortex compression.

We did not directly investigate the effect of surface tension on the QR profiles, but it can be argued that an increase in surface tension will further amplify vortex compression and axial strain (if our hypothesis of the mechanism is correct). This is because a higher γ will lead to a stronger surface tension force which will counteract any increase in surface area due to deformation or breakup. At the limit of zero surface tension both fluids will perfectly mix, and one will recover the usual tear-drop like QR profile found for single phase turbulence. This can also be related to the effect of the average droplet size, where a higher surface tension will lead to larger droplets on average, which will influence turbulence topology more than small droplets. Hints of this effect are visible in results from the increasing volume fraction simulations, where on average the droplet sizes increase, which results in greater turbulence modification. A direct comparison, however, has not been performed in this study, and it would require larger droplet sizes

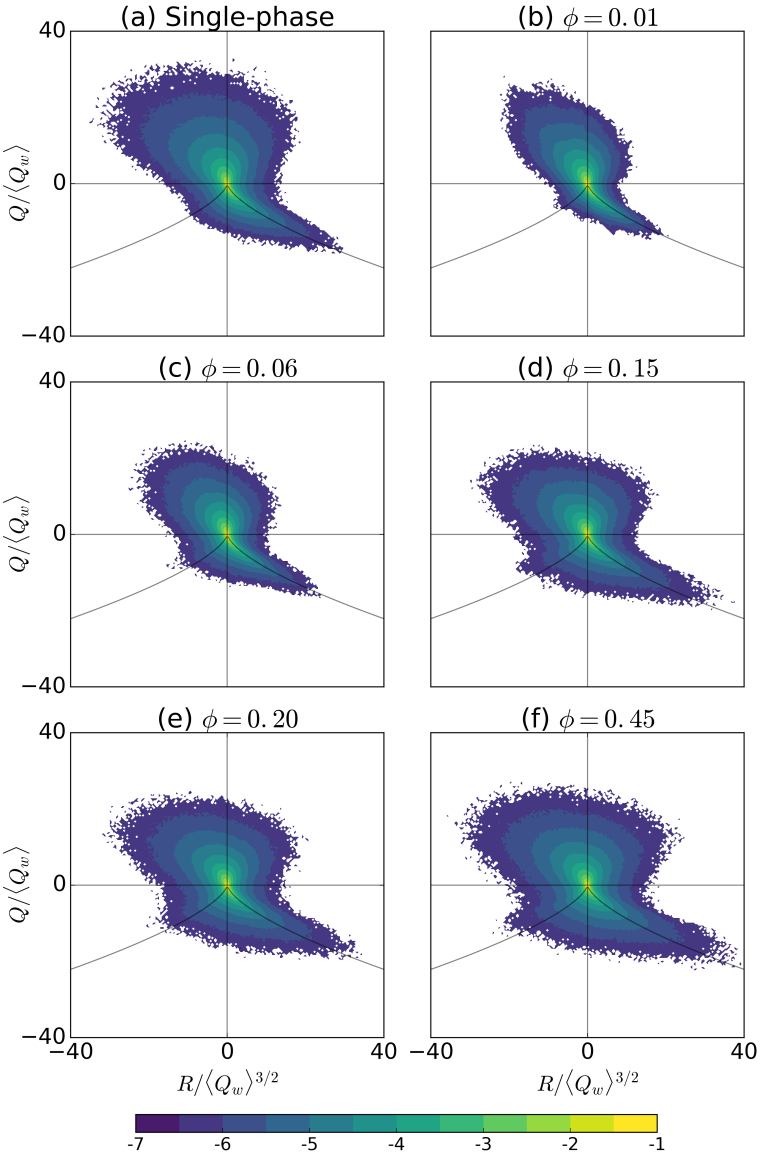

Figure 5.28: Joint PDFs of the second and third invariants (Q and R) of the velocity gradient tensor shows the typical teardrop profile characteristic of single-phase turbulence being modified into a more symmetric profile with an increase in axial straining and vortex compression. Here $\langle Q_w \rangle = \langle \omega^2 \rangle / 4$ and the quantities are calculated over the entire multiphase velocity field, sampled at 5 time instances separated by $20\tau_k$. The solid lines mark $Q = 0$, $R = 0$ and $D = 27R^2/4 + Q^3 = 0$, and the contour levels have been logarithmically spaced.

while keeping the volume fraction and turbulence intensity the same.

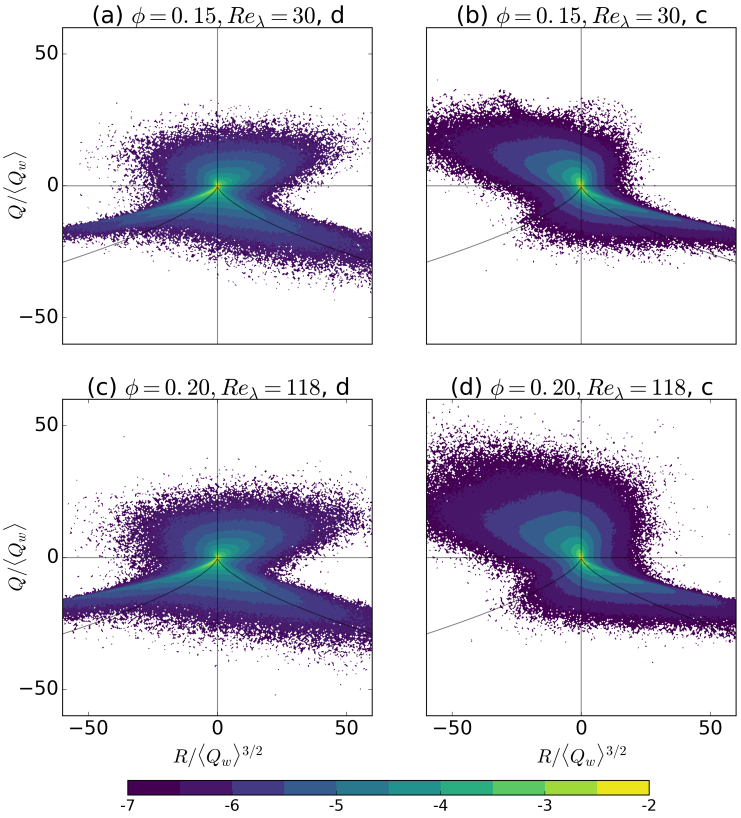

Figure 5.29: Joint PDFs of QR sampled in the droplet phase ("d") and continuous phase ("c") for cases D4 and D5. The QR profile appears to flip on the $R = 0$ axis for the droplet phase, with a striking increase in vortex compression and axial straining. The continuous phase QR profile remains mostly tear-drop like with minor increase in axial straining.

5.6. CONCLUSIONS

We perform direct numerical simulations of emulsions under homogeneous, isotropic turbulence conditions performed by using the pseudopotential lattice-Boltzmann method. New findings on droplet size distributions, multiphase kinetic energy spectra, coupled kinetic energy and droplet number density dynamics, interface-dissipation interactions and modification of turbulence flow topology in emulsions are reported.

The process of dispersion formation is investigated for varying volume fractions of the dispersed phase and varying turbulence intensities for an emulsion with a density and viscosity ratio of 1. Using an appropriate set of parameters (such that the pseudopotential repulsive force between components dominates the local turbulence force), the effect of droplet dissolution is mitigated, an issue that was found limiting in previous

work [12, 16]. While further maintaining spurious currents to well below the physical velocity scales, the multiphase kinetic energy spectra were shown to exhibit signatures of breakup and coalescence at wavenumbers smaller and larger than the inverse Hinze scale respectively.

At small wavenumbers, energy is primarily extracted from the flow, where a higher dispersed phase volume fraction ϕ extracts more energy due to the profusion of interfaces. At large wavenumbers, for successively higher ϕ, the energy content of the dissipation range increases due to more frequent coalescence which generates smaller scale motions. The droplet distribution is shown to follow the $d^{-10/3}$ scaling that has been previously found for purely inertial breakup of the dispersed phase [3, 9]. High volume fraction dispersions under moderate turbulence intensities do not exhibit the $k^{-5/3}$ inertial range scaling, and in these cases coalescence cannot be ignored either, in which case the classical Hinze [2] scale becomes invalid. We propose a generalization of the Hinze scale for these situations, where instead of using the dissipation rate $\langle\epsilon\rangle$ to determine the characteristic velocity at the droplet scale d, we use the multiphase kinetic energy spectra $\langle E(k)\rangle$ (which reflects the average energetics including coalescence and breakup at each scale) and the droplet wavenumber k_d. This gives a Weber number spectrum $We(k)$, which in turn can be used as an indication for the lengthscale at which inertia and surface tension become comparable (i.e. $We(k) \approx 1$, or $We(k) \approx We_{\text{crit}}$ if the critical Weber number is known). This criterion was found to predict the lengthscale at which the droplet distribution transitions into the $d^{-10/3}$ scaling reasonably well, which is known to hold in the breakup dominated range of scales [3]. Our criterion also reduces to the classical Hinze scale when $E(k)$ is of the Kolomogorov form i.e. $E(k) \sim \epsilon^{2/3} k^{-5/3}$.

The importance of the relative resolution between the various length scales that govern turbulence droplet simulations is emphasized. We show that it is important to resolve $N_x > \mathscr{L}$ to correctly capture droplet deformation and breakup at relatively weaker turbulence intensities and high volume fractions, where otherwise the droplet fluid can form a complex tangle of elongated filaments as the maximum droplet deformation becomes unresolved. We also maintain that $\mathscr{L} \gg d \gg \eta$, such that the droplets interact mainly with the inertial range of turbulence.

In line with recent results [20], vorticity is shown to strongly align tangentially to droplet interfaces. This effect was shown to be stronger for higher vorticity magnitudes. The presence of dispersed phase is also shown to significantly alter the flow topology represented by the joint pdf of QR, i.e. the second and third invariants of the velocity gradient tensor, much more acutely than recognized [20]. The well known tear-drop like profile becomes almost flipped across the $R = 0$ axis when sampled inside the droplet in comparison to sampling in the carrier phase. An striking increase in axial straining and vortex compression is found in the droplets, which hints at an interplay of interfacial tension with turbulence, where droplets try to minimize any increase in surface energy by suppressing flow types that cause more deformation - namely bi-axial straining and vortex stretching. This result hints that droplets might cause enhanced dissipation in their interior. The carrier fluid topology retains features of the well known tear-drop profile [76] with only minor increase in axial straining and vortex compression.

Last but not the least, we show for the first time the dynamics of the quasi-equilibrium between coalescence and breakup under constant energy input to the system which leads to sustained turbulence over very long simulation times (around $100\mathscr{T}$). This state

is often called a "steady state", although the dynamics more closely resembles a limit-cycle in the state-space of kinetic energy $\langle E_k \rangle$, enstrophy $\langle \omega^2 \rangle$, droplet number density N_d and surface energy $\langle E_\gamma \rangle$. The extreme values of $\langle E_k \rangle$ manifest in the $\langle \omega^2 \rangle$ evolution with a certain time delay, which then again show up in the N_d evolution leading to a time-delayed dynamics. The dispersion oscillates between two morphologies, the journey between them being mediated by alternating bouts of dominant breakup and coalescence. Surface energy was found to peak prior to droplet breakup, reflecting the underlying breakup mechanism which involves the stretching of droplet fluid filaments, which have a higher surface area than the subsequently formed daughter droplets.

We believe that this time delayed dynamics will be found in localized regions of much larger droplet laden systems, where the overall system may not exhibit significant fluctuations in state-space variables, as the localized fluctuations would cancel each other. However, in smaller, finite systems (as prevalent in turbulence resolving droplet laden simulations [4]), this can be an important consideration, as the "steady state" can have its own interesting dynamics. These considerations of delayed temporal dynamics may also be relevant to developing more realistic breakup and coalescence kernels which currently correlate state-space variables instantaneously [71], which we have not explored given the limits of the current work.

Further investigation of the system evolution in the $\langle E_k \rangle - \langle E_\gamma \rangle$ phase space would help describe the exact exchange of energy, where the effects of coalescence and breakup would need to be isolated. This may be done by simulating larger droplets in weak turbulence, which would correspond to a detailed view on individual droplets near the dissipation range, and it is something we wish to investigate in the future.

We hope that this chapter brings to attention the avenue of considering the details of resolved simulations from different perspectives (as we have attempted, while considering the limitations of our work). This helps reinforce our understanding of the phenomena at different levels. A statistical perspective (looking at spectra, time averaged quantities etc) helps with an overall description, while a dynamical systems perspective on the state-space helps pave the way for deciphering the true mediation of cause and effect like droplet-dissipation interactions and the modification of turbulence due to droplets, which we are only beginning to now understand.

APPENDIX

5.A. CLUSTERING THRESHOLD

In this section we briefly discuss the segmentation of droplets. The simulations output a continuous density field for both components α and β. As mentioned, the density variation of a component indicates the presence of droplets, where the density of component β inside the droplet $\rho_\beta^{\text{in}} \approx 4.4$ and that outside the droplet $\rho_\beta^{\text{out}} \approx 0.4$ [lu] when the flow is fully developed. The droplet identification is done by fixing a threshold density value ρ^{c}. Every contiguous droplet fluid region, i.e. a cluster of neighbouring lattice cells with values above the chosen threshold ($\rho_\beta > \rho^{\text{c}}$), is identified as a droplet. For a point (i, j, k), only the 6 neighbours $(i \pm 1, j \pm 1, k \pm 1)$ are considered in our spatial segmentation (or clustering) algorithm, which was originally developed by Siebesma and Jonker [58]. This is a post-processing step with a single parameter ρ_c, which gives the total number of droplets in the system N_d, the individual droplet volumes V (and equivalent diameters

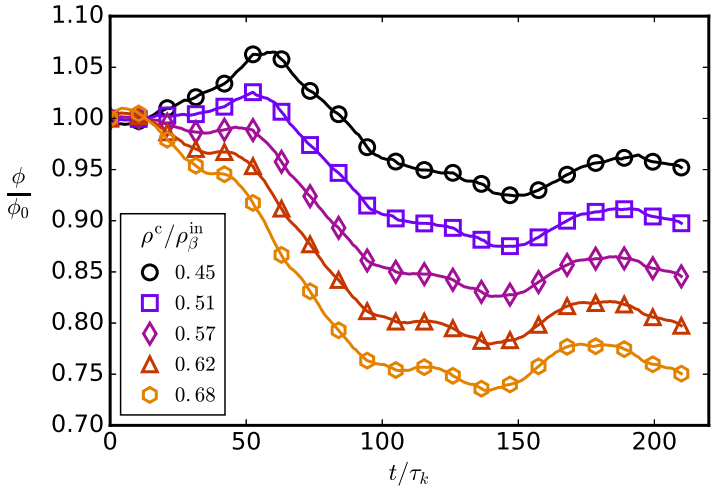

Figure 5.30: Normalized phase fraction evolution for varying ρ^c used to segment droplets. Here ρ^c is reported as a fraction of ρ_β^{in}, while $\rho_\beta^{out}/\rho_\beta^{in} = 0.1$, therefore the useful range of ρ^c/ρ_β^{in} is 0.1 to 1.0, and $\rho^c/\rho_\beta^{in} = 0.55$ is halfway.

$d = (6V/\pi)^{1/3}$), the droplet surface area S_A and the droplet center of mass. These results should not significantly depend on the choice of ρ^c.

As the dispersed phase density values within the interface vary between $0.1\rho_\beta^{in} \leq \rho_\beta \leq \rho_\beta^{in}$, the useful range of thresholding values $\rho^c/\rho_\beta^{in} \in [0.1, 1.0]$, as ρ^c should lie within the interface. Figure 5.30 shows the relative evolution of the volume fraction over time for the case $\phi = 0.06$, for different threshold values around the middle of the usable range. Lower values of ρ^c account for more of the dispersed phase as droplets, which is why the total volume fraction increases as ρ^c decreases. Note that this is not a *physical* increase in volume fraction (as the density field is determined by the dynamics alone) and is only a post-processing estimate - as ρ^c merely differentiates whether a point is inside the droplet region or not. So the choice of ρ^c also determines when a dissolving droplet stops being counted as part of the dispersed phase (though the mass of each fluid is conserved). This is why in figure 5.30, a higher ρ^c gives a lower ϕ, as more small droplets are not counted as part of the dispersed phase.

So although a lower ρ^c gives a higher estimate of ϕ, it may not be the most appropriate choice. This is because the interface is considered to be roughly in the middle of $[\rho_\beta^{out}, \rho_\beta^{in}]$, which is approximately $0.55\rho_\beta^{in}$. The clustering threshold value used in this study, i.e. $\rho^c = 0.57\rho_\beta^{in}$, is very close to the mid-way value. The minor difference between the two values has virtually no influence on the results, and is due to the slight change in the equilibrium density values of the dispersed phase which is difficult to exactly ascertain *a priori*.

Notwithstanding, we verify that our specific choice of ρ^c has little influence on results other than the evolution of ϕ. Figure 5.31 shows the evolution of the number of droplets N_d in the system for different threshold magnitudes, which is seen to have min-

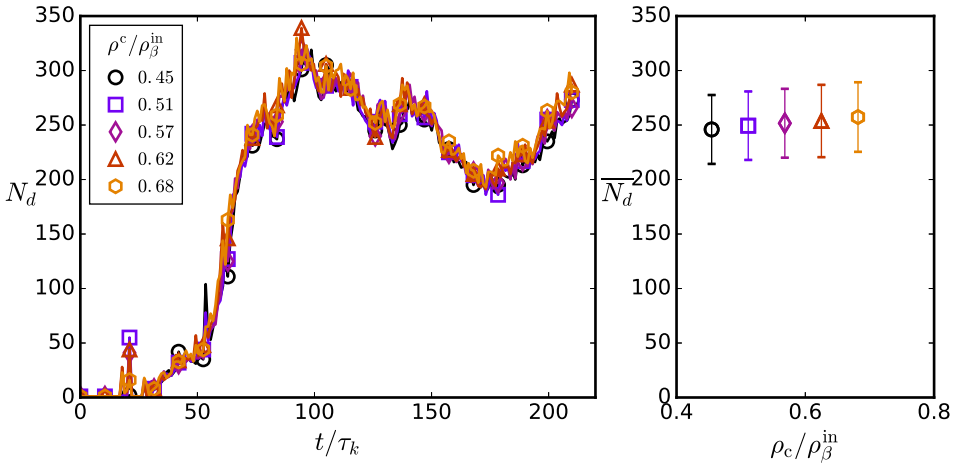

Figure 5.31: Evolution of droplet number density N_d for varying ρ^c shows that the number of droplets identified is almost independent of ρ^c.

imal influence on N_d. Similarly, the droplet distribution was also found to be virtually unaffected by the choice of ρ^c as long as it lies within the droplet interface.

REFERENCES

[1] S. Mukherjee, A. Safdari, O. Shardt, S. Kenjeres, and H. Van den Akker, *Droplet-turbulence interactions and quasi-equilibrium dynamics in turbulent emulsions,* Journal of Fluid Mechanics **878**, 221 (2019).

[2] J. O. Hinze, *Fundamentals of the hydrodynamic mechanism of splitting in dispersion processes,* AIChE Journal **1**, 289 (1955).

[3] G. B. Deane and M. D. Stokes, *Scale dependence of bubble creation mechanisms in breaking waves,* Nature **418**, 839 (2002).

[4] S. Elghobashi, *Direct numerical simulation of turbulent flows laden with droplets or bubbles,* Annual Review of Fluid Mechanics (2019).

[5] D. J. McClements, *Food emulsions: principles, practices, and techniques* (CRC press, 2015).

[6] A. D. Griffiths and D. S. Tawfik, *Miniaturising the laboratory in emulsion droplets,* Trends in biotechnology **24**, 395 (2006).

[7] S. L. Kokal, *Crude oil emulsions: A state-of-the-art review,* SPE Production & facilities **20**, 5 (2005).

[8] I. M. Banat, *Biosurfactants production and possible uses in microbial enhanced oil recovery and oil pollution remediation: a review,* Bioresource technology **51**, 1 (1995).

[9] C. Garrett, M. Li, and D. Farmer, *The connection between bubble size spectra and energy dissipation rates in the upper ocean,* Journal of physical oceanography **30**, 2163 (2000).

[10] M. S. Dodd and A. Ferrante, *On the interaction of taylor length scale size droplets and isotropic turbulence,* Journal of Fluid Mechanics **806**, 356 (2016).

[11] J. J. Derksen and H. E. A. Van den Akker, *Multi-scale simulations of stirred liquid–liquid dispersions,* Chemical Engineering Research and Design **85**, 697 (2007).

[12] P. Perlekar, L. Biferale, M. Sbragaglia, S. Srivastava, and F. Toschi, *Droplet size distribution in homogeneous isotropic turbulence,* Physics of Fluids **24**, 065101 (2012).

[13] L. Biferale, P. Perlekar, M. Sbragaglia, S. Srivastava, and F. Toschi, *A lattice boltzmann method for turbulent emulsions,* in *Journal of Physics: Conference Series*, Vol. 318 (IOP Publishing, 2011) p. 052017.

[14] P. Perlekar, R. Benzi, H. J. H. Clercx, D. R. Nelson, and F. Toschi, *Spinodal decomposition in homogeneous and isotropic turbulence,* Physical review letters **112**, 014502 (2014).

[15] R. Skartlien, E. Sollum, and H. Schumann, *Droplet size distributions in turbulent emulsions: breakup criteria and surfactant effects from direct numerical simulations,* The Journal of Chemical Physics **139**, 174901 (2013).

[16] A. E. Komrakova, D. Eskin, and J. J. Derksen, *Numerical study of turbulent liquid-liquid dispersions,* AIChE Journal **61**, 2618 (2015).

[17] A. W. Pacek, C. C. Man, and A. W. Nienow, *On the sauter mean diameter and size distributions in turbulent liquid/liquid dispersions in a stirred vessel,* Chemical Engineering Science **53**, 2005 (1998).

[18] J. Lovick, A. A. Mouza, S. V. Paras, G. J. Lye, and P. Angeli, *Drop size distribution in highly concentrated liquid–liquid dispersions using a light back scattering method,* Journal of Chemical Technology & Biotechnology: International Research in Process, Environmental & Clean Technology **80**, 545 (2005).

[19] A. Roccon, M. De Paoli, F. Zonta, and A. Soldati, *Viscosity-modulated breakup and coalescence of large drops in bounded turbulence,* Physical Review Fluids **2**, 083603 (2017).

[20] C. Shao, K. Luo, Y. Yang, and J. Fan, *Direct numerical simulation of droplet breakup in homogeneous isotropic turbulence: The effect of the weber number,* International Journal of Multiphase Flow **107**, 263 (2018).

[21] X. Shan and H. Chen, *Lattice boltzmann model for simulating flows with multiple phases and components,* Physical Review E **47**, 1815 (1993).

[22] X. Shan and H. Chen, *Simulation of nonideal gases and liquid-gas phase transitions by the lattice boltzmann equation,* Physical Review E **49**, 2941 (1994).

[23] X. Shan and G. Doolen, *Multicomponent lattice-boltzmann model with interparticle interaction,* Journal of Statistical Physics **81**, 379 (1995).

[24] T. Inamuro, T. Ogata, S. Tajima, and N. Konishi, *A lattice boltzmann method for incompressible two-phase flows with large density differences,* Journal of Computational physics **198**, 628 (2004).

[25] T. Inamuro, S. Tajima, and F. Ogino, *Lattice boltzmann simulation of droplet collision dynamics,* International journal of heat and mass transfer **47**, 4649 (2004).

[26] K. Sun, M. Jia, and T. Wang, *Numerical investigation on the head-on collision between unequal-sized droplets with multiple-relaxation-time lattice boltzmann model,* International Journal of Heat and Mass Transfer **70**, 629 (2014).

[27] A. M. Moqaddam, S. S. Chikatamarla, and I. V. Karlin, *Simulation of binary droplet collisions with the entropic lattice boltzmann method,* Physics of Fluids **28**, 022106 (2016).

[28] A. Montessori, P. Prestininzi, M. La Rocca, and S. Succi, *Entropic lattice pseudopotentials for multiphase flow simulations at high weber and reynolds numbers,* Physics of Fluids **29**, 092103 (2017).

[29] H. Liu, A. J. Valocchi, and Q. Kang, *Three-dimensional lattice boltzmann model for immiscible two-phase flow simulations,* Physical Review E **85**, 046309 (2012).

[30] A. E. Komrakova, O. Shardt, D. Eskin, and J. J. Derksen, *Effects of dispersed phase viscosity on drop deformation and breakup in inertial shear flow,* Chemical Engineering Science **126**, 150 (2015).

[31] A. Gupta and R. Kumar, *Lattice boltzmann simulation to study multiple bubble dynamics,* International Journal of Heat and Mass Transfer **51**, 5192 (2008).

[32] H. Xi and C. Duncan, *Lattice boltzmann simulations of three-dimensional single droplet deformation and breakup under simple shear flow,* Physical Review E **59**, 3022 (1999).

[33] D. Lycett-Brown, I. V. Karlin, and K. H. Luo, *Droplet collision simulation by a multi-speed lattice boltzmann method,* Communications in Computational Physics **9**, 1219 (2011).

[34] A. Gupta and R. Kumar, *Droplet impingement and breakup on a dry surface,* Computers & Fluids **39**, 1696 (2010).

[35] W. Wang, Z. Liu, Y. Jin, and Y. Cheng, *Lbm simulation of droplet formation in microchannels,* Chemical engineering journal **173**, 828 (2011).

[36] H. Liu and Y. Zhang, *Lattice boltzmann simulation of droplet generation in a microfluidic cross-junction,* Communications in computational physics **9**, 1235 (2011).

[37] M. R. Kamali and H. E. A. Van den Akker, *Simulating gas–liquid flows by means of a pseudopotential lattice boltzmann method,* Industrial & Engineering Chemistry Research **52**, 11365 (2013).

[38] L. Chen, Q. Kang, Y. Mu, Y. L. He, and W. Q. Tao, *A critical review of the pseudopotential multiphase lattice boltzmann model: Methods and applications,* International journal of heat and mass transfer **76**, 210 (2014).

[39] D. L. Albernaz, M. Do-Quang, J. C. Hermanson, and G. Amberg, *Droplet deformation and heat transfer in isotropic turbulence,* Journal of Fluid Mechanics **820**, 61 (2017).

[40] O. Shardt, J. J. Derksen, and S. K. Mitra, *Simulations of droplet coalescence in simple shear flow,* Langmuir **29**, 6201 (2013).

[41] P. Berghout and H. E. A. Van den Akker, *Simulating drop formation at an aperture by means of a multi-component pseudo-potential lattice boltzmann model,* International Journal of Heat and Fluid Flow **75**, 153 (2019).

[42] A. Zarghami, N. Looije, and H. E. A. Van den Akker, *Assessment of interaction potential in simulating nonisothermal multiphase systems by means of lattice boltzmann modeling,* Physical Review E **92**, 023307 (2015).

[43] S. Mukherjee, A. Zarghami, C. Haringa, K. van As, S. Kenjereš, and H. E. A. Van den Akker, *Simulating liquid droplets: A quantitative assessment of lattice boltzmann and volume of fluid methods,* International Journal of Heat and Fluid Flow **70**, 59 (2018).

[44] A. N. Kolmogorov, *Dissipation of energy in locally isotropic turbulence,* in *Akademiia Nauk SSSR Doklady*, Vol. 32 (1941) p. 16.

[45] O. Shardt, S. K. Mitra, and J. J. Derksen, *The critical conditions for coalescence in phase field simulations of colliding droplets in shear,* Langmuir **30**, 14416 (2014).

[46] T. Krüger, H. Kusumaatmaja, A. Kuzmin, O. Shardt, G. Silva, and E. M. Viggen, *The Lattice Boltzmann Method* (Springer, 2017) pp. 297–329.

[47] S. Succi, *The lattice Boltzmann equation: for fluid dynamics and beyond* (Oxford university press, 2001).

[48] K. Alvelius, *Random forcing of three-dimensional homogeneous turbulence,* Physics of Fluids **11**, 1880 (1999).

[49] V. Eswaran and S. B. Pope, *An examination of forcing in direct numerical simulations of turbulence,* Computers & Fluids **16**, 257 (1988).

[50] C. Rosales and C. Meneveau, *Linear forcing in numerical simulations of isotropic turbulence: Physical space implementations and convergence properties,* Physics of fluids **17**, 095106 (2005).

[51] A. Ten Cate, J. J. Derksen, L. M. Portela, and H. E. A. Van den Akker, *Fully resolved simulations of colliding monodisperse spheres in forced isotropic turbulence,* Journal of Fluid Mechanics **519**, 233 (2004).

[52] A. Ten Cate, E. Van Vliet, J. J. Derksen, and H. E. A. Van den Akker, *Application of spectral forcing in lattice-boltzmann simulations of homogeneous turbulence,* Computers & fluids **35**, 1239 (2006).

[53] L. Scarbolo, D. Molin, P. Perlekar, M. Sbragaglia, A. Soldati, and F. Toschi, *Unified framework for a side-by-side comparison of different multicomponent algorithms: Lattice boltzmann vs. phase field model,* Journal of Computational Physics **234**, 263 (2013).

[54] P. Moin and K. Mahesh, *Direct numerical simulation: a tool in turbulence research,* Annual review of fluid mechanics **30**, 539 (1998).

[55] B. R. Pearson, T. A. Yousef, N. E. L. Haugen, A. Brandenburg, and P. Krogstad, *Delayed correlation between turbulent energy injection and dissipation,* Physical Review E **70**, 056301 (2004).

[56] A. Tsinober, *An informal conceptual introduction to turbulence*, Vol. 483 (Springer, 2009).

[57] Y. Li, E. Perlman, M. Wan, Y. Yang, C. Meneveau, R. Burns, S. Chen, A. Szalay, and G. Eyink, *A public turbulence database cluster and applications to study lagrangian evolution of velocity increments in turbulence,* Journal of Turbulence , N31 (2008).

[58] A. P. Siebesma and H. J. J. Jonker, *Anomalous scaling of cumulus cloud boundaries,* Physical review letters **85**, 214 (2000).

[59] S. Popinet and T. Jones, *Gts: Gnu triangulated surface library,* (2004).

[60] G. Windreich, N. Kiryati, and G. Lohmann, *Voxel-based surface area estimation: from theory to practice,* Pattern Recognition **36**, 2531 (2003).

[61] Z. Yu and L. S. Fan, *An interaction potential based lattice boltzmann method with adaptive mesh refinement (amr) for two-phase flow simulation,* Journal of Computational Physics **228**, 6456 (2009).

[62] P. Yue, C. Zhou, and J. J. Feng, *Spontaneous shrinkage of drops and mass conservation in phase-field simulations,* Journal of Computational Physics **223**, 1 (2007).

[63] A. Freund and A. Ferrante, *Decomposing the wavelet spectrum of droplet-laden isotropic turbulence,* Bulletin of the American Physical Society (2018).

[64] F. Lucci, A. Ferrante, and S. Elghobashi, *Modulation of isotropic turbulence by particles of taylor length-scale size,* Journal of Fluid Mechanics **650**, 5 (2010).

[65] A. Alexakis and L. Biferale, *Cascades and transitions in turbulent flows,* Physics Reports (2018).

[66] H. Chen, B. M. Boghosian, P. V. Coveney, and M. Nekovee, *A ternary lattice boltzmann model for amphiphilic fluids,* Proc. R. Soc. Lond. A **456**, 2043 (2000).

[67] F. Toschi and E. Bodenschatz, *Lagrangian properties of particles in turbulence,* Annual review of fluid mechanics **41**, 375 (2009).

[68] J. T. Davies, *Drop sizes of emulsions related to turbulent energy dissipation rates,* Chemical Engineering Science **40**, 839 (1985).

[69] N. Vankova, S. Tcholakova, N. D. Denkov, I. B. Ivanov, V. D. Vulchev, and T. Danner, *Emulsification in turbulent flow: 1. mean and maximum drop diameters in inertial and viscous regimes,* Journal of Colloid and Interface Science **312**, 363 (2007).

[70] J. A. Boxall, C. A. Koh, E. D. Sloan, A. K. Sum, and D. T. Wu, *Droplet size scaling of water-in-oil emulsions under turbulent flow,* Langmuir **28**, 104 (2011).

[71] B. Sajjadi, A. A. A. Raman, R. S. S. R. E. Shah, and S. Ibrahim, *Review on applicable breakup/coalescence models in turbulent liquid-liquid flows,* Reviews in Chemical Engineering **29**, 131 (2013).

[72] A. Pumir and M. Wilkinson, *Orientation statistics of small particles in turbulence,* New journal of physics **13**, 093030 (2011).

[73] A. Roy, A. Gupta, and S. S. Ray, *Inertial spheroids in homogeneous, isotropic turbulence,* Physical Review E **98**, 021101 (2018).

[74] A. Ooi, J. Martin, J. Soria, and M. S. Chong, *A study of the evolution and characteristics of the invariants of the velocity-gradient tensor in isotropic turbulence,* Journal of Fluid Mechanics **381**, 141 (1999).

[75] M. S. Chong, A. E. Perry, and B. J. Cantwell, *A general classification of three-dimensional flow fields,* Physics of Fluids A: Fluid Dynamics **2**, 765 (1990).

[76] J. M. Chacin and B. J. Cantwell, *Dynamics of a low reynolds number turbulent boundary layer,* Journal of Fluid Mechanics **404**, 87 (2000).

[77] D. W. I. Rouson and J. K. Eaton, *On the preferential concentration of solid particles in turbulent channel flow,* Journal of Fluid Mechanics **428**, 149 (2001).

[78] M. J. Bijlard, R. V. A. Oliemans, L. M. Portela, and G. Ooms, *Direct numerical simulation analysis of local flow topology in a particle-laden turbulent channel flow,* Journal of Fluid Mechanics **653**, 35 (2010).

[79] P. Perlekar, D. Mitra, and R. Pandit, *Direct numerical simulations of statistically steady, homogeneous, isotropic fluid turbulence with polymer additives,* Physical Review E **82**, 066313 (2010).

6

CONCLUSIONS AND OUTLOOK

6.1. CONCLUSIONS

EMulsification is a physical process, which over a century of research, investigation and experiments, has become reasonably controllable in some settings, and yet we have only begun to unravel the underlying processes behind it. Part of this dissonance comes from the difficulty of probing emulsions experimentally to study the dynamics, which is inherently three dimensional, and is an outcome of strong interactions between the dispersed and continuous phases. Most experimental studies hence inform empirical modelling of averaged quantities, like droplet size distributions, coalescence and breakup rates modeled in the form of kernels and modification of mean turbulence quantities - all without explaining the mechanisms. This has led to a wealth of models that populate the literature, and are used without any deeper understanding of the system.

Of course, it poses the question whether a deeper understanding would greatly improve industrial processes. Why do we need to model this system from the bottom-up? I shall quote three of the sixteen reasons suggested by Epstein [1] in favour of modelling beyond its first obvious goal of prediction - (1) to *"explain"*, (2) *"illuminate core dynamics"* and (3) *"discover new questions"*. With the work presented in this thesis, it is these three aspects that have been highlighted most prominently. While the first two of these is what one begins to probe with their inquiry, the third erupts serendipitously.

We began with an intercomparison of the volume-of-fluid (VoF, as available in OpenFOAM and FLUENT) and pseudopotential lattice-Boltzmann method (using Palabos) to ascertain and quantify the relative strengths and weaknesses of the two methods. One of the main findings was that different numerical methods can give disparate results when simulating *physical* problems (an issue not evident if one only applies them to numerical benchmarks). Both methods had strong points in favour, and few points against them. Briefly, these were the freedom to independently vary density/viscosity ratio and interfacial tension in VoF as opposed to computational speed, spontaneous phase segregation and low spurious currents in PP-LB. For a new practitioner, depending very much on the problem they wish to simulate, it would be useful to first try to apply the VoF method to their problem, for its conceptual simplicity, ease of use and ready availability

in commercial codes and open-source CFD packages. It is relatively easy to implement different boundary conditions, initial conditions, and freely vary surface tension, density ratio and viscosity ratio in this method, which make it very valuable, particularly when applied to relatively simple flows and pure fluid mixtures, in parameter ranges not dominated with spurious currents. It may also be worthwhile to consider the Level-Set method for multiphase flows. For more complex multiphase flow situations, like those involving turbulence, the computational cost of finite volume methods increases tremendously, in which case LB simulations are an attractive alternative.

For the purpose of this study, we chose PP-LB, since it was better suited for our needs, namely (1) simulation of surfactants via relatively easy extensions to the model, and (2) the possibility of simulating coalescence and breakup in turbulence at significantly lower computational cost than finite-volume methods. We then modeled surfactant laden emulsions by considering a three component PP-LB system. The surfactant was shown to reduce surface tension following a Langmuir-like isotherm. This behaviour arose naturally from fundamental particle interactions, without any such form of surface tension reduction being pre-set in the model. However, the model lacked a mechanism for coalescence inhibition, though similar effects could be simulated by varying the liquid-liquid repulsion strength by utilizing the information on local surfactant density. Further improvements to the model will be required before surfactant effects can be simulated to a degree that coincides strongly with observed surfactant induced effects in real emulsions. More accurate calculations of the surfactant diffusion to the interface can be performed by simulating a clean pendant droplet formed and hanging on a capillary tip in a surfactant laden matrix phase. Changes in the droplet shape due to surfactant diffusion to the interface will allow estimating the diffusion coefficient using the Ward Tordai equation.

Next, we incorporated a low-wavenumber turbulence forcing scheme in our LB framework for a single-phase fluid. Since turbulence forcing schemes have been well studied and validated over time, we instead focused on a more fundamental, important aspect, namely the emergence of structures in turbulence, which are essential to its composition. We focused on spatial structures arising in the velocity and vorticity fields, which are hard to define but are often invoked in describing turbulence as a superposition of 'eddies'. We introduced new mathematical tools (correlation pseudo-vectors) for identifying particular flow patterns, namely regions of parallel flow streamlines associated with high local field values and regions with swirling flow streamlines associated with high vorticity in the core of these regions. Using the specific form of the Helmholtz decomposition applicable for divergence-free flows—the Biot-Savart law—we were able to disentangle the local and non-local vorticity contributions, in a Biot-Savart sense, in generating these structures. High kinetic energy regions were found to be consistently *jet-like*. It was found that, due to their low vorticity content, these structures are not self-generating. Strong vorticity regions also contribute negligibly to the generation of high kinetic energy regions, and their coherence was found to be almost entirely induced by non-local intermediate vorticity contributions. Regions of high vorticity, which form vorticity 'worms', on the other hand, were found to be associated with *swirling-flow* structures (as has been found before [2]). The Biot-Savart reconstruction shows that swirling flow regions are a superposition of intermediate background vorticity induced flow and a degree of self-generating swirl. These results reveal the structure of

turbulence in a new light, showing the spatial organization of high kinetic energy and high vorticity regions. Upon the addition of particles, or droplets, to turbulent flows, these structures may be modified due to inhibition/enhancement of certain inter-scale interactions, which remains to be studied.

We finally simulate turbulent emulsions, reverting back to two pure fluids (ignoring the surfactant). The PP-LB method is shown, for the first time, to be capable of simulating turbulent emulsions over long durations in certain regions of the parameter space governing the problem (for a chosen numerical resolution of the simulation grid). In these regions of the parameter space, droplet dissolution is a minimal effect which does not influence the results or dynamics, and this numerical artifact can be further alleviated by increasing the resolution of the droplets with respect to the interface width. Several new findings regarding the emulsification process are presented. These include the droplet distribution with its associated power laws for purely inertial droplet breakup, coalescence and breakup effects on the energy spectra, modification of turbulence topology, and state-space dynamics of the turbulent emulsion when it attains a quasi-equilibrium state. The evolution of state-space variables as time delayed limit cycles casts into doubt the usual practice of modelling the droplet number density and distribution as instantaneous functions of flow quantities like the turbulent kinetic energy and energy dissipation rate. A generalization of the classical Hinze scale is also proposed, which is valid for dense and dilute suspensions alike, and it does not ignore the effect of coalescence. It is used to predict the critical lengthscale separating breakup and coalescence dominated droplet scales. These findings also show that a lot of modelling assumptions, that are believed to be obvious, might require reassessment.

6.2. NATURE VIS-À-VIS NUMERICS

A crucial aspect, that should not go unattended, is the discord between natural phenomena and our attempts to model them (in this case numerically). While one is the truth, the other grapples to be in its vicinity. This section serves as a brief reflection on whether, and if so then under which circumstances, the results presented in this thesis can be considered representative of the physical reality.

The most important phenomena, at the heart of our work, are the breakup and coalescence of droplets. Droplet breakup poses a first great challenge that the moment of breakup is a singular event [3, 4], as the collapsing fluid bridge eventually passes through a radius of zero. This event also has associated aspects that are quite non-trivial. First is that near breakup, there is usually a strong asymmetry across the collapsing fluid bridge, which goes against any naive assumption of a symmetric (hourglass-like) interfacial profile before breakup [5]. The collapsing fluid bridge, via an eventual change in topology, leads to two separate, receding interfaces, which is the instant of droplet breakup (or bifurcation). Further, the interfacial shape (the cross-section of the collapsing fluid bridge and its neighbourhood) has been conjectured to be self similar [4–7]. Since the local length and timescales involved are of decreasing magnitude before breakup, the process can hold no memory of any initial conditions - which means that droplet bifurcation is a universal phenomena no matter the original causes for a droplet breaking apart. In coalescence, the reverse happens when the thin liquid film between approaching interfaces drains out, and there is a first point of contact between the two interfaces. This happens at a lengthscale where even the thermal fluctuations of the film begin to play a role in

determining film drainage times [8].

The main difference between nature and numerics (or theory) here is one that brings to mind Tsinober's observation regarding turbulence [9] - *"It is of importance to make at the outset a clear distinction between the phenomenon and the problem of turbulence - just like between the observations and the theories attempting to explain them, which are far from being synonymous"*. In nature, there are no distinctions like a continuum description or a particle description. Continuum behaviour 'emerges' from more fundamental molecular interactions, which in turn emerge from even more fundamental field-particle interactions - the entire edifice being a hierarchy of emergence. Natural phenomena, hence, can appear to pass through different levels of description quite smoothly. Our tools of analysis, theories and equations are sufficiently well suited to describe phenomenon at different levels of detail, but are not conducive for traversing across different descriptive levels. An example to the point is the Laplace law for pressure across a static droplet which holds for finite droplet radii (a continuum description), although during breakup, the radius passes through zero which is a point of singularity (where clearly the continuum description breaks down). Another example would be molecular dynamics simulations where individual molecules and their interactions are resolved, and these can be used to simulate, for instance, nano-droplets. It is inconceivable to use such simulations for the situations described in this thesis, primarily due to the number of molecules required for representing a macroscopic system.

The fact that none of the current multiphase CFD models will accurately reproduce physical phenomena like droplet breakup across different levels of detail is a trivial point at best. The real question is whether accurately resolving the entire breakup process, across all levels, is *necessary* to say *anything* meaningful about droplet breakup at all through simulations. And there the answer is, of course, that one can make reasonable estimates for approximate breakup times, very close to the real values observed in experiments. The self similarity of the breakup process works in favour of this, since near breakup, the length and timescales get successively smaller, and these contribute to the 'overall' description only infinitesimally. The resolution of this level of detail is beyond the scope of flow resolving simulations, and also unnecessary.

Coalescence is more difficult to address, and is tied to a more glaring difference between reality and simulations, i.e interfaces are very thin surfaces in real systems, while in diffuse interface simulations (like in PP-LB, or VoF), they extend over a few grid cells. The ratio of the droplet diameter d to interface width ζ in real systems is of the order $\mathcal{O}(10^6)$ (for a millimeter sized droplet with an interface extending over a nanometer). In simulations, this ratio can vary depending on the detail to which coalescence is being resolved. In simulations of binary droplet collision, where focus is on an individual coalescence event, d/ζ may be of the order $\mathcal{O}(10^2)$ or more. For turbulent emulsion simulations, such a high grid resolution is not possible at the individual droplet scale, due to the proliferation of multiple droplets, and there this ratio can be anywhere in the range of $\mathcal{O}(10^0) - \mathcal{O}(10^2)$, depending on the droplet size. Here, the difference with physical systems is irreconcilable, and reality is grossly under-represented.

Further, whether droplets coalescence also depends on the relative resolution of the droplet size to the interface width [10], such that in the limit of infinite resolution $d/\zeta \rightarrow \infty$, coalescence would cease to occur as there will always be a thin liquid film separat-

ing the interfaces[1]. Droplets in diffuse interface methods coalesce when the grid resolution is not large enough to resolve the fluid film between interfaces, in which case the interfaces overlap. Hence, having a finite value of d/ζ is important in these simulations. To be able to simulate coalescence at much finer resolutions, additional numerical procedures will be required. These may be models developed using detailed studies of interfacial rupture phenomena, accounting for molecular or physiochemical properties, to cause spontaneous interfacial rupture in the simulations based upon a critical separation distance between droplets. Doing so, traditionally, would require simulating the droplet phase as a separate numerical mesh where surfaces can be cut and merged, which comes at a high computational cost and additional issues regarding the generation of acceptable mesh topologies and conservation of mass. However, in simulations with a finite d/ζ, statistical or integral quantities like droplet size distributions, kinetic energy spectra and dissipation rates may be expected to more closely resemble real systems, since successively smaller which will be resolved as $d/\zeta \to \infty$, should only have a small effect on the overall statistics.

6.3. FUTURE WORK

So far, very few studies have looked into the details of emulsification with numerical simulations that resolve both turbulence and interfacial dynamics. This is because only recently (over the past decade or so), it has become feasible to perform these computationally demanding simulations. Part of the reason is, of course, the increase in computational power, but the more empowering factor is the combination and development of the relevant numerical tools that enable resolved simulations. The algorithmic simplicity and computational speedup of the lattice-Boltzmann method gives it the upper hand for turbulent emulsion simulations as far as the current state of numerical methods is concerned, with the main drawback of interfaces being diffuse and its associated issues like droplet dissolution and enhanced coalescence.

The most interesting questions worth studying next that follow from this thesis have been discussed below, and have been characterized into two categories. First are a few fundamental issues regarding droplet-laden turbulence, while the second aims at its more applied aspects, relevant from the point of view of modelling turbulent emulsions for general industrial applications. The two are related issues, however, where the first informs the second.

6.3.1. FUNDAMENTAL ISSUES REGARDING DROPLET-LADEN TURBULENCE

As simulations begin to reveal droplet-turbulence interactions in a new degree of detail, it shall become possible to study the following phenomena, leading to new fundamental insights about droplet-laden turbulence.

[1] This is in a way reminiscent of Zeno's paradox of measure, for instance see [11]. Paraphrased, one of its statements is that "to arrive at her destination, a traveler must first cover half the distance, then another half of the remainder i.e. 1/2, then 1/4th, then 1/8th, *ad infinitum*". Similarly, each time in a diffused interface method, when interfaces are about to overlap leading to coalescence, an increase in the grid resolution will lead to an additional thin layer of fluid that will separate the interfaces, preventing coalescence.

ORIENTATION OF DROPLETS

Our study showed a time delayed limit-cycle dynamics of the state-space variables. This is an interesting finding, although how the observed effects are mediated, needs to be further investigated. One question that has come to the fore is how enstrophy interacts with droplets, since strong vortical motion has been shown to align parallel to the interfaces (as shown in Chapter 5 of this thesis, and originally shown by Shao *et al.* [12]). Enstrophy then causes interfacial wrinkling and breakup. The increase in axial straining and vortex compression also indicates that vorticity *inside* droplets possibly aligns with the droplet axis (considering a sheared droplet to be like an elongated ellipsoid). In this configuration, surface tension would tend to compress the droplet along its axis, hence causing vortex compression. It has been shown that sub-Kolmogorov ellipsoidal objects indeed align with the local vorticity vector [13, 14]. This is due to the preference of rigid, oblate objects to spin along their major axis instead of tumbling in turbulent flow.

For simulations with low volume fractions of the dispersed phase, droplets remain spatially separated with fewer coalescence events and can more or less be approximated as deformed ellipsoids. How they align with the background strain and vorticity fields will reveal the dynamics of deformation in more detail.

INTERFACES SAMPLING THE STRAIN FIELD

How droplets modify the flow was also shown in Chapter 5. There is an increase in vortex compression inside droplets, as well as a predominance of axial strain as opposed to bi-axial strain. Since droplets are deformable elastic objects, their interfaces can oscillate (further depending on the presence of surfactants [15]), which in turn generates smaller scale flow motions. A further question worth investigating is what is the probability distribution of the three strain eigenvalues at the droplet interfaces, along with in the droplet interiors and the continuous fluid region, and how this depends on the Weber and Reynolds numbers. This has been shown already to an extent with the QR joint probability distribution plots presented in Chapter 5 since Q and R can be calculated from the strain eigenvalues. Additional questions to be studied are how the QR distributions vary with distance from interfaces and what their distributions are in the immediate vicinity of the interfaces. This will show how elastic material surfaces sample and influence the strain field, which is closely tied to the generation of excess surface energy due to droplet deformation. A first step in this direction has already been taken, with the recent work of Dodd and Jofre [16], albeit for the case of decaying homogeneous isotropic turbulence.

DROPLETS AND INTERMITTENCY

A related fundamental question is also regarding the effect of droplets on intermittency. For two simulations with the same amount of energy dissipation $\langle\epsilon\rangle$, where one is single-phase and the second droplet laden, it is worth looking into the differences in the probability distribution of vorticity and dissipation. This will quantify the effect of droplets on spatial intermittency. Since droplet coalescence generates smaller scales, there is an increase in the dissipation range energy content, which contributes to global energy dissipation. However, these vortical motions have dynamical origins vastly different from the small-scale intermittent vorticity generated by the dynamics of single-phase turbulence. Hence, despite the same amount of energy dissipation, the spatial dissipation and

vorticity fields can be expected to differ for single-phase and droplet laden turbulence. The additional question would be how this depends on the Weber number and volume fraction.

DROPLETS IN THE DISSIPATION RANGE

The current study focused on the breakup of droplets in the inertial range, where the smallest droplets in the system were still sufficiently larger than the Kolmogorov scale η. In most DNS, η is comparable to the grid size, which generates the maximum separation of scales and the highest possible Re_λ. There are a few reasons for considering a different system, where the droplet sizes $d \sim \eta$. This in principle can be be easily done by weakening the turbulence forcing intensity, which will generate a flow with a lower Re_λ which has a higher η and a relatively larger Hinze scale.

Apart from the benefit that this will eliminate dissolution of small droplets in the system (as was shown by Komrakova *et al.* [17]), this system can be used to better investigate the interplay of kinetic energy, surface energy and dissipation. At sufficiently weak turbulence intensities, the droplet diameter may be comparable to or smaller than the Hinze scale, with only deformation and fluctuations of the interface. Since this droplet does not undergo breakup, the additional complexity due to coalescence and breakup to the changes in surface energy is excluded. Pal *et al.* [18] showed that droplet deformations follow multifractal dynamics for droplets in 2D turbulence. This can be studied for realistic droplets in 3D, and the dynamics of the interface can be directly compared to the kinetic energy and dissipation dynamics and fluctuations.

With this established, a simpler system with a few large droplets can be studied to gradually introduce coalescence and breakup effects, which will be resolved in greater detail than in the dense suspensions considered in this thesis.

INCLUDING SURFACTANTS IN TURBULENT EMULSIONS

This was the original aim of this thesis, but unfortunately it was not possible to perform these simulations for a few reasons. First was that the turbulent emulsions numerical setup took time to develop. It was found that the multiphase fluid models used for the surfactant-laden emulsions study (Chapter 3), which were based on non-ideal fluids, attained weak phase-segregation with decreasing viscosity (while a low viscosity was required to generate turbulence). This could in principle be remedied by using much larger domains with higher viscosity values, or by changing the collision operator. A more feasible alternative was to use simpler fluid models, which maintained strict phase-segregation at low viscosity values, while using the BGK collision operator.

It is conceptually easy to introduce a third surfactant component to the turbulent emulsions numerical framework, although, it would require detailed testing to ascertain the model behaviour like surface tension reduction. Secondly, the original surfactant model was shown to be incapable of simulating coalescence inhibition. Before adding surfactants to turbulent emulsions, this would be an important intermediate step. Lastly, droplet dynamics in clean systems posed enough new questions - proceeding with a much more complicated physics with surfactants would be naive before we improve our understanding of clean systems to a higher degree.

Chapter 5 is a step in the direction of improving what we know about emulsification. After a closer look at the system energetics and dispersion formation, now one can begin

to include surfactants. With a mechanism for surfactant induced coalescence inhibition, significant changes to the evolution of surface energy and droplet number density can be expected. This will also have consequences for dissipation of kinetic energy, as once a characteristic morphology is formed with a typical distribution around the Hinze scale, further breakup and coalescence may not be possible due to the shielding of coalescence. This will be in contrast to the surfactant free dispersions considered in Chapter 5 - where coalescence and breakup dominated dynamics ensue cyclically.

EXPLORING A WIDER RANGE OF FLUID PROPERTIES

A further important extension to this study would be simulations that span a wider range of the parameter space of fluid properties, since the investigation in Chapter 5 was limited to a density and viscosity ratio of unity. Emulsions encountered in practice are very often composed of fluids with a large density and viscosity ratio. A change in viscosity ratio between the droplet fluid and continuous fluid will also influence several aspects of the dynamics, at times significantly. For instance, viscous damping of the flow in the droplet interior will cause an additional viscous resistance to droplet breakup, as opposed to a purely surface tension driven resistance to breakup for inviscid droplets. There will be a change in the droplet response to deformations, an interplay between surface tension and viscosity effects, and consequently, the droplet breakup mechanism that is at play can be modified. It is known that increasing dispersed phase viscosity leads to a broadening of the droplet size distribution, with an increase in the number of smaller satellite droplets, and a decrease in the number of large droplets whose size increases as well [19], which reflects a change in the underlying breakup mechanism [20].

The definition of the Hinze scale, i.e. the maximum stable droplet diameter, assumes a inviscid droplet phase and a dilute suspension (i.e. ignoring coalescence effects). In Chapter 5, the generalization of the Hinze scale to a Weber number spectrum was done to include the average effect of coalescence in determining the approximate, stable droplet scale. With droplets of a higher viscosity, a further modification of the Hinze scale is required to account for the influence of a dimensionless viscosity group on the dynamics [19]. Calculation of the multiphase kinetic energy spectra, to generate a Weber number spectra, will also need to be done while considering a sharp change in the velocity profile across the interface at high viscosity ratios. It might be more suitable to use the wavelet spectra in such a case, which allows for sharp changes in the field values without adversely effecting the spectra.

Hints regarding the changes in the breakup mechanism may be found from a similar, or extended analysis, to the one presented in Chapter 5. For instance, for the same turbulence intensity, at high viscosity ratios, when the droplet distribution broadens, the generation of a higher number of satellite droplets will be reflected in the evolution of the droplet number density N_d and surface energy E_γ. The breakup dominated arm of the breakup-coalescence dynamic equilibrium will begin to yield higher values of N_d. The time-delayed intermittency correlation between N_d and E_γ may also change when extreme droplet deformation is resisted by viscous droplets, which instead form more satellite droplets, which are smaller and usually spherical. In this case, peaks in the evolution of E_γ will begin to coincide with peaks in the evolution of N_d, rather than preceding them. Changes will also be found in the turbulence flow topology inside the droplets, where the flow will become more quiescent at higher viscosities. This may lead to a sup-

pression of extreme velocity gradients, hence shrinking the distribution of the velocity gradient invariants to a smaller region centered around low values.

To describe breakup mechanisms more explicitly (and more accurately), an extension of the droplet segmentation (clustering) algorithm is required, which can track droplets over their life-cycles. This will allow studying the droplet "history", comprising the evolution of the typical scale of velocity fluctuations acting over the droplet, and the change in distribution of surface and inertial forces around the droplet, which can then be linked to the event of droplet breakup to reveal details of the mechanisms at work.

From an implementation perspective, the viscosity ratio between the droplet and continuous fluid can be varied, for instance, by using the model of Porter *et al.* [21], which also considers a multicomponent LB system. The current model used in Chapter 5 does not allow varying the viscosity and density ratio much. The method of Porter *et al.* [21] ensures viscosity-independent equilibrium densities (which will help in maintaining a low viscosity in the continuous phase, important for sustaining turbulence), while also maintaining low spurious currents using a higher isotropy inter-fluid interaction term. These modification, together with the turbulence forcing mechanism, can be used to study turbulent emulsions of varying viscosity ratios.

EXPERIMENTAL MEASUREMENT OF DROPLET DISTRIBUTIONS AND VELOCITY FIELDS

Lastly, many of these simulation results still need to be experimentally verified, which is still a distant hope as emulsions remain elusive to the experimental eye. Bridging experiments and simulations will soon be the major hurdle, as highly resolved numerical simulations are slowly becoming the norm. Although most of the qualitative features reproduced in simulations can be expected to be found in experiments, true prediction relies on quantitative agreement between the two. Only in tandem can experiments and simulations benefit each other.

Experimentally, a major challenge is to characterize droplet sizes *during* emulsification, including the dynamical aspect to droplet distributions. Typically, a sample of the emulsion after its formation is collected and then analyzed *ex situ*, although optical techniques have been applied to measure these distributions *in-situ* [22, 23]. Deane and Stokes [24] had similarly reported the dynamical bubble size distribution for breaking waves. The greater challenge is to measure velocity components and gradients (to quantify the strain fields and dissipation) locally. These may be the most elusive to measure currently, but will be the most important for a fuller synthesis of simulation and experiment.

6.3.2. PRACTICAL APPLICATIONS

The essence of all the detailed understanding of coalescence and breakup eventually should be distilled in well informed 'kernels'. Kernels are simply models for coalescence and breakup applied in large scale flow simulations which cannot resolve droplet level dynamics and can only incorporate dispersed phase effects via population balance modelling. Simulations on larger systems often cannot even resolve the flow due to the separation of scales involved, and in turn rely on turbulence modelling (for instance the $k-\epsilon$ model prevalent in RANS simulations). This makes the overall modelling a twofold problem, where inaccuracies of one model will amplify inaccuracies in the other. As it

goes, there are a plethora of droplet dynamics models (see the review by Sajjadi *et al.* [25]) drawn from various simplified experiments.

The extrapolation from small scales to large scales is not straightforward, since droplet dynamics inherently differs across scales. Within smaller regions of droplet laden turbulent flow, coalescence and breakup compete and there is significant fluctuation of state-space variables, while larger fluid parcels are convected around in swarms. Simplified kernels may not be accurate in bridging these different aspects. Detailed information regarding the evolution of droplet size distributions and droplet-turbulence interactions is needed for improving current kernel formulations. For instance, the finding that state-space variables evolve as time delayed limit cycles (Chapter 5), implies that using instantaneous variables like E_k and ϵ to predict droplet number densities (virtually all the models presented in Sajjadi *et al.* [25]) and morphology is not accurate. This particular example may not significantly influence the outcome of kernel modelling as the fluctuations in quantities are local phenomena which on an average cancel out for larger systems, but it shows that many implicit assumptions in the general modelling approach may not be correct. This is only aggravated by the fact that these models are not robust and depend upon the type of flow.

One of the aims would be to improve the formulation of these kernels by incorporating as much of the dynamics as required. The findings from droplet orientation in flow and their response to the background strain field can greatly benefit modelling droplet deformations. For a typical Re_λ of the flow, typical strain rate distributions can be found, which in turn can translate into deformation distributions. Studying turbulence mediated droplet breakup more closely, better predictions can be made regarding the probability of droplets breaking apart when experiencing a typical turbulent shear. Similarly, the probability for droplet collisions and associated changes to the droplet size distribution can be better understood via resolved simulations. These simulations would greatly benefit if coupled with a Lagrangian tracking algorithm for droplets, which can be used to track droplets over their lifecycles in turbulence - this is required to pin point droplet breakup and coalescence events - which is essential to accurately determine the frequency and efficiency of these events.

Lastly, incorporating surfactant effects into these kernels is another additional step. These effects first need to be identified via resolved simulations, and the surfactant 'strength' needs to be quantified in a robust sense (as having surfactant specific results will add another parameter to the modelling approach, which has no dearth of parameters to begin with). Surfactant effects will most likely translate into reduced coalescence efficiency, in turn manifesting as a shift in the droplet size distribution. This in turn can be expected to also alter the energetics, as small stable droplets deform less, hence extracting less energy from the flow for the excess surface energy of deformations. Reduced coalescence will reflect in a weaker enhancement of the dissipation range. Since the droplet interface becomes more rigid due to the surfactants, the free-slip boundary condition turning into a no-slip boundary condition will cause increased energy dissipation due to additional gradients being generated. Overall, the modification of the energy spectra may more closely resemble turbulence laden with solid spheres, while the modification to flow topology will reflect the presence of elastic interfaces, as vortex stretching and bi-axial strain will still be counteracted by the elastic interfaces, although the overall velocity gradients inside the droplet will also be damped due to a reduced internal

circulation.

6.4. OUTLOOK

This thesis shows how numerical simulations can be a powerful tool for unravelling complex flows, and highly non-linear physical systems in general. Simulations also allow greater control over the 'numerical experiments', which are repeatable, and are not sensitive to external factors like experiments tend to be. The caveats here are that typically a smaller region of the associated phase-space can be spanned (with current computational abilities) and numerics can introduce its own uncertainties. The major challenge such work must deal with is using models that closely approximate physical phenomena, often involving painstaking code validation and benchmarking. The reward, however, is access to complex fields in unparalleled detail, resolved both in space and time. Such a view into the heart of a physical process, even under limitations, can shed new light on the mediation of causes and effects, reveal new aspects of the problem that were unknown, and open new channels for questioning our understanding.

The topic of turbulent emulsions has only been briefly breached upon with this work, and a lot remains to be done. As detailed simulations, like those presented in this work, become the norm, and additional complexities are included in the modelling, the domain of numerical research will begin to approach realistic multiphase flow scenarios. A similar effort will be required on the part of experimental research, to test the many new findings from simulations. Eventually, when the two proceed in tandem, it will become feasible to develop more accurate models for the complex processes that underlie the dynamics of larger systems involving droplets in turbulence. Even so, most of our understanding shall remain mostly 'phenomenological', since none of the examined phenomena can be divined from the equations of fluid dynamics, and only upon observing them are relations drawn, if at all, to the underlying conservation laws. Perhaps in the future, with newer theories, we will be able to fashion our understanding of dynamical systems after more abstract, yet 'conceivable', notions, like sets of 'structures' that emerge in these systems, their 'interactions' and 'life-cycles'. This would require understanding the system beyond the equations alone, which perhaps are so fundamental that their essence is divorced from our everyday experience of reality. Building such a different perspective will also first require breaking the 'artificial compartmentalization'[2] of the sciences, and to instead consider a natural process for just what it actually is—*a symphony of natural order.*

REFERENCES

[1] J. M. Epstein, *Why model?* Journal of Artificial Societies and Social Simulation **11**, 12 (2008).

[2] Z.-S. She, E. Jackson, and S. A. Orszag, *Intermittent vortex structures in homogeneous isotropic turbulence,* Nature **344**, 226 (1990).

[3] H. A. Stone and L. G. Leal, *Relaxation and breakup of an initially extended drop in an otherwise quiescent fluid,* Journal of Fluid Mechanics **198**, 399 (1989).

[2] As famously opined by *Richard Feynman* regarding the divisions we have drawn between the various sciences.

[4] P. Constantin, T. F. Dupont, R. E. Goldstein, L. P. Kadanoff, M. J. Shelley, and S.-M. Zhou, *Droplet breakup in a model of the hele-shaw cell,* Physical Review E **47**, 4169 (1993).

[5] D. H. Peregrine, G. Shoker, and A. Symon, *The bifurcation of liquid bridges,* Journal of Fluid Mechanics **212**, 25 (1990).

[6] J. B. Keller and M. J. Miksis, *Surface tension driven flows,* SIAM Journal on Applied Mathematics **43**, 268 (1983).

[7] T. F. Dupont, R. E. Goldstein, L. P. Kadanoff, and S.-M. Zhou, *Finite-time singularity formation in hele-shaw systems,* Physical Review E **47**, 4182 (1993).

[8] D. G. Aarts and H. N. Lekkerkerker, *Droplet coalescence: drainage, film rupture and neck growth in ultralow interfacial tension systems,* Journal of fluid mechanics **606**, 275 (2008).

[9] A. Tsinober, *The essence of turbulence as a physical phenomenon,* Dordrecht: Springer **10**, 978 (2014).

[10] O. Shardt, J. Derksen, and S. K. Mitra, *Simulations of droplet coalescence in simple shear flow,* Langmuir **29**, 6201 (2013).

[11] B. Skyrms, *Zeno's paradox of measure,* in *Physics, philosophy and psychoanalysis* (Springer, 1983) pp. 223–254.

[12] C. Shao, K. Luo, Y. Yang, and J. Fan, *Direct numerical simulation of droplet breakup in homogeneous isotropic turbulence: The effect of the weber number,* International Journal of Multiphase Flow **107**, 263 (2018).

[13] A. Pumir and M. Wilkinson, *Orientation statistics of small particles in turbulence,* New journal of physics **13**, 093030 (2011).

[14] A. Roy, A. Gupta, and S. S. Ray, *Inertial spheroids in homogeneous, isotropic turbulence,* Physical Review E **98**, 021101 (2018).

[15] A. Piedfert, B. Lalanne, O. Masbernat, and F. Risso, *Numerical simulations of a rising drop with shape oscillations in the presence of surfactants,* Physical Review Fluids **3**, 103605 (2018).

[16] M. S. Dodd and L. Jofre, *Small-scale flow topologies in decaying isotropic turbulence laden with finite-size droplets,* Physical Review Fluids **4**, 064303 (2019).

[17] A. E. Komrakova, D. Eskin, and J. Derksen, *Numerical study of turbulent liquid-liquid dispersions,* AIChE Journal **61**, 2618 (2015).

[18] N. Pal, P. Perlekar, A. Gupta, and R. Pandit, *Binary-fluid turbulence: Signatures of multifractal droplet dynamics and dissipation reduction,* Physical Review E **93**, 063115 (2016).

[19] R. V. Calabrese, T. Chang, and P. Dang, *Drop breakup in turbulent stirred-tank contactors. part i: Effect of dispersed-phase viscosity,* AIChE Journal **32**, 657 (1986).

[20] R. V. Calabrese, S. M. Kresta, and M. Liu, *Recognizing the 21 most influential contributions to mixing research,* Chemical Engineering Progress **110**, 20 (2014).

[21] M. L. Porter, E. Coon, Q. Kang, J. Moulton, and J. Carey, *Multicomponent interparticle-potential lattice boltzmann model for fluids with large viscosity ratios,* Physical Review E **86**, 036701 (2012).

[22] J. A. Boxall, C. A. Koh, E. D. Sloan, A. K. Sum, and D. T. Wu, *Measurement and calibration of droplet size distributions in water-in-oil emulsions by particle video microscope and a focused beam reflectance method,* Industrial & Engineering Chemistry Research **49**, 1412 (2009).

[23] A. Khalil, F. Puel, Y. Chevalier, J.-M. Galvan, A. Rivoire, and J.-P. Klein, *Study of droplet size distribution during an emulsification process using in situ video probe coupled with an automatic image analysis,* Chemical Engineering Journal **165**, 946 (2010).

[24] G. B. Deane and M. D. Stokes, *Scale dependence of bubble creation mechanisms in breaking waves,* Nature **418**, 839 (2002).

[25] B. Sajjadi, A. A. A. Raman, R. S. S. R. E. Shah, and S. Ibrahim, *Review on applicable breakup/coalescence models in turbulent liquid-liquid flows,* Reviews in Chemical Engineering **29**, 131 (2013).

OUTREACH

JOURNAL PAPERS

4. **Mukherjee, S.**, Mascini, M., Portela, L.M. *Identifying and disentangling flow structures in turbulence: insights into turbulence organization*, To be submitted to Journal of Fluid Mechanics (2019).

3. **Mukherjee, S.**, Safdari, A., Shardt, O., Kenjeres, S. and Van den Akker, H.E.A., *Droplet-turbulence interactions and quasi-equilibrium dynamics in turbulent emulsions*, Journal of Fluid Mechanics, 878, 221-276 (2019).

2. **Mukherjee, S., Berghout, P.** and Van den Akker, H.E.A., *A lattice-Boltzmann approach to surfactant laden emulsions*, AIChE Journal, 65(2), 811-828, (2019).

1. **Mukherjee, S.**, Zarghami, A., Haringa, C., van As, K., Kenjeres, S. and Van den Akker, H.E.A., *Simulating liquid droplets: A quantitative assessment of lattice Boltzmann and Volume of Fluid methods*, International Journal of Heat and Fluid Flow, 70, 59-78, (2018).

CONFERENCE PAPERS

1. **Mukherjee, S.**, Zarghami, A., Haringa, C., Kenjeres, S. and Van den Akker, H. E., *A comparative assessment of lattice Boltzmann and volume of fluid (VOF) approaches for generic multiphase problems*, Proceedings of the 9th International Conference on Multiphase Flow.

CONFERENCE PRESENTATIONS

10. Physics at Veldhoven, Netherlands — Jan 2019

9. APS Division of Fluid Dynamics (APS-DFD2018), Atlanta, USA — Nov 2018

8. Burgers symposium, Lunteren, Netherlands — Jun 2018

7. Netherlands Process Technology Symposium, University of Twente, Netherlands — May 2018

6. Turbulence from Angstrom to Light Years, ICTS, Bangalore, India — Jan 2018

5. ISPT Water Cluster meeting, Amersfoort, Netherlands — Oct 2017

4. Discrete Simulation of Fluid Dynamics (DSFD2017), Erlangen, Germany — Jun 2017

3. Burgers Symposium, Lunteren, Netherlands — May 2017

2. Burgers Symposium, Lunteren, Netherlands — May 2016

1. International Conference of Multiphase Flows (ICMF2016), Florence, Italy — May 2016

OTHERS

- Cover image for the biography of J.M. Burgers, edited by Prof. Jan V Sengers and Prof. Gijs Ooms, published by J.M. Burgerscentrum Research School for Fluid Mechanics.

PROPOSITIONS

1. Multiphase flow solvers are a democratic lot. (*Chapter 1, this thesis*)
2. "*Big whorls are streams, potential / surrounding, mild curls generate them.*
   Small whorls are lonely whirlwinds / yet, experts tend to venerate them."
   (*Chapter 4, this thesis*)
3. The Weber number spectrum is a suitable generalization of the Hinze scale.
   (*Chapter 5, this thesis*)
4. Describing the equilibrium behaviour of a dynamical system as "statistically steady" is a euphemism for "ignoring the dynamics". (*Chapter 5, this thesis*)
5. Turbulence is best studied in a "box", when you can think out of the box.
6. What happens in Fourier space, stays in Fourier space.
7. Experimentalists do whatever they can, while numericists do whatever they want.
8. Science is a lot like photography in that one can only be taught *how* to look, but not *where* to look.
9. Keywords surrounding research have gone from "informing" in the manner of road-signs to "buzzing" in the manner of flies.
10. The Graduate School's penchant for the taxonomy of people's personalities is the art of classifying multiple outliers into a handful of boxes.
11. A limit on the cumulative output of a researcher will immensely improve the quality of scientific papers.
12. The collective intelligence of large populations is due to non-additive emergence, and can equally well appear or disappear.
13. Awards in the sciences and the arts say more about the jury than about the winners.
14. Past struggles were mostly to obtain *freedom from*, future struggles shall be for *freedom to*.

These propositions are regarded as opposable and defendable, and have been approved as such by the promotor prof. dr. ir. H.E.A. Van den Akker.

ACKNOWLEDGEMENTS

To paraphrase Emerson - “I cannot remember all the interactions, any more than all the meals, I’ve had: even so, they have made me.” I thank everyone who has been a part of this journey, big or small, and would like to go on and extend my gratitude to those who shaped the past years.

My motivation to do a PhD derived largely from how much I enjoyed my MSc research, so I’ll start by thanking **Harm** and **Jerome**, for the exciting research experience, and for instilling in me an everlasting passion for dynamical systems and chaos. Your support in my quest to find a PhD was crucial, and I also thank **Patrick** who pointed me to the Transport Phenomena (TP) group.

Sasa and **Rob**, I remember walking into the Waterzaal to give you an ‘informal’ presentation about my MSc research, followed by a Skype meeting with **Harry**. You were all generous enough to believe I could work on this project, and I joined TP as a PhD student in February 2015, knowing precious little about Chemical Engineering and multiphase flows. I want to thank you all for giving me the chance to work on this exciting topic, in this excellent group.

Harry, I cannot imagine having done this PhD without the freedom you gave me to follow my interests. You helped arrange a few visits to Limerick, when our work required more collaboration, and that proved invaluable in shaping this thesis. Many thanks for your kindness and patience, the good humour that lit up every meeting I eagerly looked forward to, your peppering of anecdotes and stories, sharp insights and often deep questions I didn’t know how to answer; not to mention your famed “scrupulous corrections” to my writing, of which I’d read much about in the Acknowledgements of other PhD theses. All of this greatly shaped my thinking, and I thank you for teaching me, by example, that research is best enjoyed as a lifestyle.

Sasa, you’ve been extremely supportive in all my work, and it was always good to have you readily available for a quick discussion, which I always enjoyed. Learning about the history of fluids research, with all your stories about science over lunch and coffee, along with your passion for teaching, have all been very inspiring. Your extensive knowledge of scientific literature is humbling, and I hope to instill a healthy reading habit from you. Also thanks for sharing my interest in art and data visualization, one day we will make it to the “Gallery”.

Rob, we met only a couple of times during my PhD, and yet all those meetings contributed either to my understanding or to shaping my research direction, since you always manage to ask the right questions. We miss your vibrant presence at TP.

At one point I was a little worried about how (or whether) I shall be able to proceed with my research, without an expert in lattice-Boltzmann around for detailed discussions. I then came to Limerick and met you **Orest**. The frequent, short meetings we had, helped me bridge many gaps in my understanding and in defining research directions - this thesis would not have taken shape without your ready guidance. The challenge to

keep up with your leaps of thought and flashes of insight made all discussions a great learning experience, and I look forward to future collaborations.

Luis, you were on sabbatical at the time I joined TP. I got to first know you through all the lunch talks with your (in)famous questions (which have now mellowed, too bad for the "new generation"). It has been a pleasure and privilege to work with you on our quest to identify turbulence structures, which has inverse-cascaded to become a much larger pursuit for an initial "side-project". I hope our post-Marxist, neo-modernist view of turbulence gains some traction over time, as we continue our efforts to disentangle myth from reality. For all the exciting discussions ranging from "time", the "distant-stars" to culture, arts and poetry, the many evening drinks and travels - *muito obrigado*.

Also thanks to **Chris**, for your efforts in keeping the group together through outings, movie nights and lunch talks, and **David**, for keeping our spirits up with your good humour. To avoid continuity errors, I will start with thanking everyone from the two research groups that I spent time with during this project.

Anton and **Bernhard**, thanks for welcoming me to join your office, when I started, which was a lively affair with your ever present humour. **Anton**, many thanks for helping me out with OpenFOAM and programming, which saved me from a couple of months worth of *sturm und drang*. **Ahad**, it was great to collaborate with you, thanks for all the LB help and tips. You also made our trips to distant Amersfoort more enjoyable. **Koen**, I enjoyed our sushi dinners, and talks over camera gear we both couldn't afford. Shifu-**Wenjie**, **Gerasimos** and **Kevin**, our valiant attempts at starting a (not-just) "Science club" will not be forgotten. **Wenjie**, your hot-pot stands unsurpassed to date, and I greatly enjoyed all our talks. **Gerasimos**, breaking our heads over Project Euler problems, that remained unsolved, was a nice exercise. You are a true icon of Greek wisdom, while being so utterly humble and kind. **Kevin**, your enthusiasm for teaching, physics and programming have been unmatched; I've learnt a lot from you on all these fronts. **Hrushikesh**, it was always fun to agree-to-disagree over this, that and the other. I enjoyed all our discussions, and also benefited a lot from your knowledge of CFD. **Chirag**, your energy (specially at the FOM@Veldhoven conference after dinner) was contagious - TP has since missed a fun colleague of your calibre. **Annekatrien**, you've been great company for lunch, and the most regular. Thanks for being the repository of anecdotes and Dutch culture, for encouraging my humble gallery and for your excellent cookies (also for ensuring our plants don't die).

Manu and **Elin**, it was great to go to Udine together. **Manu**, it has been good fun discussing the ultimate laminar regime, all the walks and coffee breaks we've had, and the occasional Tamil songs when the office was empty. **Elin**, apart from bothering you about all HPC and Bash issues, I've learnt a lot from you about German culture (although you deny having it), European law (and lawlessness) and the ever elusive beast that is "correctness" (I hope it is correct to say this). **Romana**, you've been great help with filching FOM wine, and we still need to make the "Hall of fame" for CTP students. **Saeid**, it is a miracle you finally got the driving license, **Xiaolin** and **Peng**, you've been great officemates, and thanks for the Chinese lessons. **Manas**, your bubbly personality lights up all our banter, when we get to see you once in a while. You also prove the adage that "man is a *social* animal". **Mattheus**, your company is great fun, with all the randomness we spew around, you now need to randomize your weekends (to be found elsewhere than TP). **Evert** and **Christiaan**, I shall not let our memorable day trip to Belgium for a few

beers fade to black in memory. Also thanks **Evert** for constantly reminding me that experimentalists do real science, while numericists have a better sense of humour.

Dries, **Cees**, **Maulik** and **Anand**, the book-club crew, you've been great company all these years. **Dries**, I enjoy all our hobnobbing and impromptu plans for dinners, drinks and concerts, specially with you being a pleasure to strike a conversation about anything with, sessions that I hope time will only increase in number, but I'll stop before this sentence breaches Middlemarch proportions. Thanks for translating my Summary so masterfully. **Cees**, the sharp edge of your wit always cut through any mundanity that dared fall upon our office. I recall the Ecast evenings of yore, plant shopping for the new office (in pouring rain) and your Russian Roulette pies, which were *to die for*. Your erudition in music, pop-culture, science and politics steers our many salon-socialism evenings from falling dry into ever greener pastures! **Maulik**, you're a true confidante, specially through all the stochastic times. It's a privilege to count such a selfless and kind person among one's friends. I fondly recall our many Idola trips, ISPT and Lunteren voyages, and the almost-misadventure that was Atlanta - I look forward to more (controlled) fun times! **Anand**, you're a great source of wisdom, be it on fluid mechanics or life itself, with the added spark of your personality that shines through all darkness and distances (specially the far reaches of Wageningen). Thanks for the many dinner invitations, which made me miss Tamil Nadu a little less. Also thanks to my colleagues **Niels**, **Snehal**, **Harish**, **Rajat**, **Ozgur**, **Saidah**, **Fei**, comrade **Artem**, **Iman**, **Lorenz**, **Rose**, **Debasish** and **Andre**, for making it a whole, and **Bries**, **Kosta** and **Valeria** - welcome to TP!

I had the pleasure to work with some excellent BSc students. **Rik** and **Martijn** - I learnt more than a thing from your excellent Python skills, and about the behaviour of sheared droplets. **Merlijn**, your project on turbulence structures seems to have set off a different clockwork. Thanks for your hard work and almost effortless ease of navigating the abstract. I also want to thank the Masters and Bachelors students who kept the group alive. From the Waterzaal days - **Jelle**, **Joep**, **Madelon**, **Harm**, **Shaikh**, **Kris**, **Boris**, **Rubin**, **Jorne**, **Ruiz**, **Jaap**, **Kelbij**, **Sagar**, **Sherwin**, you made it all memorable. Although much changed with the move to the new building, we still managed to feel more group-like thanks to **Pranav**, **Manu**, **Arvind**, **Amit**, **Dimitrios**, **Jorrit**, **Jonathan**, **Yoran**, **Roland**, **Adriana**, **Julia**, **Stefan**, **CC**, **Doedo**, **Katarina**, **Rense**, **Eva**, **Anne**, **Bob**, **Alireza** and all the others. Many thanks to the secretaries of TP and Chem-E, **Anita**, **Elly**, **Jennifer**, **Fiona**, **Sandra** and **Astrid**, for making sure things worked out well, and for always being available for help.

Victor, **Rita**, **Joana** and **Deborah**, the Botanical garden borrels were great fun. **Victor**, thanks for spreading the gospel of EasyBuild, and for all the programming and OpenFOAM sessions - I'll also remember the great sub-genre concert we attended. Many thanks to my **PPE** friends from across the corridor, for saving the coffee breaks and Friday borrels from dying out. **Shaurya**, your wicked sense of humour is always a delight, and your ability to joke about immediate worries in light of a bigger picture is a great lesson. **Kartik**, I've always left rejuvenated after a chat with you, with all the stand-up references that refuse to get old. **Aswin**, **Dominik** and **Isabell**, you taught me the true meaning of "one last drink at Doerak" - it was never to be taken literally, and **Dominik**, your pizzas are a hit! **Georg**, **Zaid** and **Alvaro**, it's on you to keep traditions alive now. Also many thanks to **Durgesh**, **Dayinta**, **Fabio**, **Hamid**, **Damiano** and **Robert**.

My visits to Limerick wouldn't be the same without the great folks of Bernal. Many

thanks to **Pieter**, **Arman** and **Mohammad** for being involved in my research. **Pieter**, you were a pleasure to collaborate with, and taught me the art of "*leven als God in Frankrijk*". I fondly recall the late evening chalkboard discussions we had (because "late morning" discussions, which we had more of, don't sound as impressive), and it was a respite to have someone to share so many common interests with, right from Gould to Godel. **Arman**, I enjoyed working on turbulent emulsions with you, specially when I had the reassurance that someone far better than me in numerics and programming had navigated the labyrinth called Palabos. **Mohammad**, thanks for the discussions and the memorable Iranian dinner.

Corne, you managed to get universal scaling, atleast in the exhaust of your car. I thoroughly enjoyed the trips in and around Limerick with you, specially the decadent milk-market mornings. **Sinead**, you shall do Skibbereen doubly proud with your research and baking skills, if not triply for your partying skills as well. **Sudarshan**, thanks for the many dinners and fun conversations, along with our mutual admiration of the LB *thalaivaa*. **Leila**, your cooking and painting skills are unique. **Neda**, I've missed your "polite" remarks, and **Brian**, your quick witticisms. **Lucas**, **Robert**, **Akim**, **Sulaiman**, **Gayathri**, **Rory**, **Gustavo**, **Laurent**, **Shaza**, **Shayon**, **Melissa** - you lit up the many breaks, outings, Stables sessions and dinners with quintessential *craic*. I may now confess that I was always keen to get back to Limerick, more to meet you all. Lastly, thanks **Sarah** and **Aisling** for helping organize my visits to UL.

The four months I spent in Ireland, each time coincidentally during the infamous Irish winters, were made comfortable by the warmth and hospitality of **Mary**, **Paddy** and **Grainne**. **Mary**, you've been a wonderful host, and I fondly recall our dinner table chats over books, culture and often the modern-day lack of it - your unabashed humour was refreshing, and your stews therapeutic. **Paddy**, thanks for inviting us to your lovely cottage in Clare, I shall remember the musical evening in Kilshanny's pub and the Cliffs of Moher. **Grainne**, thanks for cooking for me so often, a privilege I only associate with "home". You all made me love a culture and its people, by being the essence of all that's good about them. Also thanks to **Martha**, **Irene**, **Cahl**, and young **Finnley**. **Vinnie**, **Mohammad**, **Robert**, **Hamid** and **Sulaiman**, you were all great house-mates.

Back to Delft, **Marlijn** and **Andrea**, thanks for being such good friends, and my Piano teachers. **Marlijn**, knowing you since my first year in Delft, I'm thankful for all the lessons, chats and dinners over the years, and specially for making me a small part of your family. It's been great to get to know the Helder-ian quirks up close. **Andrea**, I've greatly enjoyed our many talks and lessons, and your positivity is contagious. Now that you've moved to India, perhaps I can continue my lessons in Bangalore sometime soon. **Jaap**, thanks for teaching me the "*doka-yoga*" as you call it. It helped me immensely in slowing down and rethinking photography, and the darkroom has been a good distraction from my work from time to time. Maestro **Florian**, **Celia**, **Felix**, **Rita** - you've been great darkroom friends. **Florian** and **Felix**, it was fun to exhibit our "ordinary" analog work at the Rotterdam Photo Festival - "Urban Identity" shall go on and take newer shapes and forms I hope - thanks for being such inspiring artists. **Florian** and **Celia**, I can't wait to visit you in Hamburg. **Eduardo** (Mendez) and **Stephen** (Picken), it is reassuring to see someone trying to bring the arts into the unbearable austerity of dry academics. **Sujata**, thanks for involving us in some of your work - I look forward to more collaborations and interesting discussions.

Lucia, thanks for trying to teach us the art of tiramisu - the many dinners together were great fun. **Kanta**, if you read this, call once in a while, I'm beginning to forget your rambling. **Satyaki**-dada, thanks for all the wonderful (and traumatic) Spacebox memories, which shall serve us a lifetime, they were indeed "*the best of times*". **Sonakshi**, thanks for mending **Satyaki**'s ways a little. Madame **Kaveri**, the movie and dinner nights at the "Biryani Boys" were a delight, specially when they descended into a long discussion over common woes, we've missed those dearly since you crossed the Atlantic. **KC**, somehow each time we meet, time doesn't seem to have passed much and we pick up where we left off, so until next time. **Adarsha** and (Siddharth) **Rajkumar**, the jam-and-tea sessions were great fun, perhaps at the cost of the neighbours' Sunday afternoon quiet. **Daniela**, thanks for always being available for a coffee and a chat, and **Radu**, for helping her baking skills soar higher than DARE. **Shu-Meng** and **Kai**, from Calcutta to Den Haag, it's been great to know you both (you three, now onward).

Shriya, thanks for being such good company, and **JP**, we should still plan to meet outside of Jumbo sometime. **Niharika**, for being around the corner but always randomly meeting at the TU. **Michał**, knowing you since my first day in Delft, you've showed that one can learn (and master) anything, with the solitary force of sincere effort. You also did the unthinkable - make Vodka taste *good*, when had the right (your) way. **Zaneta** and **Take**, thanks for the Tango lessons, and for being such good friends who are great photography subjects. **Anisa**, your creativity knows no bounds. I mean it does, but it is also boundless. It is bound by the boundless (I'm calling this one "knows"). Thanks for being such an inspiration and a riot!

Soumya, I'm not sure if you consume more memes, more TV shows or more aloo, but I'm glad for all three, which we shall continue sharing for long with Madan-da's blessings. **Tulika**, thanks for being party to this madness. **Faisal**, I'm glad to have met a fellow Faiz-lover, except it's a pity life seems to bear more fidelity to Elia. Dr. Sahab (**Udai**), what can I say - it has been a pleasure, and our evening ritual has been the most constant respite through it all. I hope I haven't been as much of a bother. **Tarini**, **Prateek**, **Rekha** aunty and **Mani** mama, your visits always brought a welcome break. **Daniel**, from the spacebox days, to our India and Italy trips, to the Copenhagen evenings - it has all been unexpected, and make my days a shade brighter. Many thanks for your support, and for being such an inspiration, I'm at a loss of slovos for your inimitable presence. Also thanks to **Sneha**, **Majken** and **Zoe**, for making my Copenhagen trips memorable.

Tushar and **Peeyush**, you've been paradoxically the greatest leg-pullers who've also given the strongest shoulders to stand upon. **Tushar**, one day we will be as great as Baba's shadow, do not despair. **Shefin**, **Thomas** and **Savio**, thanks for keeping the spirit of VIT alive and for being so dependable. **Faiz**, you've shown that the sieve of time leaves behind very few. Thanks for being a part of every journey I remember. **Sanjna**, your kindness is reassuring and your crookedness refreshing, thanks for meeting all my inanities so zealously with yours. **Jason**, you've set standards a bit too high on all fronts. Knowing you has been a sheer joy, from talking Ghazals to turbulence, and now it's also a privilege to have a close friend and collaborator in Powai - to many years of working together! **Dhruv**, we've had some unforgettable trips from the desolate Mara and quaint Madras Katcheris to the nondescript Mandya - I look forward to many more with your fine Tamil-Oxonian company.

Madhumita ma'am, thanks for being an irreplaceable source of hope, wisdom and

happiness all my life, and for truly wearing your deep values of empathy and humility. Many thanks to **Ranjana** ma'am, **Waseema** ma'am, **Lalti** ma'am, **Chandana** ma'am, **Shahid** sir and all my teachers from Woodbine Gardenia school, for your continued support and blessings. Thanks **Sushil** bhaiya for always being there. Many thanks to **Joydeep** kaku, **Kundu** kaku and **Javed** sir, for your counsel and support.

To my family in Pondicherry, your unbridled love and encouragement give me strength and purpose beyond measure - my gratitude to **Rama-di**, **Sudha-di**, **Swadhin-da**, **Priti-di**, **Manoj-da**, **Kati** and **Arul**-anna. **Ghosh-sir**, thank you for making all of this possible, from the crucible of GDN101 and the sanctum of Vaithikuppam, I shall truly scorn to change my state with kings for it all.

It is a little vain to "thank" you **Dadu** and **Achhima** for making our lives the centre of your own. Your love has meant the world to me. **Dadu**, it took me a while to realize your work also revolved around emulsions. You would have been the happiest, among all, to hold this thesis, so this is for you. **Didi**, **Ma** and **Papa**, your support, love, blessings, prayers, and encouragement to follow my heart, almost to a fault, have been my biggest strength. None of this would be possible without you. **Guddu**-bhaiya, thanks for being part of the family, and ever so reliable. Finally, the Mother - *to thee my infinite gratitude.*

CURRICULUM VITÆ

Siddhartha Mukherjee was born on 13th of July 1989, in Kanpur, India. He finished his primary and secondary education from Woodbine Gardenia School, Kanpur, in 2008. He went on to do a Bachelors (BTech) in Mechanical Engineering from the Vellore Institute of Technology (VIT), Vellore, Tamil Nadu, India, graduating in 2012.

He then came to TU Delft in 2012, on a DRI Climate Scholarship, for a Masters in Mechanical Engineering with a specialization in Fluid Mechanics. During his Masters, he did a brief research internship at the Royal Netherlands Meteorological Institute (KNMI), Utrecht, in 2013. He worked in the Atmospheric Physics group at TU Delft for his MSc thesis on the predictability of dry convective boundary layers, graduating in 2014. Siddhartha then joined the Transport Phenomena group as a PhD student in 2015, in the Department of Chemical Engineering, TU Delft. Here he worked on turbulent emulsions, and a project on the identification of structures in turbulence fields. His research interests include non-linear dynamics and chaos, complex flows, turbulence and the emergence of structure and self-organization in physical systems.

Also interested in art and music, Siddhartha is a street/documentary photographer (a member of the international Progressive-street collective), and does both digital and analog/darkroom photography. Some of his work was exhibited in the Rotterdam Photo Festival, in Feb 2019. He also works intermittently on generative art, and introduced an Algorithmic Art course in the ACT Lab of the TU Delft Culture Center. He likes to dabble with playing music, and greatly enjoys reading literature and poetry.